Journal of Applied Mathematics

Uncertainty-Based Design Optimization in Engineering: Model, Algorithm, and Application

Guest Editors: Xiaojun Wang, Zhiping Qiu, and Dirk Söffker

Uncertainty-Based Design Optimization in Engineering: Model, Algorithm, and Application

Journal of Applied Mathematics

Uncertainty-Based Design Optimization in Engineering: Model, Algorithm, and Application

Guest Editors: Xiaojun Wang, Zhiping Qiu, and Dirk Söffker

Copyright © 2013 Hindawi Publishing Corporation. All rights reserved.

This is a special issue published in "Journal of Applied Mathematics." All articles are open access articles distributed under the Creative Commons Attribution License, which permits unrestricted use, distribution, and reproduction in any medium, provided the original work is properly cited.

Editorial Board

Saeid Abbasbandy, Iran
Mina B. Abd-El-Malek, Egypt
Mohamed A. Abdou, Egypt
Subhas Abel, India
Mostafa Adimy, France
Carlos J. S. Alves, Portugal
Mohamad Alwash, USA
Igor Andrianov, Germany
Sabri Arik, Turkey
Francis T.K. Au, Hong Kong
Olivier Bahn, Canada
Roberto Barrio, Spain
Alfredo Bellen, Italy
Jafar Biazar, Iran
Hester Bijl, The Netherlands
Anjan Biswas, Saudi Arabia
Stephane P.A. Bordas, USA
James Robert Buchanan, USA
Alberto Cabada, Spain
Xiao Chuan Cai, USA
Jinde Cao, China
Alexandre Carvalho, Brazil
Song Cen, China
Qianshun S. Chang, China
Tai-Ping Chang, Taiwan
Shih-sen Chang, China
Rushan Chen, China
Xinfu Chen, USA
Ke Chen, UK
Eric Cheng, Hong Kong
Francisco Chiclana, UK
Jen-Tzung Chien, Taiwan
C. S. Chien, Taiwan
Han H. Choi, Republic of Korea
Tin-Tai Chow, China
M. S. H. Chowdhury, Malaysia
Carlos Conca, Chile
Vitor Costa, Portugal
Livija Cveticanin, Serbia
Eric de Sturler, USA
Orazio Descalzi, Chile
Kai Diethelm, Germany
Vit Dolejsi, Czech Republic
Bo-Qing Dong, China
Magdy A. Ezzat, Egypt
Meng Fan, China
Ya Ping Fang, China
Antonio J. M. Ferreira, Portugal
Michel Fliess, France
M. A. Fontelos, Spain
Huijun Gao, China
Bernard J. Geurts, The Netherlands
Jamshid Ghaboussi, USA
Pablo González-Vera, Spain
Laurent Gosse, Italy
K. S. Govinder, South Africa
Jose L. Gracia, Spain
Yuantong Gu, Australia
Zhihong GUAN, China
Nicola Guglielmi, Italy
Frederico G. Guimarães, Brazil
Vijay Gupta, India
Bo Han, China
Maoan Han, China
Pierre Hansen, Canada
Ferenc Hartung, Hungary
Xiaoqiao He, Hong Kong
Luis Javier Herrera, Spain
J. Hoenderkamp, The Netherlands
Ying Hu, France
Ning Hu, Japan
Zhilong L. Huang, China
Kazufumi Ito, USA
Takeshi Iwamoto, Japan
George Jaiani, Georgia
Zhongxiao Jia, China
Tarun Kant, India
Ido Kanter, Israel
Abdul Hamid Kara, South Africa
Hamid Reza Karimi, Norway
Jae-Wook Kim, UK
Jong Hae Kim, Republic of Korea
Kazutake Komori, Japan
Fanrong Kong, USA
Vadim . Krysko, Russia
Jin L. Kuang, Singapore
Miroslaw Lachowicz, Poland
Hak-Keung Lam, UK
Tak-Wah Lam, Hong Kong
PGL Leach, Cyprus
Yongkun Li, China
Wan-Tong Li, China
J. Liang, China
Ching-Jong Liao, Taiwan
Chong Lin, China
Mingzhu Liu, China
Chein-Shan Liu, Taiwan
Kang Liu, USA
Yansheng Liu, China
Fawang Liu, Australia
Shutian Liu, China
Zhijun Liu, China
Julián López-Gómez, Spain
Shiping Lu, China
Gert Lube, Germany
Nazim Idrisoglu Mahmudov, Turkey
Oluwole Daniel Makinde, South Africa
Francisco J. Marcellán, Spain
Guiomar Martín-Herrán, Spain
Nicola Mastronardi, Italy
Michael McAleer, The Netherlands
Stephane Metens, France
Michael Meylan, Australia
Alain Miranville, France
Ram N. Mohapatra, USA
Jaime E. Munoz Rivera, Brazil
Javier Murillo, Spain
Roberto Natalini, Italy
Srinivasan Natesan, India
Jiri Nedoma, Czech Republic
Jianlei Niu, Hong Kong
Roger Ohayon, France
Javier Oliver, Spain
Donal O'Regan, Ireland
Martin Ostoja-Starzewski, USA
Turgut Öziş, Turkey
Claudio Padra, Argentina
Reinaldo Martinez Palhares, Brazil
Francesco Pellicano, Italy
Juan Manuel Peña, Spain
Ricardo Perera, Spain
Malgorzata Peszynska, USA
James F. Peters, Canada
Mark A. Petersen, South Africa
Miodrag Petkovic, Serbia

Vu Ngoc Phat, Vietnam
Andrew Pickering, Spain
Hector Pomares, Spain
Maurizio Porfiri, USA
Mario Primicerio, Italy
Morteza Rafei, The Netherlands
Roberto Renò, Italy
Jacek Rokicki, Poland
Dirk Roose, Belgium
Carla Roque, Portugal
Debasish Roy, India
Samir H. Saker, Egypt
Marcelo A. Savi, Brazil
Wolfgang Schmidt, Germany
Eckart Schnack, Germany
Mehmet Sezer, Turkey
Naseer Shahzad, Saudi Arabia
Fatemeh Shakeri, Iran
Jian Hua Shen, China
Hui-Shen Shen, China
Fernando Simões, Portugal
Theodore E. Simos, Greece
Abdel-Maksoud A. Soliman, Egypt
Xinyu Song, China
Qiankun Song, China
Yuri N. Sotskov, Belarus
Peter J. C. Spreij, The Netherlands
Niclas Strömberg, Sweden
Ray KL Su, Hong Kong
Jitao Sun, China
Wenyu Sun, China
XianHua Tang, China
Alexander Timokha, Norway
Mariano Torrisi, Italy
Jung-Fa Tsai, Taiwan
Ch Tsitouras, Greece
Kuppalapalle Vajravelu, USA
Alvaro Valencia, Chile
Erik Van Vleck, USA
Ezio Venturino, Italy
Jesus Vigo-Aguiar, Spain
Michael N. Vrahatis, Greece
Baolin Wang, China
Mingxin Wang, China
Qing-Wen Wang, China
Guangchen Wang, China
Junjie Wei, China
Li Weili, China
Martin Weiser, Germany
Frank Werner, Germany
Shanhe Wu, China
Dongmei Xiao, China
Gongnan Xie, China
Yuesheng Xu, USA
Suh-Yuh Yang, Taiwan
Bo Yu, China
Jinyun Yuan, Brazil
Alejandro Zarzo, Spain
Guisheng Zhai, Japan
Jianming Zhan, China
Zhihua Zhang, China
Jingxin Zhang, Australia
Shan Zhao, USA
Chongbin Zhao, Australia
Renat Zhdanov, USA
Hongping Zhu, China

Contents

Uncertainty-Based Design Optimization in Engineering: Model, Algorithm, and Application, Xiaojun Wang, Zhiping Qiu, and Dirk Söffker
Volume 2013, Article ID 595719, 2 pages

A Weighted Multiobjective Optimization Method for Mixed-Model Assembly Line Problem, Şükran Şeker, Mesut Özgürler, and Mehmet Tanyaş
Volume 2013, Article ID 531056, 10 pages

Time-Dependent Reliability-Based Design Optimization Utilizing Nonintrusive Polynomial Chaos, Yao Wang, Shengkui Zeng, and Jianbin Guo
Volume 2013, Article ID 513261, 16 pages

A Probabilistic Damage Identification Approach for Structures under Unknown Excitation and with Measurement Uncertainties, Ying Lei, Ying Su, and Wenai Shen
Volume 2013, Article ID 759102, 7 pages

Generalized Linear Spatial Models to Predict Slate Exploitability, Angeles Saavedra, Javier Taboada, María Araújo, and Eduardo Giráldez
Volume 2013, Article ID 531062, 7 pages

Restricted Isometry Property of Principal Component Pursuit with Reduced Linear Measurements, Qingshan You, Qun Wan, and Haiwen Xu
Volume 2013, Article ID 959403, 6 pages

Fuzzy Multiobjective Traffic Light Signal Optimization, N. Shahsavari Pour, H. Asadi, and M. Pour Kheradmand
Volume 2013, Article ID 249726, 7 pages

The Effect of Exit Strategy on Optimal Portfolio Selection with Birandom Returns, Guohua Cao and Dan Shan
Volume 2013, Article ID 236579, 6 pages

Antioptimisation of Trusses Using Two-Level Population-Based Incremental Learning, Phinit Tontragunrat and Sujin Bureerat
Volume 2013, Article ID 434636, 12 pages

The Complex Network Synchronization via Chaos Control Nodes, Yin Li and Chun-long Zheng
Volume 2013, Article ID 823863, 11 pages

Hindawi Publishing Corporation
Journal of Applied Mathematics
Volume 2013, Article ID 595719, 2 pages
http://dx.doi.org/10.1155/2013/595719

Editorial

Uncertainty-Based Design Optimization in Engineering: Model, Algorithm, and Application

Xiaojun Wang,[1] Zhiping Qiu,[1] and Dirk Söffker[2]

[1] *Institute of Solid Mechanics, Beihang University, Beijing 100191, China*
[2] *Department of Mechanical Engineering, University of Duisburg-Essen, 47048 Duisburg, Germany*

Correspondence should be addressed to Zhiping Qiu; zpqiu@buaa.edu.cn

Received 25 September 2013; Accepted 25 September 2013

Copyright © 2013 Xiaojun Wang et al. This is an open access article distributed under the Creative Commons Attribution License, which permits unrestricted use, distribution, and reproduction in any medium, provided the original work is properly cited.

Uncertainty widely exists in inherent characteristics or external environment of practical engineering problems. The comprehensive influence of uncertainty on products has already been one of the most significant evaluation criterions to better guide the subsequent R&D design. Thus, the uncertainty-based design optimization (UBDO) will become an inexorable trend and main attention in the fields of academic study and engineering applications.

Three parts should be emphasized particularly in UBDOE. The first is the construction of uncertain analytical model, that is, to estimate/quantify uncertainty and further make it embody in the objective function or constraint condition of optimal process. Next in importance is the development of algorithm. Efficiency, convergence and stability are all needed to take account of. The third is the combination of the theoretical approaches and practical problems, namely, to formulate mathematical system reasonably from true environment. This issue complies 17 existing papers, most of which are commendably performed with reference to one of the above 3 aspects.

Four of the papers deal with the first aspect in great depth. Ş. Şeker et al. proposed a weighted multiobjective optimization method for mixed-model assembly line problem based on a mixed integer programming technique. A. Saavedra et al. established a generalized linear spatial model (GLSM) to explore relationship between exploitability and different explanatory variables that characterize slate quality. A time-dependent reliability-based design optimization (RBDO) method by Y. Wang et al. was developed to consider both the time-dependent kinematic reliability and the time-dependent structural reliability as constrains. In this study, a nonintrusive time-dependent surrogate model derived from polynomial chaos with the moving least squares (PCMLS) was proposed to achieve uncertainty quantification. Furthermore, the paper authored by Y. Lei et al. presented a probabilistic approach for the identification of structural damage and unknown external excitations using only limited measurements of structural acceleration responses contaminated by intensive measurement noises.

The research on the second algorithm is addressed on two papers, one of which by P. Tontragunrat and S. Bureerat investigated a metaheuristic method by virtue of population-based incremental learning (PBIL) to solve the anti-optimization problem subjected to the truss structure. Another one is contributed by Y. Li and C.-L. Zheng who launched an investigation in the complex network synchronization via chaos control nodes. They adopted different order chaotic systems as the nodes for complex network with the help of symbolic computation, and the structure of coupling functions among the connected nodes was obtained based on Lyapunov stability theory.

In the aspect of engineering application, a fuzzy multiobjective design model used to minimize the length of traffic queue and pedestrian delays is proposed by N. S. Pour et al., who also introduced the genetic algorithm and a new defuzzification method. Treatments in other fields, including by principal component pursuit (PCP) as well as estimation of stock return are, respectively, studied by Q. You and G. Cao.

We sincerely hope that our efforts by compiling these papers can enrich our readers and inspire researchers with regard to the seemingly common but actually important issue of UBDOE.

Xiaojun Wang
Zhiping Qiu
Dirk Söffker

Hindawi Publishing Corporation
Journal of Applied Mathematics
Volume 2013, Article ID 531056, 10 pages
http://dx.doi.org/10.1155/2013/531056

Research Article

A Weighted Multiobjective Optimization Method for Mixed-Model Assembly Line Problem

Şükran Şeker,[1] Mesut Özgürler,[1] and Mehmet Tanyaş[2]

[1] *Department of Industrial Engineering, Yildiz Technical University, 34349 Istanbul, Turkey*
[2] *Department of International Trade and Logistic Management, Maltepe University, Maltepe, 34857 Istanbul, Turkey*

Correspondence should be addressed to Şükran Şeker; seker.sukran@gmail.com

Received 27 November 2012; Revised 22 June 2013; Accepted 27 June 2013

Academic Editor: Zhiping Qiu

Copyright © 2013 Şükran Şeker et al. This is an open access article distributed under the Creative Commons Attribution License, which permits unrestricted use, distribution, and reproduction in any medium, provided the original work is properly cited.

Mixed-model assembly line (MMAL) is a type of assembly line where several distinct models of a product are assembled. MMAL is applied in many industrial environments today because of its greater variety in demand. This paper considers the objective of minimizing the work overload (i.e., the line balancing problem) and station-to-station product flows. Generally, transportation time between stations are ignored in the literature. In this paper, Multiobjective Mixed-Integer Programming (MOMIP) model is presented to optimize these two criteria simultaneously. Also, this MOMIP model incorporates a practical constraint that allows to add parallel stations to assembly line to decrease higher station time. In the last section, MOMIP is applied to optimize the cycle time and transportation time simultaneously in mixed-model assembly line of a real consumer electronics firm in Turkey, and computational results are presented.

1. Introduction

Mixed-model assembly lines are one of the important parts of mass production systems and generally useful in small product variety and high-volume industries such as automotive, electronics, and machinery. An assembly line comprises several successive workstations where a set of parts for one or more product types are assembled [1]. The assembly line balancing problem (ALBP) has had significant industrial importance since Henry Ford's introduction of the assembly line. ALBP is the assignment of product tasks to different stations with considering precedence relations between tasks. In spite of the high cost of settings and operating an assembly line, manufacturers often simultaneously produce one model with different features or several models on a single line [2]. Assembly lines can be classified as "single model," "multimodel," and "mixed model" with respect to the number of different products assembled on an assembly line. We can see difference between single-model, mixed-model, and multimodel assembly lines in Figure 1.

In *single-model assembly lines*, only one model product is produced in the same line. The assembly lines where products of one similar model are assembled with batches are called *multimodel assembly lines*. *Mixed-model assembly lines* are the lines on which in the simultaneous production products of more than one model are assembled [3]. In order to meet the customers' demand of individual and different models of product, mixed-model assembly lines are used. Thus, there can be produced various models but small quantity of products without setup operations on the same line. This is required to respond to the demand of market quickly and adjust to the change of market environment in time. Mixed-model assembly lines have a strong impact to improve the goal of Just in Time (JIT) and balanced production [4].

Mixed-model assembly has had a big importance because of its diversity. Although other goals of mixed model assembly lines such as low costs, high productivity, and standardization are in contrast with diversity, the success of a company is related to its ability to deal with complex products and process designs [5].

There are two types of mixed-model assembly line problems (MMALPs), which are referred as dual problems in the literature.

(i) MMALBP-I minimises the number of workstations for a given cycle time.

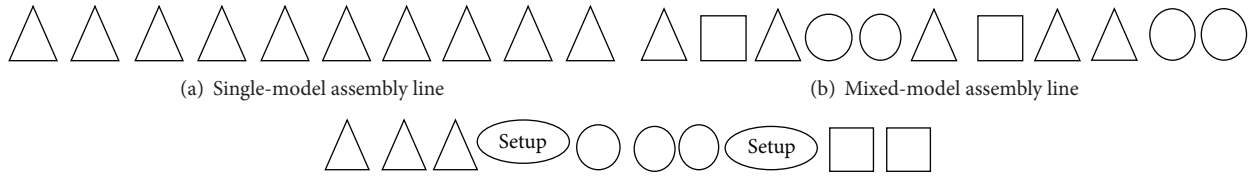

(a) Single-model assembly line (b) Mixed-model assembly line

(c) Multimodel assembly line

Figure 1: Difference between single-model, mixed-model, and multi-model assembly lines.

(ii) MMALBP-II minimises the cycle time for a given number of workstations.

In type I problems, the cycle time (the time elapsed between two consecutive products at the end of the assembly line) and the production rate have to be prespecified. Thus, it is more frequently used in the design of a new assembly line for which the demand can be easily forecasted. Type II problems deal with the maximisation of the production rate of an existing assembly line. For instance, the MMALBP-II is applied when changes in the assembly process or in the product range require the line to be redesigned [6].

Material movement is an important factor in the production line. Although it is an important factor in nonvalue-added cost function, it increases the cost of production. So, in a well-designed system, work and storage areas should be near to their point of use. In an assembly line material handling system, transportation of materials and storage devices require huge capital investment. However, transportation does not add value to the final product.

Transportation time is usually added to the processing time or negligible in assembly line systems. However, minimization of assembly parts from a machine to another decreases the completion time and cost of products. But, minimization of part unit movements can cause workloads imbalance. This leads to unequal total assembly times assigned to stations and longer intermediate queues and bottlenecks in the system as a result. In order to have the best assembly system capabilities, balancing of the line and transfer times between stations should be taken into account simultaneously. Routings of part units are completely defined by the sequence of machines they have to visit.

Although there is a vast literature on the mixed-model assembly line balancing and sequencing problem, transportation times between stations consist of process routings of products and balancing problem generally is not considered in an integrated fashion. In this paper, we propose a mixed-integer programming model to tackle this problem. Also, we assume that there can be parallel machine in some stations, and we add this as a criterion to mathematical model.

With this point, this paper includes two main objectives.

(1) The workload balancing assigns tasks to stations in order to equalize station workloads.

(2) The total amount of transfers of components from a station to another is minimized. In other words, we look for balancing routings of part units to minimize transportation times that cause the increase of completion time of the product.

To reach these objectives, some constraints are added to the mathematical model. If it is required, we add parallel machine to minimize cycle times of stations. MOMIP model also includes a finite workspace constraint that is considered with line balance. Finite working space might be subject to technical restrictions and space requirements of assigned station. The limited workspace capacity restricts the number of tasks which are assigned to each station.

In Section 2, there is a review of literature on MMALP. Then in Sections 3 and 4, MOMIP model is proposed with results of experiments and real-world application in consumer electronics in Turkey. In Section 5, conclusions are presented.

2. Review of the Existing Literature in MMAL

The mixed-model assembly line deals with solving two primary problems in a production line. The first problem is the design and balancing of the production line, whereas the second problem is the determination of the production sequence for different models [7]. The line balancing comprises the assignment of tasks to stations and determination of the work content and model type per station. However, the production sequence is the model mix arranged with regard to minimum overloads on the assembly line. Balancing and sequencing problems are known as an NP-hard class of combinatorial optimization problems in mixed model assembly line literature.

Several researchers have studied MMAL balancing problems. Thomopoulos [8] and Macaskill [9] are the initial researchers in solving this problem. Macaskill [9] and Chakravarty and Shtub [10] have also studied the line balancing for traditional mixed model straight lines (MMSLs). Also, [11] presents a balancing methodology for mixed-model lines with deterministic task times. The objective is minimizing the total cost of stations (essentially the regular time labor cost) and work overload. Erlebacher and Singh [12] proposes a method to allocate a fixed total processing time variance among multiple stations and to minimize the total expected work overload. Zhang and Gen [13] present random key-based representation method with adapting Genetic Algorithm to assign the suitable task to the suitable station and the allocation of the proper worker to the proper station. The objective is to minimizate the variation of workload and the total cost under the constraint of precedence relationships.

The mixed model assembly line sequencing is investigated in [14] for the first time. Various objectives are reported in the literature in determining the optimal sequence for a mixed model assembly line. The common objectives are minimizing the overall line length [15–19], minimizing the risk of stopping a conveyor [20], minimizing the total utility work [21, 22], and keeping a constant rate of part usage [23–27]. Also, Bard et al. [15], Scholl [28], and Yano and Bolat [29] present several procedures for different versions of the mixed-model-sequencing problems [30].

However, Celano et al. [31] investigate the sequencing of MMAL assuming that the parts usage smoothing is the goal of the sequence selection. Mirzapour Al-E-Hashem et al. [7] present a sequencing problem with a bypass subline with the goals of leveling the part usage rates and reducing line stoppages. To solve this problem, a novel hybrid algorithm incorporating genetic algorithm and event-based procedure is developed to solve the problem.

However, there are a couple of papers dealing with simultaneous assembly line balancing and sequencing [32–37]. Hu et al. [38] also analyze the balancing of mixed model assembly lines and design a new algorithm based on the process exchange according to its attributes and characters. The algorithm could be utilized to make further optimization of mixed model assembly lines on the basis of the best production sequence.

Merengo et al. [39] develop a new balancing and production sequencing method for manual mixed-model assembly lines. Minimization of the number of stations is provided by the balancing method, and a uniform part usage is obtained by the sequencing method. Kim et al. [40] present a new method using a coevolutionary algorithm that can simultaneously solve balancing and sequencing problems in mixed-model assembly lines. Karabatı and Sayın [41] propose the MMALBP with the objective of minimizing the total cycle time by combining the cyclic sequencing information. They propose a mathematical model and an alternative heuristic approach to minimize the maximum subcycle time [42]. Fattahi and Salehi [43] consider a mixed-integer programming model with a variable rate launching interval between products on the assembly line, to minimize the idle and utility time cost, with optimization sequencing and launching interval for each sequence.

Although transportation of units is very important in assembly systems, there are few studies that take into account that part units' movements in assembly lines. Transportation time is usually added to the processing times or negligible in assembly systems. However, minimization of assembly parts movements from a machine to another decreases the completion time of products.

In our study, we propose a mixed-integer programming that can simultaneously deal with both balancing and sequencing problems in MMAL, and identical parallel machines are allowed at each stage of the serial system. With this approach, we obtain the best task sequences for the models by taking into consideration the minimization of transportation of models between stations; we also solve the balancing problem in the line at the same time. The mathematical model intends for balancing of workloads and routing of unit parts.

3. Model Description

This paper introduces a mathematical model for MMAL, and it can be categorized as MOMIP model. This mathematical model is integrated to real-world application. Our mathematical model is based on Sawik's integer programming models about mixed model assembly line [44, 45]. The problem objectives are the determination of allocation of assembly tasks among the stations, where they have parallel machines and selection of assembly sequences and assembly routes for a set of products simultaneously to balance station workloads and to minimize total transportation time in assembly line.

We give weights to objectives to solve this multiobjective problem. This problem is solved using ILOG OPL optimization software [46]. The proposed model is used for a mixed model assembly line problem from real world in a Turkish consumer electronics firm. Due to the NP-hard nature of the problem, the size of our model would be large to obtain optimal solutions for problems of realistic sizes. Also, the model suggested in this paper presents a significant improvement relative to the models in the literature.

The assumptions of the proposed model are as follows.

(1) Each assembly task must be assigned to at least one station (alternative assignments are allowed).

(2) There are parallel machines in some stations.

(3) Total space required for the tasks assigned to each station must not exceed the station's finitework space available.

(4) Each product must be routed to the stations subject to precedence relations defined by its assembly plan.

(5) Revisiting of stations is not allowed.

(6) Each station can perform at most one task at any given time.

(7) Transfer times between stations are not negligible.

Notation

Indices

i: assembly station $i \in I$, $I = \{1, \ldots, m\}$

j: assembly task $j \in J = \{1, \ldots, n\}$

p: parallel machine at station i $\{h = 1, \ldots, m_i\}$

k: product, $k \in K = \{1, \ldots, v\}$

s: assembly sequence, $s \in S = \{1, \ldots, w\}$.

Input Parameters

a_{ij}: working space of station i for task j

b_i: working space for station I

m_i: number of parallel machines in station I

p_{jk}: process time for task j of model k

q_{il}: transportation time from station i to station l

I_j: the set of stations capable of performing task j

J_k: the set of tasks required for product k

R_s: the set of immediate predecessor-successor pairs of tasks (j, r) for assembly sequence $s \in S$ such that task j must be performed immediately before task r

S_k: the set of assembly sequences available for product k

T_s: the set of tasks in assembly sequence s.

The following decision variables are introduced to model the loading and routing problem:

α: the weight factor $(0 < \alpha < 1)$,

M: a big number.

Decision Variables

$u_s = 1$, if assembly sequence $s \in S$ is selected; otherwise 0;

$x_{ij} = 1$, if task j is assigned to station $i \in I_j$; otherwise $x_{ij} = 0$;

$z_{sjih} = 1$, if task j is assigned to parallel machine h in station $i \in I_j$; otherwise $z_{sihj} = 0$;

$y_{iljs} = 1$, if product in s sequence is transferred from station i after the completion of task j to station l to perform next task; otherwise $y_{iljs} = 0$;

$P_{\max}$ is the maximum station workload (cycle time),

Q_{sum} represents the weighted sum of total assembly and transportation time.

We can state the problem formally as follows:

$$\text{Min}\left(\alpha P_{\max} + (1-\alpha) Q_{\text{sum}}\right) \tag{1}$$

subject to

$$\sum_{i \in I_j} \sum_{l \geq i} y_{iljs} = u_s; \quad s \in S,\ j \in T_s, \tag{2}$$

$$\sum_{l \leq i} y_{lijs} - \sum_{l \geq i} y_{ilrs} = 0; \quad i \in I_r,\ (j,r) \in R_s,\ s \in S, \tag{3}$$

$$\sum_{k \in K} \sum_{s \in Sk} \sum_{j \in T_s} p_{jk} z_{sjih} \leq P_{\max}; \quad i \in I,\ h \in H, \tag{4}$$

$$\sum_{i \in I} y_{iljs} \leq \sum_{h=1}^{m_i} z_{sjih}; \quad i \in I, j \in J, s \in S, \tag{5}$$

$$\sum_{s \in S} \sum_{h=1}^{m_i} z_{sjhi} \leq m_i * \sum_{i \in I} \sum_{s \in S} y_{iljs}; \quad i \in I, j \in J, \tag{6}$$

$$\sum_{s \in S} \sum_{j \in T_s} \sum_{i \in I} \sum_{l \in I} q_{il} y_{iljs} = Q_{\text{sum}}, \tag{7}$$

$$\sum_{i \in I_j} x_{ij} \geq 1; \quad j \in J, \tag{8}$$

$$\sum_{j \in J} a_{ij} x_{ij} \leq m_i b_i; \quad i \in I, \tag{9}$$

$$\sum_{j \in J} a_{ij} z_{sjih} \leq b_i; \quad i \in I,\ h \in H,\ s \in S, \tag{10}$$

$$\sum_{s \in S} \sum_{i \in I} \sum_{h > m_i} \sum_{j \in J} z_{sjih} = 0, \tag{11}$$

$$z[s][j][i][h] \leq u[s]; \quad i \in I,\ j \in J,\ h \in H,\ s \in S, \tag{12}$$

$$y_{iljs} \leq x_{ij}; \quad i \in I_j,\ l \geq i,\ l \in l_r,\ (j,r) \in R_s,\ s \in S, \tag{13}$$

$$y_{iljs} \leq x_{lr}; \quad i \in I_j,\ l \geq i,\ l \in l_r,\ (j,r) \in R_s,\ s \in S, \tag{14}$$

$$y_{iljs} \leq u_s; \quad i \in I_j,\ l \geq i,\ l \in l_r,\ (j,r) \in R_s,\ s \in S, \tag{15}$$

$$\sum_{s \in S_k} u_s = 1; \quad k \in K, \tag{16}$$

$$\sum_{i \in I} \sum_{l < i} \sum_{s \in S} \sum_{j \in T_s} y_{iljs} = 0, \tag{17}$$

$$\sum_{s \in S} \sum_{j \in J} \sum_{i \in I} \sum_{i \notin I_j} y_{iljs} = 0, \tag{18}$$

$$\sum_{j_2 \in J} \sum_{h_2 \neq h} z_{sj_2ih_2} \leq M\left(1 - z_{sjih}\right); \quad s \in S,\ j \in J,\ i \in I,\ h \in H. \tag{19}$$

The objective function is the minimization of the weighted maximum workload $P_{\max}$ and sum of transportation time Q_{sum}. Equation (2) shows for each product and assembly sequence selected that all of its required tasks are allocated among the stations. Equation (3) is the flow of tasks for each station, for selected assembly sequence, and for successively performed tasks. Equations (4) and (7) ensure the workload of the bottleneck station with parallel machines and the total transportation time, respectively. Equations (5) and (6) define the tasks that are assigned to at least one machine and not more than all "m_i" parallel machines of such a station "i" when the product moves from station "i" to station "l" to perform task "j". Equation (8) ensures that each task is assigned to at least one station, and by this, it admits alternative assembly routes for products. Equation (9) is the station capacity constraint. Equation (10) shows the total flexibility capacity of all parallel machines at related station. Equation (11) represents the capacity constraint of the number of parallel machines in station "i". Equation (12) shows that if the sequence "s" is not selected, all variables of related sequence are made zero. Equation (12) shows that if we do not select any sequence, we make all of variables in this sequence zero. Equations (13), (14), and (15) ensure that each product successively visits stations where the required tasks may be assembled subject to precedence relations defined by the assembly sequence selected. Equation (16) ensures that only one assembly sequence is selected for each product. Equation (17) eliminates upstream flow of products in a unidirectional flow system. Equation (18) eliminates assignment of tasks and products to inappropriate stations. Equation (19) ensures that all tasks, which are in the same "s" sequence, are assigned to the same station and the same parallel machine and that also the tasks of the same product models are assigned to the same station and the same parallel machine.

Multiobjective integer programming problems may be thought as an extension of the classical single objective integer programming problem. Scalarizing functions used in subproblems are very important in solving multi-objective optimization problems [47].

Different scalarization methods have been presented in the literature, some of which include the weighted sum method, ε-constraints method, hierarchical approach, weighted metrics methods, and goal attainment method [48].

In this paper, there are two objective functions to be optimized with multi-objective integer programming technique in mixed model assembly line problem.

We use the most convenient scalarization method with related objective functions of the problem. In this sense, the weighted sum (WS) method is used to solve multi-objective integer programming problem. With solution procedure, we would produce the most preferred nondominated solutions. The weighted sum (WS) method involves a linear or convex combination of the objectives $f_i(x), i = 1, \ldots, p$. Each objective $f_i(x)$ is multiplied by a normalized weight factor w_i and the product added to give the scalar objective $\phi(x, w_i)$ as follows:

$$\varphi(x, w) = \sum_{i=1}^{p} \alpha_i f_i(x), \tag{20}$$

where p is the number of the objectives, $\sum_{i=1}^{p} \alpha_i = 1$, and $\alpha_i > 0, i = 1, \ldots, p$.

Its drawbacks are also well known and discussed as follows.

(i) It misses solution points on the nonconvex part of the pareto surface.

(ii) Its diversity cannot be controlled; therefore even the distribution of weights does not translate to uniform the distribution of the solution points.

(iii) The distribution of solution points is highly dependent on the relative scaling of the objective [48].

In this paper, there are two objective functions. We minimize the weighted sum of the objectives to obtain only one solution. The weight factor $\alpha \in [0, 1]$ is used for interactive solution between two objectives. Therefore, decision makers modify the weighting coefficients after each iteration, so he/she would produce the most preferred nondominated solution.

In the following section, firstly we perform experimental test problems to validate this mixed integer model, then we apply the model to real-world mixed model assembly line problem, and computational results are summarized.

4. Experiments and Computational Results

In this section, the experiments are used to test the performance of the mathematical model. Then, their analysis and the application to the real-world consumer electronics firm problem are described. For the experiments, the number of stations and the number of tasks are changed with the weight factor in each iteration. The problem includes optimization of balancing and transportation times of mixed model assembly line. To solve the underlying multi-objective mixed integer programming model, we use ILOG OPL optimization software. The experimental results are seen in Table 1.

Experimental results show that $\alpha = 0$ and $\alpha = 1$ produce weakly nondominated solutions for the objectives. For $\alpha = 0$, transportation time is minimized and dominated whereas for $\alpha = 1$ cycle time is minimized and dominated. Other weights produce strongly nondominated solutions. As a result, while weight of α increases, cycle time decreases and transportation time increases.

In addition to these test instances, we have solved a real-world problem from a consumer electronics plant in Turkey. The firm we have obtained is a household appliances's manufacturer. It principally engages in production, marketing, and after sales service of durable goods, allied components, and consumer electronics. The assembly system of the firm is made up of 18 identical stations which produce three different LCD model TV types, and this number is constant. There are 73 tasks to produce three different model types. Some of these tasks are common. Common tasks can have different task times in each model. Thus, we assume that there is one machine in each station. According to the cycle time we have obtained, we placed one more parallel machine to the station where its cycle time is high. The objectives are the minimization of the weighted maximum workload $P_{\max}$ and the sum of transportation time Q_{sum}. The performance of the proposed algorithm is analyzed through variance between stations and balance loss of the system. In our system, each model has its own set of precedence relationships, but there is a subset of tasks common to all models. To solve this mixed model assembly line problem, the precedence diagrams for all the models are combined, and then we use adjusted processing time to transform the mixed model line balancing problem into a single model line balancing problem and determine average task processing times for the tasks that are required by more than one model [49–52]. The average processing time of task j, t_j, can be calculated by

$$t_j = \sum_k f_k p_{jk}, \tag{21}$$

where p_{jk} equals the processing time of task j in model k, and f_k is the relative frequency or the demand for each model. The demand for each model is assumed to be equal because of the daily production rates, so process time for each task is divided based on demand ratio. Task times of each model are shown in Table 2.

The other variables of the proposed model are as follows.

The transportation times q_{il} from station i to station l are 1 unit time. The set of tasks required for product k (JK) and alternative assembly sequences (plans) (TS) are shown in Tables 3 and 4. Each product modelhas two alternative assembly plans which include task sequences. Working space of station i for task j is 2 units and working space for each stations is 10 units.

The balancing procedure operates as shown in Figure 2.

To determine the weights of objectives in multi-objective integer programming model, we use the preferences of the

Table 1: Experimental results.

Number of product models/Number of tasks	$\alpha = 0$ P_{max}-Q_{sum}	$\alpha = 0.2$ P_{max}-Q_{sum}	$\alpha = 0.4$ P_{max}-Q_{sum}	$\alpha = 0.6$ P_{max}-Q_{sum}	$\alpha = 0.8$ P_{max}-Q_{sum}	$\alpha = 1$ P_{max}-Q_{sum}
3/5	10-8	8-8	6-8	6-8	6-10	6-10
3/10	58-4	25-6	20-8	20-8	18-12	18-12
4/10	46-6	41-6	27-10	20-16	20-16	20-16
3/20	38-6	19-10	19-10	19-10	19-10	19-12
4/20	42-8	41-8	28-12	28-12	27-14	27-16
3/30	58-6	27-8	27-8	25-10	24-12	24-12
4/30	61-8	41-8	41-8	32-16	32-16	32-18

Table 2: Adjusted task times.

Number of task	Model 1	Model 2	Model 3	Number of task	Model 1	Model 2	Model 3	Number of task	Model 1	Model 2	Model 3
1	0,11300	0,11600	0,11600	26	0,10267	0,10267	0,10267	51	—	0,05533	0,02967
2	0,02100	0,02100	0,02100	27	0,01700	—	—	52	—	0,09200	0,09200
3	0,09967	0,09500	0,09600	28	0,08533	0,08933	0,08933	53	—	0,05467	0,01733
4	0,10633	—	—	29	0,05133	0,04800	0,04800	54	—	0,01967	0,01567
5	0,04800	0,04833	0,04833	30	0,15933	0,14567	0,14567	55	—	0,04533	—
6	0,01533	—	0,01533	31	0,11367	—	0,10700	56	—	0,09767	—
7	0,04333	—	—	32	0,03500	—	—	57	—	0,04267	—
8	0,09167	—	—	33	0,12967	—	0,12967	58	—	0,03500	—
9	0,06200	—	—	34	0,04367	—	—	59	—	0,05433	0,06533
10	0,07467	—	—	35	0,02500	—	—	60	—	—	0,07767
11	0,04300	—	—	36	0,07933	—	—	61	—	—	0,03200
12	0,06400	—	—	37	0,06067	0,06067	0,06067	62	—	—	0,03900
13	0,04300	—	—	38	0,07733	0,07733	0,07733	63	—	—	0,08167
14	0,03533	0,03533	0,03533	39	0,02900	—	—	64	—	—	0,04167
15	0,07767	—	—	40	0,02133	—	—	65	—	—	0,02233
16	0,11800	—	—	41	—	0,01833	—	66	—	—	0,04267
17	0,04300	—	—	42	—	0,07067	0,07067	67	—	—	0,05333
18	0,11933	0,11933	0,11933	43	—	0,06733	—	68	—	—	0,07767
19	0,02500	0,02967	0,02967	44	—	0,06533	—	69	—	—	0,01900
20	0,01733	0,01733	0,01733	45	—	0,04433	0,04433	70	—	—	0,02633
21	0,02000	0,01733	0,01733	46	—	0,06567	—	71	—	—	0,01967
22	0,01733	0,01733	0,02133	47	—	0,34000	—	72	—	—	0,07767
23	0,03600	0,03900	0,03200	48	—	0,08700	0,08567	73	—	—	0,07767
24	0,03933	0,02767	0,04067	49	—	0,08067	—				
25	0,08100	—	—	50	—	0,14567	—				

Table 3: Sequencing of tasks for LCD TV product models.

Model	JK
1	1 2 3 4 5 6 7 8 9 10 11 12 13 14 39 15 16 17 18 40 19 20 21 22 23 24 25 26 27 28 29 30 31 32 33 34 35 36 37 38
2	1 41 42 2 3 43 44 5 45 46 47 48 49 50 14 51 52 19 53 18 54 22 21 20 23 26 55 24 28 29 56 30 57 58 59 37 38
3	1 42 2 3 60 61 62 5 6 45 63 64 48 65 66 67 51 68 14 52 69 53 70 18 54 22 19 21 20 23 71 26 24 28 29 31 33 30 72 73 59 37 38

decision makers. To determine the important weights of each objective, we select six participants from the production planning department. We ask them about two objectives of the problem in a meeting. Peers being aware of the optimization objectives choose one of the objectives as their preference. The weights assigned to each objective function are f_g. P_{f_g} represents the number of peers that prefer f_i to the other optimization objectives. n is the number of participants in the meeting. The important weights are determined using the number of participants in the meeting. One has

$$\alpha f_i = \frac{p_{f_g}}{n}. \tag{22}$$

Thus, we obtain 0.8 value for the first objective (P_{max}) weight and 0.2 value weight for the second objective (Q_{sum}). Using these weights, we obtain the following results. Also to minimize the cycle time, we assign parallel machines to stations where cycle time is high. Decision of parallel machine

Table 4: Assembly plans for LCD TV product models.

TS	JK
1	1 2 3 4 5 6 7 8 9 10 11 12 13 14 39 15 16 17 18 40 19 20 21 22 23 24 25 26 27 28 29 30 31 32 33 34 35 36 37 38
2	1 3 2 4 5 7 6 8 9 10 11 12 14 13 39 15 17 16 18 40 19 20 21 22 23 24 26 25 27 28 29 30 32 31 33 34 35 36 37 38
3	1 41 42 2 3 43 44 5 45 46 47 48 49 50 14 51 52 19 53 18 54 22 21 20 23 26 55 24 28 29 56 30 57 58 59 37 38
4	1 42 41 2 3 44 43 5 45 46 47 48 49 50 14 51 52 53 19 18 54 22 21 20 23 55 26 24 28 29 56 30 57 58 59 37 38
5	1 42 2 3 60 61 62 5 6 45 63 64 48 65 66 67 51 68 14 52 69 53 70 18 54 22 19 21 20 23 71 26 24 28 29 31 33 30 72 73 59 37 38
6	1 2 42 3 60 62 61 5 6 45 63 64 48 65 66 67 51 68 14 52 69 53 70 18 54 19 22 21 20 71 23 26 28 24 29 31 33 30 72 73 59 37 38

Table 5: Sequences after solving mathematical model.

TS	JK
1	1 2 3 4 5 6 7 8 9 10 11 12 13 14 39 15 16 17 18 40 19 20 21 22 23 24 25 26 27 28 29 30 31 32 33 34 35 36 37 38
3	1 41 42 2 3 43 44 5 45 46 47 48 49 50 14 51 52 19 53 18 54 22 21 20 23 26 55 24 28 29 56 30 57 58 59 37 38
6	1 2 42 3 60 62 61 5 6 45 63 64 48 65 66 67 51 68 14 52 69 53 70 18 54 19 22 21 20 71 23 26 28 24 29 31 33 30 72 73 59 37 38

Table 6: Assignment of task to stations.

Number of station	Assigned task
1	1, 2, 4, 42
2	2
3	2, 3, 43, 44
4	4, 5, 60, 61, 62, 73
5	6, 7, 8, 9, 45, 46, 47, 48, 63, 64
6	10, 11, 48, 49, 50, 65, 66, 67
7	12, 13, 14, 51, 68
8	52, 53, 69
9	15, 16, 17, 39, 70
10	18, 19, 21, 22, 40, 53, 54
11	20, 21, 23, 26, 71
12	22, 23, 24, 25, 26
13	24, 27, 28, 55
14	29, 30, 56, 57, 58
15	30, 31, 33, 72
16	30, 31, 32, 33, 34
17	35, 36, 37, 59
18	38

depends on the firm's preference because of the high costs of machines. But when we place one more machine to stations 1, 5, 6, and 10, the cycle time decreases from 0.931 to 0.481. Also, according to the results, transportation time is 51 time unit. After solving this optimization problem in ILOG OPL programming $S = 1, 3, 6$ is obtained for sequences of model 1, model 2, and model 3, respectively. Selected sequences after solving mathematical model are shown in Table 5.

Task assignment to stations is shown in Table 6.

After the assignment of tasks to stations with parallel machines, station time (P_{ih}) is handled by mixed integer programming model as shown in Table 7.

Table 7: Stations times (P_{ih}) with parallel machines handled by mixed integer programming model.

Station workload	Machine	P_{ih} (time)	Station	Machine	P_{ih} (time)
1	1	0.3206	9	1	0.294
1	2	0.205	10	1	0.4063
2	1	0.021	10	2	0.2033
3	1	0.4443	11	1	0.2436
4	1	0.4773	12	1	0.418
5	1	0.481	13	1	0.3946
5	2	0.45	14	1	0.4683
6	1	0.1176	15	1	0.460
6	2	0.4316	16	1	0.4813
7	1	0.3756	17	1	0.406
8	1	0.2203	18	1	0.2319

After solving integer programming model, performance of the mathematical model is evaluated with balancing loss and variance of station workloads. Balancing loss is a measure of the line inefficiency which results from idle time due to imperfect allocation of work among stations. In this study, we measure system performance with well-balanced assembly line, when the idle time in each work station is at minimum level and the balancing loss is minimized. The balancing loss is shown with E_{line} and calculated by

$$E_{line} = \frac{n * P_{max} - \sum_{i=1}^{N} t_i}{n * P_{max}}. \tag{23}$$

The total work, t_i, content is the aggregate of all the work elements to be done on the line, n is the number of stations, and P_{max} is the cycle time. One has

$$E_{line} = \frac{n * P_{max} - \sum_{i=1}^{N} t_i}{n * P_{max}},$$
$$E_{line} = 18 * 0.481 - \frac{7.55}{18 * 0.481} = 0.12. \tag{24}$$

As we can observe from the results, decision of parallel machine depends on the firm's preference because of the high cost of machines. But, when we place one more machine to stations 1, 5, 6, and 10, cycle time decreases from 0.931 to 0.481. In addition, production rate increases from 426 units to 813 units daily. According to the results, transportation time is 51 time unit. After solving this optimization problem in ILOG OPL programming $S = 1, 3, 6$ is obtained for sequences of model 1, model 2, and model 3, respectively. The balancing loss of the system works out of 12%, and the

Figure 2: General flow chart of algorithm.

variance between station times is computed as 0.15 which can be acceptable for MMALBP, because mixed-model assembly occurs when more than one model of the same general product are intermixed on one assembly line. This line design makes the balancing problem more complex than others and causes big balance loss in these systems.

Results show that in terms of total assembly time, processing assembly of different LCD TV models in the same line is more advantageous than processing in different assembly lines. With this study, the workloads at stations are balanced, the production rate is increased, the work flow between stations is improved, and the utilization of machines and labor is increased. Also our research concentrates on testing the method with large-scale instance from real world, eventually solving mixed integer programming models.

5. Conclusion

Mixed model assembly lines are widely used to produce different models as per customer's demands. The problem of mixed-model assembly line balancing is more complex than that of the single-model assembly line, because there are different tasks in different models on mixed assembly line and the processing times for common tasks may be different. In this paper, the MOMIP of a mixed model assembly line problem is formulated.

The goals of this study are to minimize station work loads and to minimize transportation time between stations. In order to achieve these goals, assembly works are assigned to stations optimally, and optimal assembly order and route is determined. The WS method is used to solve multi-objective integer programming problem. Also, to minimize the cycle time in related stations, parallelization is added as a criterion to mathematical model. An other criterion is related to the working space due to transportation times between stations. In the literature, generally, time spent between stations for transporting goods is ignored. In this study, we aim to fill this gap and solve a real-world problem.

In the first step, mixed model assembly line problem is converted to single model assembly line problem. For this, precedence diagrams for each single model are combined in combined precedence diagrams, and adjusted tasks times are computed for each task. The experiments are solved to test the performance of the mathematical model. Then, the proposed model is adapted to the real-world consumer electronics firm problem.

Computational experiments show that this optimization method is capable of obtaining good results both in terms

of solution quality and in terms of execution times. The main contribution of this research is the definition of a new problem with practical relevance, and the objective function models trade off between cycle time and transportation time related to selecting route for each product model. Also, the parallelization and station length are added to the mathematical model as a constraint with balancing and sequencing, so transportation of product models is taken into account to be different from other papers in assembly sytems.

After solving mixed model assembly line problem in consumer electronics firm, line efficiency is measured with balancing loss and variance between station workloads.

Processing assembly of different LCD TV models in the same line is more advantageous than processing in different assembly lines in terms of total assembly time. In this way, the firm can meet the demands of different model products at the same time. This means that customer satisfaction and sales increase. Also with this study many improvements are obtained; for example, workloads at stations are balanced, the production rate is increased, the work flow between stations is improved, and the utilization of machines and labor increased. Also our research concentrates on testing the method with large-scale instance from real world, eventually solving mixed integer programming models.

References

[1] Y. Kara, C. Özgüven, N. Yalçin, and C. Chang, "Multi-objective approaches to balance mixed-model assembly lines for model mixes having precedence conflicts and duplicable common tasks," *International Journal of Advanced Manufacturing Technology*, vol. 52, pp. 725–737, 2011.

[2] I. Weida and X. Tianyuan, "Strategic robust mixed model assembly line balancing based on scenario planning," *Tsinghua Science and Technology*, vol. 16, no. 3, pp. 308–314, 2011.

[3] H. Güden, *An Adaptive Simulated Annealing Method For Assembly Line Balancing and A Case Study [In Partial Fulfillment of the Requirements for The Degree of Master of Science In Industrial Engineering]*, Graduate School of Natural And Applied Sciences of Middle East Technical University, 2006.

[4] L.-K. Hu, F.-Y. Shao, and G.-X. He, "Balancing analysis and algorithm design for mixed model assembly lines," in *Proceedings of the 18th International Conference on Industrial Engineering and Engineering Management (IE & EM '11)*, pp. 67–71, September 2011.

[5] F. Hellman, B. Lindahl, and J. Malmberg, *Mixed-Model Assembly Line at Volvo Construction Equipment Requirements for Mixed-Model Assembly Line at Volvo Construction Equipment and a Case Study at the Arvika Plant [Master of Science Thesis in Production Engineering]*, Department of Technology Management and Economics, Division of Logistics and Transportation, Chalmers University of Technology, 2011.

[6] A. S. Simaria and P. M. Vilarinho, "A genetic algorithm based approach to the mixed-model assembly line balancing problem of type II," *Computers and Industrial Engineering*, vol. 47, no. 4, pp. 391–407, 2004.

[7] S. M. J. Mirzapour Al-E-Hashem, M. B. Aryanezhad, and A. Jabbarzadeh, "A new approach to solve a mixed-model assembly line with a bypass subline sequencing problem," *International Journal of Advanced Manufacturing Technology*, vol. 52, no. 9–12, pp. 1053–1066, 2011.

[8] N. T. Thomopoulos, "Mixed model line balancing with smoothed station assignments," Management Science, JSTOR, 1970.

[9] J. L. C. Macaskill, "Production-line balances for mixed-model lines," *Management Science*, vol. 19, no. 4, pp. 423–434, 1972.

[10] A. K. Chakravarty and A. Shtub, "Balancing mixed model lines with in-process inventories," *Management Science*, vol. 31, no. 9, pp. 1161–1174, 1985.

[11] L. Y. Hsu, *Design of an Assembly Line with Stochastic Task Times [Master of Sciencethesis]*, Sloan School of Management, Massachusetts Institute of Technology, Cambridge, Mass, USA, 1992.

[12] S. J. Erlebacher and M. R. Singh, "Optimal variance structures and performance improvement of synchronous assembly lines," *Operations Research*, vol. 47, no. 4, pp. 601–618, 1999.

[13] W. Zhang and M. Gen, "An efficient multiobjective genetic algorithm for mixed-model assembly line balancing problem considering demand ratio-based cycle time," *Journal of Intelligent Manufacturing*, vol. 22, no. 3, pp. 367–378, 2011.

[14] M. D. Kilbridge and L. Wester, "The line model-mix sequencing problem," in *Proceedings of the 3rd International Conference on Operations Research*, p. 247, English Universities Press, Paris, France, 1963.

[15] J. F. Bard, E. Dar-El, and A. Shtub, "An Analytic frame work for sequencing mixed model assembly lines," *International Journal of Production Research*, vol. 30, no. 1, pp. 35–48, 1992.

[16] J. F. Bard, A. Shtub, and S. B. Joshi, "Sequencing mixed-model assembly lines to level parts usage and minimize line length," *International Journal of Production Research*, vol. 32, pp. 2431–2454, 1994.

[17] E. M. Dar-El, "Mixed-model assembly line sequencing problems," *Omega*, vol. 6, no. 4, pp. 313–323, 1978.

[18] E. M. Dar-El and R. F. Cother, "Assembly line sequencing for model mix," *International Journal of Production Research*, vol. 13, no. 5, pp. 463–477, 1975.

[19] M. D. Kilbridge and L. Wester, "The assembly line model-mix sequencing problem," in *Proceedings of the 3rd International Conference on Operations Research*, pp. 247–260, Paris, France, 1963.

[20] K. Okamura and H. Yamashina, "A heuristic algorithms for the assembly line model-mix sequencing problem to minimize the risk of stopping the conveyor," *International Journal of Production Research*, vol. 17, no. 3, pp. 233–247, 1979.

[21] C. A. Yano and R. Rachamadugu, "Sequencing to minimize work overload in assembly lines with product options," *Management Science*, vol. 37, pp. 572–586, 1991.

[22] J. F. Bard, A. Shtub, and S. B. Joshi, "Sequencing mixed-model assembly lines to level parts usage and minimize line length," *International Journal of Production Research*, vol. 32, pp. 2431–2454, 1994.

[23] E. A. Duplaga, C. K. Hahn, and D. Hur, "Mixed-model assembly line sequencing at Hyundai Motor Company," *Production and Inventory Management Journal*, vol. 37, no. 3, pp. 20–25, 1996.

[24] P. R. McMullen, "An ant colony optimization approach to addressing a JIT sequencing problem with multiple objectives," *Artificial Intelligence in Engineering*, vol. 15, no. 3, pp. 309–317, 2001.

[25] J. Miltenburg, "Level schedules for mixed-model assembly lines in just-intime production systems," *Management Science*, vol. 35, no. 2, pp. 192–207, 1989.

[26] Y. Monden, *Toyota Production System: Practical Approach To Production Management*, Industrial Engineering and Management Press, Atlanta, Ga, USA, 1983.

[27] P. R. McMullen and G. V. Frazier, "A simulated annealing approach to mixed-model sequencing with multiple objectives on a just-in-time line," *IIE Transactions*, vol. 32, no. 8, pp. 679–686, 2000.

[28] A. Scholl, *Balancing and Sequencing of Assembly Lines*, Physica, Heidelberg, Germany, 2nd edition, 1999.

[29] C. A. Yano and A. Bolat, "Survey, development and application of algorithms for sequencing paced assembly lines," *Journal of Intelligent Manufacturing*, vol. 2, pp. 172–198, 1989.

[30] C. Copaceanu, "Mixed-model assembly line balancing problem: variants and solving techniques," in *Proceedings of ICMI*, vol. 45, pp. 337–360, Bacau, Romania, September 2006, Stud. Cercet. Stiint. , Ser.Mat., vol. 16, supplement, 2006.

[31] G. Celano, A. Costa, and S. Fichera, "A comparative analysis of sequencing heuristics for solving the Toyota Goal Chasing problem," *Robotics and Computer-Integrated Manufacturing*, vol. 20, no. 6, pp. 573–581, 2004.

[32] P. R. McMullen and G. V. Frazier, "Using simulated annealing to solve a multiobjective assembly line balancing problem with parallel workstations," *International Journal of Production Research*, vol. 36, no. 10, pp. 2717–2741, 1998.

[33] Y. K. Kim, J. Y. Kim, and Y. Kim, "A coevolutionary algorithm for balancing and sequencing in mixed model assembly lines," *Applied Intelligence*, vol. 13, no. 3, pp. 247–258, 2000.

[34] Y. K. Kim, S. J. Kim, and J. Y. Kim, "Balancing and sequencing mixed-model U-lines with a co-evolutionary algorithm," *Production Planning and Control*, vol. 11, no. 8, pp. 754–764, 2000.

[35] J. Miltenburg, "Balancing and scheduling mixed-model U-shaped production lines," *International Journal of Flexible Manufacturing Systems*, vol. 14, no. 2, pp. 123–155, 2002.

[36] T. Sawik, "Monolithic vs. hierarchical balancing and scheduling of a flexible assembly line," *European Journal of Operational Research*, vol. 143, no. 1, pp. 115–124, 2002.

[37] S. Bock, O. Rosenberg, and T. van Brackel, "Controlling mixed-model assembly lines in real-time by using distributed systems," *European Journal of Operational Research*, vol. 168, no. 3, pp. 880–904, 2006.

[38] L.-K. Hu, F.-Y. Shao, and G.-X. He, "Balancing analysis and algorithm design for mixed model assembly lines," in *Proceedings of the 18th International Conference on Industrial Engineering and Engineering Management (IE & EM '11)*, pp. 67–71, chn, September 2011.

[39] C. Merengo, F. Nava, and A. Pozzetti, "Balancing and sequencing manual mixed-model assembly lines," *International Journal of Production Research*, vol. 37, no. 12, pp. 2835–2860, 1999.

[40] Y. K. Kim, J. Y. Kim, and Y. Kim, "A coevolutionary algorithm for balancing and sequencing in mixed model assembly lines," *Applied Intelligence*, vol. 13, no. 3, pp. 247–258, 2000.

[41] S. Karabatı and S. Sayın, "Assembly line balancing in a mixed-model sequencing environment with synchronous transfers," *European Journal of Operational Research*, vol. 149, no. 2, pp. 417–429, 2003.

[42] B. Yagmahan, "Mixed-model assembly line balancing using a multi-objective ant colony optimization approach," *Expert Systems with Applications*, vol. 38, no. 10, pp. 12453–12461, 2011.

[43] P. Fattahi and M. Salehi, "Sequencing the mixed-model assembly line to minimize the total utility and idle costs with variable launching interval," *International Journal of Advanced Manufacturing Technology*, vol. 45, no. 9-10, pp. 987–998, 2009.

[44] T. Sawik, "Flexible assembly line balancing with alternate assembly plans and duplicate task assignments," in *Proceedings of the 6th International Conference on Emerging Technologies and Factory Automation (ETFA '97)*, pp. 171–176, September 1997.

[45] T. Sawik, "Monolithic vs. hierarchical balancing and scheduling of a flexible assembly line," *European Journal of Operational Research*, vol. 143, no. 1, pp. 115–124, 2002.

[46] T. K. Ralphs, M. J. Saltzman, and M. M. Wiecek, "An improved algorithm for solving biobjective integer programs," *Annals of Operations Research*, vol. 147, pp. 43–70, 2006.

[47] ILOG OPL, http://www-01.ibm.com/software/integration/optimization/cplex-optimization-studio/.

[48] A. M. Jubril, "A nonlinear weights selection in weighted sum for convex multiobjective optimization," *Facta Universitatis*, vol. 27, no. 3, pp. 357–372, 2012.

[49] A. L. Arcus, "COMSOAL a computer method of sequencing operations for assembly lines," *The International Journal of Production Research*, vol. 4, no. 4, pp. 259–277, 1966.

[50] R. V. Johnson, "A branch and bound algorithm for assembly line balancing problems with formulation irregularities," *Management Science*, vol. 29, no. 11, pp. 1309–1324, 1983.

[51] G. H. Milas, "Assembly line balancing: let's remove the mystery," *Industrial Engineering*, vol. 22, no. 5, pp. 31–36, 1990.

[52] P. Vrat and A. Virani, "A cost model for optimal mix of balanced stochastic assembly line and the modular assembly system for a customer oriented production system," *International Journal of Production Research*, vol. 14, no. 4, pp. 445–463, 1976.

Hindawi Publishing Corporation
Journal of Applied Mathematics
Volume 2013, Article ID 513261, 16 pages
http://dx.doi.org/10.1155/2013/513261

Research Article

Time-Dependent Reliability-Based Design Optimization Utilizing Nonintrusive Polynomial Chaos

Yao Wang,[1] Shengkui Zeng,[1,2] and Jianbin Guo[1,2]

[1] *School of Reliability and Systems Engineering, Beihang University, Beijing 100191, China*
[2] *Key Laboratory for Reliability & Environmental Engineering, Beijing 100191, China*

Correspondence should be addressed to Jianbin Guo; guojianbin@buaa.edu.cn

Received 13 December 2012; Revised 16 April 2013; Accepted 26 May 2013

Academic Editor: Xiaojun Wang

Copyright © 2013 Yao Wang et al. This is an open access article distributed under the Creative Commons Attribution License, which permits unrestricted use, distribution, and reproduction in any medium, provided the original work is properly cited.

Time-dependent reliability-based design optimization (RBDO) has been acknowledged as an advance optimization methodology since it accounts for time-varying stochastic nature of systems. This paper proposes a time-dependent RBDO method considering both of the time-dependent kinematic reliability and the time-dependent structural reliability as constrains. Polynomial chaos combined with the moving least squares (PCMLS) is presented as a nonintrusive time-dependent surrogate model to conduct uncertainty quantification. Wear is considered to be a critical failure that deteriorates the kinematic reliability and the structural reliability through the changing kinematics. According to Archard's wear law, a multidiscipline reliability model including the kinematics model and the structural finite element (FE) model is constructed to generate the stochastic processes of system responses. These disciplines are closely coupled and uncertainty impacts are cross-propagated to account for the correlationship between the wear process and loads. The new method is applied to an airborne retractable mechanism. The optimization goal is to minimize the mean and the variance of the total weight under both of the time-dependent and the time-independent reliability constraints.

1. Introduction

In recent decades, numerous endeavors have been made to develop the reliability-based design optimization (RBDO) methods, due to the fact that RBDO maximizes the performance under constrains of target reliability level accounting for various sources of uncertainty [1, 2]. These developed RBDO methodologies can be classified into two groups: time-independent RBDO and time-dependent RBDO.

Time-independent RBDO, which assumes reliability constraints are time independent, has been studied widely [2]. However, in many engineering cases, because of the degradation and stochastic loads, systems deterioration with time is such a severe problem that it must be taken into account. For instance, wear is one of the most critical failures that substantially affect the life span of bearings, hinges, and other mechanisms, and it should be considered in design phase [3]. For these applications, time-dependent RBDO methods should be conducted because the reliability is time varying. Most literatures on this topic concentrate on the time-dependent structural reliability problem. Two basic scenarios are presented, which are out-crossing methods [4–7] and extreme value methods [8, 9].

The out-crossing methods require the calculation of the crossing rate of the likelihood that the performance falls into the failure domain. The most fundamental equation of solving the out-crossing problems is the Rice formula. Kuschel and Rackwitz [4, 5] proposed a method based on the out-crossing approach to evaluate the time-dependent reliability in the context of first-order reliability methods (FORM) and asymptotic second-order reliability methods (SORM). The most probable point (MPP) in this method is defined as "point of maximum local crossing rate." Rectangular wave renewal processes and Gaussian processes are derived for load models, and the optimization goal is to minimize the total cost which contains initial cost and failure cost. Streicher and Rackwitz [6] improved this method by considering the dependencies among different failure modes, and

the numerical Laplace transforms are used for the treatment of aging components. Andrieu-Renaud et al. [7] presented an out-crossing-based method which is called PHI2. The limit state function is considered as a random process whose out-crossing of the zero level is to characterize.

The extreme value methods consider the failure event to be equivalent to the event that the extreme value is greater than or less than the threshold in a time interval, and time-dependent reliability can be translated to a time-independent one if the distribution of the extreme value is identified. Li et al. [8] discovered that correlative information among the component random events is inherent in the equivalent extreme-value event. Thus an equivalent extreme value approach is presented to evaluate the structural reliability. In the approach proposed by Chen and Li [9], a virtual stochastic process associated to the extreme value of the studied stochastic process is constructed. The probability density evolution method is used to evaluate the instantaneous probability density function (PDF) of the virtual stochastic process, which would generate the PDF of the extreme value simultaneously.

According to Bhatti [10], kinematic reliability is defined as the probability of output member's position and orientation falling into a specified range from the desired position and orientation. Fewer researches focus on time-dependent kinematic reliability analysis. Zhang et al. [11, 12] proposed a mean value first-passage method based on the out-crossing methods in structural reliability to evaluate the time-dependent reliability of the function generator mechanisms. This method is under the assumption of normality for random dimension variables with small variances; thus the motion error is a nonstationary Gaussian process, but their work only contains the randomness of parameters. The degradation of mechanisms which is a significant factor to the time-dependent kinematic reliability was not taken into account.

Wear is one of the most critical degradation failures for mechanisms. Worn joints would lead to motion errors as well as raise the stress. Thus wear would substantially deteriorate the kinematic reliability and structural reliability through the changing kinematics. Meanwhile, loads dominate the wear of joints, and worn joints would result in fluctuation of the motion of mechanisms and thus change the loads on joints conversely. The correlationship between the wear process and loads is required to be considered in the analysis of wear-related time-dependent reliability. Furthermore, each type of mechanisms has its particular wear characteristic which is determined by its function and operation condition. Because of the scarcity of the full-scale wear tests, it is hardly to obtain the accurate time-varying wear data in design phase especially for those newly designed mechanisms. Therefore, stochastic degradation process of system responses is difficult to obtain. All of these factors make the conventional out-crossing methods and extreme value methods inapplicable to the wear-related time-dependent RBDO problem.

In this paper, a new time-dependent RBDO strategy is proposed to account for both of the time-dependent kinematic reliability and the time-dependent structural reliability as constrains. In order to perform the uncertainty quantification, a time-dependent surrogate model, which is called polynomial chaos combined with the moving least squares (PCMLS), is presented to approximate the stochastic process. Nonintrusive polynomial chaos (NIPC) is used to describe the stochastic nature of system responses at selected time points. Then moving least squares (MLS) method is employed to approximate the time variant functions of PCE coefficients. Because of the explicit polynomial formula and simple structure, Monte Carlo simulation (MCS) is able to be conducted on the surrogate model to evaluate the time-dependent kinematic reliability and structure reliability.

To tackle with the scarcity of wear data, a multidiscipline reliability model is constructed according to Archard's wear law. Disciplines in the model are closely coupled and uncertainty impacts are cross-propagated to simulate the wear process. The model takes an iterative simulation to generate the stochastic processes of system responses. The correlationship between the wear process and loads is considered in the model, and the uncertain inputs include random variables and stochastic loads. Thus the time-dependent degradation tests and data are not necessary.

The proposed time-dependent RBDO method includes three stages: (1) multidiscipline reliability model and simulation for generation of degradation process; (2) PCMLS for time-dependent uncertainty quantification; (3) genetic algorithm (GA) for the global optimum.

The whole approach is demonstrated at an airborne retractable mechanical system under the stochastic wind load. Wear of the hinge is considered to be the most critical failure. The multidiscipline reliability model, which involves kinematics model and structural FE model, is constructed. The optimization goal is to minimize the mean and variance of the total weight under the time-dependent probabilistic constraints related to the kinematic reliability and the structure reliability.

The paper is organized as follows. In Section 2, the theories of NIPC and MLS are presented, respectively, and the PCMLS model is derived. In Section 3, the theoretical basis and the numerical procedure of the multidiscipline reliability model are presented. In Section 4, the proposed time-dependent RBDO is formulated. The case of the airborne retractable mechanical system is studied in Section 5. Conclusions are drawn in Section 6.

2. Polynomial Chaos Combined with the Moving Least Squares

The polynomial chaos expansion is a promising surrogate model that uses a set of orthogonal polynomial bases to approximate the random space of the system response [13]. According to whether it requires the modification of the deterministic code, the polynomial chaos approaches can be divided into two groups: intrusive approach and nonintrusive approach. Intrusive approach calculates the unknown polynomial chaos coefficients by projecting resulting equations onto basis functions for different modes. It requires the modification of the deterministic code. Thus it is difficult, expensive, and time consuming for many complex computational problems [14]. On the contrary, in the nonintrusive

PC (NIPC), simulations are used as black boxes and the calculation of chaos expansion coefficients is based on a set of simulation response evaluations. Most nonintrusive approaches are based on sampling or quadrature methods. Hosder et al. [14] applied the point-collocation NIPC to an aerospace problem with multiple uncertain variables. Sudret [15] proposed a nonintrusive regression-based PCE to conduct the global sensitivity analysis. Cheng and Sandu [16] proposed a least squares NIPC approach based on collocation at a low-discrepancy set of points which is demonstrated to have similar accuracy with the Galerkin approach by numerical experiments.

Most NIPC methods are used to approximate the time-independent responses. However, a few literatures concentrate on the improvement of NIPC methods to propagate the time-dependent uncertainty. Witteveen et al. [17] proposed the probabilistic collocation for limit cycle oscillation (PCLCO) to modeling the long-term stochastic behavior of dynamical systems. PCLCO transforms the time-dependent issue into a time-independent one through the time-independent parametrization of the periodic response. Then the NIPC can be performed due to the independence of time, but PCLCO is only applicable to approximate the periodically time-dependent response. This paper proposes a surrogate model method which involves polynomial chaos combined with the moving least squares (PCMLS) to quantify more general time-dependent uncertainty. The surrogate model is essentially a time-dependent polynomial chaos expansion, and the coefficients of which are approximation functions achieved by the MLS method. The polynomial chaos expansion with time-dependent coefficients is used to approximate the stochastic process.

2.1. Polynomial Chaos Expansion. The polynomial chaos of a system response can be described as follows [18–20]:

$$r(\boldsymbol{\xi}) = a_0 + \sum_{i_1=1}^{\infty} a_{i_1}\Gamma_1\left(\xi_{i_1}\right) + \sum_{i_1=1}^{\infty}\sum_{i_2=1}^{i_1} a_{i_1 i_2}\Gamma_2\left(\xi_{i_1},\xi_{i_2}\right) + \sum_{i_1=1}^{\infty}\sum_{i_2=1}^{i_1}\sum_{i_3=1}^{i_2} a_{i_1 i_2 i_3}\Gamma_3\left(\xi_{i_1},\xi_{i_2},\xi_{i_3}\right) + \cdots, \tag{1}$$

where $r(\boldsymbol{\xi})$ is the random system response, a_i is the coefficient of PCE, $\Gamma_p(\xi_{i_1},\ldots,\xi_{i_p})$ is the polynomial of the selected base, ξ_i is a random variable with a suitable PDF agreed with the polynomial base, and p is the polynomial degree. According to the Wiener-Askey scheme, there are several families of polynomials (e.g., Hermite, Legendre, Jacobi, etc.) that could be employed depending on the random distributions. When ξ_i represents for a standard normal random variable, Hermite's polynomials are selected as bases. The multidimensional Hermite polynomials in (1) is given by

$$\Gamma_p\left(\xi_{i_1},\ldots,\xi_{i_p}\right) = (-1)^p e^{(1/2)\boldsymbol{\xi}^T\boldsymbol{\xi}}\frac{\partial^p}{\partial\xi_{i_1}\cdots\partial\xi_{i_p}}e^{-(1/2)\boldsymbol{\xi}^T\boldsymbol{\xi}}, \tag{2}$$

where $\boldsymbol{\xi}$ is the vector of normal random variables $\{\xi_{i_k}\}_{k=1}^{p}$. In practical engineering, PCE contains limited input uncertainties. Thus (1) can be simplified as follows:

$$r(\boldsymbol{\xi}) = \sum_{j=0}^{N_c-1} a_j\Psi_j(\boldsymbol{\xi}), \tag{3}$$

where $\Psi_j(\boldsymbol{\xi}) = \prod_{i=1}^{p}\psi_{m_i}^{j}(\xi_i) = \Gamma_p(\xi_{i_1},\ldots,\xi_{i_p})$ and N_c is the total number of PCE coefficients, which can be calculated as

$$N_c = 1 + \frac{n!}{(n-1)!} + \frac{(n+1)!}{(n-1)!2!} + \cdots + \frac{(n-1+p)!}{(n-1)!p!} = \frac{(n+p)!}{n!p!}, \tag{4}$$

where n is the number of random variables in the system.

The multidimensional Hermite polynomials form an orthogonal basis for the space of square-integrable PDFs, and the PCE is convergent in the mean-square sense [21]. In general, the approximation accuracy rises with the order of the PCE.

Probabilistic collocation method is one of the most efficient NIPC methods. The coefficients of the PCE are obtained according to evaluations of the system response at selected collocation points, and these collocation points correspond to the roots of the polynomial of one degree higher than the order of the PCE [14]. Furthermore, the probabilistic collocation method just requires calls of the simulation the same as the number of PCE coefficients thus it is very efficient. The matrix form of probabilistic collocation method is describe as follows:

$$\begin{bmatrix} r(\boldsymbol{\xi}_1) \\ r(\boldsymbol{\xi}_2) \\ \vdots \\ r(\boldsymbol{\xi}_{N_c}) \end{bmatrix} = \begin{bmatrix} \Psi_0(\boldsymbol{\xi}_1) & \Psi_1(\boldsymbol{\xi}_1) & \cdots & \Psi_{N_c-1}(\boldsymbol{\xi}_1) \\ \Psi_0(\boldsymbol{\xi}_2) & \Psi_1(\boldsymbol{\xi}_2) & \cdots & \Psi_{N_c-1}(\boldsymbol{\xi}_2) \\ \vdots & \vdots & \ddots & \vdots \\ \Psi_0(\boldsymbol{\xi}_{N_c}) & \Psi_1(\boldsymbol{\xi}_{N_c}) & \cdots & \Psi_{N_c-1}(\boldsymbol{\xi}_{N_c}) \end{bmatrix} \times \begin{bmatrix} a_0 \\ a_1 \\ \vdots \\ a_{N_c-1} \end{bmatrix}, \tag{5}$$

where $\boldsymbol{\xi}_j$ represents the jth set of collocation points. Total N_c sets of collocation points are required. Equation (5) can be written in a compact form

$$\mathbf{r}(\boldsymbol{\Xi}) = \boldsymbol{\Psi}(\boldsymbol{\Xi})\,\mathbf{a}. \tag{6}$$

As a linear algebraic equation, (6) can be solved by Gauss elimination method and so forth. The sets of collation points are required to be chosen carefully to keep the matrix $\boldsymbol{\Psi}(\boldsymbol{\Xi})$ nonsingular, and the vector of coefficients can be derived as

$$\mathbf{a} = \boldsymbol{\Psi}^{-1}(\boldsymbol{\Xi})\,\mathbf{r}(\boldsymbol{\Xi}) = \mathbf{D}(\boldsymbol{\Xi})\,\mathbf{r}(\boldsymbol{\Xi}). \tag{7}$$

2.2. Moving Least Squares. In order to reduce the cost of constructing numeral PCEs along the time period of

degradation, the PCE is only built at some selected time points, and the moving least squares (MLS) method is employed to approximate the time-dependent functions of PCE coefficients. MLS is a generalization of the least squares technique, and it has become a widespread and powerful tool in interpolating and approximating implicit surfaces [22–25]. MLS starts with a weighted least squares formulation for an arbitrary fixed point in $\mathbb{R}^d$, and then this point moves over the entire parameter domain, where a weighted least squares fit is computed and evaluated for each point individually. Suppose a compact set $\Omega \subseteq \mathbb{R}^d$ is given and a continuous function f will be reconstructed from its values $f(x_1), f(x_2), \ldots, f(x_N)$ on scattered pairwise distinct centers $\mathbf{X} = \{x_1, x_2, \ldots, x_N\}$. Then the approximate value $\widehat{f}(\mathbf{x})$ is given by [23]

$$\min_{\widehat{f} \in \Pi_q^d} \sum_i w\left(\|\mathbf{x} - \mathbf{x}_i\|\right) \left\| \widehat{f}\left(\mathbf{x}_i\right) - f\left(\mathbf{x}_i\right) \right\|^2, \tag{8}$$

where d represents the dimension of the function f, q represents the order of $\mathbf{p}(\mathbf{x})$ which is the polynomial basis vector, and $w(\|\mathbf{x} - \mathbf{x}_i\|)$ is the weighting function. The functional form and parameters of the weighting function determine the accuracy of the MLS approximation. The weighting function should satisfy the principles as follows [26].

(1) The weighting function is nonnegative,

$$w\left(\|x - x_i\|\right) > 0 \text{ inside the support domain } \Omega. \tag{9}$$

(2) The weighting function has compact support,

$$w\left(\|x - x_i\|\right) > 0 \text{ outside the support domain } \Omega. \tag{10}$$

(3) The weighting function should be normalized,

$$\int_\Omega w\left(\|x - x_i\|\right) d\Omega = 1. \tag{11}$$

(4) The weighting function should be monotone decreasing, and the weight values should decrease with the increase of the distance from x.

The most common weighting functions are spline function, compactly supported radial basis function (CSRBF), Gaussian function, and so forth. Among these weighting functions, the spline functions are used widely because its order can be chosen to obtain high approximation accuracy. Note that the higher the order of the spline functions would not necessarily perform a better approximation, and the order of the spline function is decided by the highest order of the approximated function derivative.

The approximation function can be written as

$$\widehat{f}\left(\mathbf{x}\right) = \mathbf{p}^{\mathbf{T}}\left(\mathbf{x}\right) \mathbf{b}\left(\mathbf{x}\right), \quad \mathbf{x} \in \boldsymbol{\Omega}, \tag{12}$$

where $\mathbf{b}(\mathbf{x})$ is the coefficient vector. For a one-dimension problem, the polynomial basis $\mathbf{p}(\mathbf{x})$ has the form

$$\begin{aligned} \mathbf{p}^{\mathbf{T}} &= (\mathbf{1}, \mathbf{x}), \quad q = 1, \\ \mathbf{p}^{\mathbf{T}} &= \left(\mathbf{1}, \mathbf{x}, \mathbf{x}^2\right), \quad q = 2. \end{aligned} \tag{13}$$

It is defined as

$$\mathbf{J} = (\mathbf{pb} - \mathbf{f})^{\mathbf{T}} \mathbf{W}\left(\mathbf{x}\right) (\mathbf{pb} - \mathbf{f}), \tag{14}$$

where $\mathbf{f} = \{f(x_1), f(x_2), \ldots, f(x_N)\}^T$. In order to compute $\mathbf{b}(\mathbf{x})$, extreme value of $\mathbf{J}$ should be taken as

$$\frac{\partial \mathbf{J}}{\partial \mathbf{b}} = \mathbf{A}\left(\mathbf{x}\right) \mathbf{b}\left(\mathbf{x}\right) - \mathbf{B}\left(\mathbf{x}\right) \mathbf{f} = 0, \tag{15}$$

and $\mathbf{b}(\mathbf{x})$ can be derived as

$$\mathbf{b}\left(\mathbf{x}\right) = \mathbf{A}^{-1}\left(\mathbf{x}\right) \mathbf{B}\left(\mathbf{x}\right) \mathbf{f}, \tag{16}$$

where

$$\mathbf{A}\left(\mathbf{x}\right) = \mathbf{p}^{\mathbf{T}} \mathbf{w}\left(\mathbf{x}\right) \mathbf{p}, \tag{17}$$

$$\mathbf{B}\left(\mathbf{x}\right) = \mathbf{p}^{\mathbf{T}} \mathbf{w}\left(\mathbf{x}\right). \tag{18}$$

Therefore, the approximation function can be derived as

$$\widehat{f}\left(\mathbf{x}\right) = \Phi\left(\mathbf{x}\right) \mathbf{f}, \tag{19}$$

where $\Phi(\mathbf{x}) = \mathbf{p}^{\mathbf{T}}(\mathbf{x})\mathbf{A}^{-1}(\mathbf{x})\mathbf{B}(\mathbf{x})$.

2.3. The Proposed PCMLS Method. The multidiscipline reliability model is simulated step by step, and one step is defined as a task execution in which the mechanism would perform a required function. The PCE is constructed on system responses at some selected steps along the service life. After this, MLS method is employed to approximate the time-dependent functions of PCE coefficients. Total N_s tasks need to be completed which is decided by the length of service life and frequency of task arrival. T_i is defined as the ith selected step (or task), and m is the total number of selected steps that PCEs are required to be built on. According to (7), the coefficients for all of the PCEs are solved by the following equation:

$$\begin{aligned} \mathbf{a}^{T_1} &= \mathbf{D}\left(\Xi\right) \mathbf{r}^{T_1}\left(\Xi\right), \\ \mathbf{a}^{T_2} &= \mathbf{D}\left(\Xi\right) \mathbf{r}^{T_2}\left(\Xi\right), \\ &\vdots \\ \mathbf{a}^{T_m} &= \mathbf{D}\left(\Xi\right) \mathbf{r}^{T_m}\left(\Xi\right), \end{aligned} \tag{20}$$

where $\mathbf{r}^{T_i}(\Xi)$ is the vector of responses at T_i and $\mathbf{a}^{T_i}$ is the vector of the coefficients of PCE at T_i. Equation (20) can be simplified as

$$\Lambda = \mathbf{D}\left(\Xi\right) \mathbf{R}\left(\Xi\right), \tag{21}$$

where $\mathbf{D}$ is $mN_c \times mN_c$ matrix, $\mathbf{R} = [\mathbf{r}^{T_1}, \mathbf{r}^{T_2}, \ldots, \mathbf{r}^{T_m}]^T$ is $mN_c \times 1$ matrix, and $\Lambda = [\mathbf{a}^{T_1}, \mathbf{a}^{T_2}, \ldots, \mathbf{a}^{T_m}]^T$ is $mN_c \times 1$ matrix.

After the calculation of Λ, a new matrix $\mathbf{H}$ of PCEs coefficients is created. Each row represents coefficients of the PCE at a selected step, and each column represents a specific

coefficient varying with steps. $\mathbf{H}$ can be then expressed in a column form

$$\mathbf{H} = \left[\mathbf{a}_0, \mathbf{a}_1, \ldots, \mathbf{a}_{N_c-1}\right], \tag{22}$$

where $\mathbf{a}_0$ is the vector of the first coefficients of PCEs along with the steps. According to (19), the approximation functions of time-dependent PCE coefficients are derived as

$$\widehat{\mathbf{f}}(\mathbf{T}) = \Phi(\mathbf{T})\,\mathbf{H}, \tag{23}$$

where $\widehat{\mathbf{f}}(\mathbf{T}) = [\widehat{f}_0(\mathbf{T}), \widehat{f}_1(\mathbf{T}), \ldots, \widehat{f}_{N_c-1}(\mathbf{T})]$, $\widehat{f}_i(\mathbf{T})$ is defined as approximation function of the ith coefficient, and $\mathbf{T} = [T_1, T_2, \ldots, T_m]$ is the vector of selected steps. Then the conventional PCE can be translated into a time-dependent PCE, which is written as follows

$$r(\boldsymbol{\xi}, \mathbf{T}) = \sum_{j=0}^{N_c-1} \widehat{f}_j(\mathbf{T})\,\Psi_j(\boldsymbol{\xi}). \tag{24}$$

The proposed PCMLS method is able to consider the statistical correlation between a pair of responses at two different time points. The multidiscipline reliability model is simulated step by step to describe the degradation behavior of the mechanical system. Uncertainties of the parameters and design variables are brought into the model at the beginning of the simulation. The system degradation at the current step is computed according to the system degradation at the step before. Thus these uncertainties would propagate through different disciplines as well as evolve over time, and the system responses at different time points have statistical correlationship. The statistical correlation information is contained in the samples of system responses at different time points.

The proposed PCMLS method is a nonintrusive method to construct the time-dependent PCE. The PCMLS model uses samples of system responses to perform the NIPC at different time steps. Then the MLS is conducted to approximate the time-dependent PCE coefficients. In this manner, the statistical correlation information is extracted into the time-dependent coefficients of the PCE, which are actually functions of time, and these time-dependent PCE coefficients would make the polynomials of PCE vary with time and thus would make the statistical properties of the approximated responses vary with time as well. Therefore, the statistical correlation is considered in the PCMLS model.

3. Multidiscipline Reliability Model Considering Wear

Wear is one of the most critical failures that substantially deteriorate the kinematic reliability and structural reliability of mechanisms in their service life. For a linkage mechanism, wear of the hinges would affect the sport stability, raise the stress in hinges, and lead to motion errors.

Numerical wear prediction develops fast recently. It helps to study the effect of the wear evolution on the stress distribution and deformation of the motion pairs, which can hardly be measured with the experimental techniques. Söderberg and Andersson [27] presented a wear simulation method based on Archard's wear law and adaptive FE method to simulate the wear of the brake pad under steady-state drag conditions. Rezaei et al. [3] proposed an adaptive wear modeling method to study the wear progress in radial sliding bearings. In this method, remeshing is performed both on the contact elements and their proximity elements. All of these proposed methods are demonstrated by experiments.

However, these methods are based on the assumption that the sliding velocity and loads on the motion pairs hardly vary during the wear process. These two parameters are then considered to be boundary conditions, which are regarded as constants. In practice, the wear process would modify the kinematics continuously and lead to variation of the loads and the sliding velocity of motion pairs all the time. Traditional methods that neglect the variation of loads and the sliding velocity will cause inaccuracy at the wear simulating results. Meanwhile, in the above-mentioned methods, wear process is simulated at nominal state. Uncertainties of geometry and material are not taken into account.

In this section, a multidiscipline reliability model that includes kinematics model, structural FE model, and wear model is constructed to simulate the wear process of the hinges in the linkage mechanism.

3.1. Wear Mechanism. To the plastically dominated wear, Archard's law would serve as the appropriate model as discussed by Lim and Ashby [28]. In this model, the worn out volume is considered to be proportional to the normal load. The model is expressed mathematically as follows:

$$\frac{dw}{dt} = K\frac{F_N v}{\mathbf{H}}, \tag{25}$$

where dw/dt is defined to be the wear volume loss rate, K is the dimensionless wear coefficient, F_N is the applied normal force, $\mathbf{H}$ is the Brinell hardness of the softer material and it is usually considered to be a constant, and v denotes the relative sliding velocity. Since the wear depth is of interest, (25) is often written in the following form

$$\frac{dh}{dt} = k_H P v, \tag{26}$$

where h is the wear depth, dh/dt is the wear depth rate, and P is the contact pressure. We have $k_H = K/H$, and it is defined as the wear coefficient with the dimension of (Pa^{-1}). The wear process is considered to be a time-dependent process.

In practical engineering, the contact pressure varies with time because the real contact area changes during the wear process. Meanwhile, the contact pressure and relative sliding velocity vary with stochastic loadings. Thus both of these two parameters are time dependent. The numerical solution for the wear depth is obtained by estimating the differential form in (26) with a finite difference to yield the following updated formula:

$$h_i = h_{i-1} + k_H P(\Theta_i, t_i)\, v(\Theta_i, t_i) \cdot \Delta t, \tag{27}$$

where h_i is the wear depth at the ith step, Θ_i is the vector of stochastic loads at the ith step, and t_i is ith step.

3.2. Multidiscipline Reliability Model. In Archard's wear law, the wear rate is a function of both the pressure and the relative sliding velocity of two contact surfaces, and the pressure is obtained through nonlinear FEA, while the relative sliding velocity requires kinematics analysis. Meanwhile, the pressure and relative sliding velocity are varying with the wear process due to the fact that worn joints would change the kinematics. Therefore, the calculation of wear depth needs an iterative process.

For a linkage mechanism, the multidiscipline reliability model includes kinematics model and structural FE model. The kinematics model is constructed on the entire mechanism to obtain the relative sliding velocity of hinges, and loads on hinges can also be given by the kinematics model. Then these loads are transmitted into the structural FE model, which is built with commercial finite element software ANSYS. FE model of hinges is solved by the nonlinear contact analysis to compute the stress distribution and contact pressure. After that, the conduct pressure and sliding velocity are delivered to the wear model to calculate the wear depth, according to which, the kinematics model and structural FE model would be updated in the next step, and the schematic of the multidiscipline reliability model is shown in Figure 1.

In Figure 1, Δh_i, $\Delta\Theta_i$, Δv_i, and ΔP_i are the variation ranges of the wear depth, loads on hinges, relative sliding velocity, and contact pressure, respectively. Variation ranges of these parameters come from the dimension tolerances, parameter distributions, and stochastic environmental disturbance. Therefore, uncertainties exist in every discipline. As these disciplines are naturally closely coupled and uncertainty impacts are cross-propagated, the correlationship between the wear process and loads is considered in the multidiscipline reliability model.

The simulation would generate the stochastic processes of stress and wear depths in hinges. The increase of wear depth would deteriorate the kinematic reliability, and the raise of stress in hinges would decrease the structural reliability. Thus the multidiscipline reliability model can be used to evaluate wear-related time-dependent kinematic reliability and structure reliability. The effect of wear process on the whole mechanism is taken into account by the coupling among wear model and other disciplines. The proposed method permits that values of parameters in wear model are obtained from relevant disciplines instead of determined by empirical assumptions; hence the multidiscipline reliability model is of higher accuracy. The simulation routine is described in Figure 2.

In this procedure, there are two different types of discretizations which include (1) the continuous geometry discretized by finite elements; (2) the continuous material removal is approximated at a discrete set of steps. These discretizations are important factors to the accuracy of the simulation results. Thus the size of the discretizations is required to be determined carefully.

Since the multidiscipline reliability model is built, wear process can be simulated and studied. Uncertainties exist in the model and propagate through different disciplines. MCS should be employed to quantify the time-dependent uncertainty. However, the non-linear contact FEA and kinematics analysis, which contain numerous nonlinear algebraic equations and differential equations required to solve numerically, are very computationally expensive. Furthermore, the iterative process in a single simulation leads to repeated calls of these expensive models. Therefore, traditional MCS are computational infeasible. The PCMLS model proposed in this paper can be employed to approximate the stochastic processes generated by the multidiscipline reliability model. Then the computational expensive implicit model is replaced by an explicit surrogate model with simple structure, and MCS is able to be conducted on the surrogate model which would substantially reduce the computational cost.

4. Time-Dependent RBDO Procedure

Time-dependent RBDO procedure is the organization of all the elements such as system optimization, system analysis, discipline analysis, and time-dependent uncertainty analysis. How to efficiently arrange these elements into an execution sequence is the key to realize time-dependent RBDO. This paper proposes a three-stage strategy, and the procedure is shown in Figure 3.

In the first stage, multidiscipline reliability model considering wear is constructed. In the second stage, the PCMLS model is applied to approximate the stochastic processes. In the third stage, a double-loop optimization is employed. In the outer loop, optimization algorithm executes optimum search. At each iteration, the inter loop calls uncertainty analysis, which applies MCS to PCMLS model, to evaluate the design and its time-dependent uncertainty characteristics. Because the PCMLS model is an explicit formula both with high accuracy and simple structure, it would significantly improve the computational efficiency of the whole time-dependent RBDO procedure. The general time-dependent RBDO based on the PCMLS model is reformulated as follows:

$$\begin{aligned}
&\min\ \widetilde{h}\left(\mathbf{x}, \mathbf{d}, \mathbf{q}\right)\\
&\text{s.t. } P\left\{\left(g_i\left(\mathbf{T}, r_i\left(\boldsymbol{\xi}, \mathbf{T}\right), c_{f_i}\right) \le 0\right)\right\} \ge R_{TD_i},\\
&\qquad\qquad i = 1, 2, \ldots, n_{TD},\\
&P\left\{g_j\left(\mathbf{x}, \mathbf{d}, \mathbf{q}\right) \le 0\right\} \ge R_{TI_j}, \quad j = 1, 2, \ldots, n_{TI},\\
&\qquad\qquad \mathbf{x}^L \le \mathbf{x} \le \mathbf{x}^U,
\end{aligned} \tag{28}$$

where $\mathbf{x}$ is the vector of random design variables, $\mathbf{d}$ is the vector of deterministic parameters, and $\mathbf{q}$ is the vector of random parameters. $r_i(\boldsymbol{\xi}, \mathbf{T})$ is the PCMLS model of the ith system response, c_{f_i} is the failure criterion of the ith system response, $g_i(\mathbf{T}, r_i(\boldsymbol{\xi}, \mathbf{T}), c_{f_i})$ is the time-dependent limit state function, R_{TDi} is the time-dependent reliability constrains, n_{TD} is the total number of the time-dependent responses, $g_j(\mathbf{x}, \mathbf{d}, \mathbf{q})$ is the jth time-independent limit state function, R_{TIj} is the time-independent reliability constrains, and n_{TI} is the total number of the time-independent responses.

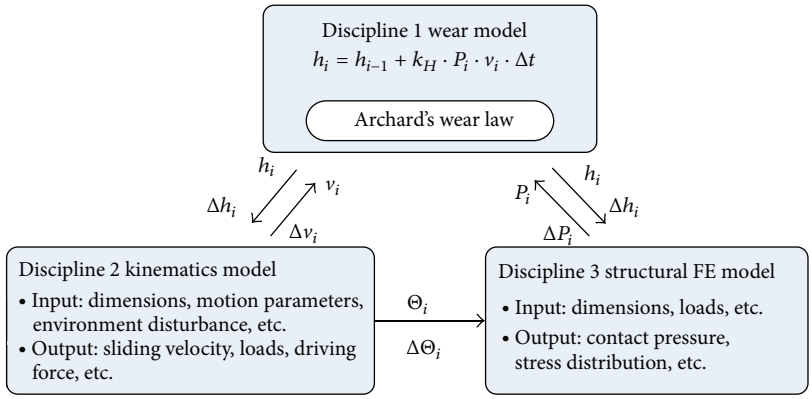

Figure 1: Schematic of the multidiscipline reliability model considering wear.

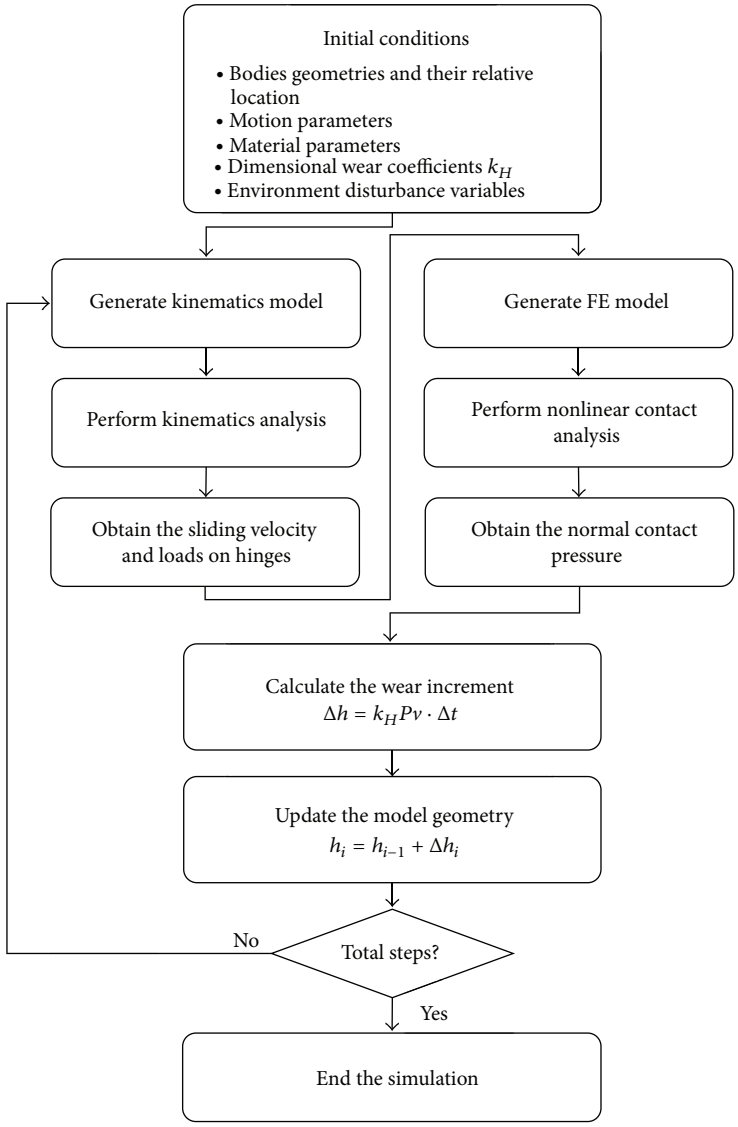

Figure 2: Simulation routine of the multidiscipline reliability model considering wear.

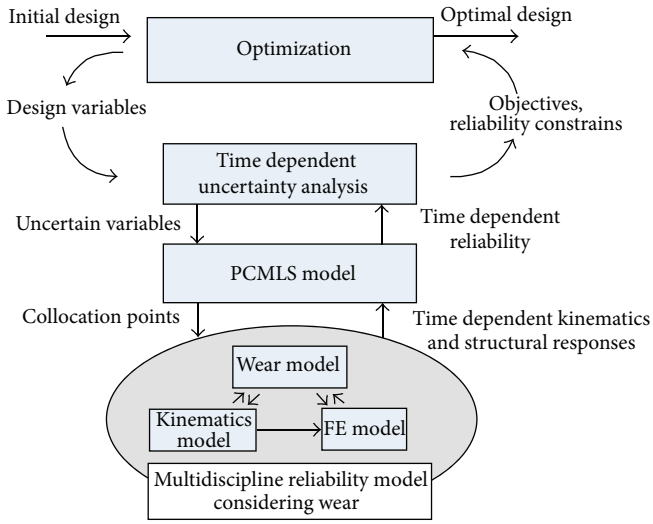

Figure 3: Procedure of time-dependent RBDO considering wear.

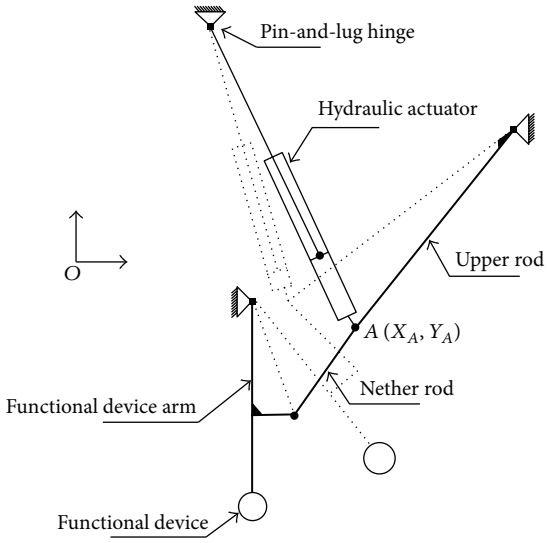

Figure 4: Schematic of the airborne retractable mechanical system.

5. Case Study

The engineering case is an airborne retractable mechanical system. It is a four-link mechanism which consists of the hydraulic actuator, rods, and pin-and-lug hinges. It is designed to carry the functional device to move in accordance with the predetermined trajectory for switching between working and stopping positions.

The system performs a retractable action when a task arrives, and it is required to work reliably during the service life. When the retractable system is performing, it is under the loads of wind and the weight of the functional device. The hinges are working in a nonlubricated environment. Therefore, wear of the hinges is considered to be a critical failure. Worn hinges give rise to fluctuation of the rod loads, decrease the kinematic accuracy, and lead to the mechanism lock during the movement. Furthermore, worn hinges would increase the stress in hinges which may cause them to fracture during the operation. The top hinge in Figure 4 is the most dangerous one for it bears the largest load. Thus wear in this hinge is considered in the multidiscipline reliability model.

5.1. Multidiscipline Reliability Model. The multidiscipline reliability model is built to simulate the system degradation caused by wear according to the proposed method in Section 3. The kinematics model of the mechanism and the FE model of the rods and hinges are built at the initial design point.

Through the kinematics simulation, the kinematics parameters are calculated and shown in Figure 5. The driving force is supplied by the hydraulic actuator to make the mechanism move properly. Because of the clearance between the pin and lug in hinges, there are fluctuations both in the driving force and instant relative velocity. The maximum driving force is 15423 N, which is below the rated pressure of the hydraulic actuator, and thus the mechanism would operate properly.

The FE model is built with commercial finite element software ANSYS. The materials of pin and lug are different, and the pin is more wear resistant than lug. Thus, the multidiscipline reliability model is based on the assumption that worn part only involves the lug. From Figure 6(b), the contact mainly occurs at the head and shoulder of the lug where the wear may be more serious.

The process that the mechanism moves from the stopping position to the working position and then moves back is defined as a task. As the total time of each task is short, the wear loss of each task is very small. Therefore, each task is as a step, during which the kinematics analysis and FEA is conducted. At the end of the step, wear depth is calculated according to the parameters delivered by the kinematics model and FE model, and kinematics model and FE model would be updated in the next step according to the changing

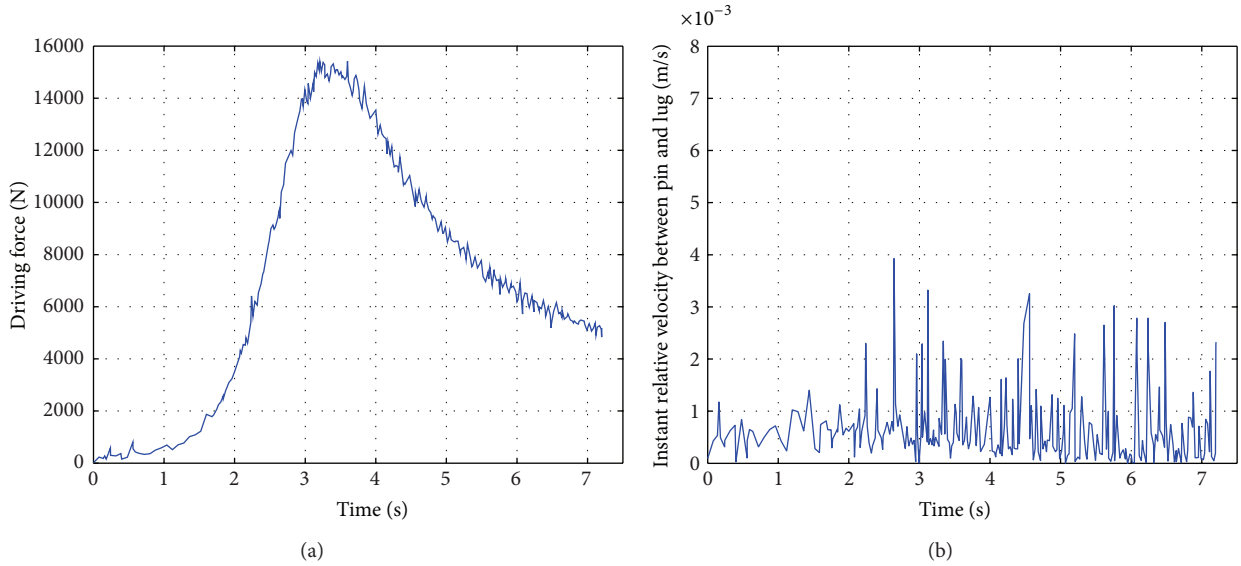

FIGURE 5: Driving force and instant relative velocity between pin and lug computed by the kinematics model. (a) Driving force curve during the movement; (b) instant relative velocity curve during the movement.

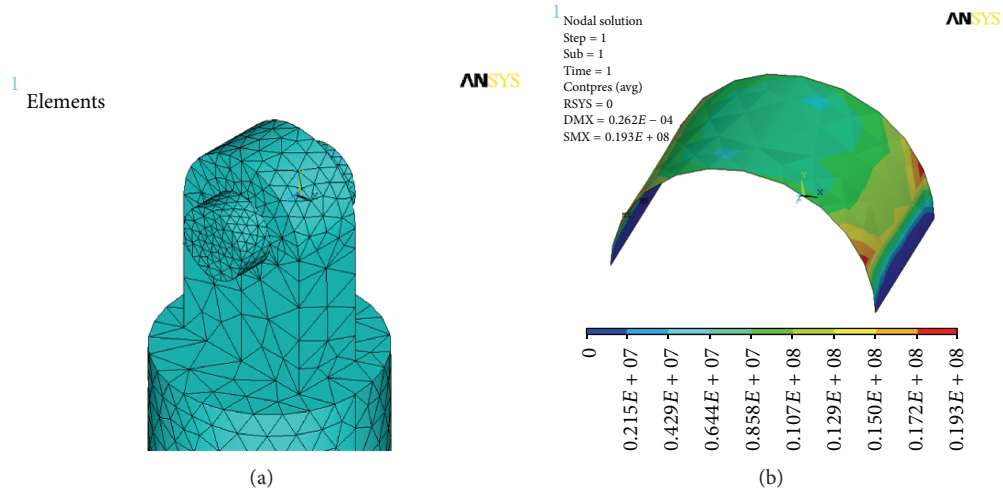

FIGURE 6: FE model and nonlinear contact analysis results exported by ANSYS. (a) FE model of the top hinge; (b) contour picture of the pressure on the contact surface of lug.

geometry. In the service life, the mechanism would act about 2000 times which is considered to be the total steps in the algorithm.

The positions of three fixed supports and the length of the functional device arm are determined by requirements from higher level system. Thus they are considered to be boundary conditions in the optimization. The coordinate (X_A, Y_A) defines the length and orientation of the upper rod and nether rod. Thus the coordinates of point A are significant design variables. Moreover, radiuses of the functional device arm and the upper rod contribute to the total weight of the mechanical system, and they are constrained by loads. Thus they are the other two design variables. In the multidiscipline reliability model, the parameter uncertainties involve machining errors and environment disturbance which are summarized in Table 1. The uncertain parameters of geometry are sampled at the beginning of the simulation, and the wind disturbance is sampled at each step.

According to results from the simulation at the initial design point, the time-dependent wear depth and contact pressure are shown in Figure 7, while the time-dependent lug stress and maximum driving force are described in Figure 8.

The contact pressure in Figure 7(b) is the average pressure of the whole contact surface. Thus the wear depth calculated by the contact pressure is also the average wear depth of lug. At the 2000th step, the wear depth is up to 13.4645 μm which is below the limit determined by the mechanism accuracy. With the increasing of the time step, the contact pressure

Table 1: Information on design variables and parameters.

Type	Symbol	Description	Mean	Std	Distribution
Random design variables	X_A	Coordinate X of point A	1176	2	Normal
	Y_A	Coordinate Y of point A	−497	2	Normal
	R_{ur}	Outer radius of the upper rod	30 mm	0.3 mm	Normal
	R_{arm}	Outer radius of the device arm	50 mm	0.5 mm	Normal
Random parameters	L_{sr}	Length of actuator slider rod	1600 mm	3 mm	Normal
	R_{nr}	Radius of the nether rod	20 mm	0.2 mm	Normal
	G_d	Weight of device	2600 N	10 N	Normal
	W_x	Wind disturbance of X direction	400 N	5 N	Normal
	W_y	Wind disturbance of Y direction	375 N	5 N	Normal
	W_z	Wind disturbance of Z direction	206 N	5 N	Normal

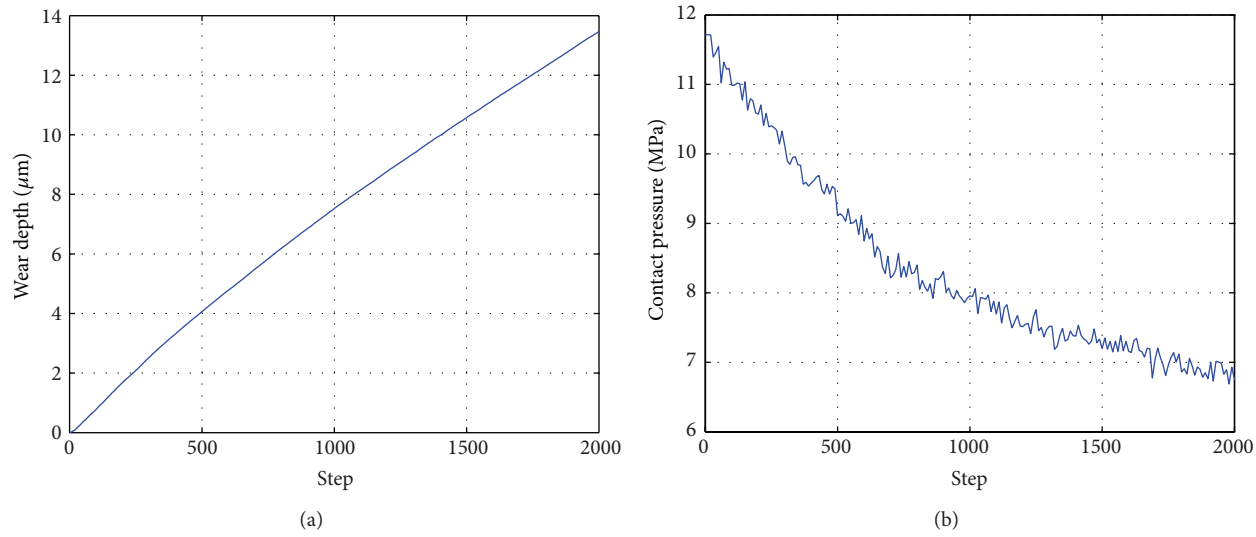

Figure 7: Time-dependent responses of wear depth and contact pressure. (a) Wear depth curve during the service life; (b) contact pressure curve during the service life.

shows a downward trend, and this trend makes the growth of the wear depth slows down gradually. These phenomena are consistent with the literatures [3, 21] which is demonstrated by experiments. The fluctuation of contact pressure is caused by the fluctuation of the driving force.

Stress of lug raises as the wear depth grows, which illustrates that the wear would deteriorate the structure of lug. The clearance between pin and lug increases with the growth of the wear depth, which leads to the maximum driving force fluctuate with time. In every task, stochastic wind disturbance is loading on the device. Thus the stochastic wind disturbance is another reason to the vibration in stress and maximum driving force. Some experiments have been conducted on the prototype, and results are extracted to employ V&V on the multidiscipline reliability model.

5.2. The PCMLS Model. Figures 7 and 8 illustrate that the wear depth and the stress of lug are time-dependent responses. The proposed PCMLS model is conducted to approximate these two responses.

The preliminary sensitivity analysis (SA) is firstly employed to screen out the critical parameters whose deviation would have a great impact on the system responses. Total 10 parameters are considered in SA, which are shown in Table 1. The forward difference method, which is commonly used in the preliminary sensitivity analysis, is executed due to its simplicity and rapidity. The sensitivity of the wear depth and von Mises stress of the lug are evaluated by several perturbation sizes of these 10 parameters to obtain reliable results.

Based on the SA results and the practical engineering experiences, four parameters are chosen which include "coordinate X of point A," "coordinate Y of point A," "length of actuator slider rod," and "weight of the device". Thus the dimension of the PCE is four. Secondly, the sets of collocation points are selected, and the total number of sets is calculated by (4). Then collocation points of standard normal random variables are transformed into inputs of the multidiscipline reliability model. The transformation functions are listed in Table 2.

Thirdly, the sets of transformed values are brought into the multidiscipline reliability model to generate

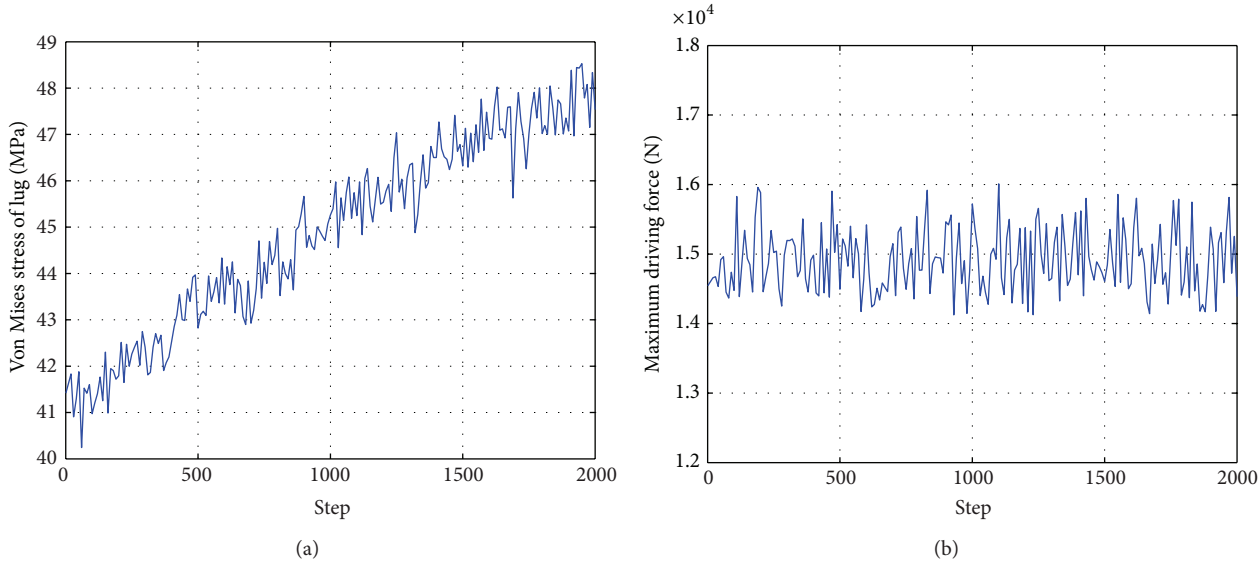

Figure 8: Time-dependent responses of stress of lug and maximum driving force. (a) Stress curve during the service life; (b) maximum driving force curve during the service life.

Table 2: Transformation functions of critical random parameters.

Symbol	Description	Transformation functions
X_A	Coordinate X of point A	$1176 + 2\xi_1$
Y_A	Coordinate Y of point A	$-497 + 2\xi_2$
L_{sr}	Length of actuator slider rod	$1600 + 3\xi_3$
G_d	Weight of the device	$2600 + 10\xi_4$

the time-varying system responses, respectively, and the responses at every 200 steps are selected to build the PCE, which means that the PCE are constructed at step 1, 200, 400, and so on till 2000. The coefficients of PCEs can be calculated by (20).

After the construction of PCEs, MLS is employed to approximate the time-varying functions of PCE coefficients. The discrete points in Figure 9 show that they have a nearly linear increase over time. In this case, as mentioned in Section 2.2, low-order spline weighting functions should be used to approximate the time-dependent functions of the PCE coefficients. In this case, the cubic spline function performed a better approximation. Thus the cubic spline function is chosen as the weighting function which is given as follows:

$$w(x) = \begin{cases} \frac{2}{3} - 4x^2 + 4x^3 & x \le \frac{1}{2}, \\ \frac{4}{3} - 4x + 4x^2 - \frac{4}{3}x^3 & \frac{1}{2} < x \le 1, \\ 0 & x > 1. \end{cases} \quad (29)$$

The order of PCMLS is determined by the PCE order. As 2-order PCE and 3-order PCE are performed to approximate the wear depth and stress of the lug at different time steps, MLS is used to obtain the time-dependent functions of the PCE coefficients, and the accuracy of PCMLS increases with the order. The comparative results are obtained at selected time steps which are 1, 500, 1000, 1500, and 2000 steps. The Monte Carlo simulation with 1000 samples is employed as a benchmark for the comparison. The statistics including the mean and the variance of the wear depth and stress of the lug are compared between the 2-order PCMLS and 3-order PCMLS, which are shown in Tables 3, 4, 5, and 6.

The accuracy of the PCMLS approximation is determined by two main factors: the PCE order and the number of MLS nodes. From Tables 3, 4, 5, and 6, the PCMLS approximation accuracy rises with the PCE order. However, high-order PCE requires more samples, in other word, more execution of the simulation of the multidiscipline reliability model, and it would increase the computation burden intensively. Meanwhile, the MLS approximation accuracy, which rises with the number of nodes (in this case the samples of PCE coefficients at different time steps), would also have an influence to the accuracy of PCMLS. More MLS nodes would obtain high-accuracy approximation [26] but would introduce more computation at the same time. In order to apply the PCMLS to the real engineering problem, a tradeoff between accuracy and efficiency should be considered and determined.

Figure 9 shows two examples of MLS approximation curves for the PCE coefficients. It can be seen that the curves fit these points well, and the root-mean-square errors of these two approximation curves are $4.116e-7$ and 0.3821, respectively. Approximation functions of the other 14 coefficients are also built by MLS. Then the PCMLS model is constructed completely, and the time consuming multidiscipline reliability model is replaced by the PCMLS model to conduct time-dependent uncertainty quantification using MCS.

The wear depth of the hinge would deteriorate the kinematics accuracy of the mechanism. According to

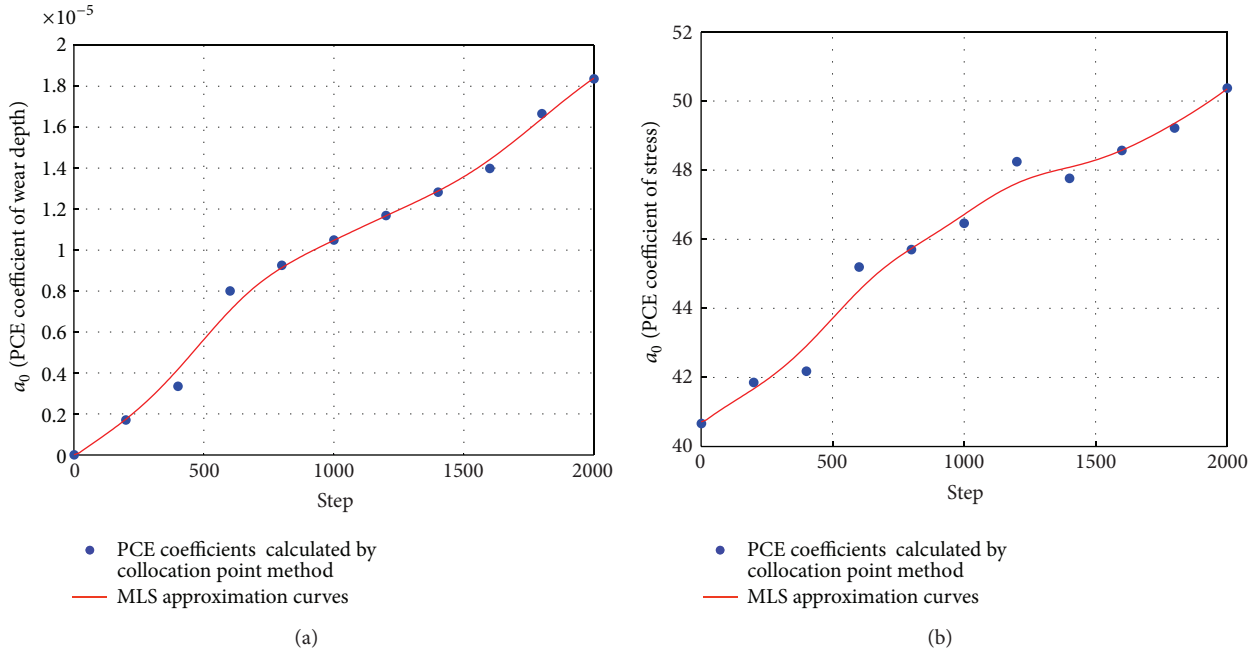

Figure 9: Examples of MLS approximation curves for PCE coefficients of the wear depth and the stress of lug. (a) MLS approximation curve for a_0 of the wear depth PCE; (b) MLS approximation curve for a_0 of the stress of lug PCE.

Table 3: Comparative results of mean of the wear depth of the lug along the time axis.

Method	Samples	Mean of the wear depth of the lug (μm)				
		1 step	500 step	1000 step	1500 step	2000 step
MCS	1000	0.9413	5.5165	10.6144	13.2563	18.4850
2-order PCMLS	15	0.9450	5.5036	10.6283	13.1739	18.3849
Relative error	—	0.0039	0.0023	0.0013	0.0062	0.0054
3-order PCMLS	35	0.9388	5.5178	10.6205	13.2022	18.4134
Relative error	—	0.0027	0.0002	0.0006	0.0041	0.0039

Table 4: Comparative results of the variance of the wear depth of the lug along the time axis.

Method	Samples	Variance of the wear depth of the lug				
		1 step	500 step	1000 step	1500 step	2000 step
MCS	1000	0.0042	0.0211	0.1501	0.1591	0.1843
2-order PCMLS	15	0.0052	0.0246	0.1349	0.1382	0.1625
Relative error	—	0.2381	0.1659	0.1013	0.1314	0.1183
3-order PCMLS	35	0.0045	0.0205	0.1409	0.1423	0.1677
Relative error	—	0.0714	0.0284	0.0613	0.1056	0.0901

Table 5: Comparative results of the mean of the Von Mises stress of the lug along the time axis.

Method	Samples	Mean of the Von Mises stress of the lug (MPa)				
		1 step	500 step	1000 step	1500 step	2000 step
MCS	1000	40.7708	43.4974	46.6781	48.1653	50.4784
2-order PCMLS	15	40.6015	43.6492	46.4639	48.2551	50.3862
Relative error	—	0.0042	0.0035	0.0046	0.0019	0.0018
3-order PCMLS	35	40.6575	43.5669	46.6246	48.1785	50.5254
Relative error	—	0.0028	0.0016	0.0011	0.0003	0.0009

Table 6: Comparative results of the variance of the Von Mises stress of the lug along the time axis.

Method	Samples	Variance of the Von Mises stress of the lug				
		1 step	500 step	1000 step	1500 step	2000 step
MCS	1000	0.4718	0.5598	0.5822	0.6020	0.6336
2-order PCMLS	15	0.3941	0.4821	0.4748	0.6624	0.6946
Relative error	—	0.1647	0.1388	0.1845	0.1003	0.0963
3-order PCMLS	35	0.4069	0.4889	0.6551	0.6593	0.6789
Relative error	—	0.1376	0.1267	0.1252	0.0952	0.0715

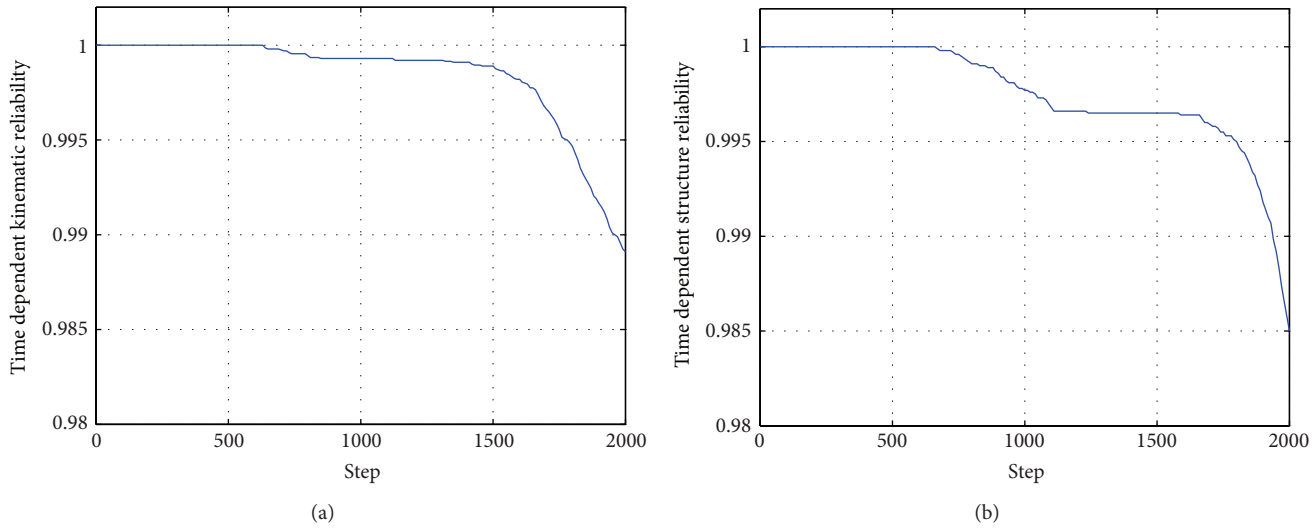

Figure 10: Time-dependent reliability computed through the PCMLS model. (a) Time-dependent kinematic reliability caused by the wear at the top hinge; (b) time-dependent structure reliability caused by the increase of stress of lug.

the requirements of the kinematics accuracy, the failure criterion of wear depth is determined as 50 μm, and the safety strength of lug is 80 MPa. MCS is applied to the PCMLS model to calculate the time-dependent kinematic reliability and structure reliability with 10000 simulations. Note that the first passage time is a critical concept in the time-dependent reliability analysis, and we use the discretization of random processes and Monte Carlo simulation method to compute the time-dependent structure reliability. When the time-dependent limit state function first falls into the failure domain, this sample would be regarded as a failure and would be eliminated from the survival ones. The results are presented in Figure 10. The kinematic reliability after the 2000th task is 0.9890, and the structure reliability is 0.9850, which all satisfy the reliability constrains of the retractable mechanism.

5.3. Time-Dependent RBDO. The time-dependent RBDO is formulated for the retractable mechanism. The design optimization problem is defined as to minimize the mean and the variance of the total weight subject to two time-dependent reliability constrains and three time-independent reliability constrains. The failures of retractable mechanism are defined as follows:

(1) the practical wear depth of lug exceeds the allowable wear depth determined by the kinematics accuracy;

(2) the stress in the lug is greater than the strength of the lug;

(3) the stress in the upper rod is greater than the strength of the upper rod;

(4) the stress in the device arm is greater than the strength of the device arm;

(5) the mechanism gets locked when the practical maximum driving force exceeds the rated output of the hydraulic actuator.

The previous two failure criteria are related to the time-dependent reliability. The design problem is formulated as

$$\begin{aligned} &\min \ F\left(\mu_{\text{weight}}\left(\mathbf{x},\mathbf{d},\mathbf{q}\right), \sigma_{\text{weight}}\left(\mathbf{x},\mathbf{d},\mathbf{q}\right)\right) \\ &\text{s.t. } P\left\{g\left(\mathbf{T}, r_{wd}\left(\boldsymbol{\xi},\mathbf{T}\right), c_{f_{wd}}\right) \le 0\right\} \ge R_{wd}, \\ &P\left\{g\left(\mathbf{T}, r_{sl}\left(\boldsymbol{\xi},\mathbf{T}\right), c_{f_{sl}}\right) \le 0\right\} \ge R_{sl}, \\ &P\left(g_i\left(\mathbf{x},\mathbf{d},\mathbf{q}\right) \le 0\right) \ge R_i, \quad i = 1, 2, 3, \\ &\mathbf{x}^L \le \mathbf{x} \le \mathbf{x}^U, \end{aligned} \tag{30}$$

where $g(\mathbf{T}, r_{wd}(\boldsymbol{\xi}, \mathbf{T}), c_{f_{wd}})$ is the time-dependent limit state function of the wear depth and $g(\mathbf{T}, r_{sl}(\boldsymbol{\xi}, \mathbf{T}), c_{f_{sl}})$ is the time-dependent limit state function of the stress of lug.

Table 7: Comparison of optimal design results between time-independent RBDO and proposed time-dependent RBDO.

Type	X_A	Y_A	R_{ur} (mm)	R_{arm} (mm)	Mean of total weight (kg)	Variance of total weight
Time-independent RBDO	1235.01	−421.40	22.45	45.24	15.3631	0.2383
Time-dependent RBDO	1239.28	−415.93	22.85	47.19	15.9832	0.3369

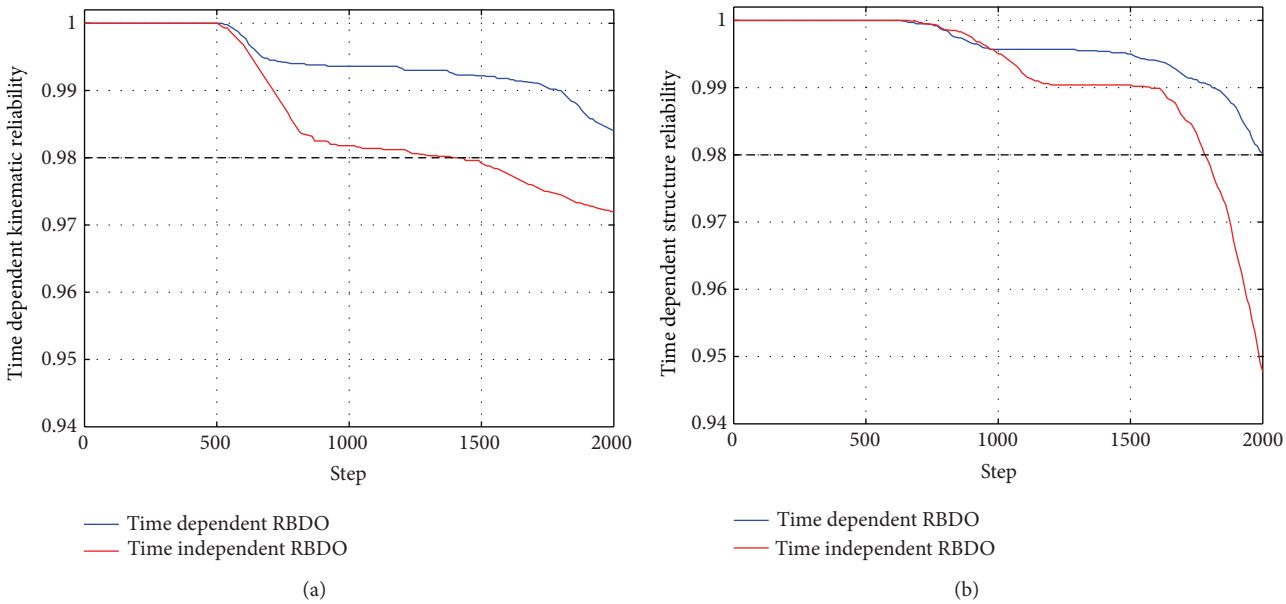

Figure 11: Comparison of time-dependent reliability curves by time-dependent RBDO and time-independent RBDO. (a) Curves of kinematic reliability; (b) curves of structure reliability.

Also $g_i(\mathbf{x}, \mathbf{d}, \mathbf{q})$ is the time-independent limit state function of time-insensitive responses which include the maximum driving force of the mechanism, stress in the upper rod, and stress in the device arm.

The RBDO in the case study is a multiobjective optimization problem which has mean and variance of the total weight as two objectives. The design objective is generally formulated as follows:

$$F = \sum_{i=1}^{l} \left[(\pm) \frac{w_{1i}}{s_{1i}} \mu_i + \frac{w_{2i}}{s_{2i}} \sigma_i \right], \tag{31}$$

where w_{1i} and w_{2i} are the weights and s_{1i} and s_{2i} are the scale factors for the mean and variance of the ith performance response, respectively. l is the total number of the performance responses. The "+" sign is used when the response mean is to be minimized, and the "−" sign is be used when the response mean is to be maximized. This formulation belongs to the weighted sum method which is the most common approach to multiobjective optimization. The weights and scale factors should be positive to make the minimum of the objective to be Pareto optimal. In this case, we decide the scale factors to be the ideal points, which are shown as follows:

$$\begin{aligned} s_1 &= \mu_{\text{weight}}^{\circ} = 12, \\ s_2 &= \sigma_{\text{weight}}^{\circ} = 0.1. \end{aligned} \tag{32}$$

The weights of these two objectives are chosen as one, which means the mean and variance of the weight are equally important.

Genetic algorithm (GA) is adopted in this paper because it is able to converge to the global solution rather than to a local solution. Since the two objectives are combined to form a single objective, a conventional single-objective GA is performed in the proposed RBDO. We have written the GA in MATLAB according to the literature [29] without modification.

The optimal design results are shown in Table 7, which involves the time-independent RBDO and the proposed time-dependent RBDO, and it is indicated that the optimal design results of these two methods are different. Because the proposed time-dependent RBDO considered the wear loss in the top hinge, its design result reallocated loads on three hinges of the mechanism, and this made the other two hinges partly share the load which was originally applied to the top hinge. Thus the wear in the top hinge was reduced to make the design of the mechanism satisfy the time-dependent reliability constrains. However, because of the increase of loads on the other two hinges, the upper rod and the device arm are required to bear more loads. Therefore, the outer radiuses of the upper rod and the device arm are greater than the design result of the time-independent RBDO. Thus the retractable mechanism in the design of the proposed time-dependent RBDO is a little heavier than the design of the time-independent RBDO.

The time-dependent reliability curves by two methods are given in Figure 11.

Figure 11 shows that the optimal design given by the proposed time-dependent RBDO is able to satisfy the time-dependent reliability constrains during the service life of 2000 tasks, but the design of time-independent RBDO would just be the optimal solution at the initial time. After the 1400th and 1800th tasks, the kinematic reliability and structural reliability fall below 0.98, respectively. The comparison indicates the necessity to account for the wear in hinges as well as time-dependent kinematic and structural reliability in design phase. The proposed time-dependent RBDO method is able to obtain the optimal design under the time-dependent reliability constrains. Thus it is applicable to engineering problem.

6. Conclusion

Existence of wear in mechanisms would deteriorate the time-dependent kinematic reliability and structural reliability through the changing kinematics. Thus wear-related time-dependent reliability should be taken into account in design phase. This work develops a time-dependent RBDO method considering wear as a critical failure. It involves both of the time-dependent kinematic reliability and time-dependent structural reliability as constrains.

The PCMLS model that combines the NIPC with the MLS is presented to conduct the time- dependent uncertainty quantification. The NIPC is expanded to propagate time-dependent uncertainty with time-dependent coefficients achieved by MLS approximation functions.

The multidiscipline reliability model, which includes kinematics model and structural FE model, is constructed according to Archard's wear law to generate the stochastic processes of system responses. As these disciplines are closely coupled and uncertainty impacts are cross-propagated, the correlationship between the wear process and loads is considered in the model. The PCMLS model is applied to approximate the stochastic processes generated by the multidiscipline reliability model. Then MCS is conducted on the PCMLS model to evaluate the time-dependent kinematic reliability and structural reliability.

The procedure of the three-stage time-dependent RBDO is given, and the new method is demonstrated at an airborne retractable mechanism. The optimization goal is to minimize the mean and the variance of the total weight. Constraints include both of the time-dependent and time-independent reliabilities. The optimal design is compared to the time-independent RBDO result. The comparison indicates that it is necessary to account for wear and time-dependent reliability in design phase, and the proposed time-dependent RBDO method is applicable to engineering problem.

References

[1] T. W. Simpson and J. R. R. A. Martins, "Multidisciplinary design optimization for complex engineered systems: report from a national science foundation workshop," *Journal of Mechanical Design*, vol. 133, no. 10, Article ID 101002, 10 pages, 2011.

[2] W. Yao, X. Q. Chen, W. C. Luo, M. Van Tooren, and J. Guo, "Review of uncertainty-based multidisciplinary design optimization methods for aerospace vehicles," *Progress in Aerospace Sciences*, vol. 47, no. 6, pp. 450–479, 2011.

[3] A. Rezaei, W. V. Paepegem, P. D. Baets, W. Ost, and J. Degrieck, "Adaptive finite element simulation of wear evolution in radial sliding bearings," *Wear*, vol. 296, pp. 660–671, 2012.

[4] N. Kuschel and R. Rackwitz, "Optimal design under time-variant reliability constraints," *Structural Safety*, vol. 22, no. 2, pp. 113–127, 2000.

[5] N. Kuschel and R. Rackwitz, "Time-variant reliability-based structural optimization using SORM," *Optimization*, vol. 47, no. 3-4, pp. 349–368, 2000.

[6] H. Streicher and R. Rackwitz, "Time-variant reliability-oriented structural optimization and a renewal model for life-cycle costing," *Probabilistic Engineering Mechanics*, vol. 19, no. 1, pp. 171–183, 2004.

[7] C. Andrieu-Renaud, B. Sudret, and M. Lemaire, "The PHI2 method: a way to compute time-variant reliability," *Reliability Engineering and System Safety*, vol. 84, no. 1, pp. 75–86, 2004.

[8] J. Li, J.-B. Chen, and W.-L. Fan, "The equivalent extreme-value event and evaluation of the structural system reliability," *Structural Safety*, vol. 29, no. 2, pp. 112–131, 2007.

[9] J.-B. Chen and J. Li, "The extreme value distribution and dynamic reliability analysis of nonlinear structures with uncertain parameters," *Structural Safety*, vol. 29, no. 2, pp. 77–93, 2007.

[10] P. Bhatti, *Probabilistic modeling and optimal design of robotic manipulators [Ph.D. thesis]*, Purdue University, West Lafayette, Ind, USA, 1989.

[11] J. F. Zhang and X. P. Du, "Time-dependent reliability analysis for function generator mechanisms," *Journal of Mechanical Design, Transactions of the ASME*, vol. 133, no. 3, Article ID 031005, 9 pages, 2011.

[12] J. F. Zhang, J. G. Wang, and X. P. Du, "Time-dependent probabilistic synthesis for function generator mechanisms," *Mechanism and Machine Theory*, vol. 46, no. 9, pp. 1236–1250, 2011.

[13] D. B. Xiu and G. E. Karniadakis, "The Wiener-Askey polynomial chaos for stochastic differential equations," *SIAM Journal on Scientific Computing*, vol. 24, no. 2, pp. 619–644, 2002.

[14] S. Hosder, R. W. Walters, and M. Balch, "Efficient sampling for non-intrusive polynomial chaos applications with multiple uncertain input variables," in *Proceedings of the 48th AIAA/ASME/ASCE/AHS/ASC Structures, Structural Dynamics, and Materials Conference*, pp. 2946–2961, Honolulu, Hawaii, USA, April 2007.

[15] B. Sudret, "Global sensitivity analysis using polynomial chaos expansions," *Reliability Engineering and System Safety*, vol. 93, no. 7, pp. 964–979, 2008.

[16] H. Y. Cheng and A. Sandu, "Efficient uncertainty quantification with the polynomial chaos method for stiff systems," *Mathematics and Computers in Simulation*, vol. 79, no. 11, pp. 3278–3295, 2009.

[17] J. A. S. Witteveen, A. Loeven, S. Sarkar, and H. Bijl, "Probabilistic collocation for period-1 limit cycle oscillations," *Journal of Sound and Vibration*, vol. 311, no. 1-2, pp. 421–439, 2008.

[18] N. Wiener, "The homogeneous chaos," *American Journal of Mathematics*, vol. 60, no. 4, pp. 897–936, 1938.

[19] R. H. Cameron and W. T. Martin, "The orthogonal development of non-linear functionals in series of Fourier-Hermite functionals," *The Annals of Mathematics*, vol. 48, pp. 385–392, 1947.

[20] R. G. Ghanem and P. D. Spanos, *Stochastic Finite Elements: A Spectral Approach*, Dover, 1991.

[21] S. S. Isukapalli, *Uncertainty analysis of transport-transformation models [Ph.D. thesis]*, The State University of New Jersey, Camden, NJ, USA, 1999.

[22] D. Levin, "The approximation power of moving least-squares," *Mathematics of Computation*, vol. 67, no. 224, pp. 1517–1531, 1998.

[23] P. Breitkopf, H. Naceur, A. Rassineux, and P. Villon, "Moving least squares response surface approximation: formulation and metal forming applications," *Computers and Structures*, vol. 83, no. 17-18, pp. 1411–1428, 2005.

[24] R. Kolluri, "Provably good moving least squares," *ACM Transactions on Algorithms*, vol. 4, no. 2, article 18, 2008.

[25] C. Y. Song and J. Lee, "Reliability-based design optimization of knuckle component using conservative method of moving least squares meta-models," *Probabilistic Engineering Mechanics*, vol. 26, no. 2, pp. 364–379, 2011.

[26] T. Belytschko, Y. Krongauz, M. Fleming, D. Organ, and W. K. S. Liu, "Smoothing and accelerated computations in the element free Galerkin method," *Journal of Computational and Applied Mathematics*, vol. 74, no. 1-2, pp. 111–126, 1996.

[27] A. Söderberg and S. Andersson, "Simulation of wear and contact pressure distribution at the pad-to-rotor interface in a disc brake using general purpose finite element analysis software," *Wear*, vol. 267, no. 12, pp. 2243–2251, 2009.

[28] S. C. Lim and M. F. Ashby, "Overview no. 55 Wear-Mechanism maps," *Acta Metallurgica*, vol. 35, no. 1, pp. 1–24, 1987.

[29] M. Gen and R. Cheng, *Genetic Algorithms and Engineering Optimization*, John Wiley & Sons, New York, NY, USA, 2000.

Hindawi Publishing Corporation
Journal of Applied Mathematics
Volume 2013, Article ID 759102, 7 pages
http://dx.doi.org/10.1155/2013/759102

Research Article

A Probabilistic Damage Identification Approach for Structures under Unknown Excitation and with Measurement Uncertainties

Ying Lei,[1] Ying Su,[1] and Wenai Shen[2]

[1] *Department of Civil Engineering, Xiamen University, Xiamen 361005, China*
[2] *Department of Civil and Environmental Engineering, The Hong Kong Polytechnic University, Hung Hom, Kowloon, Hong Kong*

Correspondence should be addressed to Ying Lei; ylei@xmu.edu.cn

Received 26 December 2012; Revised 4 May 2013; Accepted 26 May 2013

Academic Editor: Xiaojun Wang

Copyright © 2013 Ying Lei et al. This is an open access article distributed under the Creative Commons Attribution License, which permits unrestricted use, distribution, and reproduction in any medium, provided the original work is properly cited.

Recently, an innovative algorithm has been proposed by the authors for the identification of structural damage under unknown external excitations. However, identification accuracy of this proposed deterministic algorithm decreases under high level of measurement noise. A probabilistic approach is therefore proposed in this paper for damage identification considering measurement noise uncertainties. Based on the former deterministic algorithm, the statistical values of the identified structural parameters are estimated using the statistical theory and a damage index is defined. The probability of identified structural damage is further derived based on the reliability theory. The unknown external excitations to the structure are also identified by statistical evaluation. A numerical example of the identification of structural damage of a multistory shear-type building and its unknown excitation shows that the proposed probabilistic approach can accurately identify structural damage and the unknown excitations using only partial measurements of structural acceleration responses contaminated by intensive measurement noises.

1. Introduction

Structural damage detection is an important task for structural health monitoring [1–5]. Usually, it is straightforward to identify structural damage based on tracking the changes of the identified values of structural physical parameters, for example, the degrading of element stiffness parameters. In practice, it is often impossible to deploy so many sensors that accurately measure all excitation inputs and response outputs of systems. It is highly desirable to deploy as few sensors as possible, so it is essential to explore efficient algorithms which can identify structural damage utilizing only a limited number of measured responses of structures subject to some unknown (unmeasured) excitations.

In the past decades, some researchers have proposed algorithms for simultaneous identification of structural parameters and unknown excitation, for example, the iterative least-square estimation approach [6, 7], the statistical average algorithm [8], the recursive least-square estimation [9], genetic algorithms [10], hybrid identification method [11], the dynamic response sensitivity method [11], the extended Kalman filter with unknown excitation inputs (EKF-UI) [12], the sequential nonlinear least-square estimation (SNLSE) [13], and structural parameters and dynamic loading identification from incomplete measurements [14]. However, these approaches suffered the deficiencies of either all structural response being assumed available or the analytical and numerical identification procedures being rather complex.

Recently, an innovative algorithm has been proposed by the authors for the identification of structural damage under unknown excitations using limited measurements of structural acceleration responses [15, 16]. The proposed algorithm is based on the sequential utilization of the extended Kalman estimator [17] for the recursive estimation of the extended state vector of a structure and the least-square estimation of its unknown excitation; that is, recursive solution for extended state vector is initially estimated followed by the subsequent estimation of the unknown excitation via least-square estimation. Thus, proposed algorithm simplifies the identification problem compared with previous simultaneous identification approaches [18, 19]. Structural damage is detected from the changes of structural parameters at the element level, such as the degradation of identified element stiffness parameters. Such a straightforward derivation and

analytical solution are not available in the previous literature. However, former numerical examples indicated that the identification accuracy of this proposed deterministic algorithm decreased with the increase of the measurement noise level [15, 16]. Therefore, it is necessary to develop an approach which can avoid the false identification of damages in the deterministic identification algorithm induced by the relatively high level of measurement noise.

Since the inevitable measurement noises are intrinsically uncertain, the identification of structural parameter and external excitation using measurements with intensive measurement noises is essentially an uncertain problem [20, 21]. The identification performed by deterministic methods often leads to incorrect identification results of structural damages and a disagreement between the identified unknown excitation and its true value while consideration of uncertainties has received more and more attention in recent years [22–26]. In this paper, a probabilistic approach is proposed for the identification of structural damage under unknown external excitations and with measurement noise uncertainties. Based on the deterministic algorithm, the statistical values of the identified structural parameters are estimated, and the probability of identified structural damage is further derived using the statistical theory and probability method. The rest of the paper is organized as follows. Section 2 briefly introduces the former deterministic algorithm for the identification of structural damage under unknown external excitations, Section 3 presents the proposed probabilistic identification approach based on the improvement of the deterministic algorithm using the statistical and probability theory, Section 4 shows a numerical example of the identification of structural damage of a multistory shear-type frame building and its unknown excitation to demonstrate the proposed probabilistic approach, and Section 5 gives the conclusions of the paper.

2. Brief Introduction of the Deterministic Algorithm for Identification of Structural Damage under Unknown Excitations

The equations of motion of a linear structural system subject to unknown external excitation can be written as

$$\mathbf{M}\ddot{\mathbf{x}}(t) + \mathbf{C}\dot{\mathbf{x}}(t) + \mathbf{K}\mathbf{x}(t) = \mathbf{B}^u\mathbf{f}^u(t), \tag{1}$$

in which $\mathbf{x}(t)$, $\dot{\mathbf{x}}(t)$, and $\ddot{\mathbf{x}}(t)$ are the vectors of displacement, velocity, and acceleration response, respectively; $\mathbf{M}$, $\mathbf{C}$, and $\mathbf{K}$ are the mass, damping, and stiffness matrices, respectively; $\mathbf{f}^u(t)$ is an unmeasured external excitation vector; and $\mathbf{B}^u$ is the influence matrix associated with $\mathbf{f}^u(t)$. Usually, the mass of a structural system can be estimated with accuracy based on its geometry and material information.

2.1. Estimation of the Extended State Vector. The extended state vector of the system is defined as

$$\mathbf{X} = \left[\mathbf{X}_1^T, \mathbf{X}_2^T, \boldsymbol{\theta}^T\right]^T; \qquad \mathbf{X}_1 = \mathbf{x};$$
$$\mathbf{X}_2 = \dot{\mathbf{x}}; \qquad \boldsymbol{\theta}^T = \left[\theta_1, \theta_2, \ldots, \theta_n\right]^T, \tag{2}$$

where $\boldsymbol{\theta}^T$ is a vector of the n-unknown structural parameters, such as damping and stiffness parameters. As the structural parameters are constant, (1) can be written in the following general nonlinear differential state equations [15, 16]:

$$\dot{\mathbf{X}} = \mathbf{g}\left(\mathbf{X}, \mathbf{f}^u\right). \tag{3}$$

Usually, only a limited number of accelerometers are deployed in structures to measure acceleration responses. Therefore, the discretized observation equation can be expressed as

$$\mathbf{y}[k] = \mathbf{h}\left(\mathbf{X}[k]\right) + \mathbf{G}^u\mathbf{f}^u[k] + \mathbf{v}[k], \tag{4}$$

where $\mathbf{G}^u = \mathbf{D}\mathbf{M}^{-1}\mathbf{B}^u$; $\mathbf{h}(\mathbf{X}[k]) = \mathbf{D}\mathbf{M}^{-1}\{-(\mathbf{C}_{\boldsymbol{\theta}})\mathbf{X}_2[k] - (\mathbf{K})_{\boldsymbol{\theta}}\mathbf{X}_1[k]\}$ in which $\mathbf{y}[k]$ is observation vector (measured acceleration responses) at time $t = k \times \Delta t$ with Δt being the sampling time step, $(\mathbf{C})_{\boldsymbol{\theta}}$ represents elements in the damping matrix $\mathbf{C}$ composed by the unknown parameters of damping in the parametric vector $\boldsymbol{\theta}$, $(\mathbf{K})_{\boldsymbol{\theta}}$ represents the constitution of stiffness matrix $\mathbf{K}$ analogously, $\mathbf{f}^u[k]$, $\mathbf{X}_1[k]$ and $\mathbf{X}_2[k]$ are the corresponding discretized values at time $t = k \times \Delta t$, $\mathbf{D}$ is the matrix associated with the locations of accelerometers, and $\mathbf{v}[k]$ is the measured noise vector assumed to be a Gaussian white noise vector with zero mean and a covariance matrix $\mathbf{E}[\mathbf{v}_i\mathbf{v}_j^T] = \mathbf{R}_{ij}\delta_{ij}$, where δ_{ij} is the Kronecker delta.

Based on the extended Kalman estimator [15, 16], the extended state vector at time $t = (k+1) \times \Delta t$ can be estimated with the observation of $(\mathbf{y}[1], \mathbf{y}[2], \ldots, \mathbf{y}[k])$ as follows:

$$\widehat{\mathbf{X}}[k+1 \mid k] = \widetilde{\mathbf{X}}[k+1 \mid k] + \mathbf{K}[k] \times \left\{\mathbf{y}[k] - h\left(\widehat{\mathbf{X}}[k \mid k-1], \mathbf{f}[k]\right) - \mathbf{G}^u\widehat{\mathbf{f}}^u[k \mid k]\right\}, \tag{5}$$

in which

$$\widetilde{\mathbf{X}}[k+1 \mid k] = \widehat{\mathbf{X}}[k \mid k-1] + \int_{t[k]}^{t[k+1]} \mathbf{g}\left(\mathbf{X}, \mathbf{f}^u\right) dt, \tag{6}$$

where $\widehat{\mathbf{X}}[k+1 \mid k]$ and $\widehat{\mathbf{f}}^u[k \mid k]$ are the estimation of $\mathbf{X}[k+1]$ and $\mathbf{f}^u[k]$ given $(\mathbf{y}[1], \mathbf{y}[2], \ldots, \mathbf{y}[k])$, respectively, and $\mathbf{K}[k]$ is the Kalman gain matrix [15, 16].

However, since the external excitation $\mathbf{f}^u(t)$ is unknown, it is impossible to obtain the recursive solution for the extended state vector by the classical extended Kalman estimator alone.

2.2. Identification of the Unknown Excitations. Under the conditions: (i) the number of output measurements is greater than that of the unknown excitations and (ii) measurements (sensors) are available at all DOFs where the unknown excitation $\mathbf{f}^u(t)$ acts; that is, matrix $\mathbf{G}^u$ in (4) is nonzero; the unknown excitations at time $t = (k+1) \times \Delta t$ can be estimated from (4) by the least-square estimation as [15, 16]

$$\widehat{\mathbf{f}}^u[k+1 \mid k+1] = \left[\left(\mathbf{G}^u\right)^T\mathbf{G}^u\right]^{-1}\left(\mathbf{G}^u\right)^T \times \left\{\mathbf{y}[k+1] - \mathbf{h}\left(\widehat{\mathbf{X}}[k+1 \mid k]\right)\right\}, \tag{7}$$

in which $\widehat{\mathbf{f}}^u[k+1 \mid k+1]$ is the estimation of $\mathbf{f}^u[k+1]$ given the observation of $(\mathbf{y}[1], \mathbf{y}[2], \ldots, \mathbf{y}[k+1])$.

Therefore, the proposed algorithm can identify structural parameters and unknown excitation in a sequential manner, which simplifies the identification problem compared with other simultaneous identification work. Structural damage is detected from the changes of structural parameters at the element level, such as the degradation of identified element stiffness parameters. Such a straightforward derivation and analytical solution are not available in the previous literature [15, 16].

However, former numerical examples indicated that the identification accuracy of this proposed deterministic algorithm decreases under high level of measurements noise [15, 16]. The identification performed by using the deterministic algorithm leads to incorrect identification results of structural damages and a disagreement between the identified excitation and its true value. Consequently, it is necessary to develop an approach for identifying the structural damage and unknown excitation when the measurements are contaminated by intensive measurement noises.

3. A Probabilistic Approach for the Identification of Structural Damage with Intensive Measurement Noises

Since the inevitable measurement noises are intrinsically uncertain, identification of structural parameter and unknown excitation using measurements with intensive measurement noises is essentially an uncertain problem. A probabilistic approach is proposed herein based on the deterministic algorithm described in Section 2.

3.1. The Statistical Results of Identification Values. In the observed equation, (4), the measured noise vector is assumed to be a Gaussian white noise vector; that is, uncertainties in the measured responses are assumed as normally distributed random variables. Then the measured acceleration response vector $\mathbf{y}$ is an observation vector with uncertainties. In practice, many sets of measured accelerations can be obtained by repetitious experiments or long-term measurement of structures. In the numerical simulation, many sets of measured accelerations can be obtained by the theoretically computed responses superimposed with many sets of measurement noise with uncertainties. Then, each set of the measured accelerations is used as an observation vector to identify the structural parameters and unknown excitation by using the deterministic identification algorithm in Section 2. Therefore, many sets of identified results can be obtained. The statistical parameters of the identified parameters can then be estimated by the statistical theory for example, the mean and standard deviations of identified structural element stiffness can be calculated, respectively, by

$$\mu_i = \frac{1}{n}\sum_{j=1}^{n} k_{ij}; \qquad \sigma_i = \sqrt{\frac{1}{n-1}\sum_{j=1}^{n}\left(k_{ij} - m_i\right)^2}, \tag{8}$$

in which μ_{i} and σ_{i} are the mean and standard deviations of the n-sets of identified stiffness of the ith structural element k_i, respectively.

Then, a damage index D_i for the ith structural element is defined as

$$D_i = \frac{\left(\mu_i^d - \mu_i^u\right)}{\mu_i^u}, \tag{9}$$

in which μ_i^d and μ_i^u are the mean values of the identified ith structural element stiffness in the damaged and undamaged structure, respectively. Thus, the damage index D_i tracks the degrading of the identified ith structural element stiffness and can also reflect its damage severity.

Analogously, the effect of uncertainties on the identified unknown excitation can be decreased by using the statistical average of multisets of identified input time histories, that is,

$$\bar{\mathbf{f}}^u = \frac{1}{n}\sum_{j=1}^{n} \mathbf{f}_j^u, \tag{10}$$

where $\bar{\mathbf{f}}^u$ is the mean value of the n-sets that identified unknown excitation time histories and $\mathbf{f}_j^u$ is the jth set of identified unknown excitation.

3.2. The Identification Probability of Structural Damage. Structural damage is assumed as the degrading of the identified ith structural element stiffness; a random variable of the relative change of the identified ith structural element stiffness in the damaged and undamaged structures is introduced as

$$r_i = \frac{\left(k_i^d - k_i^u\right)}{m_i^u}, \tag{11}$$

where k_i^d and k_i^u are the identified values of the ith structural element in the damaged and undamaged structures, respectively.

Then, the probability of structural damages in this study is estimated based on the reliability theory; that is, the probability of structural damages of the ith structural element P_{D_i} is identified as

$$P_{D_i} = \int_{r_i \le 0} p\left(r_i\right) dr_i, \tag{12}$$

where $p(r_{\mathrm{i}})$ is the probability density function of the random variable r_{i} in (11).

The random variable r_{i} can be assumed as a normal random variable. Then, damage probability P_{D_i} can be estimated based on the definition of the standard normal distribution as

$$P_{D_i} = 1 - \Phi\left(\frac{\mu_{r_i}}{\sigma_{r_i}}\right), \tag{13}$$

where $\Phi(\bullet)$ denotes the probability of a standard normal distribution.

Based on the probability P_{D_i} defined in (13), the P_{D_i} value presents the probability of whether the ith structural element is damaged, and it is in the range of 50%–100%. A value of 50% indicates that the structural element has no damage, whereas a value of larger than 50% means the occurrence of damage. The closer to 100% of the P_{D_i} value, the larger the damage probability.

4. A Numerical Simulation Example

In this paper, a numerical simulation example of the identification of structural damage of a 10-story shear building model and its unknown excitation at the top floor is used to demonstrate the efficiency of the proposed probabilistic approach. The following structural parametric values are used in the numerical study of the 10-story shear building: each story stiffness $k_1 = k_2 = \cdots = k_{10} = 6.79 \times 10^3$ kN/m, the concentrated mass at each floor level is $m_1 = 3.45 \times 10^3$ kg, $m_2 = m_3 = 2.65 \times 10^3$ kg, $m_4 = m_5 = \cdots = m_{10} = 1.81 \times 10^3$ kg. Rayleigh damping assumption is employed in this study and the two Rayleigh damping coefficients are $\alpha = 2.88$ and $\beta = 5.65$.

The building is excited by a random Gaussian white noise at the top floor; however, this excitation is assumed unknown in the identification process. Partial structural acceleration responses at the 1st, 2nd, 3rd, 5th, 7th, 9th, and 10th floor levels are used as the observation vector.

The uncertainties of measurement noises on the results of system identification are considered by superimposition of noise process with the theoretically computed response quantities, that is,

$$\mathbf{y}_j = \mathbf{y}_{j0} + \eta_j \nu_j \sigma\left(\mathbf{y}_{j0}\right), \tag{14}$$

where $\mathbf{y}_j$ and $\mathbf{y}_{j0}$ are the jth set of measured acceleration vector and calculated acceleration vector, respectively, ν_j is the jth random vector with standard normal random distribution, $\sigma(\mathbf{y}_{j0})$ is the standard deviation of the calculated accelerations $\mathbf{y}_{j0}$, and η_j is the level of noise in measurements, which is an important parameter representing the level of uncertainties in the measured accelerations.

Structural damages of the building are assumed as follow: the 3rd story stiffness k_3 is reduced by 5%, the 5th story stiffness k_5 is reduced by 20%, and the 8th story stiffness k_8 is reduced by 10%.

Each set of the measured acceleration responses with uncertainties of measurement noise is used to identify structural physical parameters, structural damage, and the unknown excitation to the building using the deterministic identification algorithm in Section 2. In the probabilistic approach as shown in Section 3, the measured accelerations contaminated by noises are taken as the uncertain variables as shown by (14). The Mote Carlo method is performed with sample size equal to 100. Two measurement noise levels, 5% and 20%, are simulated to examine the effectiveness of proposed algorithms.

Figures 1(a)-1(b) show the comparisons of the identification results by the deterministic identification algorithm and the probabilistic approach when the measurement noise levels are equal to 5% and 20%, respectively. It is seen from Figure 1(a) that the identification values of the relative stiffness change by the deterministic and the probabilistic approach are very close to the true values, indicating that both approaches can identify structural element damage when the measurement noise level is low. However, Figure 1(b) shows that when measurement noise level is quite high, which is equal to 20%, the identification error by the deterministic algorithm increases and the false positives of damages occur in several undamaged floor stiffness, especially the false damage identification of about 7% reduction of k_1. On the other hand, the damage index D_i in the probabilistic approach can still accurately indicate the location and severity of structural damage as shown in Figure 1(b) and Table 1. This demonstrates that the proposed probabilistic approach can avoid the false identification of damages by the deterministic algorithm.

Figures 2(a)–2(c) compare the identification results of unknown excitation by the deterministic algorithm and the probabilistic approach. Form these comparisons, it is shown that the identification accuracy on the unknown excitation by the deterministic algorithm decreases with the increase of the measurement noise level. There is an obvious deviation between the identified and the true excitations. However, Figure 2(c) demonstrates that the effect of uncertainties of measurement noise on the identified unknown excitation can be diminished by using the statistical average of multisets of identified unknown excitation time histories.

The identification results of structural damage probabilities defined in Section 3.2 for all the elements are summarized in Table 1. It is shown that the damage probabilities of elements 3, 5, and 8 are close to 100%, which are much larger than 50%. The damage probabilities of all the undamaged elements are very close to 50%. This indicates that the proposed identification probability of structural damage can accurately indicate all the structural damages locations.

5. Conclusions

In this paper, a probabilistic approach is proposed for the identification of structural damage and unknown external excitations using only limited measurements of structural acceleration responses contaminated by intensive measurement noises. The probabilistic approach is an improvement of the deterministic identification algorithm recently proposed by the authors. Structural parameters and unknown excitation are identified in a sequential manner, which simplifies the identification problem compared with other simultaneous identification algorithms. The statistical parameters of the identified structural parameters are estimated using the statistical theory, and a damage index is defined to indicate the location and severity of structural damage. The probability of identified structural damage is further derived based on the reliability theory. The unknown external excitation on the structure can also be derived by statistical average of multisets of identified unknown excitation time-histories. Therefore, the novelty of the research is that it proposes a probabilistic approach which can accurately identify

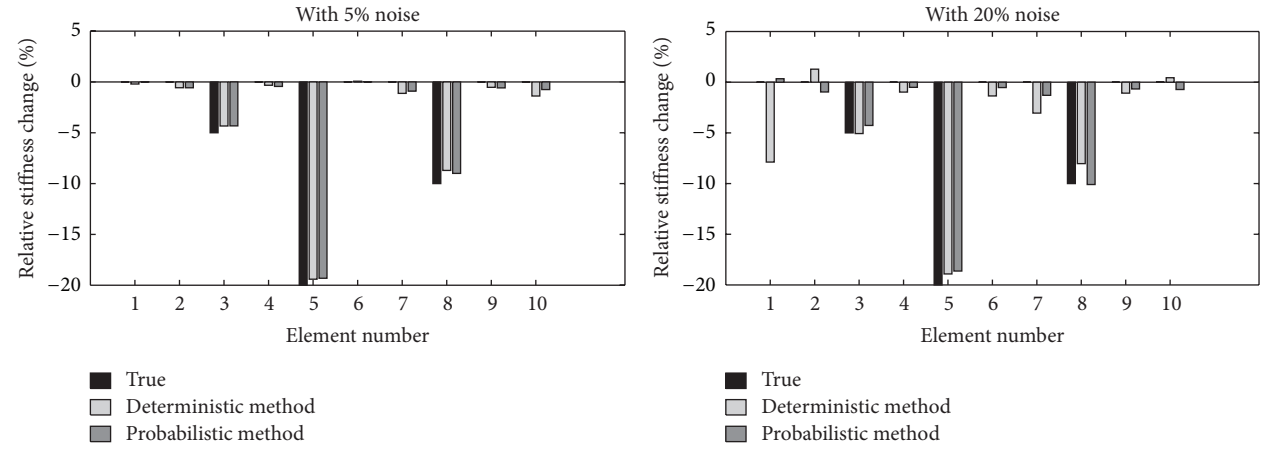

(a) Comparisons of identified stiffness with 5% measurement noise

(b) Comparisons of identified stiffness with 20% measurement noise

Figure 1: Comparisons of identification stiffness with different measurement noise levels.

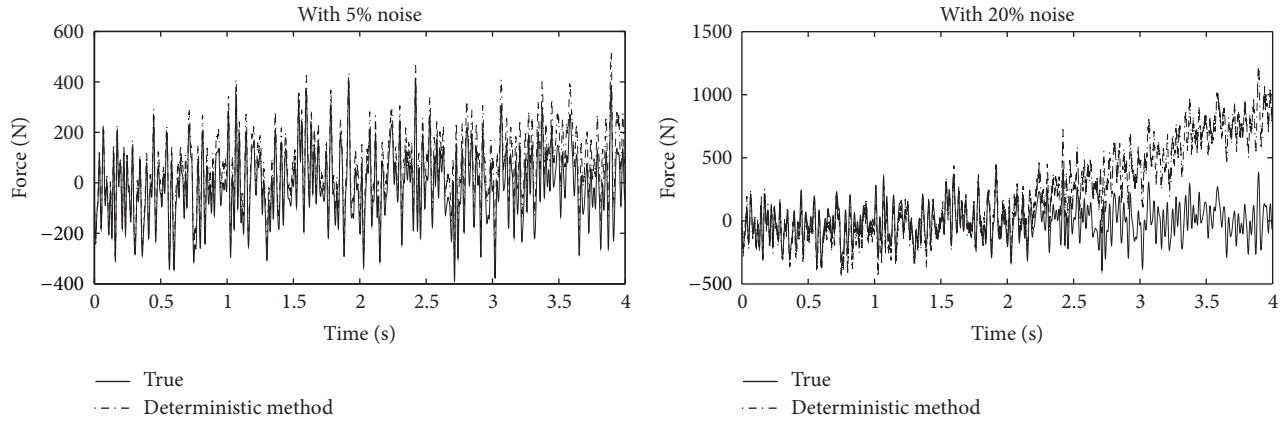

(a) Identified unknown excitation by the deterministic algorithm with 5% noise

(b) Identified unknown excitation by the deterministic algorithm with 20% noise

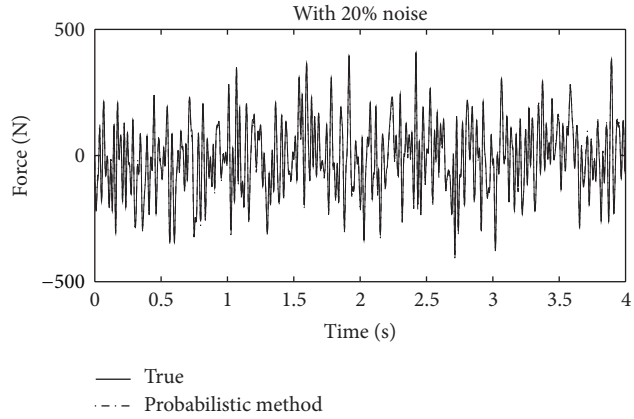

(c) Identified unknown excitation by the probabilistic approach with 20% noise

Figure 2: Comparison of identified unknown excitation.

Table 1: Comparisons of identified damage indices and damage probabilities.

Story no.	Actual damage (%)	Noise level					
		5%			20%		
		D_i (%)	Error (%)	P_i (%)	D_i (%)	Error (%)	P_i (%)
1	0.00	0.01	0.01	49.2	0.34	0.34	49.4
2	0.00	−0.58	0.58	50.3	−0.97	0.97	56.6
3	−5.00	−4.32	0.68	99.2	−4.27	0.73	90.8
4	0.00	−0.45	0.45	50.3	−0.51	0.51	54.2
5	−20.00	−19.32	0.68	100	−18.63	1.37	100
6	0.00	0.01	0.01	49.9	−0.53	0.53	55.7
7	0.00	−0.900	0.900	51.8	−1.30	1.30	61.4
8	−10.00	−9.00	1.00	100	−8.58	1.41	92.1
9	0.00	−0.58	0.58	50.7	−0.67	0.67	56.5
10	0.00	−0.75	0.75	51.4	−0.73	0.73	57.2
Total error	—	—	0.88		—	0.85	

structural damage and the unknown excitations more than the deterministic identification algorithm under high-level measurement noises. The proposed probabilistic approach is clear and simple compared with other previous algorithms. A numerical simulation example demonstrates that the proposed probabilistic approach can accurately identify structural damage and the unknown excitations using only partial measurements of structural acceleration responses contaminated by intensive measurement noises.

It is important to investigate the efficiency of the proposed probabilistic approach for the identification of other types of structural systems. Moreover, damage identification is only verified by the numerical simulation in this paper. Experimental studies to fully assess the performances of the proposed algorithm are needed. Such work is investigated by the authors and the results will be reported in future.

Acknowledgments

This research is funded by the National Natural Science Foundation of China (NSFC) through Grant no. 51178406, the research funding SLDRCE10-MB-01 from the State Key Laboratory for Disaster Reduction in Civil Engineering at Tongji University, China, and by the Fujian Natural Science Foundation through Grant no. 2010J01309.

References

[1] in *Proceedings of the 7th and 8th International Workshops on Structural Health Monitoring*, F. K. Chang, Ed., Stanford University, Palo Alto, Calif, USA, 2011.

[2] "Structural health monitoring of intelligent infrastructure," in *Proceedings of the 4th International Conference on Structural Health Monitoring of Intelligent Infrastructures*, U. Meier, B. Havaranek, and M. Motavalli, Eds., Zurich, Switzerland, 2009.

[3] H. Sohn, C. R. Farrar, F. M. Hemez, D. D. Shunk, D. W. Stinemates, and B. R. Nadler, "A review of structural health monitoring literature: 1996–2001," Los Alamos National Laboratory Report LA-13976-MS, 2003.

[4] R. Ghanem and M. Shinozuka, "Structural-system identification. I: theory," *Journal of Engineering Mechanics*, vol. 121, no. 2, pp. 255–264, 1995.

[5] X. Wang, C. Yang, L. Wang, H. Yang, and Z. Qiu, "Membership-set identification method for structural damage based on measured natural frequencies and static displacements," *Structural Health Monitoring*, vol. 12, pp. 23–34, 2013.

[6] D. Wang and A. Haldar, "System identification with limited observations and without input," *Journal of Engineering Mechanics*, vol. 123, no. 5, pp. 504–511, 1997.

[7] M. Katkhuda, R. Martinez, and A. Haldar, "Health assessment at local level with unknown input excitation," *Journal of Structural Engineering*, vol. 131, no. 6, pp. 956–965, 2005.

[8] L. Jie and C. Jun, "A statistical average algorithm for the dynamic compound inverse problem," *Computational Mechanics*, vol. 30, no. 2, pp. 88–95, 2003.

[9] J. N. Yang, S. Pan, and S. Lin, "Least-squares estimation with unknown excitations for damage identification of structures," *Journal of Engineering Mechanics*, vol. 133, no. 1, pp. 12–21, 2007.

[10] M. J. Perry and C. G. Koh, "Output-only structural identification in time domain: numerical and experimental studies," *Earthquake Engineering and Structural Dynamics*, vol. 37, no. 4, pp. 517–533, 2008.

[11] X. Zhao, Y. L. Xu, J. Li, and J. Chen, "Hybrid identification method for multi-story buildings with unknown ground motion: theory," *Journal of Sound and Vibration*, vol. 291, no. 1-2, pp. 215–239, 2006.

[12] J. N. Yang, S. Pan, and H. W. Huang, "An adaptive extended Kalman filter for structural damage identifications II: unknown inputs," *Structural Control and Health Monitoring*, vol. 14, no. 3, pp. 497–521, 2007.

[13] J. N. Yang and H. W. Huang, "Sequential non-linear least-square estimation for damage identification of structures with unknown inputs and unknown outputs," *International Journal of Non-Linear Mechanics*, vol. 42, no. 5, pp. 789–801, 2007.

[14] B. Xu, J. He, R. Rovekamp, and S. J. Dyke, "Structural parameters and dynamic loading identification from incomplete measurements: approach and validation," *Mechanical Systems and Signal Processing*, vol. 28, pp. 244–257, 2012.

[15] Y. Lei, Y. Q. Jiang, and Z. Q. Xu, "Structural damage detection with limited input and output measurement signals," *Mechanical Systems and Signal Processing*, vol. 28, pp. 229–243, 2012.

[16] Y. Lei and Y. K. Mao, "A technique based on kalman filter and least square estimation for time domain structural damage detection," *Advanced Materials Research*, vol. 163–167, pp. 2683–2688, 2011.

[17] P. Kettle, A. Murray, and F. Moynihan, "Sensor less control of a brushless DC motor using an Extended Kalman estimator," in *Proceedings of the International Power Conversion Conference, Intelligent Monitoring (PCIM '98)*, pp. 385–392, 1998.

[18] J. Chen and J. Li, "Simultaneous identification of structural parameters and input time history from output-only measurements," *Computational Mechanics*, vol. 33, no. 5, pp. 365–374, 2004.

[19] Q. Zhang, L. Jankowski, and Z. Duan, "Simultaneous identification of excitation time histories and parametrized structural damages," *Mechanical Systems and Signal Processing*, vol. 33, pp. 56–68, 2012.

[20] K.-V. Yuen and L. S. Katafygiotis, "Substructure identification and health monitoring using noisy response measurements only," *Computer-Aided Civil and Infrastructure Engineering*, vol. 21, no. 4, pp. 280–291, 2006.

[21] X. Y. Li and S. S. Law, "Damage identification of structures including system uncertainties and measurement noise," *AIAA Journal*, vol. 46, no. 1, pp. 263–276, 2008.

[22] K. Zhang, H. Li, Z. D. Duan, and S. S. Law, "A probabilistic damage identification approach for structures with uncertainties under unknown input," *Mechanical Systems and Signal Processing*, vol. 25, no. 4, pp. 1126–1145, 2011.

[23] Y. Xia and H. Hao, "Statistical damage identification of structures with frequency changes," *Journal of Sound and Vibration*, vol. 263, no. 4, pp. 853–870, 2003.

[24] T. Saito, S. Mase, and K. Morita, "A probabilistic approach to structural damage estimation," *Structural Control and Health Monitoring*, vol. 12, no. 3-4, pp. 283–299, 2005.

[25] M. Chandrashekhar and R. Ganguli, "Uncertainty handling in structural damage detection using fuzzy logic and probabilistic simulation," *Mechanical Systems and Signal Processing*, vol. 23, no. 2, pp. 384–404, 2009.

[26] R. Palma, G. Rus, and R. Gallego, "Probabilistic inverse problem and system uncertainties for damage detection in piezoelectrics," *Mechanics of Materials*, vol. 41, no. 9, pp. 1000–1016, 2009.

Hindawi Publishing Corporation
Journal of Applied Mathematics
Volume 2013, Article ID 531062, 7 pages
http://dx.doi.org/10.1155/2013/531062

Research Article

Generalized Linear Spatial Models to Predict Slate Exploitability

Angeles Saavedra,[1,2] Javier Taboada,[3] María Araújo,[3] and Eduardo Giráldez[3]

[1] *Department of Statistics, University of Vigo, 36310 Vigo, Spain*
[2] *E.T.S.I. MINAS, Universidad de Vigo, Campus Lagoas-Marcosende, Rúa Maxwell, 36310 Vigo, Spain*
[3] *Department of Natural Resources, University of Vigo, 36310 Vigo, Spain*

Correspondence should be addressed to Angeles Saavedra; saavedra@uvigo.es

Received 11 November 2012; Revised 3 May 2013; Accepted 26 May 2013

Academic Editor: Zhiping Qiu

Copyright © 2013 Angeles Saavedra et al. This is an open access article distributed under the Creative Commons Attribution License, which permits unrestricted use, distribution, and reproduction in any medium, provided the original work is properly cited.

The aim of this research was to determine the variables that characterize slate exploitability and to model spatial distribution. A generalized linear spatial model (GLSMs) was fitted in order to explore relationship between exploitability and different explanatory variables that characterize slate quality. Modelling the influence of these variables and analysing the spatial distribution of the model residuals yielded a GLSM that allows slate exploitability to be predicted more effectively than when using generalized linear models (GLM), which do not take spatial dependence into account. Studying the residuals and comparing the prediction capacities of the two models lead us to conclude that the GLSM is more appropriate when the response variable presents spatial distribution.

1. Introduction

The exploitability of a slate deposit depends on many quality-determining factors that are spatially correlated. Knowledge and study of these factors are essential for the evaluation of deposits [1, 2]. Therefore, it can be fairly safely assumed that better evaluations of quality parameters and better predictions of slate exploitability could be obtained by using specific statistical models that take spatial correlation into account.

Traditionally, the main aim of geostatistical models has been to predict a spatially correlated response variable. Under this approach, estimating the parameters of the geostatistical model is not usually the main interest. However, estimating and inferring parameters enables a more precise identification of the factors influencing the geographical distribution of exploitable slate, thus allowing greater knowledge to be gained regarding the response variable of interest.

In our research, the model-based geostatistics methodology was adapted in the analysis of slate exploitability using a generalized linear spatial model (GLSM). With this type of model, the objective of inference can be focused on the parameters of the regression function, on the properties of the residuals, or on the distribution of the residuals conditionally on the response variable.

A brief description of the statistical models used in this study is given in Section 2. The data studied and the formulated model are described in Section 3. The statistical results and analyses are presented in Section 4, and some comments and the discussion can be found in Section 5.

2. Statistical Analysis Methods

2.1. Generalized Linear Spatial Models. Generalized linear models (GLMs) were introduced by [3] and studied in depth by [4] and later by several authors (see [5–9]).

In a GLM, a response variable $Y = (Y_1, Y_2, \ldots, Y_n)$ is assumed so that the variables $Y_1, Y_2, \ldots, Y_n$ are mutually independent and with its expected value related to a linear predictor $E[Y] = g^{-1}(d^T\beta)$, where $\beta \in \Re^p$ is a vector of unknown regression parameters, d are known explanatory variables, and g is a known function called link function.

An important extension of the GLM is the generalized linear mixed model (GLMM) [10], in which the response variables are considered independent of one another conditionally on the values for a set of latent variables. The generalized linear spatial model (GLSM) [11] is basically a GLMM, in as much as the latent variables derive from a spatial process. The term "model-based geostatistics" was first used by these authors to describe an approach to geostatistical

problems based on formal statistical models and inference procedures. This leads to the following specification of the model.

Consider n different locations $\{x_1, \ldots, x_n\} \subset I \subset \mathfrak{R}^2$ and assume that a realization $y = (y_1, \ldots, y_n)^T$ of Y is observed, where $y = Y(x_i)$.

Let $S = \{S(x) : x \in I\}$, $I \subset \mathfrak{R}^2$ be a Gaussian process with mean function $E[S(x)] = d(x)^T\beta$ and covariance $\text{cov}(S(x), S(x')) = \sigma^2\rho(x, x'; \varphi) + \tau^2 1\{x = x'\}$, where $\beta \in \mathfrak{R}^p$ is, as in the GLM case, a vector of unknown regression parameters, $d(x)$ are known explanatory variables now with spatial dependence, $\rho(x, x'; \varphi)$ is a correlation function in $\mathfrak{R}^2$, φ is a scale parameter that controls the speed at which spatial correlation approaches 0 as the distance between locations grows, and, finally, $\tau^2 \geq 0$ is known as the nugget effect, in accordance with the usual geostatistical terminology. The nugget effect can be interpreted as a measurement error or a microscale variation or a combination of both.

Conditionally on S, the process $\{Y(x), x \in I\}$ consists of random mutually independent variables and, for each location $x \in I$, the error distribution or $[Y(x) \mid S]$ has a density that depends only on the conditional mean $E[Y(x_i) \mid S(x_i)]$. A known link function g relates the conditional mean and $S(x)$ so that $E[Y(x_i) \mid S(x_i)] = g^{-1}(S(x_i))$.

When the regression parameters β are of interest, it is important to remember that their interpretation is more conditional than marginal. In particular, $E[Y(x_i) \mid S(x_i)]$ and $E[Y(x_i)]$ differ in terms of the structural dependence of the explanatory variables $d(x_i)$; thus, the interpretation of β calls for caution. Only in the case where $Y(x_i) \mid S(x_i)$ is Gaussian and the link function is identity parameter, comparison is direct. The need to distinguish between conditional and marginal regression parameters, which is not possible in Gaussian linear models, is well known in the context of GLMs for longitudinal data (see, e.g., [12]).

To estimate the parameters for the GLSM and due to the fact that the stationary Gaussian process $S(x)$ is not observable, it is not possible to obtain a closed-form likelihood function except as a high-dimension integral. Reference [11] suggests using algorithms based on Markov chain Monte Carlo (MCMC) to calculate GLSM parameters in a Bayesian framework. This is the approach used in our analysis, implemented using geoR and geoRglm packages (free open-source programs for use with *R* statistical software [13]).

2.2. ROC Curves. When the marginal distribution (in the GLM) or conditional distribution (in the GLSM) of the response variable Y follows a binomial distribution, the models can be called binary classification systems. The exactitude of a diagnostic test for a binary classification system can be summarized as a receiver operating characteristic (ROC) curve, which is a graphic representation of true positive versus false positive rates when the discrimination threshold is varied. Within the framework of binary GLMs, it is normal to estimate the ROC curves of models in which one or more explanatory variables have been excluded so as to evaluate the effects of these variables. Analysing ROC curves provides tools for comparing and selecting the best models. More precisely, the area under the curve (AUC) of the ROC curve is usually calculated in order to compare the different binary models and thereby select the explanatory variables to be included in the model. Reference [14] described a bootstrap-based method for testing the significant effect of dependent variables on the ROC curve.

We used the AUC and residual semivariograms to demonstrate the goodness-of-fit of the binary GLSM compared with the binary GLM when working with spatially correlated data.

3. Data Description and Model Formulation

3.1. The Studied Area and the Geographic Database. The data used to build the proposed model was collected from borehole samples taken from slate deposits in Baja Cabrera Leonesa (northwest Spain), an area with a long tradition of extracting, processing, and exporting roofing slate.

When surveying a slate deposit, in-depth studies of the rock are performed by taking continuous borehole samples, which enable geologists to study the living rock and analyse the possibility of using it as ornamental slate, see [15]; these samples also reveal the degree of fracturation inside the rock mass.

The specific borehole logging process was based on manual and visual inspection of the borehole by an expert who, after evaluating the aesthetic and functional defects and properties of the slate, differentiated between seams of commercial and unusable slate. The survey was performed by taking a control sample every 25 centimetres; rock quality designation (RQD), however, was defined by homogeneously fractured sections.

A total of 313 equally spaced in-depth observations were obtained, resulting from prior evaluation of various parameters affecting the ornamental quality of the slate and from direct binary values (0 or 1) assigned by the expert to indicate exploitation potential. The 9 specific variables that affected the results of borehole logging were as follows.

(i) RQD: borehole core samples recovered in pieces greater than 10 cm long as a percentage of the total borehole length. This is an indicator of the degree of rock mass fracturing.

(ii) Veins: presence of microfractures filled with quartz that determine the breakage resistance of a commercial slab.

(iii) Crenulations: effect of crenulation cleavage on the main schistosity planes. This increases the roughness of the foliation surfaces of the slate and reduces fissility.

(iv) Kink bands: Presence of microfolding caused by late Variscan deformations.

(v) Sandy laminations: presence of sedimentary sand layers which cut the schistosity planes and have a negative effect on fissility.

Table 1: Correlation matrix of the $p = 9$ explanatory variables that affected the results of borehole logging.

(a)

	RQD	Veins	Crenulation	Kink bands	Sandy laminations
RQD	1				
Veins	0.1624	1			
Crenulation	0.3038	0.1631	1		
Kink bands	0.1040	0.0408	0.1962	1	
Sandy laminations	0.0177	0.0187	0.0200	0.0736	1
Microfractures	0.6696	0.0035	0.1284	−0.0590	−0.0138
Pyrite	−0.1953	−0.0403	−0.1221	−0.0891	−0.1202
Oxidation	0.2053	0.0837	0.1722	0.0821	−0.0645
Rough cleavage	−0.0908	−0.0593	0.2096	−0.0058	−0.0454

(b)

	Microfractures	Pyrite	Oxidation	Rough cleavage
Microfractures	1			
Pyrite	−0.1587	1		
Oxidation	0.1162	−0.1152	1	
Rough cleavage	−0.0989	0.0065	−0.0366	1

(vi) Microfractures: presence of barely visible fractures which determine the breakage resistance of slabs measuring 3–5 mm thick.

(vii) Pyrite: presence of iron sulphides.

(viii) Oxidation: degree of oxidation of iron sulphides in the slate.

(ix) Rough cleavage: slate with poor fissility due to textural heterogeneity.

In-depth knowledge of the variability and distribution of exploitable slate and possible correlation between properties are conducive to the use of GLSM to spatially model the geographic database.

Table 1 shows the correlation matrix of the explanatory variables given above in order to know the degree of dependence between them.

3.2. Model Formulation. The response variable, $Y(x)$, takes the values 0 or 1 to indicate disposable or exploitable slate respectively, in a particular location x. It is assumed in what follows that slate exploitability is a spatial phenomenon that can be modelled using a GLSM. In other words, conditional to the Gaussian process $S(x)$, the data $Y(x_i)$, $i = 1, \ldots, n$ follow the classic GLM. The role of $S(x)$ is, therefore, to explain the residual spatial variation after considering all the known explanatory variables. It is also reasonable to assume that the conditional distribution of exploitability can be modelled as a binomial distribution, which is why a binomial error distribution was considered in our study.

Binomial error distribution was used by Diggle et al. [6] and Zhang [8]. A class of transformations that can be used as link functions for this distribution was described by [16]. We assume the stationary Gaussian process $S(\cdot)$ to be the basis for a model of spatial variation in the probability, $P(x)$, that the slate in x is exploitable, but with a logit transformation to map the domain of $S(\cdot)$ onto the unit interval. Thus,

$$g\left[P\left(x\right)\right] = \log\left\{\frac{P\left(x\right)}{\left[1 - P\left(x\right)\right]}\right\} = \mu + S\left(x\right). \quad (1)$$

The regression function $E[Y(x_i) \mid S(x_i)]$ varies spatially only through $S(x)$ in the locations x_i.

We adopted a Bayesian framework for inference and prediction of the parameters, using algorithms based on MCMC.

The parameters of this binomial GLSM are $\theta = (\sigma^2, \varphi)$ and $\beta = (\beta_0, \ldots, \beta_p)$, where β_0 is the independent term and $\beta_1, \ldots, \beta_p$ are the regression coefficients corresponding to each known dependent variable.

4. Statistical Analysis

We initially included all the variables that characterize slate exploitability, namely, RQD, veins, crenulations, kink bands, sandy laminations, microfractures, pyrite, oxidation, and poor fissility. Taking this data and, considering slate exploitability as the response variable, we fitted a binary GLM, called GLM1. A ROC curve was estimated for this complete binary model and the AUC was 0.99.

Next, binary GLMs were fitted to different groups of dependent variables in an attempt to find the minimum number of variables that would provide a high AUC value, that is, close to 0.99. The model, called GLM2, fitted with the RQD, crenulation, kink band, and microfracture variables obtained an AUC of 0.92. Figure 1 shows the ROC curves and the corresponding AUC values for both GLM1 and GLM2. The study was continued with the four variables included in GLM2, given that the reduction in the number of variables did not overly affect the accuracy of the model. A binary nonspatial GLM was fitted using Bayesian methods and the

Table 2: Estimated coefficients and 2.5%, 25%, 75%, and 97.5% quantiles for the GLM.

	Coefficient	2.5% quantile	25% quantile	75% quantile	97.5% quantile
β_0 (intercept)	−35.6747	−77.6804	−49.0098	−26.0904	−18.6385
β_1 (RQD)	1.2826	−1.1476	0.4192	2.0516	3.9633
β_2 (crenulation)	0.5875	0.3288	0.5089	0.6761	0.8352
β_3 (kink band)	0.5668	0.3965	0.5019	0.6395	0.7857
β_4 (microfracture)	2.5815	0.9221	1.6093	3.9181	6.7967

Table 3: Estimated coefficients and 2.5%, 25%, 75%, and 97.5% quantiles for the GLSM.

	Coefficient	2.5% quantile	25% quantile	75% quantile	97.5% quantile
β_0 (intercept)	−27.7021	−32.0664	−29.6753	−24.7446	−17.7297
β_1 (RQD)	0.2521	−0.0385	0.1291	0.3726	0.5388
β_2 (crenulation)	0.7334	0.3762	0.6121	0.8283	1.0691
β_3 (kink band)	0.9189	0.5881	0.7802	1.0274	1.2261
β_4 (microfracture)	1.2911	0.8834	1.0125	1.4480	1.6261

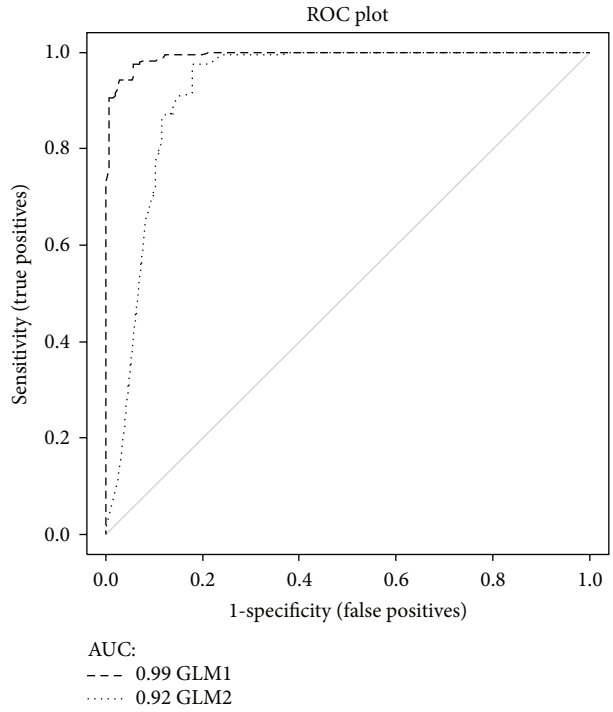

Figure 1: ROC curves and the corresponding AUC values for the two binary GLMs included in the study.

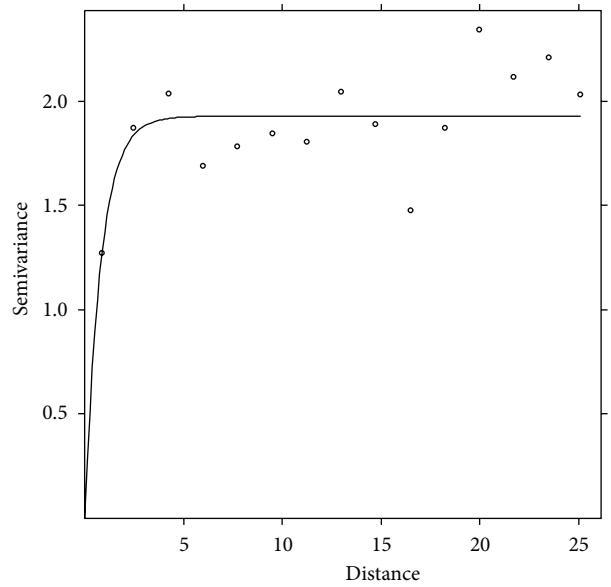

Figure 2: Experimental semivariogram for the GLM2 residuals (points), together with the fitted theoretical model fitted according to an exponential model (continuous line).

MCMClogit function from the MCMCpack (R language). The vector β of the parameters fitted for the GLM2 model was $\beta = (-35.6747, 1.2826, 0.5875, 0.5668, 2.5815)$, where the first value is the independent term and the remaining values are the corresponding coefficients of the explanatory variables in the same order as they were mentioned above.

Table 2 shows the estimated coefficients and the 2.5%, 25%, 75%, and 97.5% quantiles for the fitted model. It can be observed that, for a significance level of $\alpha = 0.05$, the only nonsignificant variable is the RQD.

The study of the residuals of the GLM2 model fitted with four explanatory variables detected a spatial dependence that could be modelled using an exponential theoretical semivariogram with range 0.81 and sill 1.61. Figure 2 shows the experimental semivariogram for the GLM2 residuals, together with the corresponding fitted theoretical model.

Given the presence of spatial dependence in the residuals, it then made sense to fit a GLSM, maintaining four explanatory variables and assuming an exponential model for the process $S(x)$. The correlation function considered was of the type $\text{cov}(S(x), S(x')) = \sigma^2\rho(x, x'; \varphi) + \tau^2 1\{x = x'\}$, with $\rho(u; \varphi) = \exp(-u/\varphi)$. The fit was made using Bayesian inference implemented via the MCMC algorithms. The first 10,000 sample observations from the simulation were ignored as burn-in, at which point it was considered that convergence time had been achieved. The subsequent samples were used to obtain the subsequent distribution of the parameters of

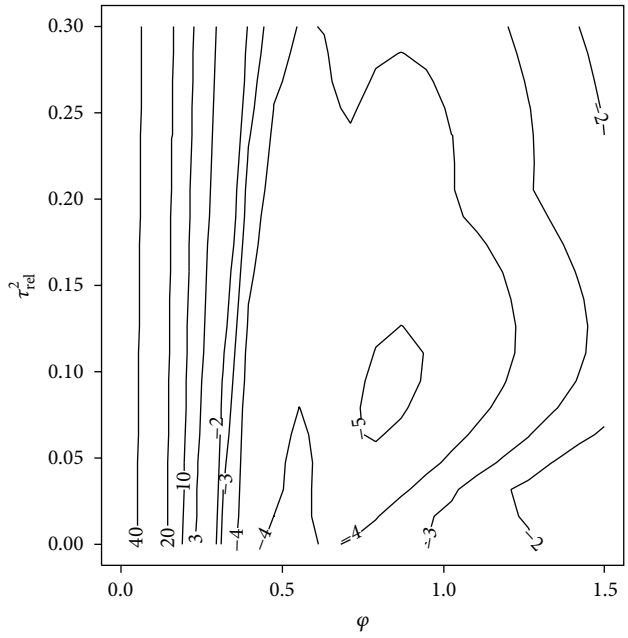

Figure 3: Two-dimensional likelihood profile for (φ, τ^2) for the GLSM.

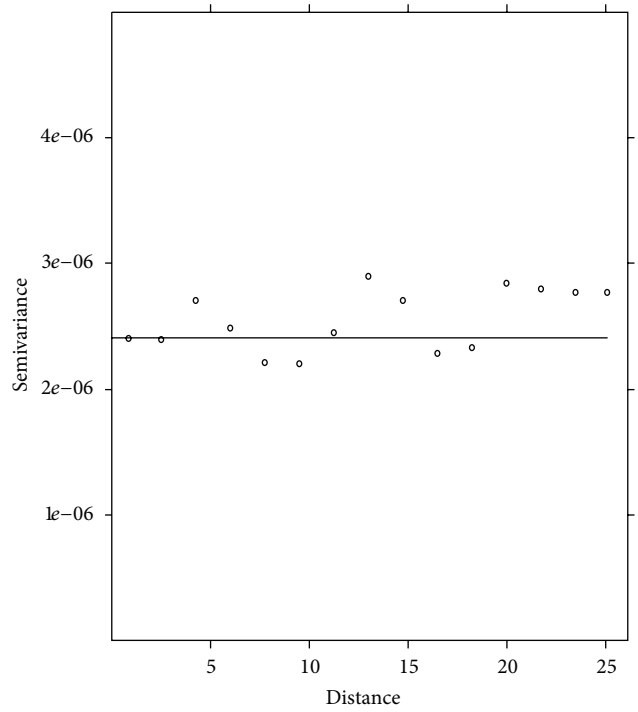

Figure 4: Experimental semivariogram for the GLSM residuals (points), together with the theoretical model fitted according to a nugget effect model (continuous line).

interest. The chain was sampled for each 100 of the 50,000 iterations to obtain samples containing 500 values (for further details, see [17]).

Using this procedure, the parameters were estimated as $\varphi = 0.82$, $\sigma^2 = 1.46$, $\tau^2 = 0.09$, and $\beta = (-27.7021, 0.2521, 0.7334, 0.9189, 1.2911)$. Table 3 shows the estimated β coefficients and their 2.5%, 25%, 75%, and 97.5% quantiles. Once again we can see how, for a significance level of $\alpha = 0.05$, only the RQD variable was not significant.

It is important to remember that these parameters should be conditionally and not marginally interpreted and so should not be directly compared with the parameters estimated for the GLM. Direct comparison of a spatial and nonspatial GLM could lead to erroneous conclusions, as the estimation methods are fundamentally different. Nonetheless, there is a certain correlation in the conclusions to be drawn from these tables, with variables such as crenulation, kink band, and microfracture remaining significant; RQD, on the other hand, was not significant at 5% level.

Figure 3 shows the likelihood profile in two dimensions for parameters (φ, τ^2) of the model, illustrating the flatness of the likelihood surface obtained using the MCMC algorithms.

A study of the spatial dependence of the GLSM residuals indicated that the spatial component had been correctly modelled on this occasion. Figure 4 shows an experimental semivariogram of the GLSM residuals and a theoretical model fitted according to a nugget effect model. It is clear that the empirical semivariogram is essentially flat, which suggests a suitable fit to the spatial structure. A direct comparison between Figures 2 and 4 leads to the conclusion that the spatial dependence has been properly captured by the stationary Gaussian process S.

The ROC curve and AUC were calculated for the GLSM. The AUC of the binary spatial model was 0.99, which indicates a substantial improvement in the precision of the GLSM. This improvement is reflected in Figure 5, which depicts the ROC curves and AUC values for the GLM2 and GLSM binary models.

Table 4: Error rates for the binary models for three scenarios representing different levels of prediction difficulty.

	5% test	10% test	15% test
GLM	$6.6E-2$	$6.3E-2$	$5.6E-2$
GLSM	$4.1E-2$	$5.1E-2$	$4.6E-2$

The comparison between the two models was completed with a simulation study, designed to compare the reliability of the predictions in three scenarios of varying levels of difficulty. Randomly selected for the first scenario was 95% of the 313 initial observations, composing the training set that was used to fit the GLM and GLSM. The fitted models were then validated with the remaining 5% of the observations. This procedure was repeated 100 times and the number of errors in the slate exploitability prediction was recorded for each repetition. For the second scenario, we randomly selected 90% of the observations for the training set and the remaining 10% made up the test set. This simulation was also repeated 100 times. The procedure for the third scenario was similar, but this time 85% and 15% of observations made up the training and test sets, respectively.

Table 4 displays the error rates for the three scenarios described, with the error rate calculated as the ratio between the number of prediction errors and the total number of predictions in the test set.

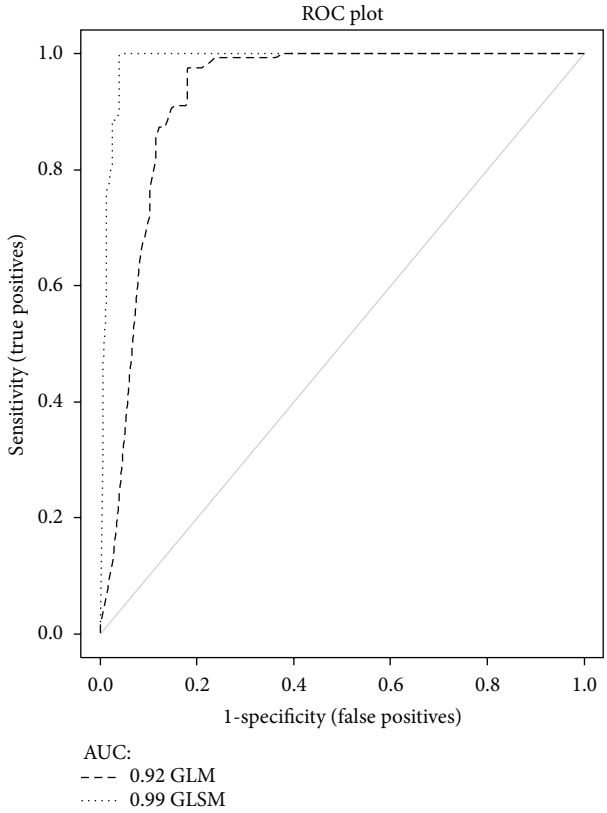

Figure 5: ROC curves and corresponding AUC values for the binary GLM2 and the GLSM.

In all the cases, it can be observed that the GLSM provided a better explanation not only of the effect of the variables determining slate quality, but also of the spatial behaviour of exploitable slate, thereby producing lower prediction error rates.

5. Conclusions

A general interpretation of the GLSM used in our analysis is that the spatial term S represents the accumulative effect of possible explanatory variables with an undetermined spatial structure, which have, therefore, not been observed.

In GLMs, the fact that the spatial correlation of the variables is not taken into account can significantly affect the quality of statistical results. Our study highlights the potential risk of using GLMs when the data is spatially structured.

The conclusion reached after comparing ROC curves and their corresponding AUCs is that GLSMs predict slate exploitability better than GLMs. Therefore, it would seem essential to include unexplained spatial variation when modelling spatially correlated variables.

Based on the comparison of the semivariograms of the GLM and GLSM residuals, we would like to draw attention to the presence of spatial dependence in the GLM residuals, in contrast to what occurs when a GLSM is implemented. This indicates that spatial dependence has been captured correctly by the stationary Gaussian process S. We can, therefore, conclude that a GLSM is more suitable for modelling spatial dependence, which is overlooked by classic GLMs.

The simulation study demonstrates that, for varying levels of prediction difficulty, the GLSM had lower error rates than the GLM.

Although the parameters of the GLSM must be interpreted conditionally rather than marginally to S, the results of the statistical analysis denote the broader potential of the GLSM compared to the classic GLM in analysing spatial data. They also underline the potential risk of reaching erroneous conclusions when using nonspatial models to analyse spatially structured data.

Acknowledgments

This work was funded partly by the Project INCITE10REM304009PR of the Xunta de Galicia and by the Projects MTM2008-03129 and MTM2011-23204 of the Ministry of Science and Innovation.

References

[1] J. M. Matías, A. Vaamonde, J. Taboada, and W. González-Manteiga, "Support vector machines and gradient boosting for graphical estimation of a slate deposit," *Stochastic Environmental Research and Risk Assessment*, vol. 18, no. 5, pp. 309–323, 2004.

[2] F. G. Bastante, J. Taboada, L. Alejano, and E. Alonso, "Optimization tools and simulation methods for designing and evaluating a mining operation," *Stochastic Environmental Research and Risk Assessment*, vol. 22, no. 6, pp. 727–735, 2008.

[3] J. A. Nelder and R. W. M. Wedderburn, "Generalized linear models," *Journal of the Royal Statistical Society A*, vol. 135, pp. 370–384, 1972.

[4] P. McCullagh and J. A. Nelder, *Generalized Linear Models*, Chapman and Hall, London, UK, 1989.

[5] O. F. Christensen and R. Waagepetersen, "Bayesian prediction of spatial count data using generalized linear mixed models," *Biometrics*, vol. 58, no. 2, pp. 280–286, 2002.

[6] P. Diggle, R. Moyeed, B. Rowlingson, and M. Thomson, "Childhood malaria in the Gambia: a case-study in model-based geostatistics," *Journal of the Royal Statistical Society C*, vol. 51, no. 4, pp. 493–506, 2002.

[7] P. J. Diggle, P. J. Ribeiro,, and O. F. Christensen, "An introduction to model-based geostatistics," in *Spatial Statistics and Computational Methods*, J. Møller, Ed., pp. 43–86, Springer, New York, NY, USA, 2003.

[8] H. Zhang, "On estimation and prediction for spatial generalized linear mixed models," *Biometrics*, vol. 58, no. 1, pp. 129–136, 2002.

[9] H. Zhang, "Optimal interpolation and the appropriateness of cross-validating variogram in spatial generalized linear mixed models," *Journal of Computational and Graphical Statistics*, vol. 12, no. 3, pp. 698–713, 2003.

[10] N. Breslow and D. Clayton, "Approximate inference in generalized linear mixed models," *Journal of the American Statistical Association*, vol. 88, pp. 9–25, 1993.

[11] P. J. Diggle, J. A. Tawn, and R. A. Moyeed, "Model-based geostatistics," *Journal of the Royal Statistical Society C*, vol. 47, no. 3, pp. 299–350, 1998.

[12] P. J. Diggle, K. Y. Liang, and S. L. Zeger, *The Analysis of Longitudinal Data*, Clarendon, Oxford, UK, 1994.

[13] R Development Core Team, *R: A Language and Environment for Statistical Computing*, R Foundation for Statistical Computing, Vienna, Austria, 2012, http://www.r-project.org/ .

[14] M. X. Rodríguez-Álvarez, J. Roca-Pardiñas, and C. Cadarso-Suárez, "ROC curve and covariates: extending induced methodology to the non-parametric framework," *Statistics and Computing*, vol. 21, no. 4, pp. 483–499, 2011.

[15] J. Taboada, A. Vaamonde, A. Saavedra, and A. Arguelles, "Quality index for ornamental slate deposits," *Engineering Geology*, vol. 50, no. 1-2, pp. 203–210, 1998.

[16] V. de Oliveira, B. Kedem, and D. A. Short, "Bayesian prediction of transformed Gaussian random fields," *Journal of the American Statistical Association*, vol. 92, no. 440, pp. 1422–1433, 1997.

[17] O. F. Christensen, "Monte Carlo maximum likelihood in model-based geostatistics," *Journal of Computational and Graphical Statistics*, vol. 13, no. 3, pp. 702–718, 2004.

Hindawi Publishing Corporation
Journal of Applied Mathematics
Volume 2013, Article ID 959403, 6 pages
http://dx.doi.org/10.1155/2013/959403

Research Article

Restricted Isometry Property of Principal Component Pursuit with Reduced Linear Measurements

Qingshan You,[1,2] Qun Wan,[2] and Haiwen Xu[1]

[1] *School of Computer Science, Civil Aviation Flight University of China, GuangHan, Sichuan 618307, China*
[2] *School of Electronic Engineering, University of Electronic Science and Technology of China, Chengdu, Sichuan 611731, China*

Correspondence should be addressed to Qun Wan; wanqun@uestc.edu.cn

Received 25 September 2012; Revised 2 April 2013; Accepted 30 April 2013

Academic Editor: Xiaojun Wang

Copyright © 2013 Qingshan You et al. This is an open access article distributed under the Creative Commons Attribution License, which permits unrestricted use, distribution, and reproduction in any medium, provided the original work is properly cited.

The principal component prsuit with reduced linear measurements (PCP_RLM) has gained great attention in applications, such as machine learning, video, and aligning multiple images. The recent research shows that strongly convex optimization for compressive principal component pursuit can guarantee the exact low-rank matrix recovery and sparse matrix recovery as well. In this paper, we prove that the operator of PCP_RLM satisfies restricted isometry property (RIP) with high probability. In addition, we derive the bound of parameters depending only on observed quantities based on RIP property, which will guide us how to choose suitable parameters in strongly convex programming.

1. Introduction

Matrix completion is a signal processing technique, which recovers an unknown low-rank or approximately low-rank matrix from a sampling of its entries. Recently, this technique has been applied in many fields, such as medical [1], imaging [2], seismology [3], and computer vision [4–6]. The dimension of data produced in practice is always vastly high, therefore, there exists a pressing challenge to develop efficient and effective tools to process, analyze, and extract useful information from a small set of linear measurements of the high-dimensional data. Many scholars had studied in detail in the recent papers [7–13]. Candès et al. address the problem of recovery of the unknown low-rank matrix and sparse matrix from the sampling of its complete entries [7–9] for large scale. As the extensions of previous works, Ganesh et al. address the problem of decomposing a superposition of a low-rank matrix and a sparse matrix when a relatively few linear measurements are available [10, 11].

These fundamental results have a great impact in engineering and applied mathematics. However, these results are limited into convex optimization; that is, nuclear norm based convex optimization leads to the exact low-rank matrix recovery under suitable conditions. It is well known that strongly convex optimization has many intrinsic advantages, such as the uniqueness of optimal solution. Especially, the strongly convex optimization was widely used in designing efficient and effective algorithm in the literature of compressive sensing and low-rank matrix recovery. Zhang et al. extend them; they proved that strongly convex optimizations can guarantee the exact low-rank matrix recovery as well in the paper [12]. The right bound of τ of strongly convex programming for robust principal component analysis was provided in paper [14].

Pertaining to the strongly convex optimization for compressive principal component pursuit, we had studied it in detail in our former work in [15], in which we prove that under suitable conditions, the corresponding strongly convex optimization also recovers the low-rank matrix and sparse matrix exactly. However, the bound of parameter strongly depends on the Frobenius norm of the data, which is not known in practice, because the data we can use is $\mathcal{P}_Q M$ only. In this paper, we will give an easy band of τ depending on $\mathcal{P}_Q M$ only.

1.1. Contents and Notations. For convenience, we will give here a brief summary of the notations that will be used throughout the paper. We denoted the operator norm of matrix by $\|X\|$, the Frobenius norm by $\|X\|_F$, the nuclear

norm by $\|X\|_*$ and the l_∞ norm by $\|X\|_\infty := \max_{ij}|x_{ij}|$. We will bound the Euclidean inner product between two matrices which is defined by the formula $\langle X, Y\rangle = \operatorname{trace}(X^*Y)$. The Cauchy-Schwarz inequality gives $\langle X, Y\rangle \le \|X\|_F\|Y\|_F$, especially $\|X\|_* \le \sqrt{r}\|X\|_F$ and $\sum_{ij}|x_{ij}| \le \sqrt{|X|_0}\|X\|_F$. We will also bound linear transformations which act on the space of matrices, and we denote these operators by $\mathscr{P}_T X$. The norm of the operator is denoted by $\|\mathscr{P}\|$; that is, $\|\mathscr{P}\| = \sup_{\{\|X\|_F=1\}}\|\mathscr{P}X\|_F$. We denote by Ω the support of S_0. By a slight abuse of notation, we also represent by Ω the subspace of matrices whose support is contained in the support of S_0. $\operatorname{Supp}(S_0) \sim \operatorname{Ber}(\rho)$ means each entry of the matrix belongs to the support of the sparse matrix S_0 independently with probability ρ.

1.2. Basic Problem and Main Result. In this paper, we only address the strongly convex programming of principal component pursuit with reduced linear measurements, which is considered in paper [10]. This problem has the following formula:

$$\begin{aligned} &\text{minimize } \|L\|_* + \lambda\|S\|_1 + \frac{1}{2\tau}\|L\|_F^2 + \frac{1}{2\tau}\|S\|_F^2 \\ &\text{subject to } \mathscr{P}_Q M = \mathscr{P}_Q(L+S), \end{aligned} \tag{1}$$

where $\tau > 0$ is some positive penalty parameter and P_Q is the orthogonal projection onto the linear subspace Q, and Q is distributed according to the Haar measure on the Grassmannian $\mathbb{G}(R^{m\times n}; q)$. Suppose that $G_1, G_2, \ldots, G_p$ are standard orthogonal basis of $Q^\perp$; that is, $G_1, G_2, \ldots, G_p$ are identical in distribution to G, where $G = H/\|H\|_F$ and $H = M/\sqrt{mn}$, whose entries are i.i.d, according to the standard normal distribution. More detail was interpreted in the paper [10].

When $\tau = \infty$ in the problem (1), we have existence and uniqueness theorems as follows.

Theorem 1 (see [10]). *Fix any $C_p > 0$, and let $Q^\perp$ be a p-dimensional random subspace of $\mathbb{R}^{m\times n}$; L_0 obeys incoherence condition with parameter μ, and $\operatorname{supp}(S_0) \sim \operatorname{Ber}(\rho)$. Then, with high probability, the solution of problem* (1) *with $\lambda = 1/\sqrt{n}$ is exact; that is, $\widehat{L} = L_0$ and $\widehat{S} = S_0$, provided that*

$$\operatorname{Rank}(L_0) < C_r n \mu^{-1} (\log m)^{-2}, \qquad p < C_p n, \qquad \rho < \rho_0, \tag{2}$$

where, C_r, C_p and $\rho_0 \in (0, 1)$ are positive numerical constants.

Remark 2. The value of ρ_0 is a fixed positive numerical constant and should obey some suitable conditions; one of those is less than 1/5. the detail derivation has been well-studied (see, e.g., [8, 10] and the many references therein). With high probability means with probability at least $1 - m^{-c}$, with $c > 0$ numerical constant.

When $\tau \neq \infty$ in the problem (1), we have existence and uniqueness theorems as follow.

Lemma 3 (see [14, 15]). *Assuming*

$$\tau \ge \frac{8\sqrt{15}\|M\|_F}{3\lambda} \tag{3}$$

under the other assumptions of Theorem 1, (L_0, S_0) is the unique solution to the strongly convex programming (1) *with high probability.*

Pertaining to the projection operator $\mathscr{P}_Q$, we obtain the following restricted isometry property of operator $\mathscr{P}_Q$ restricted in a superposition of low-rank matrices and sparse matrices.

Theorem 4. *Suppose that L is low-rank matrix with rank r, S is sparse matrix with $\operatorname{Supp}(S_0) \sim \operatorname{Ber}(\rho)$, $\rho \le \delta^2/(64 \times 25p\log(mnp))$, and $r \le (mn\delta^2/(12 \times 25p)) - (5/3)\log(n)$, and assume that the conditions of Theorem 1 hold. Then, with high probability, one has*

$$(1-\delta)\|M\|_F \le \left\|\mathscr{P}_Q M\right\|_F \le (1+\delta)\|M\|_F. \tag{4}$$

According to Lemma 3 and Theorem 4, we can easy obtain the following theorem.

Theorem 5. *Supposing that L is low-rank matrix with rank r, S is sparse matrix with $\operatorname{Supp}(S) \sim \operatorname{Ber}(\rho)$. If*

$$\tau \ge \frac{8\sqrt{15}\left\|\mathscr{P}_Q M\right\|_F}{3(1-\delta)\lambda} \tag{5}$$

under the other assumptions of Theorem 4, (L_0, S_0) is the unique solution to the strongly convex programming (1) *with high probability.*

It is obvious that the band of τ depends on $\mathscr{P}_Q M$ only, which is obtained very easily in practice.

1.3. Contributions and Organization. In this paper, we first prove that although the operator $\mathscr{P}_Q$ does not satisfy the restricted isometry property (RIP) in entire space, it obeys restricted isometry property (RIP) with high probability if the rank of low-rank matrix is not large and the sparse matrix is enough sparse. Second, we will use the restricted isometry property to improve the band of parameter which just depends on $\mathscr{P}_Q M$.

The main center of the paper provides the proof of Theorem 4. The rest of paper is organized as follows. In Section 2, we will provide some important lemmas which are important composition of our main result and then will give the proof of Theorem 4. Conclusion and further works are discussed in Section 3.

2. The Proof of Theorem 4

In this section, we will provide the proof of Theorem 4. We first bound the behaviors of the operator $\mathscr{P}_{Q^\perp}$ implying on the space of low-rank matrices and the space of sparse matrices, respectively. Then, the relation of $\|M\|_F$ and $\|L\|_F + \|S\|_F$, we can obtain Theorem 4.

2.1. Bounding the Behavior of $\|\mathscr{P}_{Q^\perp}(S)\|_F$. We will provide some important lemmas, which are used in the main theorem.

Lemma 6 (see [10, Lemma 6]). *Let* $Q^\perp$ *be a linear subspace distributed according to the random subspace model described earlier. Then, for any* $(i, j) \in [m] \times [n]$, *with high probability*

$$\left\|\mathscr{P}_{Q^\perp} e_i e_j^T\right\|_F \leq 4\sqrt{\frac{p\log(mnp)}{mn}}. \tag{6}$$

Bernstein's Inequality [16, 17]. Assume that $X_1, X_2, \ldots, X_n$ are independent random variables with $\mathbb{E}[X_i] = 0$, for all i. Furthermore, suppose that $|X_i| \leq M$. Then,

$$\mathbb{P}\left\{\left|\sum_i X_i\right| > t\right\} \leq 2\exp\left(-\frac{t^2}{2\sum_i \mathrm{Var}(X_i) + 2Mt/3}\right). \tag{7}$$

Lemma 7. *If* $\rho \geq \log n/mn$, *then with high probability*

$$\|S\|_0 \leq 2\rho mn. \tag{8}$$

Proof. Let ω_{ij} be the indicator variables with $\omega_{ij} = 1$ if $(ij) \in \Omega$ and $\omega_{ij} = 0$ for otherwise. For $S \in \Omega$, we have

$$\|S\|_0 \leq \sum_{ij} \omega_{ij}. \tag{9}$$

Let $Y_{ij} := \omega_{ij} - \rho$ and $Z := \sum_{ij} Y_{ij}$. For $\mathbb{E}[Y_{ij}] = \mathbb{E}[\omega_{ij}] - \rho = 0$ and $|Y_{ij}| \leq 1$, it is obvious that Y_{ij} satisfies Bernstein's inequality. Note that

$$\sum_{ij} \mathrm{Var}\left(Y_{ij}\right) = \rho(1-\rho)mn \leq \rho mn. \tag{10}$$

According to Bernstein's inequality, letting $t = \rho mn$, we have

$$\mathbb{P}\left\{\left|\sum_{ij}\omega_{ij} - \rho mn\right| > \rho mn\right\} \leq 2\exp\left(-\frac{3\rho mn}{8}\right). \tag{11}$$

Combining with $\rho \geq \log n/mn$, we have

$$\mathbb{P}\left\{\left|\sum_{ij}\omega_{ij} - \rho mn\right| > \rho mn\right\} \leq n^{-3/8}. \tag{12}$$

In other words, $\| S \|_0 \leq 2\rho mn$ with high probability. Note that $\lim_{n\to\infty} \log n/mn = 0$. That means ρ can obtain very small value when n is very large. □

Theorem 8(a). *Suppose that* S *is sparse matrix with* $\mathrm{Supp}(S) \sim \mathrm{Ber}(\rho)$ *and* $Q^\perp$ *is a* p*-dimensional random subspace of* $\mathbb{R}^{m\times n}$. *If* $\rho \leq \delta^2/64p\log(mnp)$, *with high probability, one has*

$$\left\|\mathscr{P}_{Q^\perp} S\right\|_F \leq \delta\|S\|_F. \tag{13}$$

Proof. According to triangle inequality, we have

$$\begin{aligned}
\left\|\mathscr{P}_{Q^\perp} S\right\|_F &= \left\|\mathscr{P}_{Q^\perp}\left(\sum_{ij} S_{ij} e_i e_j^T\right)\right\|_F \\
&\leq \sum_{ij}\left|S_{ij}\right|\left\|\mathscr{P}_{Q^\perp} e_i e_j^T\right\|_F \\
&\leq 4\sqrt{\frac{p\log(mnp)}{mn}}\sum_{ij}\left|S_{ij}\right| \\
&\leq 2\sqrt{\rho mn}\|S\|_F\, 4\sqrt{\frac{p\log(mnp)}{mn}} \\
&\leq \sqrt{64p\rho\log(mnp)}\|S\|_F.
\end{aligned} \tag{14}$$

In the third inequality, we have used Lemma 6. In the foarth inequality, we have used Cauchy-Schwarz inequality and Lemma 7. Combining with $\rho \leq \delta^2/64p\log(mnp)$, we can obtain

$$\left\|\mathscr{P}_{Q^\perp} S\right\|_F \leq \delta\|S\|_F. \tag{15}$$

□

Theorem 8(b). *Suppose that* S *is sparse matrix with* $\mathrm{Supp}(S) \sim \mathrm{Ber}(\rho)$, *and* $Q^\perp$ *is a* p*-dimensional random subspace of* $\mathbb{R}^{m\times n}$. *If* $\rho \leq \delta^2/64p\log(mnp)$, *with high probability, one has*

$$(1-\delta)\|S\|_F \leq \left\|\mathscr{P}_Q S\right\|_F \leq (1+\delta)\|S\|_F. \tag{16}$$

Proof. For $\|\mathscr{P}_Q\| \leq 1$, we have $\|\mathscr{P}_Q S\|_F \leq \|S\|_F \leq (1+\delta)\|S\|_F$. On the other hand, we have

$$\left\|\mathscr{P}_Q S\right\|_F = \left\|S - \mathscr{P}_{Q^\perp} S\right\|_F \geq \|S\|_F - \left\|\mathscr{P}_{Q^\perp} S\right\|_F \geq (1-\delta)\|S\|_F. \tag{17}$$

□

2.2. Bounding the Behavior of $\|\mathscr{P}_{Q^\perp}(L)\|_F$.

Lemma 9 (see [7, 18]). *Suppose that* Y_d *is distributed as a chi-squared random variable with* d *degrees of freedom. Then, for each* $t > 0$

$$\mathbb{P}\left\{Y_d - d \geq t\sqrt{2d} + t^2\right\} \leq e^{-t^2/2}, \tag{18}$$

$$\mathbb{P}\left\{Y_d \leq d(1-\epsilon)\right\} \leq e^{-\epsilon^2 d/4}. \tag{19}$$

Lemma 10. *With high probability, one has*

$$\|H\|_F \geq \frac{1}{2}. \tag{20}$$

Proof. According to the definition of H, we have

$$\|H\|_F^2 = \frac{\|M\|_F^2}{mn}, \tag{21}$$

where $(M)_{ij} \sim \mathcal{N}(0.1)$. It is necessary to bound $\|M\|_F^2$. It is easy to note that $\|M\|_F^2$ is distributed as a chi-squared random variable with mn degrees of freedom. Letting $\epsilon = 3/4$, we have

$$\mathbb{P}\left\{Y_d \le mn(1-\epsilon)\right\} \le e^{-\epsilon^2 mn/4}, \tag{22}$$

where we have used (19). Equation (22) tells us: $\|M\|_F^2 \ge mn/4$ with high probability. Therefore, Lemma 9 is established. □

Lemma 11 (see [8, 9]). *Assume that* $\Omega \sim \mathrm{Ber}(\rho)$. *If* $1-\rho \ge C\epsilon^{-2}(\mu r \log n/n)$, *then with high probability*

$$\left\|\mathscr{P}_\Omega \mathscr{P}_T\right\|^2 \le \rho + \epsilon. \tag{23}$$

According to Lemma 11, if ϵ and ρ are small enough, we have the below formula with high probability

$$\left\|\mathscr{P}_\Omega \mathscr{P}_T\right\| \le \frac{1}{2}. \tag{24}$$

Lemma 12. *Under the assumption of Theorem 1, with high probability, one has*

$$\|L\|_F + \|S\|_F \le 5\|M\|_F. \tag{25}$$

Proof. Note that $L \in T$, and we have

$$\begin{aligned}\left\|\mathscr{P}_\Omega L\right\|_F^2 &= \left\|\mathscr{P}_\Omega \mathscr{P}_T L\right\|_F^2 \\ &\le \frac{1}{4}\|L\|_F^2 \\ &= \frac{1}{4}\left(\left\|\mathscr{P}_\Omega L\right\|_F^2 + \left\|\mathscr{P}_{\Omega^\perp} M\right\|_F^2\right).\end{aligned} \tag{26}$$

In the first inequality, we have used Lemma 11. In the second equality, we have used $\mathscr{P}_{\Omega^\perp} L = \mathscr{P}_{\Omega^\perp} M$, because $S \in \Omega$. It is obvious that

$$\left\|\mathscr{P}_\Omega L\right\|_F \le \frac{\sqrt{3}}{3}\left\|\mathscr{P}_{\Omega^\perp} M\right\|_F. \tag{27}$$

Therefore,

$$\begin{aligned}\|L\|_F &\le \left\|\mathscr{P}_\Omega L\right\|_F + \left\|\mathscr{P}_{\Omega^\perp} L\right\|_F \\ &\le \frac{\sqrt{3}}{3}\left\|\mathscr{P}_{\Omega^\perp} M\right\|_F + \left\|\mathscr{P}_{\Omega^\perp} M\right\|_F \\ &\le \frac{5}{3}\|M\|_F.\end{aligned} \tag{28}$$

And thus, we can obtain

$$\begin{aligned}\|L\|_F + \|S\|_F &= \|L\|_F + \|M - L\|_F \\ &\le 2\|L\|_F + \|M\|_F \\ &\le 5\|M\|_F.\end{aligned} \tag{29}$$

Lemma 12 is established. □

Next, we will bound the behavior of $\left\|\mathscr{P}_{Q^\perp}(L)\right\|_F$, based on Lemma 9 to Lemma 12.

Theorem 13(a). *Suppose that L be r-rank matrix and* $Q^\perp$ *is a p-dimensional random subspace of* $\mathbb{R}^{n\times n}$. *If* $r \le (mn\delta^2/12p) - (5/3)\log(n)$, *with high probability, one has*

$$\left\|\mathscr{P}_{Q^\perp} L\right\|_F \le \delta\|L\|_F. \tag{30}$$

As pointed out by one reviewer, Lemma 15 in [10] is similar to Theorem 13(a). Lemma 15 in [10] tells us (30) is established if $r \le n\delta^2/p\upsilon$; however it is obvious that r is strongly based on υ which is defined as if there exists an orthonormal basis $\{G_i\}$ for L satisfying $\max_i \|G_i\|^2 \le \upsilon/n$, which is very difficult to compute. The condition of r in Theorem 13(a) is just based on m, n, p, and δ, which is easy to determine.

Proof. According to the definition of $Q^\perp$, we have

$$\left\|\mathscr{P}_{Q^\perp} L\right\|_F = \sqrt{\sum_{k=1}^{p}\left|\langle G_k, L\rangle\right|^2} \le \sqrt{p}\max_k\left|\langle G_k, L\rangle\right|, \tag{31}$$

where $G_1, G_2, \ldots, G_k$ are independent and identically distributed to G mentioned before. According to (31), it is necessary to bound $|\langle G, L\rangle|$. Suppose that $U\Sigma V^T$ is singular value decomposition of matrix L; that is, $L = U\Sigma V^T = \sum_{l=1}^{r}\sigma_l u_l v_l^T$. Therefore, according to triangle inequality, we have

$$\begin{aligned}|\langle G, L\rangle| &\le \sum_{l=1}^{r}\sigma_l\left|\left\langle G, u_l v_l^T\right\rangle\right| \\ &= \sum_{l=1}^{r}\sigma_l\left|u_l^T G v_l\right| \\ &\le \sqrt{\sum_{l=1}^{r}\sigma_l^2}\sqrt{\sum_{l=1}^{r}\left(u_l^T G v_l\right)^2} \\ &= \frac{\|L\|_F}{\|H\|_F\sqrt{mn}}\sqrt{\sum_{l=1}^{r}\left(u_l^T M v_l\right)^2} \\ &\le \frac{2\|L\|_F}{\sqrt{mn}}\sqrt{\sum_{l=1}^{r}\left(u_l^T M v_l\right)^2},\end{aligned} \tag{32}$$

where u_l, v_l are the lth rows of U, V, respectively. In the second inequality, we have used Cauchy-Schwarz inequality. In the last inequality, we have used Lemma 10. Let $y_l := u_l^T M v_l = \sum_{ij} u_{li} m_{ij} v_{lj}$; note that

$$\begin{aligned}\mathbb{E}\left\{y_l\right\} &= \sum_{ij} u_{li} v_{lj}\mathbb{E}\left\{m_{ij}\right\} = 0, \\ \mathrm{Var}\left\{y_l\right\} &= \sum_{ij}\mathrm{Var}\left\{u_{li} v_{lj} m_{ij}\right\} \\ &= \sum_{ij} u_{li}^2 v_{lj}^2\,\mathrm{Var}\left\{m_{ij}\right\} = 1,\end{aligned} \tag{33}$$

where we have used the fact $\sum_i u_{li}^2 = 1$ and $\sum_j v_{lj}^2 = 1$. In other word $y_l \sim \mathcal{N}(0,1)$. Let $z := \sum_{l=1}^r (u_l^T M v_l)^2 = \sum_{l=1}^r y_l^2$. It is obvious that z is distributed as a chi-squared random variable with r degrees of freedom.

According to Lemma 9, letting $t = 2\sqrt{\log n}$, we can obtain

$$\mathbb{P}\left(Y_d \geq d + 2\sqrt{\log n}\sqrt{2d} + 4\log n\right) \leq n^{-2}. \tag{34}$$

It implies that with high probability

$$Y_d \leq d + 2\sqrt{\log n}\sqrt{2d} + 4\log n. \tag{35}$$

That is, with high probability

$$z \leq r + 2\sqrt{\log n}\sqrt{2r} + 4\log n. \tag{36}$$

Combining with (31), (32), and (36), with high probability, we can obtain

$$\begin{aligned}\left\|\mathscr{P}_{Q^\perp} L\right\|_F &\leq \frac{2\sqrt{p}\|L\|_F}{\sqrt{mn}}\sqrt{r + 2\sqrt{\log n}\sqrt{2r} + 4\log n} \\ &\leq \frac{2\sqrt{p}\|L\|_F}{\sqrt{mn}}\sqrt{3r + 5\log n},\end{aligned} \tag{37}$$

where we have used the fact: if $a, b \geq 0$, $2\sqrt{ab} \leq a + b$. Let

$$\frac{2\sqrt{p}}{\sqrt{mn}}\sqrt{3r + 5\log n} \leq \delta. \tag{38}$$

That is,

$$r \leq \frac{mn\delta^2}{12p} - \frac{5}{3}\log(n). \tag{39}$$

Theorem 13(a) is established. □

Theorem 13(b). *Suppose that L is μ-incoherent matrix and $Q^\perp$ is a p-dimensional random subspace of $\mathbb{R}^{n\times n}$. If $r \leq (mn\delta^2/12p) - (5/3)\log(n)$, with high probability, one has*

$$(1-\delta)\|L\|_F \leq \left\|\mathscr{P}_Q L\right\|_F \leq (1+\delta)\|L\|_F. \tag{40}$$

Proof. The main idea of the proof follows the arguments of Theorem 8(b). □

Proof of Theorem 4. According to Theorems 8 and 13 and the assumption of Lemma 3, we have

$$\begin{aligned}\left\|\mathscr{P}_{Q^\perp} L\right\|_F &\leq \delta\|L\|_F, \\ \left\|\mathscr{P}_{Q^\perp} S\right\|_F &\leq \delta\|S\|_F.\end{aligned} \tag{41}$$

Therefore,

$$\begin{aligned}\left\|\mathscr{P}_{Q^\perp}(L+S)\right\|_F &\leq \left\|\mathscr{P}_{Q^\perp} L\right\|_F + \left\|\mathscr{P}_{Q^\perp} S\right\|_F \\ &\leq \delta\left(\|L\|_F + \|S\|_F\right) \\ &\leq 5\delta\|M\|_F.\end{aligned} \tag{42}$$

Then,

$$\begin{aligned}\left\|\mathscr{P}_Q M\right\|_F &= \left\|M - \mathscr{P}_{Q^\perp} M\right\|_F \\ &\geq \|M\|_F - \left\|\mathscr{P}_{Q^\perp} M\right\|_F \\ &\geq (1-5\delta)\|M\|_F.\end{aligned} \tag{43}$$

Theorem 4 is established. □

3. Conclusion

In this paper, we address the problem of principal component pursuit with reduced linear measurements (PCP_RLM). In order to obtain an easy handed band of τ, we prove that operator $\mathscr{P}_Q$ obeys RIP with high probability if the low-rank matrix satisfies incoherent conditions and the sparse matrix is enough sparse. And then, based on the RIP of operator $\mathscr{P}_Q$, we provide the bound of parameters depending only on observed quantities. In the future, we will try to analyze the robustness of optimum solution of the strongly convex programming (1) with RIP property.

Acknowledgments

The authors would like to thank the anonymous reviewers for their comments that helped to improve the quality of the paper. This research was supported by the National Natural Science Foundation of China (NSFC) under Grant 61172140, and "985" Key Projects for the excellent teaching team support (postgraduate) under Grant A1098522-02. Haiwen Xu is supported by Joint Fund of the National Natural Science Foundation of China and the Civil Aviation Administration of China (Grant no. U1233105).

References

[1] J. Ellenberg, "Fill in the blanks: using math to turn lo-res datasets into hi-ressamples," http://www.wired.com/magazine/2010/02/ff_algorithm/.

[2] A. Chambolle and P.-L. Lions, "Image recovery via total variation minimization and related problems," *Numerische Mathematik*, vol. 76, no. 2, pp. 167–188, 1997.

[3] J. F. Claerbout and F. Muir, "Robust modeling of erratic data," *Geophysics*, vol. 38, pp. 826–844, 1973.

[4] B. Zeng and J. Fu, "Directional discrete cosine transforms—a new framework for image coding," *IEEE Transactions on Circuits and Systems for Video Technology*, vol. 18, no. 3, pp. 305–313, 2008.

[5] M. Elad and M. Aharon, "Image denoising via sparse and redundant representations over learned dictionaries," *IEEE Transactions on Image Processing*, vol. 15, no. 12, pp. 3736–3745, 2006.

[6] H. Ji, C. Q. Liu, Z. W. Shen, and Y. Xu, "Robust video denoising using Low rank matrix completion," in *Proceedings of the IEEE Computer Society Conference on Computer Vision and Pattern Recognition (CVPR '10)*, pp. 1791–1798, June 2010.

[7] E. J. Candès and B. Recht, "Exact matrix completion via convex optimization," *Foundations of Computational Mathematics*, vol. 9, no. 6, pp. 717–772, 2009.

[8] E. J. Candès, X. Li, Y. Ma, and J. Wright, "Robust principal component analysis?" *Journal of the ACM*, vol. 58, no. 3, article 11, 2011.

[9] Z. Zhou, X. Li, J. Wright, E. Candès, and Y. Ma, "Stable principal component pursuit," in *Proceedings of the IEEE International Symposium on Information Theory (ISIT '10)*, pp. 1518–1522, June 2010.

[10] A. Ganesh, K. Min, J. Wright, and Y. Ma, "Principal component pursuit with reduced linear measurements," *IEEE International Symposium on Information Theory Proceedings*, pp. 1281–1285, 2012.

[11] J. Wright, A. Ganesh, K. Min, and Y. Ma, "Compressive principal component pursuit," *IEEE International Symposium on Information Theory Proceedings*, pp. 1276–1280, 2012.

[12] H. Zhang, J.-F. Cai, L. Cheng, and J. Zhu, "Strongly convex programming for exact matrix completion and robust principal component analysis," *Inverse Problems and Imaging*, vol. 6, no. 2, pp. 357–372, 2012.

[13] B. Recht, M. Fazel, and P. A. Parrilo, "Guaranteed minimum-rank solutions of linear matrix equations via nuclear norm minimization," *SIAM Review*, vol. 52, no. 3, pp. 471–501, 2010.

[14] Q. S. You, Q. Wan, and Y. P. Liu, "A short note on strongly convex programming for exact matrix completion and robust principal component analysis," *Inverse Problems and Imaging*, vol. 7, no. 1, pp. 305–306, 2013.

[15] Q. S. You and Q. Wan, "Strongly convex programming for principal component pursuit," http://arxiv.org/abs/1209.4405.

[16] R. Meka, P. Jain Inderjit, and S. Dhillon, "Guaranteed rank minimization via singular value projection," in *Neural Information Processing Systems*, 2010.

[17] L. Mackey, M. I. Jordan, R. Y. Chen, B. Farrell, and J. A. Tropp, "Matrix concentration inequalities via the method of exchangeable Pairs," http://arxiv.org/abs/1201.6002.

[18] B. Laurent and P. Massart, "Adaptive estimation of a quadratic functional by model selection," *The Annals of Statistics*, vol. 28, no. 5, pp. 1302–1338, 2000.

Hindawi Publishing Corporation
Journal of Applied Mathematics
Volume 2013, Article ID 249726, 7 pages
http://dx.doi.org/10.1155/2013/249726

Research Article

Fuzzy Multiobjective Traffic Light Signal Optimization

N. Shahsavari Pour, H. Asadi, and M. Pour Kheradmand

Department of Industrial Engineering, Science and Research Branch, Islamic Azad University, Kerman, Iran

Correspondence should be addressed to H. Asadi; hamed_assadi2000@yahoo.com

Received 18 September 2012; Revised 26 March 2013; Accepted 9 April 2013

Academic Editor: Zhiping Qiu

Copyright © 2013 N. Shahsavari Pour et al. This is an open access article distributed under the Creative Commons Attribution License, which permits unrestricted use, distribution, and reproduction in any medium, provided the original work is properly cited.

Traffic congestion is a major concern for many cities throughout the world. In a general traffic light controller, the traffic lights change at a constant cycle time. Hence it does not provide an optimal solution. Many traffic light controllers in current use are based on the "time-of-the-day" scheme, which use a limited number of predetermined traffic light patterns and implement these patterns depending upon the time of the day. These automated systems do not provide an optimal control for fluctuating traffic volumes. In this paper, the fuzzy traffic light controller is used to optimize the control of fluctuating traffic volumes such as oversaturated or unusual load conditions. The problem is solved by genetic algorithm, and a new defuzzification method is introduced. The performance of the new defuzzification method (NDM) is compared with the centroid point defuzzification method (CPDM) by using ANOVA. Finally, an illustrative example is presented to show the competency of proposed algorithm.

1. Introduction

Delays in urban road networks depend largely on the performance of the networks' signalled Intersections. Traffic congestion is one of the challenging problems in many countries. Traffic congestion wastes a huge portion of the national income for fuel and traffic-related environmental and socioeconomic problems. One of the major problems is the oversaturated network conditions, especially during peak hours.

In urban networks the flow is controlled by traffic lights, and traffic engineers are often faced with the question if the capacity of the networks is exploited by the chosen control strategy. One possible method to answer such questions could be the use of vehicular traffic models in control systems as well as in the planning and design of transportation networks. For almost half a century there were strong attempts to develop a theoretical framework for traffic science.

As is known to all, the main places responsible for traffic congestion are urban intersections, and the primary reason for traffic congestion in urban intersections is the irrational cycle time of traffic lights. In order to separate the conflict of the traffic flow effectively and improve traffic capacity, how to assign the red and green time in a cycle is obviously important.

Generally, longer cycle time leads to greater traffic capacity, but traffic queue and number of pedestrians also increase with increasing the cycle time. In other words, when the saturation of an intersection is small enough, the increase of the cycle time does not go far enough towards traffic capacity, and it only leads to the increase of traffic queue and number of pedestrians.

Even though Bayley [1] showed that long cycle times have negative impacts on pedestrian delays, current policies for traffic signal control still consider primarily vehicle delays. Noland [2, 3] showed with London data for small networks that extending pedestrian green times could reduce total delays at a junction. Traffic signals generally aim at minimizing average vehicle delays, while pedestrian delays are not taken into account. Such strategy is reasonable for rural areas or highways where very few pedestrians interfere with vehicular traffic. However, in a central business district with a lot of pedestrians walking around, the strategy that optimizes only vehicle flows would not be suitable because the pedestrian delays are ignored. Ignoring pedestrian delays might even result in people choosing to use vehicles more frequently than walking. So, it is reasonable that pedestrian signal plans be also optimized.

In this paper, the pedestrians' waiting time does not have any costs for the system, but reducing it will result in increase of the citizens' satisfaction.

Brockfeld and his colleagues [4] focused on global traffic light control strategies and tried to find optimal model parameters in order to maximize the network flows. Gradinescu and his colleagues [5] studied traffic control system using wireless communications, where the vehicles send information to the nearby traffic control system, and then the system will optimize the traffic lights based on the received information. Teo et al. [6] used genetic algorithm to optimize the total green time of all traffic lights at intersections and split of the traffic flows.

Webster [7] pioneered the use of computer simulation to analyse traffic patterns and chose to set traffic light cycle length and cycle splits to improve traffic flow. Yang [8] developed an effective procedure to optimize intersection signal timing by minimizing total delay for both vehicles and pedestrians.

Dong et al. [9] developed simulated annealing particle swarm optimization (Sa-PSO) algorithm based on particle swarm optimization (PSO) and simulation was carried out in a nine-intersection network, and the result shows that the use of Sa-PSO method can reduce 41.0% of the average delay per vehicle and 30.6% of the average stop rates compared with fixed time plans. But the research of Sa-PSO was just at the beginning; there were still so much problems for further study.

Also there are certain systems that take advantage of sensors to detect the incoming vehicles and use fuzzy theory to make decisions for extending the green light periods to let more vehicles pass through [10]. Favilla et al. [11] applied fuzzy theory to control of two-way streets. The number of vehicles that have already passed during green time and the length of the traffic queue during red time are used as inputs to the fuzzy rules; the output of the rules is the amount of extension to be applied to the current signal state. They also proposed additional strategies for adopting the numerical bounds on the input and output variables. The concept of pedestrian progression was also proposed in some researches.

The average pedestrian delays model is proposed in "Pedestrian compliance effects on signal delay" by Virkler, based on the assumption that all pedestrians arrive randomly, which means pedestrians who arrive in green enter the intersection without any delay, and pedestrian flow arrives uniformly in red. It is also assumed in the model that the cycle length is constant, and no pedestrian actuation is applied in the intersection [12].

Chilukuri and Virkler [13] proved that the pedestrian delays calculation which assumes random arrivals might not be accurate in a coordinated arterial. Bhattacharya and Virkler [14] studied cyclic flow profiles generated from arrival patterns and developed a method to estimate the delay from the offset with respect to the upstream signal cycle. Then, they used the method to determine favorable signal offsets for pedestrian progression.

In this paper, we present a new fuzzy multiobjective mathematical model to minimize the length of traffic queue and pedestrian delays.

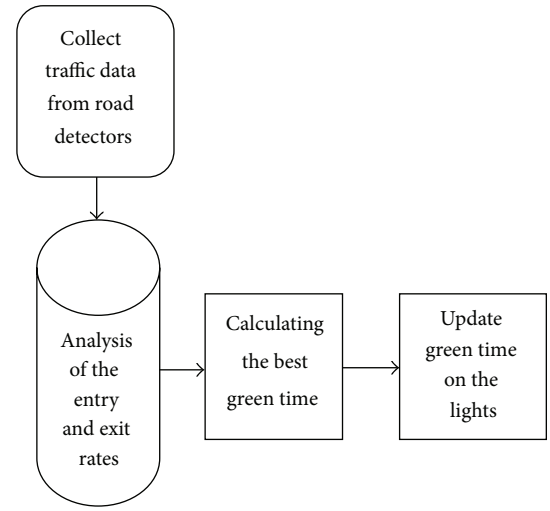

Figure 1: Scheme of traffic optimization process using data collected from road detectors.

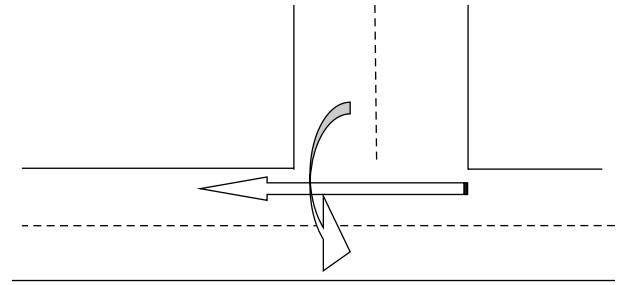

Figure 2: A "two-phase intersection."

The paper is organized as follows. In Section 2, the problem definition is provided. In Section 3 a new defuzzification method is introduced. This is followed by the problem formulation in Section 4. An illustrative example is provided in Section 5; then, in Section 6, experimental evaluation is provided to show the competency of algorithm. Section 7 then concludes this paper.

2. Problem Description

The problem discussed in this paper is minimizing the queue length on each side of the intersection during peak hours with considering the entrance and exit rates of each side of the intersection as fuzzy rates.

This study is to calculate green time duration in order to minimize traffic jam length. Before beginning the optimization process, road detector should gather related data of intersection traffic. This data are required to make a decision if current conditions are sufficient or they have to be improved (see Figure 1).

Queue length is the total number of vehicles that line up in front of the intersection waiting to be given the permission for passing the intersection. At each intersection, the side that the traffic flows in is called "phase." For example, in Figure 2 there are two phases at intersection.

Amber is the signal appearing between the red and green signal, indicating a warning to the traffic flow to slow down as the green signal is going to be ended.

At first, a sensitivity analysis is done on the traffic light at a two-phase intersection, and then it is developed for a four-phase traffic problem.

When phase I has red time (T1), traffic jam length in this phase has an increasing rate. On the contrary, traffic jam length of phase II—experiencing green time—has a decreasing rate. Red time in each phase is sum of green time in other phases which increases as green time devoted to each phase increases. Therefore, jam length in other phases may also increase.

The pedestrians' queue length has an incremental rate and at the end of the green time reaches its highest level (points A1 and A2). As soon as intersection's red time starts, all pedestrians cross the intersection immediately. As a result, pedestrians' queue is equal to zero (see Figure 3).

2.1. Fuzzy Entry and Exit Rate. Since entrance/exit rate of traffic jams at an intersection in a traffic network is uncertain, it is necessary to consider it in an uncertainty condition. One of the best tools to take this uncertainty into account is fuzzy theory.

Definition 1 (fuzzy sets and membership functions). If X is a collection of objects denoted generically by x, then a fuzzy set A in X is defined to be a set of ordered pairs $A = \{(x, \mu_{\widetilde{A}}(x)) \mid x \in X\}$, where $\mu_{\widetilde{A}}(x)$ is called the membership function for the fuzzy set. The membership function maps each element of X to a membership value between 0 and 1.

Definition 2. The triangular fuzzy numbers can be denoted as $\widetilde{A} = (a_1, a_2, a_3)$, where a_2 is the central value (if $\mu_{\widetilde{A}}(a_2) = 1$ then $\widetilde{A}$ is a normal fuzzy number) (see Figure 4). The membership function of such triangular fuzzy number is defined as

$$\mu_{\widetilde{A}}(x) = \begin{cases} 0 & x \le a_1, \\ \dfrac{x - a_1}{a_2 - a_1} & a_1 < x \le a_2, \\ \dfrac{a_3 - x}{a_3 - a_2} & a_2 < x \le a_3, \\ 0 & x > a_3. \end{cases} \tag{1}$$

Let $\widetilde{A}$ and $\widetilde{B}$ be two triangular fuzzy numbers (TFN) parameterized by the triplets (a_1, a_2, a_3), and (b_1, b_2, b_3) respectively, then the operational rules of these two triangular fuzzy numbers are as follows:

$$\begin{aligned} \widetilde{A}(+)\widetilde{B} &= (a_1 + b_1, a_2 + b_2, a_3 + b_3), \\ \widetilde{A}(-)\widetilde{B} &= (a_1 - b_1, a_2 - b_2, a_3 - b_3), \\ \widetilde{A}(\times)\widetilde{B} &= (a_1 \cdot b_1, a_2 \cdot b_2, a_3 \cdot b_3). \end{aligned} \tag{2}$$

Entrance/exit rate is considered in terms of triangular fuzzy numbers, and a new defuzzification method is presented for division of two fuzzy numbers.

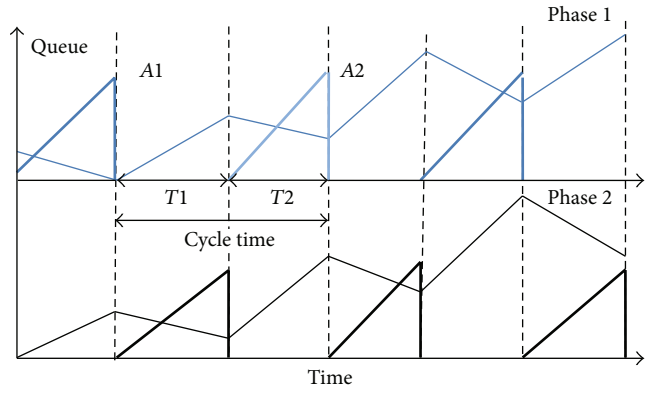

Figure 3: Sensitivity analysis for two-phase intersection.

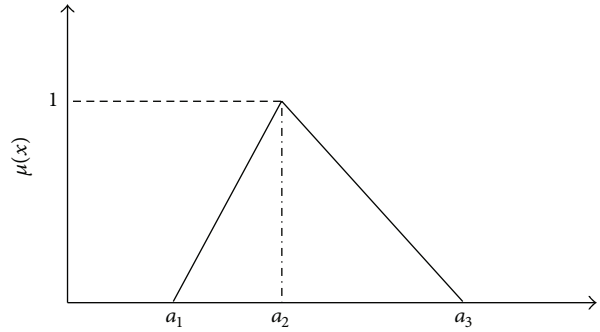

Figure 4: A triangular fuzzy number $\widetilde{A}$.

3. New Defuzzification Method

Defuzzification and ranking fuzzy numbers are complex and challenging. This is because fuzzy numbers, usually represented by possibility distributions, can often overlap each other in many practical situations. It is difficult, if not impossible, to clearly determine whether one fuzzy number is larger or smaller than another, in particular when these two fuzzy numbers are similar to each other. As a result, defuzzification and ranking of fuzzy numbers are critical problems in fuzzy decision making.

Defuzzication methods have been widely studied for some years and were applied to fuzzy control and fuzzy expert systems [15, 16]. The major idea behind these methods was to obtain a typical value from a given fuzzy set according to some specified characters, such as central gravity and median. In other words, each defuzzication method provides a correspondence from the set of all fuzzy sets into the set of real numbers [17].

There may be situations where the output of a fuzzy process needs to be a crisp set. Defuzzification is the conversion of a fuzzy quantity to a precise quantity, just as fuzzification is the conversion of a precise quantity to a fuzzy quantity. Among the many methods that have been proposed in recent years, seven are described here for defuzzifying the output of fuzzy functions (membership functions) [18].

In this section we present a new defuzzification method that is used in fitness function of the GA.

The centroid point of a fuzzy number corresponds to $\overline{x}$ value on the horizontal axis and $\overline{y}$ value on the vertical axis. Suppose $\widetilde{A}_1, \widetilde{A}_2, \widetilde{A}_3, \ldots, \widetilde{A}_n$ are triangular fuzzy numbers. First we calculate the gravity center of all numbers (e.g., if $\widetilde{A}_i$ is a fuzzy number, the center of its gravity will be $(\widetilde{x}_{A_i}, \widetilde{y}_{A_i})$). We calculate the distance of gravity center of all fuzzy numbers from three points $(a_1(\widetilde{A}_i), a_2(\widetilde{A}_i), a_3(\widetilde{A}_i))$ as follows:

$$
\begin{aligned}
L1\left(\widetilde{A}_i\right) &= \sqrt{\left(\widetilde{x}_{A_i} - a_1\left(\widetilde{A}_i\right)\right)^2 + \left(\widetilde{y}_{A_i} - \mu_{(a_2)}\right)^2},\\
L2\left(\widetilde{A}_i\right) &= \sqrt{\left(\widetilde{x}_{A_i} - a_2(\widetilde{A}_i)\right)^2 + \left(\widetilde{y}_{A_i} - \mu_{(a_2)}\right)^2},\\
L3\left(\widetilde{A}_i\right) &= \sqrt{\left(\widetilde{x}_{A_i} - a_3\left(\widetilde{A}_i\right)\right)^2 + \left(\widetilde{y}_{A_i} - \mu_{(a_2)}\right)^2}.
\end{aligned}
\tag{3}
$$

Defuzzification value of fuzzy number $\widetilde{A}_i$ is calculated via the following equation:

$$
\begin{aligned}
R\left(\widetilde{A}_i\right) = {} & w_{a_1} \times L1\left(\widetilde{A}_i\right) \times a_1\left(\widetilde{A}_i\right) + w_{a_2} \times L2\left(\widetilde{A}_i\right)\\
& \times a_2\left(\widetilde{A}_i\right) + w_{a_3} \times L3\left(\widetilde{A}_i\right) \times a_3\left(\widetilde{A}_i\right)\\
& \times \left(w_{a_1} \times L1\left(\widetilde{A}_i\right) + w_{a_2} \times L2\left(\widetilde{A}_i\right)\right.\\
& \left. + w_{a_3} \times L3\left(\widetilde{A}_i\right)\right)^{-1},
\end{aligned}
\tag{4}
$$

where w_{a_1}, w_{a_2}, and w_{a_3} are the planner-specified weights. They indicate the relative importance of a_1, a_2, and a_3 for manager in defuzzification procedure. The values of weight coefficients w_{a_1}, w_{a_2}, and w_{a_3} are subjectively selected in the range of $[0, 1]$, and they should satisfy the equation $w_{a_1} + w_{a_2} + w_{a_3} = 1.0$.

If $\widetilde{A}_1$, $\widetilde{A}_2$ are two fuzzy numbers then the ranking will be performed as follows:

$$
\begin{aligned}
&(1)\ \text{if } R\left(\widetilde{A}_1\right) > R\left(\widetilde{A}_2\right) \text{ then } \widetilde{A}_1 > \widetilde{A}_2;\\
&(2)\ \text{if } R\left(\widetilde{A}_1\right) = R\left(\widetilde{A}_2\right) \text{ then } \widetilde{A}_1 \cong \widetilde{A}_2;\\
&(3)\ \text{if } R\left(\widetilde{A}_1\right) < R\left(\widetilde{A}_2\right) \text{ then } \widetilde{A}_1 < \widetilde{A}_2.
\end{aligned}
\tag{5}
$$

3.1. Example. Consider the two fuzzy numbers

$$
\begin{aligned}
&\widetilde{A} = (1, 2, 6), \qquad \widetilde{B} = (1, 3, 6),\\
&\left(w_{A_1} = .25,\ w_{A_2} = .5,\ w_{A_3} = .25\right).
\end{aligned}
\tag{6}
$$

By using the proposed method we have

$$
R\left(\widetilde{A}\right) = 3.367, \qquad R\left(\widetilde{B}\right) = 3.532, \qquad \widetilde{A}\,(\div)\,\widetilde{B} = .9534.
\tag{7}
$$

Hence the ranking order is $\widetilde{B} > \widetilde{A}$.

4. Problem Formulation

Notations used for the problem formulation are as follows.

i: The number of phases in intersection.

L_i: The Lower bound of the green time in phase i.

U_i: The upper bound of the green time in phase i.

TS: The studied period of time.

TR_i: The red time duration in phase i.

TG_i: The green time duration in phase i.

CT_i: The cycle time duration in phase i.

NCT_i: Number of cycles in the TS.

$\widetilde{\mathrm{QR}}_{(i,j)}$: The fuzzy queue length when red time duration in phase i and jth cycle time ends.

$\widetilde{\mathrm{QG}}_{(i,j)}$: The fuzzy queue length when green time duration in phase i and jth cycle time ends.

$\widetilde{\mathrm{TIR}}_i$: The fuzzy entrance rate of cars during red time in phase i.

$\widetilde{\mathrm{TIG}}_i$: The fuzzy entrance rate of cars during green time in phase i.

$\widetilde{\mathrm{TOG}}_i$: The fuzzy exit rate during green time in phase i.

$\mathrm{N}\widetilde{\mathrm{TIR}}_i$: The fuzzy entrance cars during red time in phase i.

$\mathrm{N}\widetilde{\mathrm{TIG}}_i$: The fuzzy entrance cars during green time in phase i.

$\mathrm{N}\widetilde{\mathrm{TOG}}_i$: The fuzzy exit cars during green time in phase i.

$\widetilde{\mathrm{TIP}}_i$: The fuzzy entrance rate of pedestrians during red time in phase i.

$\mathrm{N}\widetilde{\mathrm{TIP}}_i$: The fuzzy entrance pedestrians during red time in phase i.

The problem is formulated as the following model:

$$
\begin{aligned}
\operatorname{Min} Q1 = \sum_{i=1}^{n} & \left(\mathrm{N}\widetilde{\mathrm{TIR}}_i + \left(\mathrm{N}\widetilde{\mathrm{CT}}_i - 1\right)\right.\\
& \left. \times \left(\mathrm{N}\widetilde{\mathrm{TIR}}_i + \mathrm{N}\widetilde{\mathrm{TIG}}_i - \mathrm{N}\widetilde{\mathrm{TOG}}_i\right)\right),
\end{aligned}
\tag{8}
$$

$$
\operatorname{Min} Q2 = \sum_{i=1}^{n} \left(\widetilde{\mathrm{TIP}}_i \times \mathrm{TR}_i\right)
\tag{9}
$$

subject to

$$L_i \le \mathrm{TG}_i \le U_i, \tag{10}$$

$$\mathrm{TR}_i = \left(\sum_{i=1}^{n} \mathrm{TG}_i\right) - \mathrm{TG}_i \quad \forall i,\ i = 1, 2, \ldots, n, \tag{11}$$

$$\mathrm{N\widetilde{TIR}}_i = \widetilde{\mathrm{TIR}}_i \times \mathrm{TR}_i \quad \forall i,\ i = 1, 2, \ldots, n, \tag{12}$$

$$\mathrm{N\widetilde{TIG}}_i = \widetilde{\mathrm{TIG}}_i \times \mathrm{TG}_i \quad \forall i,\ i = 1, 2, \ldots, n, \tag{13}$$

$$\mathrm{N\widetilde{TOG}}_i = \widetilde{\mathrm{TOG}}_i \times \mathrm{TG}_i \quad \forall i,\ i = 1, 2, \ldots, n, \tag{14}$$

$$\mathrm{CT}_i = \mathrm{TR}_i + \mathrm{TG}_i \quad \forall i,\ i = 1, 2, \ldots, n, \tag{15}$$

$$\mathrm{NCT}_i = \frac{\mathrm{TS}}{\mathrm{CT}_i} \quad \forall i,\ i = 1, 2, \ldots, n, \tag{16}$$

$$\widetilde{\mathrm{QR}}_{(i,j)} = \widetilde{\mathrm{QG}}_{(i,j-1)} + \mathrm{N\widetilde{TIR}}_i \quad \forall i,\ i = 1, 2, \ldots, n. \tag{17}$$

Equation (8) minimizes the total length of traffic queue in all phases of the intersection, and (9) minimizes the total length of pedestrian queue in all phases of the intersection. Equation (10) restricts green time per phase to take a value within a lower bound L_i and an upper bound U_i. Equation (11) represents the red time duration in phase i, and (12) represents the fuzzy entrance rate of cars during red time duration in phase i.

Equation (13) represents the fuzzy rate of entering cars during green time in Phase i. Equation (14) represents the fuzzy rate of leaving cars during green time in phase i. Equation (15) shows that the cycle time duration per phase is equal to the sum of green and red time. Equation (16) represents the number of cycle times per phase. The fuzzy queue length when green time duration in phase i and jth cycle times end will be calculated through (16). If the last cycle time duration in the studied period of time (TS) is equal to m, the objective function in (8) minimizes the $\widetilde{\mathrm{QR}}_{(i,m)}$.

4.1. Genetic Algorithms for Problem Solving. In this paper, the genetic algorithm is used to optimize the cycle time of the traffic light systems.

4.1.1. Fitness Function. We have fuzzy multiobjective function. In this case, to determine the fitness function ($F_{(s)}$) and the probability of selection ($P_{(s)}$) for each parent chromosome "S", initially, we should defuzzify the fuzzy values obtained by (8) and (9) by using the new defuzzification Method described in Section 3. Then, using the following equations, we can determine the ($F_{(s)}$) and ($P_{(s)}$):

$$F_{(s)} = w_v \times \frac{Q1_s - Q1_{\min}}{Q1_{\max} - Q1_{\min}} + w_p \times \frac{Q2_s - Q2_{\min}}{Q2_{\max} - Q2C_{\min}}, \tag{18}$$

$$P_{(s)} = \frac{\left(\sum_{s=1}^{N} F_{(s)}\right)/F_{(s)}}{\sum_{s=1}^{N}\left(\left(\sum_{s=1}^{N} F_{(s)}\right)/F_{(s)}\right)}, \tag{19}$$

where w_v and w_p are the planner-specified weights. They indicate the relative importance of vehicles queue cost and pedestrians' queue cost, respectively. The values of weight coefficients w_v and w_p are subjectively selected in the range $[0, 1]$ by project managers, and they should satisfy the equation $w_v + w_p = 1.0$ [19].

$Q1_{\max}$, $Q1_{\min}$, $Q2_{\max}$, and $Q2_{\min}$ are the maximal and minimal values of the length of traffic and pedestrian queues in the current population. As chromosomes with lower $F_{(s)}$ are more desirable, $P_{(s)}$ should be so defined that the probability of selecting chromosome "S" with lower $F_{(s)}$ is more than other chromosomes. So, equation (19) is introduced for $P_{(s)}$.

4.1.2. Genetic Operators. In this study to produce offsprings from parents for entering the next generation, we used one-point crossover and one-point mutation. For instance, in an intersection with two phases, two random chromosomes with feasible genes can be as follows:

Parent 1 = [**0**, **1**, **1**, **1**, **0**, **0**, **1**, **0**, **0**, 1, 1, 0, 0, 0].

Parent 2 = [**1**, **1**, **0**, **0**, **1**, **1**, **1**, **1**, **0**, 0, 1, 1, 0, 1].

The offsprings produced from these parents are as follows: ONE-cut-point crossover with random points ($e_1 = 9$)

Offspring 1 = [**0**, **1**, **1**, **1**, **0**, **0**, **1**, **0**, **0**, 0, 1, 1, 0, 1].

Offspring 2 = [**1**, **1**, **0**, **0**, **1**, **1**, **1**, **1**, **0**, 1, 1, 0, 0, 0].

One-point mutation with random points ($e_1 = 6$)

Parent = [0, 1, 1, 1, 0, **0**, 1, 0, 0, 1, 1, 0, 0, 0].

Offspring = [0, 1, 1, 1, 0, **1**, 1, 0, 0, 1, 1, 0, 0, 0].

It should be mentioned that the mutation rate ($\mathrm{Fm}_{(g)}$) (g is number of generations) decreases with increasing repetition, (20); so, in the final generation, the mutation rate will be zero:

$$\mathrm{Fm}_{(g)} = \frac{\mathrm{Fm}_{(g-1)}}{g}. \tag{20}$$

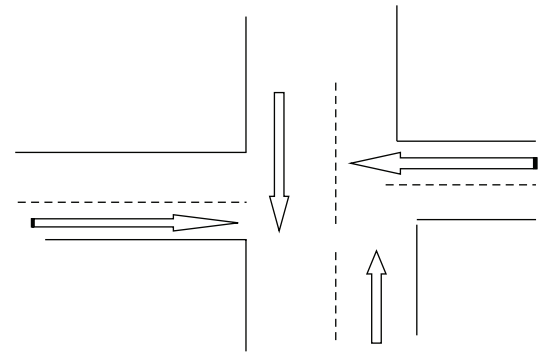

Figure 5: An intersection in a traffic network with four phases.

5. Illustrative Example

We considered an intersection, formed by four phases, in a network (see Figure 5).

As an example, an intersection consisting of four phases is presented in this section as depicted in Figure 5. The model

Table 1: The fuzzy entry and exit rates per phase of intersection.

	$\widetilde{\mathrm{TIR}}_i$ (vehicle/second)	$\widetilde{\mathrm{TIG}}_i$ (vehicle/second)	$\widetilde{\mathrm{TOG}}_i$ (vehicle/second)	$\widetilde{\mathrm{TIP}}_i$ (man/second)
Phase 1	(5, 7, 8)	(5, 7, 8)	(1, 2, 3)	(5, 6, 7)
Phase 2	(2, 3, 4)	(2, 3, 4)	(3, 4, 5)	(11, 12, 13)
Phase 3	(6, 7, 8)	(6, 7, 8)	(6, 7, 9)	(13, 14, 15)
Phase 4	(3, 4, 5)	(3, 4, 5)	(4, 5, 6)	(8, 10, 12)

Table 2: Final outputs of the GA.

w_v	w_p	w_{a_1}	w_{a_2}	w_{a_3}	$Q1$	$Q2$	TG_1	TG_2	TG_3	TG_4
0.7	0.3	0.25	0.5	0.25	24563	59	10	15	106	36
0.8	0.2	0.25	0.5	0.25	24838	59	11	12	120	20
0.6	0.4	0.3	0.3	0.4	25779	94	16	11	132	22
0.6	0.4	0.5	0.2	0.3	24002	65	16	14	100	16
0.5	0.5	0.3	0.4	0.3	24578	60	12	12	120	14
0.3	0.7	0.1	0.8	0.1	25219	59	10	12	103	39
0.3	0.7	0.2	0.7	0.1	23719	57	12	11	120	16
0.2	0.8	0.4	0.2	0.4	24329	59	11	11	128	14
0.2	0.8	0.25	0.5	0.25	25289	59	10	12	130	59

is programmed in the Microsoft Excel 2007 software, using the Visual Basic Application (VBA). We assumed that the studied period of time (AT) is equal to 30 minutes. In other words, every 30 minutes road detectors send the traffic data to optimization process. We also assumed that the lower bound of the green time duration per phase, l_i, equals 10 Seconds, and the upper bound of the green time duration per phase, u_i, equals 138 Seconds. The collected data from the road detectors is shown in Table 1.

In this example, there are than 265 million solutions. The presented model is solved in order to obtain the optimal solution. The planner-specified weights are selected by the manager (($w_v = 0.7$, $w_p = 0.3$) and ($w_{a_1} = .1$, $w_{a_2} = .8$, $w_{a_3} = .1$)). The GA parameters are set as follows:

$G = 100$, $N = 70$, one-point crossover rate = 0.85, mutation rate = 0.2.

The output of the proposed algorithm are as: $\mathrm{TG}_2 = 15$, $\mathrm{TG}_3 = 110$, $\mathrm{TG}_4 = 34$ and its length of traffic and pedestrian queue are ($Q1 = 24563$, $Q2 = 59$) are obtained as the output. The traffic manager may then obtain other optimum solutions by changing the values for the planner-specified weights, which are presented in Table 2.

6. Experimental Evaluation

This section evaluates the performance of our proposed new defuzzification method (NDM) and the centroid point defuzzification method (CPDM) with GA. These algorithms are coded and implemented with the same parameters for twenty-five times. We use the weight relative deviation (WRD) as a common performance measure to compare these algorithms, computed by

$$\mathrm{WRD} = \left(w_v \times \frac{Q1_{\mathrm{alg}} - Q1_{\min}}{Q1_{\min}} + w_p \times \frac{Q2_{\mathrm{alg}} - Q2_{\min}}{Q2_{\min}} \right). \tag{21}$$

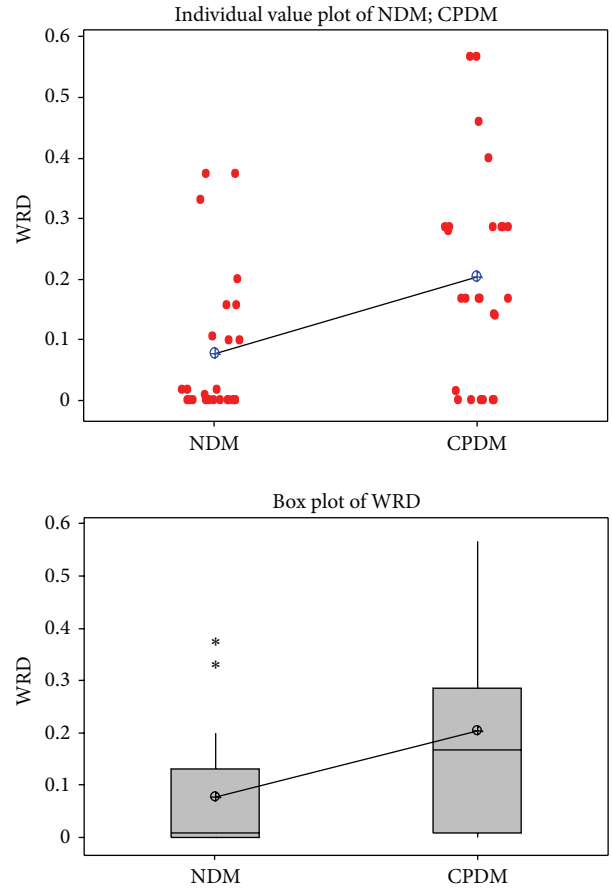

Figure 6: Mean plot and LSD intervals for the NDM and CPDM.

Their results are analysed via the analysis of variance (ANOVA) method. The mean plot and least significant different (LSD) interval for the NDM and CPDM are shown in Figures 6 and 7. It demonstrates that in this problem the NDM gives better outputs than CPDM statistically.

7. Conclusion

In this paper, a new multiobjective mathematical model to optimize the timing of traffic light signal of an individual intersection was presented, which minimizes the total traffic queue and pedestrian delays.

Considering the uncertainty in real world, we used fuzzy theory in calculation, and the entrance and exit rates of an intersection were considered as triangular fuzzy numbers. To solve the given problem, we applied genetic algorithm. For more accurate calculation we proposed a new defuzzification

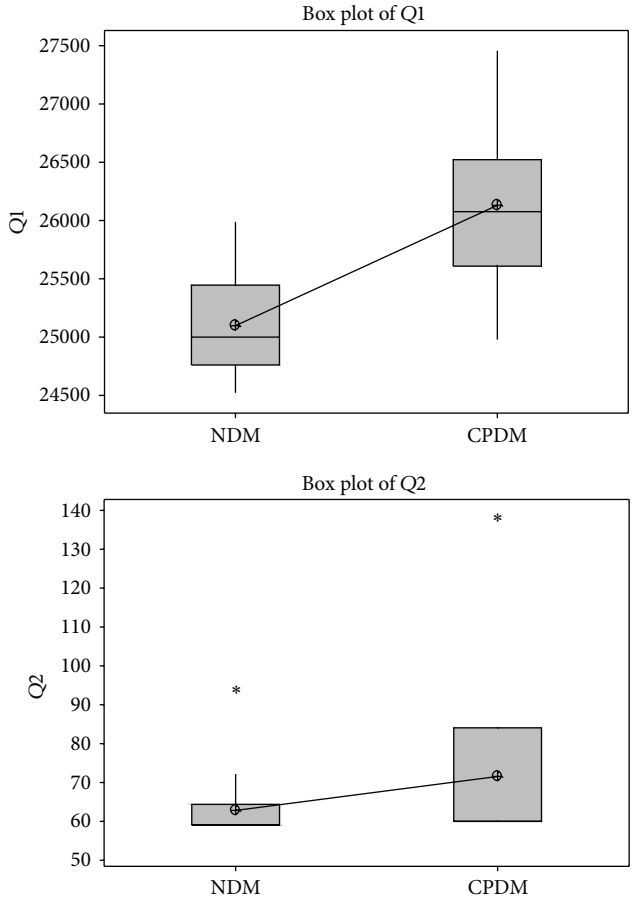

Figure 7: Mean plot of Q1 and Q2 for the NDM and CPDM.

method. The competency of the proposed method was demonstrated, using the weight relative deviation (WRD) measure to compare the performance of the new defuzzification method (NDM) and centroid point defuzzification method (CPDM).

References

[1] J. M. Bayley, "Pedestrian and traffic control," *Traffic Engineering and Control*, vol. 8, pp. 311–312, 1966.

[2] R. Noland, "Pedestrian travel times and motor vehicle traffic signals," in *Proceedings of the Annual Meeting of the Transportation Research Board*, Washington, DC, USA, 1996, paper no. 1553.

[3] R. Noland, "Optimal travel time trade-offs at signalized pedestrian crossings," Unpublished Work, 2003.

[4] E. Brockfeld, R. Barlovic, A. Schadschneider, and M. Schreckenberg, "Optimizing traffic lights in a cellular automaton model for city traffic," *Physical Review E*, vol. 64, Article ID 056132, 2001.

[5] V. Gradinescu, C. Gorgorin, R. Diaconescu, and V. Cristea, *Adaptive traffic light using car-to-car communication [Dissertation]*, Computer Science Department, University of Bucharest, 2007.

[6] K. T. K. Teo, W. Y. Kow, and Y. K. Chin, *Optimization of Traffic Flow within an Urban Traffic Light Intersection with Genetic Algorithm*, School of Engineering and Information Technology, University Malaysia Sabah, Kota Kinabalu, Malaysia, 2010.

[7] F. V. Webster, *Traffic Signal Settings*, Road Research Technical Paper no. 39, Department of Scientific and Industrial Research, 1958.

[8] Z. Yang, *Thesis signal timing optimization based on minimizing vehicle and pedestrian delay by genetic algorithm [Dissertation]*, Graduate College of the University of Illinois at Urbana-Champaign, 2010.

[9] C. Dong, S. Huang, and X. Liu, "Urban area traffic signal timing optimization based on Sa-PSO," in *Proceedings of the International Conference on Artificial Intelligence and Computational Intelligence*, vol. 3, pp. 80–84, 2010.

[10] K. K. Tan, M. Khalid, and R. Yusof, "Intelligent traffic lights control by fuzzy logic," *Malaysian Jurnal of Computer Science*, vol. 3, pp. 45–58, 1996.

[11] J. Favilla, A. Machion, and F. Gomide, "Fuzzy traffic control: adaptive strategies," in *Proceedings of the 2nd IEEE International Conference on Fuzzy Systems*, pp. 506–511, San Francisco, Calif, USA, March 1993.

[12] M. R. Virkler, *Pedestrian Compliance Effects on Signal Delay*, Research Record no. 1636, TRB, National Research Council, Washington, DC, USA, 1998.

[13] V. Chilukuri and M. R. Virkler, "Validation of HCM pedestrian delay model for interrupted facilities," *Journal of Transportation Engineering*, vol. 131, no. 12, pp. 939–945, 2005.

[14] P. Bhattacharya and M. R. Virkler, *Optimization for Pedestrian and Vehicular Delay in a Signal Network*, Transportation Research Record no. 1939, TRB, National Research Council, Washington, DC, USA, 2005.

[15] D. P. Filev and R. R. Yager, "A generalized defuzzification method via bad distribution," *International Journal of Intelligent Systems*, vol. 6, pp. 687–697, 1991.

[16] R. R. Yager and D. P. Filev, "SLIDE: a simple adaptive defuzzification method," *IEEE Transactions on Fuzzy Systems*, vol. 1, no. 1, pp. 69–78, 1993.

[17] L. A. Zadeh, "Fuzzy sets," *Information and Control*, vol. 8, no. 3, pp. 338–353, 1965.

[18] H. Hellendoorn and C. Thomas, "Defuzzification if fuzzy controllers," *Journal of Intelligent Fuzzy Systems*, vol. 1, pp. 109–123, 1993.

[19] N. Shahsavari-Pour, M. Modarres, R. Tavakoli-Moghadam, and E. Najafi, "Optimizing a multi-objectives time-cost-quality trade-off problem by a new hybrid genetic algorithm," *World Applied Science Journal*, vol. 10, no. 3, pp. 355–363, 2010.

Hindawi Publishing Corporation
Journal of Applied Mathematics
Volume 2013, Article ID 236579, 6 pages
http://dx.doi.org/10.1155/2013/236579

Research Article

The Effect of Exit Strategy on Optimal Portfolio Selection with Birandom Returns

Guohua Cao and Dan Shan

School of Economics and Business Administration, Chongqing University, Room 240, No. 12, Dormitory Building, Area A, Shapingba District, Chongqing 400030, China

Correspondence should be addressed to Dan Shan; 332167699@qq.com

Received 18 October 2012; Revised 15 April 2013; Accepted 17 April 2013

Academic Editor: Xiaojun Wang

Copyright © 2013 G. Cao and D. Shan. This is an open access article distributed under the Creative Commons Attribution License, which permits unrestricted use, distribution, and reproduction in any medium, provided the original work is properly cited.

The aims of this paper are to use a birandom variable to denote the stock return selected by some recurring technical patterns and to study the effect of exit strategy on optimal portfolio selection with birandom returns. Firstly, we propose a new method to estimate the stock return and use birandom distribution to denote the final stock return which can reflect the features of technical patterns and investors' heterogeneity simultaneously; secondly, we build a birandom safety-first model and design a hybrid intelligent algorithm to help investors make decisions; finally, we innovatively study the effect of exit strategy on the given birandom safety-first model. The results indicate that (1) the exit strategy affects the proportion of portfolio, (2) the performance of taking the exit strategy is better than when the exit strategy is not taken, if the stop-loss point and the stop-profit point are appropriately set, and (3) the investor using the exit strategy become conservative.

1. Introduction

During decades of development of Chinese stock market, plentiful practice has proved that some technical patterns occur repeatedly in stock market. Stocks with some technical patterns are much more likely to profit than those with other technical patterns. Douglas [1] pointed out that investors should distinguish the recurring technical patterns, summarize the laws, and use them to choose stocks, which can greatly improve the performance of profit. If investors can consider the features of technical patterns and investors' heterogeneity in estimating the stock return, then they can not only enhance the accuracy of estimation but also make it conform to the actual decision-making process of investors more. So a natural question is how to reflect the features of these technical patterns and investors' heterogeneity in the stock return? To the best of our knowledge, there has been no literature in this respect. In this paper, we try to answer this question for the first time.

Estimating the stock return has always been one of the theoretical hot issues, and much progress has been made in this area. The stock return was assumed to follow the normal distribution [2], which had been verified not to coincide with the facts by a great deal of afterward researches. In order to describe the stock return better, the Logistic distribution [3], Student-t distribution [4], and stable Paretian distribution [5] were put forward. Later, fuzzy random distribution [6] and random fuzzy distribution [7] were used separately via combining randomness with fuzziness. In [8, 9], the stock return was assumed to follow birandom distribution. All of the above distributions have certain theoretical meaning, but there are two limitations: one is that they do not consider the stock's technical patterns, thus hiding the particularity of technical patterns, and the other is that investors' heterogeneity cannot be reflected from the above distributions. In this paper, we propose a method to estimate the stock return and the stock return gained finally can be indicated with a birandom variable and thus solving the above two limitations well.

After the stock return being determined, it is important to choose a portfolio model to help investors make decisions. Roy [10] proposed the safety-first model. The main

point was investors would try to make the probability of a disaster smallest when allocating asset. Pyle and Turnovsky [11] summarized the three forms of the safety-first rule. A safety-first chance constrained model [12] was proposed by combining the safety-first rule with chance constraint. Based on the safety-first rule, a birandom chance constrained model [8] and a birandom expected value model [9] were put forward when the stock return follows birandom distribution. However, the model in [8] just takes the budget constraint into consideration without considering the effect of a disaster. The model in [9] uses the expected value to describe the profit, but the expected value model is only applied to risk neutral investors not to risk aversion and risk loving ones. In this paper, a birandom safety-first model is acquired by combining the two models in [8, 9]. In fact, the new model not only considers the effect of disaster, but also can apply to all investors through parameters adjustment.

As we all know, there are two important parts in investment process: how to buy and how to sell. The theory of portfolio selection is widely used to help us decide the proportion of portfolio, which to solve the problem of how to buy. However, to the best of our knowledge, there is no research on the effect of selling strategy on portfolio selection. Exit strategy proposed in behavioral finance has been proved to be an effective selling strategy, and we try to study the effect of exit strategy on birandom portfolio selection in this paper.

The rest of the paper is organized as follows: in Section 2, we illustrate how to describe the stock return using a birandom variable. In Section 3, we propose a birandom safety-first model, a hybrid intelligent algorithm, and a numerical example. In Section 4, we study the effect of exit strategy on birandom portfolio selection. Finally, in Section 5, we draw the conclusion.

2. Estimate the Stock Return

In the following paragraphs, firstly we will introduce the birandom theory, secondly show how to describe the stock return using a birandom variable, and finally give a numerical example.

2.1. Birandom Theory

Definition 1 (Jin and Bao-Ding [13]). A birandom variable ε is a mapping from a probability space (Ω, A, P_r) to a collective of random variables such that for any *Borel* subsets B of the real line R, the induced function $P_r(\varepsilon(\omega) \in B)$ is a measure function with respect to ω.

Example 2. Let $\Omega = (\omega_1, \omega_2)$, and $P_r(\omega_1) = a$, $P_r(\omega_2) = b$. Assume that ε is a function on (Ω, A, P_r) as follows:

$$\varepsilon(\omega) = \begin{cases} \varepsilon_1, & \text{if } \omega = \omega_1, \\ \varepsilon_2, & \text{if } \omega = \omega_2, \end{cases} \tag{1}$$

where ε_1 and ε_2 are random variables. Then ε is a birandom variable according to Definition 1. In Example 2, Ω represents stock, ω_1 represents stock rising, ω_2 represents stock falling, a and b represent the probabilities of stock rising and falling, respectively, and ε_1 represents profit distribution, ε_2 represents loss distribution.

Definition 3 (Jin and Bao-Ding [13]). Let $\varepsilon = (\varepsilon_1, \varepsilon_2, \ldots, \varepsilon_n)$ be a birandom vector on (Ω, A, P_r) and $f : R^n \to R^m$ be a vector-valued *Borel* measurable function. Then the primitive chance of birandom event characterized by $f(\varepsilon) \le 0$ is a function from (0,1] to [0, 1], defined as

$$\begin{aligned} &\mathrm{Ch}\left\{f(\varepsilon) \le 0\right\}(\alpha) \\ &\quad = \sup\left\{\beta \mid P_r\left\{\omega \in \Omega \mid P_r\left\{f(\varepsilon(\omega)) \le 0\right\} \ge \beta\right\} \ge \alpha\right\}. \end{aligned} \tag{2}$$

2.2. Method to Estimate the Stock Return.

Assuming that an investor selects stock S in accordance with technical pattern T, a new method is proposed to estimate the return distribution of stock S. The specific steps are listed as follows.

Step 1. Calculate the probabilities of stock rising and falling after the appearance of technical pattern T. The method is to select n representative stocks and inspect the occurrence number of technical pattern T of the n stocks during a certain period, and then figure out the numbers of price rising and falling separately. When the sample size is large enough, it is reasonable to substitute the frequencies of stock rising and falling for the probabilities of stock rising and falling. Through the comparison of probabilities, the technical patterns can be divided into three types where the probability of rising is larger than, equal to, and smaller than the probability of falling. What we care for is the first type, and it is named as the advanced technical pattern.

Step 2. Because stock S has the features of technical pattern T, we substitute its probabilities of rising and falling by the corresponding probabilities in Step 1. Thus $P_r(\omega_1) = a$, $P_r(\omega_2) = b$ in Example 2 are obtained.

Step 3. When stock S rises, we estimate the profit distribution of stock S. When stock S falls, we estimate the loss distribution of stock S. Thus ε_1 and ε_2 in Example 2 are obtained. Here the following two things should be emphasize.

(1) ε_1 and ε_2 can be obtained from the investors' experience, the stock historical data, and the existing stock forecast methods. In this paper, we assume that ε_1 and ε_2 are random variables.

(2) Different investors have different opinions and judgments on the stock market; therefore, different assumptions of ε_1 and ε_2 can demonstrate the heterogeneity of investors.

From the above, the stock return is quantified by the birandom variable in Example 2. Among them, the formulas $P_r(\omega_1) = a$, $P_r(\omega_2) = b$ demonstrate the features of technical patterns and the distributions of ε_1 and ε_2 reflect the investors' heterogeneity.

2.3. A Numerical Example.

Because stock S follows the birandom distribution in Example 2, we can calculate a, b, ε_1, and ε_2 in the following steps.

Step 1 (calculate a and b). Suppose that we select fifty representative stocks and the appearance numbers of technical pattern T of the fifty stocks are equal to one hundred during the last year. If price goes up 60 times and down 40 times, then the probabilities of stock S rising and falling are equal to 0.6 and 0.4, respectively, so $a = 0.6$ and $b = 0.4$.

Step 2 (the determination of ε_1 and ε_2). After selecting stock S based on technical pattern T, the investor concludes, by various analytical methods such as fundamental analysis and technical analysis, that the profit of stock S should be distributed uniformly in the interval $[0, 7\%]$. Therefore, the profit distribution ε_1 can be assumed to follow the uniform distribution $U\ [0, 7\%]$. Similarly, we can also assume that the loss distribution ε_2 follows the uniform distribution $U\ [-9\%, 0]$.

Remark 4. The detailed statistic process in Step 1 is not included in the paper.

Remark 5. ε_1 and ε_2 can be arbitrary random variable and different distributions of ε_1 and ε_2 have no effect on the validity of the model and the algorithm given in the following paragraphs. Here, the assumption of uniform distribution is to simplify calculation.

Now we get the distribution of stock S. The distribution is given by the following.

Example 6. $\Omega = (\omega_1, \omega_2)$ (Ω represents stock S, ω_1 represents stock S rising, and ω_2 represents stock S falling), and $P_r(\omega_1) = 0.6$, $P_r(\omega_2) = 0.4$,

$$\varepsilon(\omega) = \begin{cases} \varepsilon_1, & \text{if } \omega = \omega_1, \\ \varepsilon_2, & \text{if } \omega = \omega_2, \end{cases} \tag{3}$$

where ε_1 follows $U\ [0, 7\%]$ and ε_2 follows $U\ [-9\%, 0]$.

3. Birandom Safety-First Model

3.1. Assumptions of the Birandom Safety-First Model

(*A*1) The investor selects n stocks based on n kinds of technical patterns. Let m_i and x_i denote the ith stock and the investment proportion of the ith stock, $i = 1, 2, \ldots, n$, respectively. And the return of stock m_i follows the birandom distribution in Example 2.

(*A*2) Stocks can be infinite subdivision. the market does not allow shorting and there is no limitation on the transaction cost.

3.2. Measures of the Profit and Risk.

In this paper, the chance that return of total asset (RTA) is no less than some value is used to measure the profit which is given by

$$\mathrm{Ch}\left\{x_1 m_1 + x_2 m_2 + \cdots + x_n m_n \geq m\right\}(\alpha_1). \tag{4}$$

The chance that RTA is no less than a disaster level is regarded to measure the risk which is given by

$$\mathrm{Ch}\left\{x_1 m_1 + x_2 m_2 + \cdots + x_n m_n \geq n\right\}(\alpha_2) \geq \beta. \tag{5}$$

3.3. Birandom Safety-First Model.

Using the measures of the profit and risk given above, the birandom safety-first model is given by

$$\begin{aligned} \max \quad & \mathrm{Ch}\left\{x_1 m_1 + x_2 m_2 + \cdots + x_n m_n \geq m\right\}(\alpha_1), \\ \text{s.t.} \quad & \mathrm{Ch}\left\{x_1 m_1 + x_2 m_2 + \cdots + x_n m_n \geq n\right\}(\alpha_2) \geq \beta, \\ & \sum_{i=1}^{n} x_i = 1, \\ & x_i \geq 0, \quad i = 1, 2, \ldots, n, \end{aligned} \tag{6}$$

where m represents the profit, n represents the disaster level, α_1 and α_2 represent the investor's tolerance, and β is the lower bound of the chance that RTA is not less than some disaster level when the tolerance is α_2.

The economic meanings of model (6) are listed as follows.

(1) The constraint condition

$$\sum_{i=1}^{n} x_i = 1 \tag{7}$$

means that the capital cannot exceed the budget.

(2) The constraint condition

$$x_i \geq 0, \quad i = 1, 2, \ldots, n \tag{8}$$

means that the market does not allow shorting.

Remark 7. Model (6) can be used for all investors as long as choosing the right parameters m, n, α_1, α_2, β.

Remark 8. When the values of n and α_2 are fixed, the value of β is in inverse ratio with the risk tolerance ability. (Proof is described in the appendix.)

Remark 9. In the case that the return distribution of stock m_i is a random variable, model (6) is reduced to the special one:

$$\begin{aligned} \max \quad & P_r\left\{x_1 m_1 + x_2 m_2 + \cdots + x_n m_n \geq m\right\}, \\ \text{s.t.} \quad & P_r\left\{x_1 m_1 + x_2 m_2 + \cdots + x_n m_n \geq n\right\} \geq \beta, \\ & \sum_{i=1}^{n} x_i = 1, \\ & x_i \geq 0, \quad i = 1, 2, \ldots, n. \end{aligned} \tag{9}$$

3.4. Hybrid Intelligent Algorithm.

Because of the uncertainty of birandom variable, it is hard to analytically solve model (6). To provide a general solution to model (6), we design a hybrid intelligent algorithm integrating genetic algorithm (GA) and birandom simulation.

3.4.1. Birandom Simulation.

The technique of birandom simulation is applied to compute (4) and (5). The specific steps are listed as follows.

Algorithm 10 (birandom simulation for (4)).

Step 1. Generate $w_1, w_2, \ldots, w_N$ from Ω according to the probability measure P_r.

Step 2. Compute the probability $\beta_n = P_r\{x_1m_1 + x_2m_2 + \cdots + x_nm_n\} \geq m$ for $n = 1, 2, \ldots, N$, respectively, by stochastic simulation.

Step 3. Set N' as the integer part of $\alpha_1 N$.

Step 4. Return the N'th largest element β^* in $(\beta_1, \beta_2, \ldots, \beta_N)$.

Step 5. β^* is the value of (4).

Algorithm 11 (birandom simulation for (5)).

Step 1. Set $l = 1$.

Step 2. Generate $w_1, w_2, \ldots, w_M$ from Ω according to the probability measure P_r.

Step 3. Compute the probability $\beta_n = P_r\{x_1m_1 + x_2m_2 + \cdots + x_nm_n\} \geq n$ for $n = 1, 2, \ldots M$, respectively, by stochastic simulation.

Step 4. Set M' as the integer part of $\alpha_2 M$.

Step 5. Return the M'th largest element β^* in $(\beta_1, \beta_2, \ldots, \beta_M)$.

Step 6. If β^* is larger than β, then $l = l * 1$, else $l = l * 0$.

Step 7. If $l = 1$, then return Yes, else return No. Here, Yes means the investment proportion x satisfies (5), and No means that x does not satisfy (5).

3.4.2. Genetic Algorithm. The specific steps of genetic algorithm are described in [8].

3.4.3. Hybrid Intelligent Algorithm

Step 1. Initialize *pop_size* chromosomes.

Step 2. Calculate the values of (4) for all chromosomes by birandom simulation.

Step 3. Give the rank order of the chromosomes according to the values of (4), and define the rank-based evaluation function of the chromosomes.

Step 4. Compute the value of each chromosome according to the rank-based evaluation function.

Step 5. Select the chromosomes by spinning the roulette wheel.

Step 6. Update the chromosomes by crossover and mutation operations.

Step 7. Repeat the second step to the sixth step for a given number of cycles.

Table 1: The distributions of stocks m_1, m_2, and m_3.

Parameters	m_1	m_2	m_3
a_i $(i = 1, 2, 3)$	2/3	1/2	1/3
b_i $(i = 1, 2, 3)$	1/3	1/2	2/3
ε_{i1} $(i = 1, 2, 3)$	$U[0, 6\%]$	$U[0, 8\%]$	$U[0, 10\%]$
ε_{i2} $(i = 1, 2, 3)$	$U[-8\%, 0]$	$U[-10\%, 0]$	$U[-12\%, 0]$

Step 8. Take the best chromosome as the solution of portfolio selection.

3.5. A Numerical Example. According to $(A1)$ in Section 3.1, an investor picks three stocks based on three kinds of technical patterns (the probability of rising is larger than, equal to, and smaller than the probability of falling). The stock return follows birandom distribution and the corresponding parameters of each stock are shown in Table 1. Besides, the investor takes $m = 0.03$, $n = -0.05$, $\alpha_1 = 0.4$, $\alpha_2 = 0.8$, and $\beta = 0.7$.

Remark 12. In Table 1, a_i, b_i, ε_{i1}, ε_{i2} represent the probability of stock rising, the probability of falling, profit distribution, and loss distribution of stock m_i, respectively.

So model (6) that satisfies the above investment goals is given by

$$\begin{aligned} \max \quad & \mathrm{Ch}\left\{x_1m_1 + x_2m_2 + x_3m_3 \geq 0.03\right\}(0.4), \\ \text{s.t.} \quad & \mathrm{Ch}\left\{x_1m_1 + x_2m_2 + x_3m_3 \geq -0.05\right\}(0.8) \geq 0.7, \\ & \sum_{i=1}^{3} x_i = 1, \\ & x_i \geq 0, \quad i = 1, 2, 3. \end{aligned} \tag{10}$$

In order to compare model (6) with the models in [8, 9], the models in [8, 9] are listed as below:

$$\begin{aligned} \max \quad & E\left[x_1m_1 + x_2m_2 + x_3m_3\right], \\ \text{s.t.} \quad & \mathrm{Ch}\left\{x_1m_1 + x_2m_2 + x_3m_3 \geq -0.05\right\}(0.8) \geq 0.7, \\ & \sum_{i=1}^{3} x_i = 1, \\ & x_i \geq 0, \quad i = 1, 2, 3, \end{aligned} \tag{11}$$

$$\begin{aligned} \max \quad & \mathrm{Ch}\left\{x_1m_1 + x_2m_2 + x_3m_3 \geq 0.03\right\}(0.4), \\ \text{s.t.} \quad & \sum_{i=1}^{3} x_i = 1, \\ & x_i \geq 0, \quad i = 1, 2, 3. \end{aligned} \tag{12}$$

The parameters of the hybrid intelligent algorithm are taken as *pop_size* = 30, the crossover probability = 0.3, the mutation probability = 0.5, the evaluate function based on the order $\alpha = 0.05$, and the number of cycles is equal to 1000. After repeating the hybrid intelligent algorithm 10 times and

Table 2: The results of models (9)–(11).

Model	Result	Optimal solution			Objective function value
		x_1	x_2	x_3	
Model (10)	Result 1	0.1916	0.6885	0.1199	0.4157
Model (11)	Result 2	0.9209	0.0668	0.0123	0.5525
Model (12)	Result 3	0.0011	0.0123	0.9866	0.6890

taking the average value of the results, the optimal solutions of models (9)–(11) are shown in Table 2.

From result 1 in Table 2, it can be seen that (1) model (10) and the hybrid intelligent algorithm are of great applicability, (2) even if stock m_1 has the advanced technical pattern, not all investors will buy it using their total asset. Some investors prefer to buy the high-risk and high-interest stock.

From result 2 in Table 2, it can be seen that the proportion of stock m_1 is very large. This is because model (11) uses the expected value to measure the profit and stock m_1 has the largest expected value, so the investor will select stock m_1 as many as possible, while the constraints are met. However, model (11) is only suitable for risk-neutral investors, so it is restricted in real application.

From result 3 in Table 2, it can be seen that the objective function value of model (12) is larger than it of model (10). This is because model (12) does not consider the risk, so consequently, model (12) has a larger solution space than model (10). Despite achieving the high yield, model (12) is unpractical in application because it ignores the risk.

Through the comparisons of models (10)–(12), it can be concluded that model (10) is more practical than model (11) and model (12), because model (10) not only considers the effect of disaster, but also can apply to all investors through parameters adjustment.

4. The Effect of Exit Strategy on the Optimal Portfolio Selection

Exit strategy is a selling strategy including the stop-loss strategy and the stop-profit strategy. If an investor sets the stop-profit point w% and the stop-loss point l% for each stock, he will sell the stocks when the stocks' actual profit exceeds w% or the actual loss exceeds l%. Now we want to ask whether result 1 in Table 2 is still available if the investor set $w = 0.4$ and $l = 0.5$ for each stock.

we know that in the simulation process of result 1, the stock return of each stock can be any sample point following corresponding birandom distribution. However, in practice, the cases that actual stock return is over 4% or below −5% will not occur due to the setting of the stop-loss point and the stop-profit point. Thus the calculation of result 1 is inconsistent with the investor's decision-making process. In other words, result 1 cannot reach the investor' objective in theory, which causes the failure of model (10).

In order to solve the above conflict, we should adjust the stock return based on the stop-loss point and the stop-profit point. Considering the assumptions of model (10), we revise the calculation in the following ways.

Step 1. The investor should adjust the stock return according to the stop-profit point and the stop-loss point. Adjustment method is to take the stop-profit point as stock return when stock return exceeds the stop-profit point and to take the stop-loss point as stock return when stock return is less than the stop-loss point. Take stock m_1 in Table 1 as an example, if an investor set the stop-profit point as 4% and the stop-loss points as −5%, the part exceeding 4% in ε_{11} is treated as 4% and the part below −5% in ε_{12} is considered as −5%.

Step 2. Because of the adjustment of the stock return, we also should modify the steps of birandom simulation. The adjustment method is that if the sample point exceeds the stop-profit point or is less than the stop-loss point, we take the stop-profit point or the stop-loss point as the sample point. The rest of the steps of the hybrid intelligent algorithm remain unchanged. Take stock m_1 in Table 1 as an example. when samples are selected from ε_{11}, the part which is more than 4% is looked upon as 4% and when samples are selected from ε_{12}, the part which is below −5% is considered as −5%.

Through the above adjustment, the calculated value can reach the investor's goal in theory. The revised result of model (10) is

$$\begin{gathered} \max \text{ Ch} = 0.4908, \\ x_1 = 0.9991, \qquad x_2 = 0.0002, \qquad x_3 = 0.0007. \end{gathered} \tag{13}$$

It can be seen from result (13) that

(1) because the objective function value in result (13) is larger than it in result 1, the performance of taking the exit strategy is better than when the exit strategy is not taken, if the stop-loss point is equal to −5% and the stop-profit point is equal to 4%;

(2) the exit strategy affects the buying strategy and the investor should adjust the stock return according to the stop-loss point and the stop-profit point, otherwise the portfolio model will become invalid;

(3) the investor using exit strategy become conservative. This is because he is concerned with the accumulated probability of stock price exceeding the stop-profit point not the higher stock return any more.

5. Conclusion

In this paper we propose a new method to estimate the stock return and use a birandom variable to denote the final stock return which can reflect the features of technology forms and investors' heterogeneity simultaneously. Besides, we build a birandom safety-first model and design a hybrid intelligent algorithm to help investors make a decision. Moreover, we innovatively study the effect of exit strategy on the given birandom safety-first model. The results indicate that the performance of taking the exit strategy is better than when the exit strategy is not taken, if the stop-loss point and the stop-profit point are appropriately set.

Appendix

Proof of Remark 8

Let A represent the solution space which satisfies

$$\mathrm{Ch}\left\{x_1m_1 + x_2m_2 + \cdots + x_nm_n \geq n\right\}(\alpha_2) \geq \beta_1. \tag{A.1}$$

Let B represent the solution space which satisfies

$$\mathrm{Ch}\left\{x_1m_1 + x_2m_2 + \cdots + x_nm_n \geq n\right\}(\alpha_2) \geq \beta_2, \tag{A.2}$$

and $\beta_1 > \beta_2$.

For any $x = (x_1, x_2, \ldots, x_n) \in A$. If $\omega = (\omega_1, \omega_2, \ldots, \omega_n) \in \Omega$ satisfies

$$P_r\left\{x_1m_1(\omega_1) + x_2m_2(\omega_2) + \cdots + x_nm_n(\omega_n) \geq n\right\} \geq \beta_1 \tag{A.3}$$

then we can obtain that $\omega = (\omega_1, \omega_2, \ldots, \omega_n) \in \Omega$ also satisfies

$$P_r\left\{x_1m_1(\omega_1) + x_2m_2(\omega_1 2) + \cdots + x_nm_n(\omega_n) \geq n\right\} \geq \beta_2. \tag{A.4}$$

So if $x = (x_1, x_2, \ldots, x_n) \in A$ satisfies

$$P_r\left\{\omega \in \Omega \mid P_r\left\{x_1m_1(\omega_1) + x_2m_2(\omega_1 2) + \cdots + x_nm_n(\omega_n) \geq n\right\} \geq \beta_1\right\} \geq \alpha, \tag{A.5}$$

then we can obtain $x = (x_1, x_2, \ldots, x_n)$ satisfies

$$P_r\left\{\omega \in \Omega \mid P_r\left\{x_1m_1(\omega_1) + x_2m_2(\omega_1 2) + \cdots + x_nm_n(\omega_n) \geq n\right\} \geq \beta_2\right\} \geq \alpha. \tag{A.6}$$

Since (A.6) is equivalent to (A.2), so $x = (x_1, x_2, \ldots, x_n) \in B$. Hence, $A \subset B$. That is to say, the value of β is in inverse ratio with the range of solution space.

Since when the range of solution space is enlarged, an investor has a larger decision range, which means he/she can try some investments that others dare not try, so the risk tolerance ability is increased vice versa.

So the range of solution space is in direct ratio to risk tolerance ability; therefore, the value of β is in inverse ratio with risk tolerance ability.

References

[1] M. Douglas, *Trading in the Zone*, Prentice Hall, New York, NY, USA, 1st edition, 2000.

[2] H. Markowitz, "Portfolio selection," *Journal of Finance*, vol. 7, no. 1, pp. 77–91, 1952.

[3] D. Da-Yong and J. Wei-Dong, "A subjective model of the distribution of returns and empirical analysis," *Chinese Journal of Management Science*, vol. 15, pp. 112–120, 2007.

[4] L. Mei-Yan, X. Hong-Gang, and Z. Feng-Qun, "Statisticsal analysis of return rates of shanghai stock market price integrated index," *Operations Research and Management Science*, vol. 14, pp. 115–119, 2005.

[5] F. Jian-Qiang and W. Fu-Xin, "A research on return distribution function of chinese stock-market," *Chinese Journal of Management Science*, vol. 11, pp. 82–90, 2007.

[6] J. Li, J. Xu, and M. Gen, "A class of multiobjective linear programming model with fuzzy random coefficients," *Mathematical and Computer Modelling*, vol. 44, no. 11-12, pp. 1097–1113, 2006.

[7] X. Huang, "A new perspective for optimal portfolio selection with random fuzzy returns," *Information Sciences*, vol. 177, no. 23, pp. 5404–5414, 2007.

[8] L. Mei-Yan, "Chance-constrained portfolio selection with birandom returns," *Modern Applied Science*, vol. 3, no. 4, pp. 161–165, 2009.

[9] L. Mei-Yan, "One type of optimal portfolio selection in birandom environments," *Modern Applied Science*, vol. 3, no. 6, pp. 121–126, 2009.

[10] A. D. Roy, "Safety-first and the holding of assets," *Econometrica*, vol. 20, no. 3, pp. 431–449, 1952.

[11] D. H. Pyle and S. J. Turnovsky, "Safety-first and expected utility maximization in mean-standard deviation portfolio analysis," *The Review of Economics and Statistics*, vol. 52, no. 1, pp. 75–81, 1970.

[12] Z. Yong-Fen, "Based on the safety first chance constrained dynamic portfolio research problems," *Modern Economic Information*, vol. 18, pp. 32–33, 2009.

[13] P. Jin and L. Bao-Ding, "Birandom variables and birandom programming," *Computers and Industrial Engineering*, vol. 53, no. 3, pp. 433–453, 2007.

Hindawi Publishing Corporation
Journal of Applied Mathematics
Volume 2013, Article ID 434636, 12 pages
http://dx.doi.org/10.1155/2013/434636

Research Article

Antioptimisation of Trusses Using Two-Level Population-Based Incremental Learning

Phinit Tontragunrat and Sujin Bureerat

Department of Mechanical Engineering, Faculty of Engineering, Khon Kaen University, Khon Kaen 40002, Thailand

Correspondence should be addressed to Sujin Bureerat; sujbur@kku.ac.th

Received 14 December 2012; Accepted 18 March 2013

Academic Editor: Xiaojun Wang

Copyright © 2013 P. Tontragunrat and S. Bureerat. This is an open access article distributed under the Creative Commons Attribution License, which permits unrestricted use, distribution, and reproduction in any medium, provided the original work is properly cited.

Practical optimum design of structures often involves parameters with uncertainties. There have been several ways to deal with such optimisation problems, and one of the approaches is an antioptimisation process. The task is to find the optimum solution of common design variables while simultaneously searching for the worst case scenario of those parameters with uncertainties. This paper proposed a metaheuristic based on population-based incremental learning (PBIL) for solving antioptimisation of trusses. The new algorithm is called two-level PBIL which consists of outer and inner loops. Five antioptimisation problems are posed to test the optimiser performance. The numerical results show that the concept of using PBIL probability vectors for handling the antioptimisation of truss is powerful and effective. The two-level PBIL can be considered a powerful optimiser for antioptimisation of trusses.

1. Introduction

A truss structure is one of the most widely used engineering structures due to its simplicity and low cost for construction and design. Such a structure can be used in many engineering applications such as bridges, roofs, and towers. Throughout its history, a great deal of research work on truss design optimisation has been investigated, for example, [1–6]. The design process can be categorised as topology, shape, and sizing optimisation. The optimisers used for tackling truss design problems could be the methods with and without using function derivatives. Some of the most popular optimisers are evolutionary algorithms (EAs), which can deal with truss design having single or multiple objective functions. Using EAs, although having low convergence rate and lacking of search consistency, is popular and advantageous since they are simple to use and robust and can deal with any kind of design problems particularly truss design with discrete design variables.

Nevertheless, practical design of trusses and other structures often has inevitable difficulties when uncertainties are involved. For example, it is always difficult to define certain applied loads on structures and material properties. This implies that the real world design problem of trusses will include parameters with uncertainties and it becomes reliability-based optimisation. The simplest way to handle this is by adding the factor of safety to structural constraints. Alternatively, multiobjective design problems which minimise cost and maximise a parameter indicating structural reliability (e.g., structural compliance and natural frequency) are posed and solved for a set of the Pareto optimum structures [6–8]. The more popular approach is the use of reliability-based optimisation techniques, which involve probabilistic design constraints. For example, the use of gradient-based optimisers [9] and evolutionary algorithms [10] for this design process has been reported.

Apart from the aforementioned approaches, a simple but effective way to deal with optimisation with uncertainties is to use the so-called antioptimisation [11]. In the antioptimisation process, there are two sets of design variables, common design variables and ones with uncertainties predefined in certain intervals. One optimisation run has two simultaneous tasks. The first task is to find the solution for the interval variables giving the worst case scenario for the structure,

Population 1				Population 2				Population 3			
0	0	1	1	1	1	1	0	0	0	0	1
1	1	1	0	0	1	0	1	1	1	0	0
0	1	0	1	1	0	1	1	0	0	0	1
1	0	0	0	0	0	0	0	0	1	0	1

Probability vectors

[0.5, 0.5, 0.5, 0.5]	[0.5, 0.5, 0.5, 0.5]	[0.25, 0.5, 0, 0.75]

Figure 1: Probability vectors and their corresponding populations.

Initialisation $P_i = 0.5$, $k = 0$, $\mathbf{b} = \{\cdot\}$
Main procedure
(1) Generate a binary population $\mathbf{B}$ according to P_i.
(2) Perform function evaluations $f(\mathbf{B})$ and find the best solution $\mathbf{b}$ from $\mathbf{B} \cup \mathbf{b}$.
(3) Update P_i using (5).
(4) Set P_i to $[0.1, 0.9]$ in cases that it is out of the interval.
(5) If the termination condition is met, stop the procedure; otherwise, set $k = k + 1$ and go to (1).

Algorithm 1: Population-based incremental learning.

while the second task is finding the optimum solution for the common design variables. Optimisers for this propose have been developed, for example, two-species genetic algorithm (GA) [12], and hybrid genetic algorithm (HybridGA) [13]. From the literature, it is found that using such evolutionary algorithms for solving an antioptimisation problem is somewhat time-consuming.

This paper is concerned with developing a metaheuristic (MH) for tackling antioptimisation of trusses. The work focuses on the metaheuristic because it can deal with discrete design variables which are usually employed in real-world truss design. Population-based incremental learning (PBIL) is chosen and adapted to deal with truss antioptimisation leading to five variants of PBIL. The five methods and HybridGA are then implemented on five antioptimisation problems of 2D trusses. Optimum results show that PBIL is a powerful optimiser for truss antioptimisation and it is superior to HybridGA.

2. Antioptimisation Problem

A typical single-objective truss optimisation is mass minimisation subject to structural design constraints, which can be expressed as

$$\begin{aligned} &\min_{\mathbf{x}} && f(\mathbf{x}), \\ &\text{subject to} && g_i(\mathbf{x}) \le 0, \quad i = 1, \ldots, m, \end{aligned} \tag{1}$$

where $\mathbf{x}$ is a vector sized $n_1 \times 1$ of common design variables, f is structural mass, and g_i are inequality constraints for safety requirements. When variables with uncertainties are included, the problem can be written as

$$\begin{aligned} &\min_{\mathbf{x}} && f(\mathbf{x}, \mathbf{y}), \\ &\text{subject to} && g_i(\mathbf{x}, \mathbf{y}) \le 0, \quad i = 1, \ldots, m, \end{aligned} \tag{2}$$

where $\mathbf{y} \in [\mathbf{y}_l, \mathbf{y}_u]$ is a vector sized $n_2 \times 1$ of variables with uncertainty having lower and upper bounds as $\mathbf{y}_l$ and $\mathbf{y}_u$, respectively.

For truss antioptimisation, the problem (2) is separated into two subproblems as the design problem (1) for searching for optimum design variables $\mathbf{x}$ and the design problem for finding the worst case $\mathbf{y}$ of a structure written as

$$\max_{\mathbf{y}} F(\mathbf{y}), \quad \mathbf{y} \in [\mathbf{y}_l, \mathbf{y}_u], \tag{3}$$

where F is a function indicating the maximum violation of structural constraints. For simplicity, F can be defined as

$$F(\mathbf{y}) = \max(g_i(\mathbf{x}, \mathbf{y})) \tag{4}$$

with the design point $\mathbf{x}$ being unchanged.

A traditional strategy for solving an antioptimisation problem is to use a two-level approach. The search process starts with initial solutions for $\mathbf{x}$ and $\mathbf{y}$. In one iteration, the method searches for the optimum solution of $\mathbf{x}$ based on the problem (1) by fixing the value of $\mathbf{y}$. Then, use the updated values of $\mathbf{x}$ for finding the worst solution of $\mathbf{y}$ based on the problem (3). The process is repeated until the termination conditions are fulfilled.

3. PBIL for Antioptimisation

Over the years, there have been a significant number of metaheuristic algorithms developed for a wide variety of real-world applications, for example, [14–18]. PBIL is chosen for this work because it is a simple but powerful MH and suits well with the concept of antioptimisation. PBIL was first proposed by Baluja in 1994 [19]. The method is based upon a simple estimation of distribution algorithm and searches for an optimum using binary strings. Unlike GA which keeps a set of binary design solutions (better known as a population), PBIL uses the so-called probability vector to represent a binary population. Figure 1 shows some probability row vectors which will be used to produce binary population matrices where one row of the matrix represents a binary design solution. The element P_i of the vector determines the probability of having the string "1" on the ith column of the binary population. From the figure, it can be seen that one probability vector can produce various binary populations. As the optimisation proceeds, the probability vector is updated iteratively leading to an optimum solution. A typical computational procedure of PBIL is given in Algorithm 1. Initially, the probability vector is set as $P_i = 0.5$. Then, the corresponding population is generated where the best binary

Initialisation $P_{x,i} = 0.5$, $P_{y,i} = 0.5$, and find $\mathbf{b} = \{\mathbf{b}_x \quad \mathbf{b}_y\}$ and $\mathbf{w} = \{\mathbf{w}_x \quad \mathbf{w}_y\}$ from an initial population.
Main procedure
(1) For $k = 1$ to N_O (outer loop)
(2) Generate a binary population $\mathbf{B}_x$ according to $P_{x,i}$ and assign $\mathbf{w}_y$ as the second part of every solution in $\mathbf{B}_x$. The population is $\mathbf{B} = [\mathbf{B} \quad \mathbf{w}_y]$.
(3) Perform function evaluations $f(\mathbf{B})$.
(4) Find the new best solution $\mathbf{b}$ from $\mathbf{B} \cup \mathbf{b}$ based on the objective function in (1).
(5) Update $P_{x,i}$ with $\mathbf{b}_x$ using (5).
(6) Set $P_{x,i}$ to $[0.1, 0.9]$ in cases that it is out of the interval.
(7) For $j = 1$ to N_I (inner loop)
(8) Generate a binary population $\mathbf{W}_y$ according to $P_{y,i}$ and assign $\mathbf{w}_x$ as the first part of every solution in $\mathbf{W}_y$. The population is $\mathbf{W} = [\mathbf{w}_x \quad \mathbf{W}_y]$.
(9) Perform function evaluations $f(\mathbf{W})$
(10) Find the new worst solution $\mathbf{w}$ from $\mathbf{W} \cup \mathbf{w}$ based on the objective function in (3).
(11) Update $P_{y,i}$ with $\mathbf{w}_y$ using (5).
(12) Set $P_{y,i}$ to $[0.1, 0.9]$ in cases that it is out of the interval.
(13) Next j
(14) Next k

Algorithm 2: Population-based incremental learning for antioptimisation.

solution $\mathbf{b}$ is found. The probability vector is then updated based upon the best solution as

$$P_i^{\text{new}} = (1 - L_R) P_i^{\text{old}} + L_R b_i, \tag{5}$$

where P_i^{old} is the ith element of the probability vector from the previous iteration, P_i^{new} is the updated ith element of the probability vector, and b_i is the ith element of the best binary solution. L_R is called a learning rate which herein is set to be a uniform random number in the range of $[0.4, 0.6]$ generated anew when the probability vector update takes place. In this work, mutation is not used to modify the probability vector, but the value of P_i after being updated will be set to the range of $[0.1, 0.9]$ (if the updated value of P_i is lower than 0.1 or higher than 0.9, it will be set as 0.1 and 0.9, resp.) in order to prevent a premature convergence.

When dealing with an antioptimisation problem, the method is modified as shown in Algorithm 2. As it involves two levels of optimisation search, the developed PBIL will be named two-level population-based incremental learning. The algorithm starts with generating an initial binary population where each binary solution contains strings for design variables $\mathbf{x}$ and variables with uncertainties $\mathbf{y}$. Then, the best binary solution $\mathbf{b}$ containing two parts as $\mathbf{b}_x$ for $\mathbf{x}$ and $\mathbf{b}_y$ for $\mathbf{y}$ is found based on the design problem (1). On the other hand, the worst binary solution $\mathbf{w} = \{\mathbf{w}_x \quad \mathbf{w}_y\}$ is obtained based on the problem (3). The method uses two probability vectors as $\mathbf{P}_x$ and $\mathbf{P}_y$ for representing binary populations of $\mathbf{x}$ and $\mathbf{y}$, respectively. Afterwards, a set of binary design solutions for $\mathbf{x}$ (denoted as $\mathbf{B}_x$) are created based on $\mathbf{P}_x$, while each solution in the population has its second part of a binary string for $\mathbf{y}$ as $\mathbf{w}_y$. The new best solution $\mathbf{b}$ is obtained from sorting the current population and the best solution from the previous iteration. The probability vector $\mathbf{P}_x$ is updated using the first part of the new best solution $\mathbf{b}_x$. This is the first level of the process which is said to be outer loops.

For inner loops (steps (7)–(13)) which are the search for the worst case scenario, a set of binary solutions for $\mathbf{y}$ (denoted as $\mathbf{W}_y$) is generated from the probability vector $\mathbf{P}_y$ where each solution has the first part of a binary string for $\mathbf{x}$ as $\mathbf{w}_x$ which is the first part of the current worst solution. The new worst solution $\mathbf{w}$ is then obtained based on the problem (3) by sorting the current population and the previous worst solution. The probability $\mathbf{P}_y$ is updated by using $\mathbf{w}_y$, the second part of $\mathbf{w}$. The inner loop procedure is stopped after N_I loops. Similarly, the outer loop search is terminated after N_O loops. This implies that if the population size for both inner and outer loops is N_P, the total number of function evaluations for each simulation run is $N_O(N_I + 1)N_P$. It should be noted that we use the worst solution for finding the worst case structures because it is expected to give the worst objective function values which may help accelerate PBIL to the worst case. In the case studies, we will examine the use of best and worst solutions for searching the worst case scenario.

4. Truss Design Case Studies

Five antioptimisation problems (AOPs) of three truss structures will be used to test the proposed algorithms. The first truss is called a 2-bar truss shown in Figure 2. The structure is subject to a vertical load F with uncertainty at node 3. The second structure is named a 10-bar truss [20] shown in Figure 3. The structure consists of 6 nodes and 10 bars where nodes 1 and 2 are fixed and nodes 4 and 6 are subject to external forces F_1 and F_2, respectively. The third structure is called a 25-bar truss as displayed in Figure 3. The truss has 12 nodes and 25 bars where nodes 1 and 12 are fixed. The structure is applied by loads F_1, F_2, F_3, F_2, and F_1 at nodes 2, 4, 6, 8, and 10, respectively. The design problems can be detailed as follows.

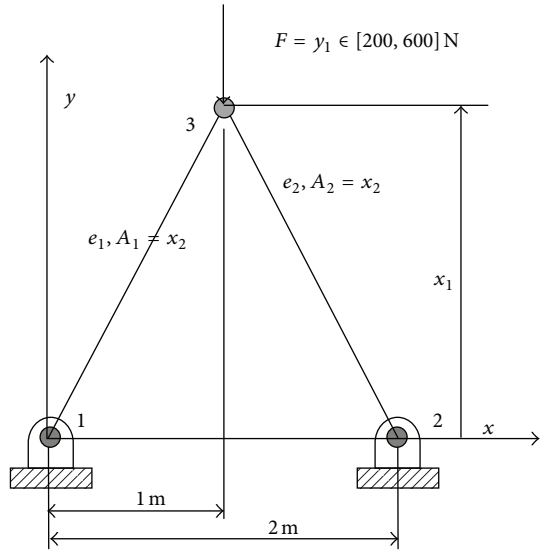

Figure 2: 2-bar truss.

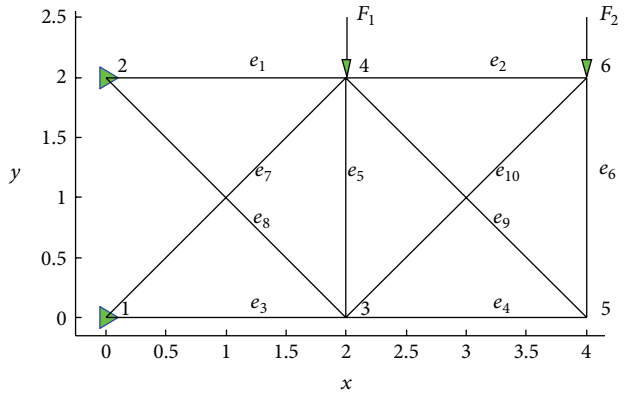

Figure 3: 10-bar truss.

AOP1: Optimisation of the 2-Bar Truss. The design problem can be written as:

$$\begin{aligned}
&\min_{\mathbf{x}} && f(\mathbf{x}, \mathbf{y}), \quad \max_{\mathbf{y}} F(\mathbf{x}, \mathbf{y}) \\
&\text{Subject to} && \sigma_{\max}(\mathbf{x}, \mathbf{y}) - \sigma_{\text{yt}} \le 0, \ \text{N/m}^2, \\
&&& P_i - P_{\text{cr}} \le 0, \ \text{N}, \\
&&& x_1 \in [0.5, 1.5], \ \text{m}, \\
&&& x_2 = A_1 = A_2 \in [0.001, 0.01], \ \text{m}, \\
&&& 200 \le y_1 = F \le 600, \ \text{N},
\end{aligned} \tag{6}$$

where A_i is the cross-sectional area of the ith bar element. $\sigma_{\max}$ is the maximum stress on truss elements. P_i is the axial load acting on the ith element, while P_{cr} is the critical buckling load for the element. The structures for all 5 test problems are made up of material with the Young modulus $E = 200 \times 10^9$ N/m^2, yield stress $\sigma_{\text{yt}} = 235 \times 10^6$ N/m^2, and density $\rho = 7800$ kg/m^3. The common design variables are shape and sizing variables. The external force F is set to be variables with uncertainties. The task is to find the external force that gives the worst case scenario for the structure while simultaneously trying to perform mass minimisation.

AOP2: Sizing Optimisation of the 10-Bar Truss. The second design problem can be written as:

$$\begin{aligned}
&\min_{\mathbf{x}} && f(\mathbf{x}, \mathbf{y}), \quad \max_{\mathbf{y}} F(\mathbf{x}, \mathbf{y}), \\
&\text{subject to} && \sigma_{\max}(\mathbf{x}, \mathbf{y}) - \sigma_{\text{yt}} \le 0, \ \text{N/m}^2, \\
&&& P_i - P_{\text{cr}} \le 0, \ \text{N}, \\
&&& U_{\max} - 0.005 \le 0, \ \text{m}, \\
&&& x_i = d_i \in \{0.04, 0.05, 0.06, 0.07, 0.08, 0.09, \\
&&&\qquad 0.10, 0.20\}, \ \text{m}, \\
&&& \{75, 150\}^T \le \mathbf{y} = \{F_1, F_2\}^T \le \{80, 175\}^T, \ \text{N},
\end{aligned} \tag{7}$$

where d_i is the diameter of the ith bar element. $U_{\max}$ is the maximum y-direction displacement of the structure. The common design variables are set to be discrete so that it is close to a practical truss design process. The external forces F_1 and F_2 are set to be variables with uncertainties. The task is to find the external forces that give the worst case scenario for the structure while, at the same time, trying to perform mass minimisation with sizing design variables.

AOP3: Sizing Optimisation of the 25-Bar Truss. The design problem can be written as:

$$\begin{aligned}
&\min_{\mathbf{x}} && f(\mathbf{x}, \mathbf{y}), \quad \max_{\mathbf{y}} F(\mathbf{x}, \mathbf{y}), \\
&\text{subject to} && \sigma_{\max}(\mathbf{x}, \mathbf{y}) - \sigma_{\text{yt}} \le 0, \ \text{N/m}^2, \\
&&& P_i - P_{\text{cr}} \le 0, \ \text{N}, \\
&&& U_{\max} - 0.005 \le 0, \ \text{m}, \\
&&& x_i \in \{0.06, 0.07, 0.08, 0.09, 0.10, 0.15, \\
&&&\qquad 0.20, 0.25\} \ \text{m}; \quad i = 1, \ldots, 13, \\
&&& \left\{150, 150, 150, 199.00 \times 10^9\right\}^T \\
&&&\quad \le \mathbf{y} = \{F_1, F_2, F_3, E\}^T \\
&&&\quad \le \{300, 300, 300, 201.00 \times 109\}^T.
\end{aligned} \tag{8}$$

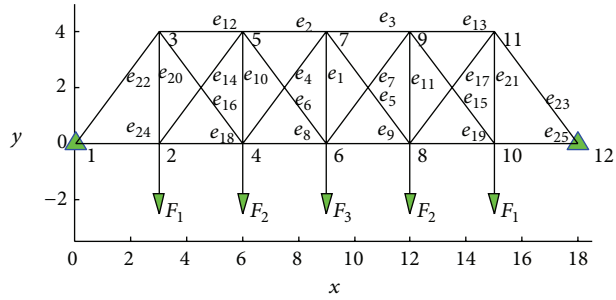

Figure 4: 25-bar truss.

Table 1: Optimum results of AOP1.

MHs	HybridGA		PBILb5		PBILw5		PBILw5m		PBILw1		PBILw10	
	Avrg	Stdev	Avrg	Stdev	Avrg	Stdev	Avrg	Stdev	Avrg	Stdev	Avrg	Stdev
x_1	0.5048	0.0242	0.5613	0.1011	0.6247	0.1176	0.6333	0.1587	0.6344	0.1558	0.5914	0.1302
x_2	0.0029	0.0001	0.0038	0.0003	0.0037	0.0004	0.0038	0.0005	0.0038	0.0004	0.0038	0.0004
y_1	200.0000	0.0000	399.1398	130.0818	370.3226	142.7784	400.8602	164.3949	405.1613	157.4620	424.0860	151.7861
$f(\mathbf{x}, \mathbf{y})$	49.9355	1.6789	67.2216	4.8174	68.2111	5.5543	70.2185	5.9409	69.9382	4.6033	69.4287	5.3346
$\max g_i$	−0.0018	0.0024	−0.0050	0.0000	−0.0050	0.0000	−0.0050	0.0000	−0.0050	0.0000	−0.0050	0.0000

In this case, there are uncertainties in applied loads and material property. The sizing design variables are set to have a symmetric structure. Thus, we have

(i) x_1 for d_1,
(ii) x_2 for d_2 and d_3,
(iii) x_3 for d_4 and d_5,
(iv) x_4 for d_6 and d_7,
(v) x_5 for d_8 and d_9,
(vi) x_6 for d_{10} and d_{11},
(vii) x_7 for d_{12} and d_{13},
(viii) x_8 for d_{14} and d_{15},
(ix) x_9 for d_{16} and d_{17},
(x) x_{10} for d_{18} and d_{19},
(xi) x_{11} for d_{20} and d_{21},
(xii) x_{12} for d_{22} and d_{23},
(xiii) x_{13} for d_{24} and d_{25}.

AOP4: Shape and Sizing Optimisation of the 10-Bar Truss. The fourth design problem is the same problem as AOP2 with additional 4 shape design variables for $\mathbf{x}$. The shape variables determine the positions of nodes 3 and 5 in both x and y directions. The design variables are used to modify the original positions (shown in Figure 3) of nodes 3 and 5. The bound constraints are set as $-0.75\,\text{m} \le x_i \le 0.75\,\text{m}$ for $i = 11, \ldots, 14$.

AOP5: Shape and Sizing Optimisation of the 25-Bar Truss. The fifth design problem is the same problem as AOP2 with additional 3 shape design variables for $\mathbf{x}$. The shape variables determine the y-direction positions of nodes 3, 5, 7, 9, and 11, where x_{14} is set for the positions of nodes 3 and 11, x_{15} is set for the positions of nodes 5 and 9, and x_{16} is set for the positions of node 7. The design variables are used to modify the original positions (shown in Figure 4) of those nodes. The bound constraints are set as $-3.00\,\text{m} \le x_i \le 3.00\,\text{m}$ for $i = 14, \ldots, 16$.

By defining a few set of design parameter settings, various versions of PBIL can be obtained as follows.

(i) PBILb5: this optimiser uses $\mathbf{b}_x$ from the best solution $\mathbf{b}$ instead of $\mathbf{w}_x$ from the worst solution $\mathbf{w}$ in step (8) of Algorithm 2. N_I is set to be 5.
(ii) PBILw5: this is PBIL detailed in Algorithm 2, where N_I is set to be 5.
(iii) PBILw5m: this is PBILw5 with GA mutation. Having generated binary populations in steps (2) and (8), The GA mutation is applied to the populations, where each solution has the probability of being mutated as 0.25.
(iv) PBILw1: this is PBIL detailed in Algorithm 2, where N_I is set to be 1.
(v) PBILw10: this is PBIL detailed in Algorithm 2, where N_I is set to be 10.

For AOP1, the population size is set to be 40, whereas the total number of function evaluations for stopping the search procedure is 2,400. For other design problems, the population size is set to be 100, whereas the total number of function evaluations for stopping the search procedure is 15,000. PBIL with various N_I values is set to examine the effect of the inner and outer loops on the search performance. The GA mutation is employed under the assumption that it may help improving PBIL convergence rate. Each optimiser is used to solve the antioptimisation problems 30 runs. Since PBIL cannot

Table 2: Optimum results of AOP2.

MHs	HybridGA		PBILb5		PBILw5		PBILw5m		PBILw1		PBILw10	
	Avrg	Stdev	Avrg	Stdev	Avrg	Stdev	Avrg	Stdev	Avrg	Stdev	Avrg	Stdev
x_1	0.0453	0.0073	0.0500	0.0000	0.0500	0.0000	0.0500	0.0000	0.0500	0.0000	0.0503	0.0018
x_2	0.0463	0.0096	0.0493	0.0025	0.0500	0.0026	0.0497	0.0032	0.0477	0.0043	0.0543	0.0063
x_3	0.0800	0.0000	0.0800	0.0000	0.0800	0.0000	0.0800	0.0000	0.0800	0.0000	0.0807	0.0025
x_4	0.0610	0.0040	0.0603	0.0018	0.0600	0.0000	0.0603	0.0018	0.0600	0.0000	0.0650	0.0068
x_5	0.0500	0.0087	0.0493	0.0025	0.0500	0.0026	0.0500	0.0000	0.0477	0.0043	0.0520	0.0041
x_6	0.0607	0.0025	0.0613	0.0051	0.0610	0.0040	0.0607	0.0025	0.0600	0.0000	0.0627	0.0064
x_7	0.0810	0.0031	0.0800	0.0000	0.0800	0.0000	0.0800	0.0000	0.0800	0.0000	0.0803	0.0018
x_8	0.0517	0.0099	0.0503	0.0018	0.0500	0.0000	0.0500	0.0000	0.0500	0.0000	0.0517	0.0038
x_9	0.0427	0.0052	0.0493	0.0025	0.0500	0.0000	0.0500	0.0000	0.0483	0.0038	0.0493	0.0025
x_{10}	0.0800	0.0000	0.0800	0.0000	0.0800	0.0000	0.0800	0.0000	0.0800	0.0000	0.0803	0.0018
y_1	74.7849	1.1783	77.5938	1.1768	80.0000	0.0000	80.0000	0.0000	80.0000	0.0000	80.0000	0.0000
y_2	171.5082	13.5158	165.3552	7.5152	175.0000	0.0000	175.0000	0.0000	174.9984	0.0089	175.0000	0.0000
$f(\mathbf{x}, \mathbf{y})$	558.7238	30.9474	567.8900	9.9080	568.7844	7.3917	568.2535	6.2552	559.2016	7.1018	594.2857	20.6724
$\max g_i$	−0.0050	0.0000	−0.0050	0.0000	−0.0050	0.0000	−0.0050	0.0000	−0.0050	0.0000	−0.0050	0.0000

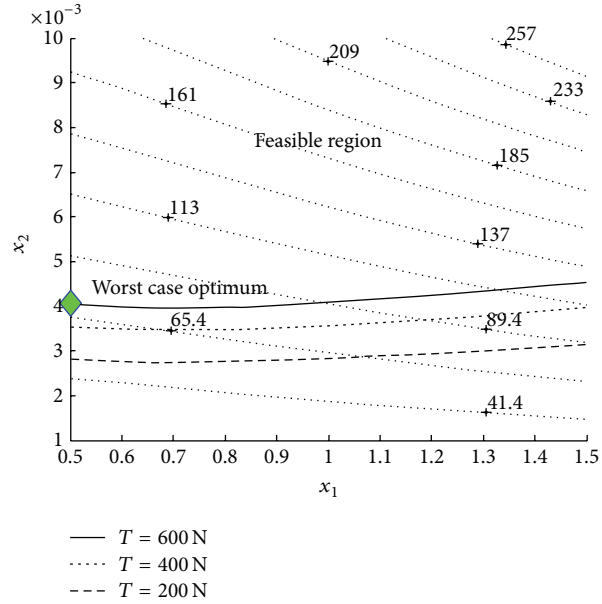

Figure 5: Optimum of AOP1.

deal with design constraints directly, the penalty function technique based on the fuzzy set theory [21] is employed. It should be noted that we have tested using several penalty function techniques earlier, and the fuzzy set theory gives the best results. The metaheuristics employed do not have reliable termination criterion, therefore, their search will be stopped based on the maximum number of function evaluations.

Furthermore, in order to verify the performance of the proposed algorithms, an existing evolutionary algorithm for antioptimisation called a hybrid genetic algorithm [13] will be employed to solve the test problems and compared with the various PBILs. For this performance test, HybridGA uses real codes for design variables. The method of Hooke and Jeeves is used for searching the worst case. The number of good solutions taken for mutation is set to be 10. The roulette wheel selection method is used to select design solutions for crossover operation. The optimiser is terminated when the maximum number of function evaluations set for PBILs in the previous paragraph is reached.

5. Optimum Results

The optimum results of AOP1 are given in Table 1. Figure 5 displays the contour of the objective function and the boundaries of buckling constraints with $F = 200$ N, 400 N, and 600 N. It should be noted that the stress constraints do not affect the feasible region for this design case. From the figure, it is seen that the buckling constraint where $F = 600$ N

Table 3: Optimum results of AOP3.

MHs	HybridGA		PBILb5		PBILw5		PBILw5m		PBILw1		PBILw10	
	Avrg	Stdev	Avrg	Stdev	Avrg	Stdev	Avrg	Stdev	Avrg	Stdev	Avrg	Stdev
x_1	0.0667	0.0106	0.0753	0.0078	0.0707	0.0037	0.0810	0.0243	0.0697	0.0032	0.0817	0.0172
x_2	0.1017	0.0091	0.1533	0.0127	0.1550	0.0201	0.1483	0.0207	0.1500	0.0000	0.1600	0.0242
x_3	0.0800	0.0037	0.0820	0.0076	0.0847	0.0073	0.0850	0.0078	0.0817	0.0046	0.0883	0.0079
x_4	0.0690	0.0109	0.0727	0.0052	0.0750	0.0078	0.0747	0.0082	0.0700	0.0037	0.0800	0.0164
x_5	0.0690	0.0109	0.0770	0.0160	0.0770	0.0084	0.0843	0.0355	0.0750	0.0051	0.0867	0.0121
x_6	0.0660	0.0104	0.0690	0.0061	0.0713	0.0035	0.0737	0.0156	0.0687	0.0043	0.0750	0.0073
x_7	0.1000	0.0000	0.1283	0.0252	0.1500	0.0131	0.1517	0.0207	0.1500	0.0000	0.1500	0.0186
x_8	0.0923	0.0043	0.1027	0.0131	0.0997	0.0018	0.1053	0.0229	0.0993	0.0025	0.1050	0.0185
x_9	0.0680	0.0092	0.0730	0.0065	0.0727	0.0069	0.0767	0.0103	0.0720	0.0081	0.0843	0.0155
x_{10}	0.0680	0.0096	0.0750	0.0078	0.0760	0.0097	0.0793	0.0083	0.0710	0.0031	0.0827	0.0108
x_{11}	0.0657	0.0068	0.0770	0.0099	0.0727	0.0074	0.0770	0.0158	0.0697	0.0032	0.0820	0.0167
x_{12}	0.1500	0.0000	0.1500	0.0000	0.1517	0.0091	0.1517	0.0091	0.1500	0.0000	0.1583	0.0190
x_{13}	0.0777	0.0057	0.0847	0.0090	0.0873	0.0078	0.0907	0.0087	0.0840	0.0056	0.0913	0.0221
y_1	150.0000	0.0000	279.9365	13.8161	297.8886	11.5648	293.5239	21.5257	300.0000	0.0000	299.7019	1.6330
y_2	150.0000	0.0000	278.6706	15.4757	296.4614	19.3818	289.2913	33.1890	300.0000	0.0000	298.5484	7.9508
y_3	150.0000	0.0000	252.3558	33.5946	297.3412	14.5631	289.8240	31.2534	300.0000	0.0000	297.0088	16.3835
y_4	$2.009E+11$	$5.409E+07$	$2.001E+11$	$5.567E+08$	$1.990E+11$	$1.820E+07$	$1.991E+11$	$3.734E+08$	$1.990E+11$	$4.828E+07$	$1.990E+11$	$8.067E+07$
$f(\mathbf{x},\mathbf{y})$	4751.2034	230.5610	5974.5867	363.5549	6222.8573	456.2727	6566.8994	1086.3438	5912.7947	92.7879	7045.4299	1006.9112
$\max g_i$	−0.0050	0.0000	−0.0050	0.0000	−0.0050	0.0000	−0.0050	0.0000	−0.0050	0.0000	−0.0050	0.0000

Table 4: Optimum results of AOP4.

MHs	HybridGA		PBILb5		PBILw5		PBILw5m		PBILw1		PBILw10	
	Avrg	Stdev	Avrg	Stdev	Avrg	Stdev	Avrg	Stdev	Avrg	Stdev	Avrg	Stdev
x_1	0.0467	0.0084	0.0517	0.0053	0.0520	0.0041	0.0513	0.0043	0.0490	0.0031	0.0533	0.0084
x_2	0.0477	0.0107	0.0510	0.0040	0.0503	0.0018	0.0513	0.0035	0.0507	0.0045	0.0543	0.0082
x_3	0.0833	0.0048	0.0867	0.0055	0.0863	0.0067	0.0867	0.0048	0.0860	0.0050	0.0873	0.0069
x_4	0.0603	0.0049	0.0577	0.0082	0.0607	0.0098	0.0577	0.0068	0.0563	0.0076	0.0610	0.0099
x_5	0.0570	0.0070	0.0543	0.0068	0.0590	0.0092	0.0533	0.0071	0.0553	0.0078	0.0583	0.0105
x_6	0.0613	0.0043	0.0603	0.0072	0.0617	0.0079	0.0603	0.0093	0.0577	0.0043	0.0653	0.0107
x_7	0.0720	0.0130	0.0783	0.0046	0.0773	0.0058	0.0797	0.0056	0.0760	0.0081	0.0793	0.0087
x_8	0.0457	0.0082	0.0507	0.0037	0.0500	0.0037	0.0507	0.0037	0.0490	0.0031	0.0523	0.0082
x_9	0.0440	0.0056	0.0510	0.0031	0.0507	0.0025	0.0497	0.0032	0.0483	0.0038	0.0507	0.0045
x_{10}	0.0787	0.0035	0.0787	0.0051	0.0797	0.0041	0.0770	0.0047	0.0780	0.0048	0.0810	0.0055
x_{11}	0.0518	0.1773	0.3132	0.2705	0.1478	0.3773	0.3319	0.3448	0.2337	0.3527	0.2345	0.4409
x_{12}	0.5991	0.1766	0.5610	0.1850	0.6211	0.1079	0.5072	0.2017	0.6345	0.1444	0.5174	0.1896
x_{13}	−0.6919	0.1381	−0.5828	0.1442	−0.5369	0.2001	−0.4271	0.2176	−0.6712	0.1039	−0.4691	0.2160
x_{14}	0.6804	0.1490	0.5697	0.1723	0.5550	0.1935	0.5924	0.1489	0.6494	0.1410	0.5549	0.1754
y_1	75.3793	1.2182	78.1703	1.5065	80.0000	0.0000	80.0000	0.0000	80.0000	0.0000	80.0000	0.0000
y_2	170.9637	7.2167	166.1746	7.4693	175.0000	0.0000	175.0000	0.0000	175.0000	0.0000	175.0000	0.0000
$f(\mathbf{x}, \mathbf{y})$	479.4000	34.7275	529.8728	21.6285	535.8320	21.6881	534.5283	22.3252	501.9159	11.7035	574.2029	37.1328
$\max g_i$	−0.0047	0.0009	−0.0050	0.0000	−0.0050	0.0000	−0.0050	0.0000	−0.0050	0.0000	−0.0050	0.0000

gives the most narrow feasible region and therefore leads to the worst case results. The optimum for the worst case scenario is $\mathbf{x} = \{0.5, 0.0041\}^T$ and $y = 600$ N. According to the results obtained from the various optimisers, HybridGA cannot capture the worst case for all runs, while PBILs can find the worst case for some optimisation runs. The best solutions obtained by using five versions of PBIL are the same, that is, $\mathbf{x} = \{0.5, 0.0042\}^T$ and $y = 600$ N, which can be classified as a near optimum of the design problem. Based on the worst cases being explored, PBILw10 gives the best results, while the second best is PBILw1.

The optimum results of AOP2 obtained from the various optimisers are given in Table 2. For this design problem, it is obvious that the worst possible case for the 10-bar truss is when $\{F_1, F_2\}^T = \{80, 175\}^T$ N. From the results, it can be seen that HybridGA and PBILb5 fail to explore the worst case, while other optimiser which are based on using $\mathbf{w}_x$ in step (8) of Algorithm 2 can find the worst case for almost every optimisation run. According to the mean value of objective function from 30 runs, PBILw1 gives the best results. However, it is found that PBILw1 cannot find the worst case for all 30 runs, although the values are not significant. This is due to the lower number of inner loops used to explore the worst case. In contrast, PBILw10 gives the worst results among PBILw variants because it spends less time in searching for the optimum mass. By comparing between PBILw5 and PBILw5m, the GA mutation gives insignificant improvement for PBIL.

The optimum results of AOP3 obtained from the various PBILs are given in Table 3. The worst case is $\{F_1, F_2, F_3, E\}^T = \{1000, 1000, 1000, 199.0 \times 10^9\}^T$. Similar conclusions as with the AOP2 case can be drawn except that PBILw5 is slightly better than PBILw5m. Table 4 shows the results of AOP4. Similar to the first two cases, HybridGA and PBILb5 fail to explore the worst case scenario, while, for this case, all the versions of PBILw can capture the worst case for all runs. PBILw1 gives the best results, while the worst among PBILw versions is PBILw10. For the fifth design case as shown in Table 5, PBILw optimisers can capture the worst case scenario for almost 30 runs, while PBILb5 and HybridGA fail to find out the worst case solutions. The best optimiser is PBILw1 whereas PBILw5m is slightly better than PBILw5.

Based on the standard deviation, the variants of PBILw are rather consistent. From the constraint violation values in Tables 1–5, it can be said that the fuzzy set theory is efficient and effective for constrained truss design. Table 6 shows the total number of worst cases captured by the optimisers having solved the design problems for 30 runs. It can be seen that PBILw is effective for exploring the worst case scenarios for AOP2-5. PBILw10 fails to capture the worst case once for AOP3 and AOP5, although it spends more time to search for the worst case scenario. This can possibly be due to a premature convergence of the algorithm. For the first design problem, all the optimisers have more difficulty to search for the worst case.

The best structures obtained from running PBILw5, PBILw5m, PBILw1, and PBILw10 for AOP2, AOP3, AOP4, and AOP5 are illustrated in Figures 6, 7, 8, and 9, respectively. The structures obtained from the 4 optimisers for each design case are rather similar in size and shape to each other. In cases of the design problems AOP2-5, with 15,000 function evaluations and population size of 100, PBILw1 has a number of outer loops as $N_O = 75$ loops, while PBILw5 and PBILw10 have only 25 and 14 loops, respectively. In the test problems, the number of inner loops $N_I = 1$ is adequate to search

Table 5: Optimum results of AOP5.

MHs	HybridGA		PBILb5		PBILw5		PBILw5m		PBILw1		PBILw10	
	Avrg	Stdev	Avrg	Stdev	Avrg	Stdev	Avrg	Stdev	Avrg	Stdev	Avrg	Stdev
x_1	0.0787	0.0157	0.0787	0.0082	0.0813	0.0111	0.0800	0.0105	0.0730	0.0065	0.0870	0.0115
x_2	0.1233	0.0286	0.1533	0.0127	0.1483	0.0091	0.1500	0.0131	0.1500	0.0000	0.1577	0.0311
x_3	0.0830	0.0174	0.0780	0.0119	0.0833	0.0175	0.0810	0.0171	0.0717	0.0087	0.0903	0.0227
x_4	0.0770	0.0124	0.0810	0.0212	0.0787	0.0111	0.0747	0.0104	0.0727	0.0087	0.0883	0.0261
x_5	0.0807	0.0141	0.0770	0.0079	0.0803	0.0096	0.0803	0.0110	0.0717	0.0065	0.0847	0.0117
x_6	0.0793	0.0131	0.0740	0.0062	0.0783	0.0099	0.0770	0.0088	0.0710	0.0031	0.0857	0.0205
x_7	0.1200	0.0249	0.1483	0.0091	0.1533	0.0183	0.1567	0.0217	0.1517	0.0091	0.1557	0.0310
x_8	0.0893	0.0187	0.0857	0.0176	0.0840	0.0214	0.0840	0.0181	0.0750	0.0107	0.0963	0.0318
x_9	0.0780	0.0140	0.0807	0.0098	0.0827	0.0120	0.0777	0.0094	0.0747	0.0094	0.0833	0.0163
x_{10}	0.0810	0.0106	0.0783	0.0095	0.0783	0.0105	0.0777	0.0101	0.0713	0.0035	0.0817	0.0162
x_{11}	0.0817	0.0109	0.0773	0.0098	0.0823	0.0205	0.0767	0.0152	0.0707	0.0052	0.0850	0.0242
x_{12}	0.1500	0.0000	0.1533	0.0127	0.1500	0.0000	0.1500	0.0000	0.1500	0.0000	0.1540	0.0234
x_{13}	0.0857	0.0161	0.0823	0.0168	0.0860	0.0203	0.0823	0.0165	0.0737	0.0089	0.0940	0.0302
x_{14}	−1.3764	0.8037	−1.9818	0.7962	−1.8035	0.7824	−1.5169	0.9604	−1.8596	0.7010	−1.5277	1.0779
x_{15}	−0.6342	0.7655	−0.9292	1.0364	−0.6835	1.0393	−0.5185	0.9608	−0.7484	0.9619	−0.5791	1.3451
x_{16}	−0.4087	0.7922	−0.3812	1.1555	−0.3243	1.1576	−0.1742	1.0618	−0.4516	0.9760	−0.3193	1.3226
y_1	194.0161	59.2515	238.8221	48.0552	300.0000	0.0000	300.0000	0.0000	300.0000	0.0000	299.5406	2.5164
y_2	168.5592	35.6225	251.6178	31.7033	300.0000	0.0000	300.0000	0.0000	300.0000	0.0000	296.8964	16.9992
y_3	239.6624	57.7826	231.6178	47.0528	300.0000	0.0000	300.0000	0.0000	300.0000	0.0000	299.4868	2.8109
y_4	$1.995E+11$	$6.119E+08$	$1.999E+11$	$5.890E+08$	$1.990E+11$	$0.000E+00$	$1.990E+11$	$0.000E+00$	$1.990E+11$	$0.000E+00$	$1.990E+11$	$1.902E+08$
$f(\mathbf{x},\mathbf{y})$	5222.3215	813.5479	5440.5355	524.4721	5616.7374	429.4775	5679.4132	654.9014	4938.2933	266.2513	6585.0710	1474.1376
$\max g_i$	−0.0050	0.0000	−0.0050	0.0000	−0.0050	0.0000	−0.0050	0.0000	−0.0050	0.0000	68.9978	377.9440

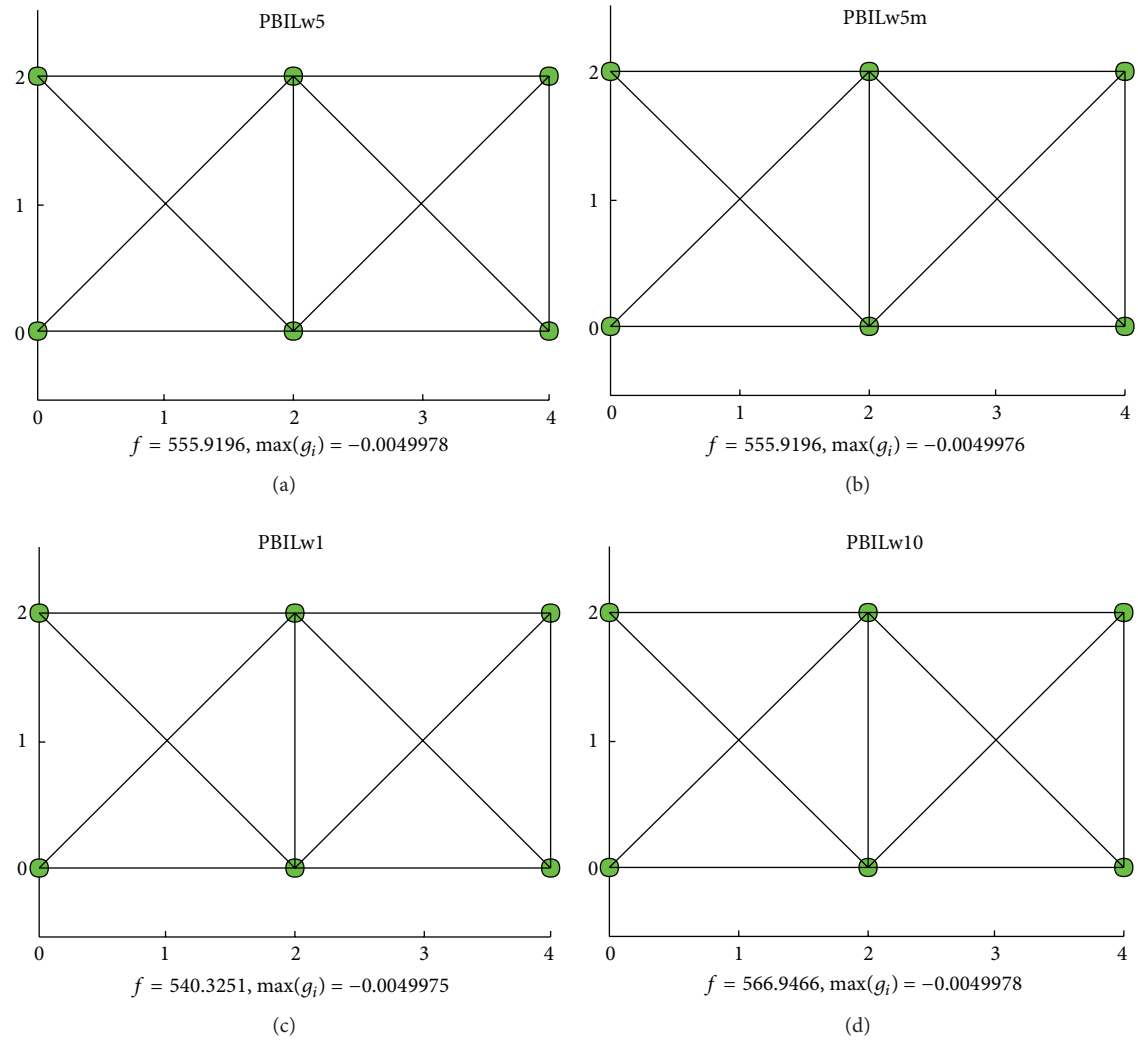

Figure 6: Optimum structures of AOP2 from various optimisers.

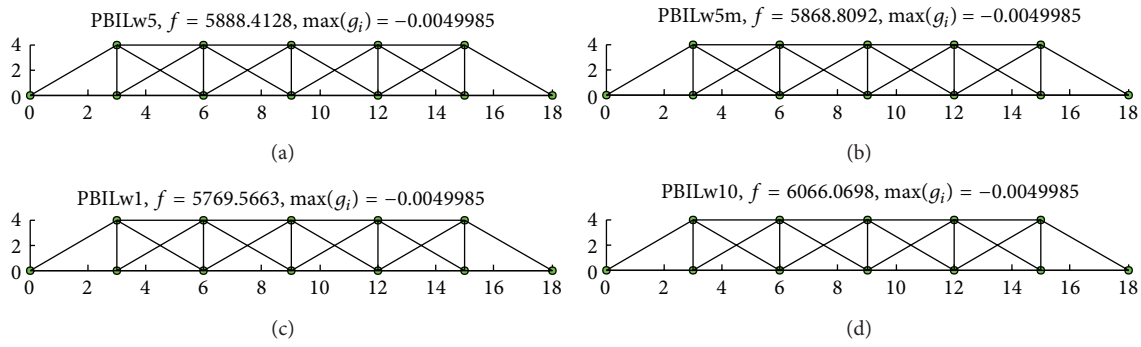

Figure 7: Optimum structures of AOP3 from various optimisers.

for the worst cases for all design cases; thus, PBILw1 which spends more time to search for the optimum solution of $\mathbf{x}$ gives the best results for all design cases. In order to use the proposed PBIL for antioptimisation of other engineering systems, predefining the proper value of N_I is important since it can affect the search performance. This relies on several factors such as the size of variables $\mathbf{x}$ and $\mathbf{y}$. The hybrid genetic algorithm, on the other hand, is not efficient for the truss design problems. However, optimisation parameter settings can affect its search performance.

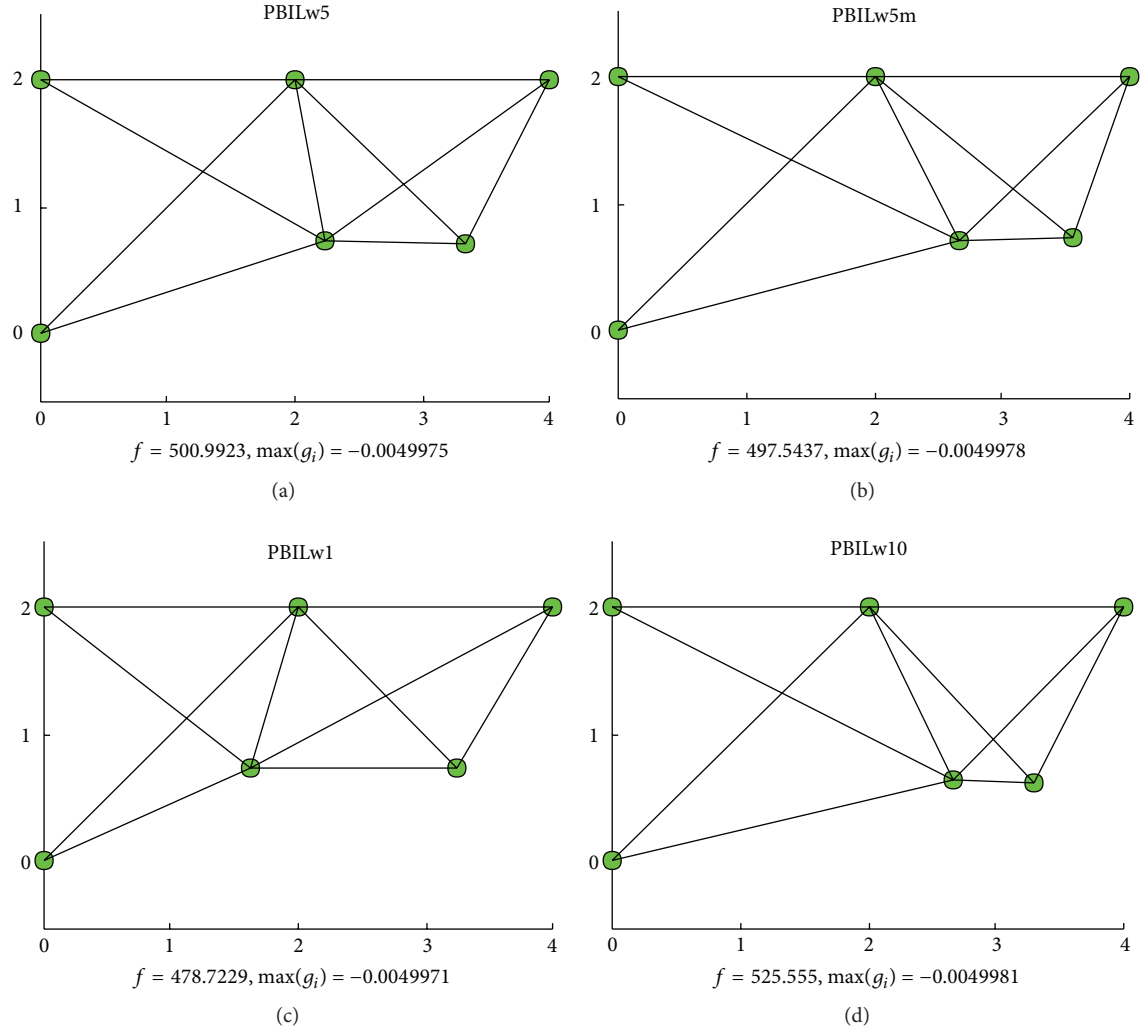

Figure 8: Optimum structures of AOP4 from various optimisers.

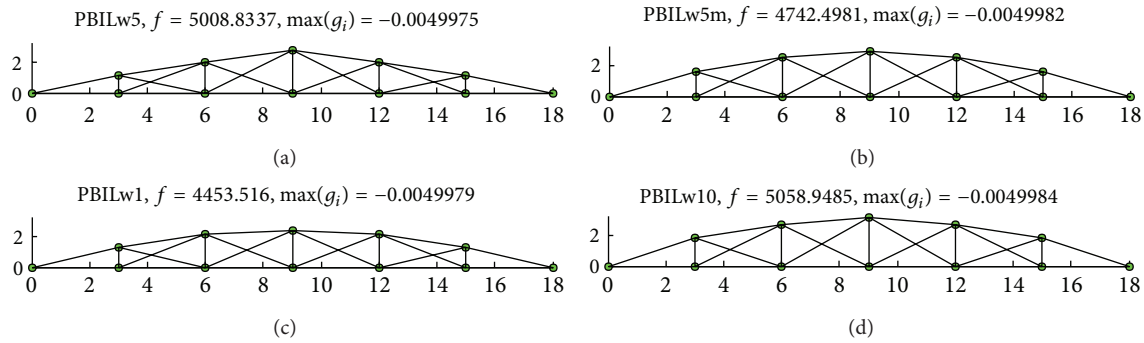

Figure 9: Optimum structures of AOP5 from various optimisers.

6. Conclusions and Discussion

A metaheuristic based on PBIL for antioptimisation of trusses is developed, and it is termed two-level PBIL. The method consists of two levels for two searching tasks. The first level is an outer loop used to explore the optimum of common design variables, while the inner loop is used to find the worst case scenario of the variables with uncertainties. It is shown that when searching for the worst case, the function evaluation based on the current worst solution gives better search results than using the current best solution. The GA mutation applied to a binary population of PBIL does not have significantly impact on PBILw search performance. The results show that the proposed PBILw is an efficient optimiser

Table 6: Number of worst cases found by the optimisers.

MHs	AOP1	AOP2	AOP3	AOP4	AOP5
HybridGA	0	0	0	0	0
PBILb5	1	0	0	0	0
PBILw5	5	30	29	30	30
PBILw5m	8	30	27	30	30
PBILw1	8	29	24	30	30
PBILw10	9	30	29	30	29

for tackling a truss antioptimisation problem. Moreover, it is superior to the hybridGA. The performance of PBILw, to a great extent, relies on the predefined number of inner loops for searching the worst case. It can be concluded that the concept of using probability vectors to represent binary populations in PBIL is powerful for dealing with antioptimisation. For future work, the hybrid approach of PBIL will be studied. Also, the applications of the two-level PBIL will be employed to tackle other antioptimisation problems.

Acknowledgments

The authors are grateful for the support from The Royal Golden Jubilee Ph. D. Program (Grant no. PHD/0145/2553) and the Thailand Research Fund (Grant no. BRG5580017).

References

[1] A. Kaveh and S. Talatahari, "Particle swarm optimizer, ant colony strategy and harmony search scheme hybridized for optimization of truss structures," *Computers and Structures*, vol. 87, no. 5-6, pp. 267–283, 2009.

[2] P. B. Thanedar, J. S. Arora, C. H. Tseng, O. K. Lim, and G. J. Park, "Performance of some SQP algorithms on structural design problems," *International Journal for Numerical Methods in Engineering*, vol. 23, no. 12, pp. 2187–2203, 1986.

[3] A. Kaveh and S. Talatahari, "Particle swarm optimizer, ant colony strategy and harmony search scheme hybridized for optimization of truss structures," *Computers and Structures*, vol. 87, no. 5-6, pp. 267–283, 2009.

[4] H. M. Gomes, "Truss optimization with dynamic constraints using a particle swarm algorithm," *Expert Systems with Applications*, vol. 38, no. 1, pp. 957–968, 2011.

[5] W. A. Bennage and A. K. Dhingra, "Single and multiobjective structural optimization in discrete-continuous variables using simulated annealing," *International Journal for Numerical Methods in Engineering*, vol. 38, no. 16, pp. 2753–2773, 1995.

[6] N. Pholdee and S. Bureerat, "Performance enhancement of multiobjective evolutionary optimizers for truss design using an approximate gradient," *Computers and Structures*, vol. 106-107, pp. 115–124, 2012.

[7] C. Noilublao and S. Bureerat, "Topology and sizing optimization of trusses with adaptive ground finite elements using multiobjective PBIL," *Advanced Materials Research*, vol. 308–310, pp. 1116–1121, 2011.

[8] N. Noilublao and S. Bureerat, "Simultaneous topology, shape and sizing optimisation of a three-dimensional slender truss tower using multiobjective evolutionary algorithms," *Computers and Structures*, vol. 89, pp. 2531–2538, 2011.

[9] B. M. Adams, M. S. Eldred, and J. W. Wittwer, "Reliability-based design optimization for shape design of compliant micro-electro-mechanical systems," in *Proceedings of the 11th AIAA/ISSMO Multidisciplinary Analysis and Optimization Conference*, pp. 1042–1056, AIAA, September 2006.

[10] K. Deb, S. Gupta, D. Daum, J. Branke, A. K. Mall, and D. Padmanabhan, "Reliability-based optimization using evolutionary algorithms," *IEEE Transactions on Evolutionary Computation*, vol. 13, no. 5, pp. 1054–1074, 2009.

[11] M. Lombardi and R. T. Haftka, "Anti-optimization technique for structural design under load uncertainties," *Computer Methods in Applied Mechanics and Engineering*, vol. 157, no. 1-2, pp. 19–31, 1998.

[12] G. Venter and R. T. Haftka, "Two-species genetic algorithm for design under worst case conditions," *Evolutionary Optimization*, vol. 2, no. 1, pp. 1–19, 2000.

[13] N. Wang and Y. Yang, "Optimization of structures under load uncertainties based on hybrid genetic algorithm," in *Evolutionary Computation*, W. P. dos Santos, Ed., pp. 321–340, I-Tech, Vienna, Austria, 2009.

[14] A. R. Yıldız, "A novel hybrid immune algorithm for global optimization in design and manufacturing," *Robotics and Computer-Integrated Manufacturing*, vol. 25, no. 2, pp. 261–270, 2009.

[15] I. Durgun and A. R. Yıldız, "Structural design optimization of vehicle components using cuckoo search algorithm," *Materials Testing*, vol. 54, no. 3, pp. 185–188, 2012.

[16] S. L. Tilahun and H. C. Ong, "Modified firefly algorithm," *Journal of Applied Mathematics*, vol. 2012, Article ID 467631, 12 pages, 2012.

[17] X. Cai, S. Fan, and Y. Tan, "Light responsive curve selection for photosynthesis operator of APOA," *International Journal of Bio-Inspired Computation*, vol. 4, no. 6, pp. 373–379, 2012.

[18] Z. Cui, F. Gao, Z. Cui, and J. Qu, "A second nearest-neighbor embedded atom method interatomic potential for Li-Si Alloys," *Journal of Power Sources*, vol. 207, p. 150, 2012.

[19] S. Baluja, "Population-based incremental learning: a method for integrating genetic search based function optimization and competitive learning," Tech. Rep. CMU_CS_95_163, Carnegie Mellon University, 1994.

[20] Z. Qiu and X. Wang, "Structural anti-optimization with interval design parameters," *Structural and Multidisciplinary Optimization*, vol. 41, no. 3, pp. 397–406, 2010.

[21] F. Y. Cheng and D. Li, "Fuzzy set theory with genetic algorithm in constrained structural optimization," in *Proceedings of the 1st US-Japan Joint Seminar on Structural Optimization*, pp. 55–66, Advances in Structural optimization, April 1997.

Hindawi Publishing Corporation
Journal of Applied Mathematics
Volume 2013, Article ID 823863, 11 pages
http://dx.doi.org/10.1155/2013/823863

Research Article

The Complex Network Synchronization via Chaos Control Nodes

Yin Li[1,2] and Chun-long Zheng[1]

[1] *School of Mathematics and Information Science and School of Physics and Electromechanical Engineering, Shaoguan University, Shaoguan, Guangdong 512005, China*
[2] *Department of Mathematics and Computational Science, Sun Yat-sen University, Guangzhou, 510275, China*

Correspondence should be addressed to Chun-long Zheng; clzheng@yahoo.cn

Received 21 July 2012; Accepted 4 February 2013

Academic Editor: Xiaojun Wang

Copyright © 2013 Y. Li and C.-l. Zheng. This is an open access article distributed under the Creative Commons Attribution License, which permits unrestricted use, distribution, and reproduction in any medium, provided the original work is properly cited.

We investigate chaos control nodes of the complex network synchronization. The structure of the coupling functions between the connected nodes is obtained based on the chaos control method and Lyapunov stability theory. Moreover a complex network with nodes of the new unified Loren-Chen-Lü system, Coullet system, Chee-Lee system, and the New system is taken as an example; numerical simulations are used to verify the effectiveness of the method.

1. Introduction

Since the most famous random graph model was proposed by Erdös and Rényi [1], the complex network has attracted much attention in many fields of research, such as biology, physics, computer networks, the World Wide Web (WWW) [2], and so on. Network synchronization has obvious advantages, it has great application value in practice. Therefore, Atay et al. [3] studied synchronization of complex network when delays exist among the nodes; Motter et al. [4] studied the influence of coupling strength on the synchronizing ability of a complex network; Timme et al. [5] studied the web synchronization law of pulse-coupled dynamical systems; Checco et al. [6] studied the synchronization of random web. Lü et al. [7] constructed general complex dynamical networks and studied the synchronization; Lu and Chen [8] studied synchronization analysis of linearly coupled networks of discrete time systems; Han and Lu [9] studied the changes of synchronization ability of coupled networks from ring networks to chain networks; He and Yang [10] studied adaptive synchronization in nonlinearly coupled dynamical networks; Hung et al. [11] studied globally generalized synchronization in scale-free networks.

Recently, network synchronization has been an important part of the dynamic study of complex network. It has aroused great interest of scholars both domestically and abroad to build weighted network models and study the characteristics of them. Lü et al. [7] studied chaos synchronization of general complex dynamic networks. Gao et al. [12] realized the adaptive synchronization of complex network. Pei et al. [13] made statistical analysis of a class of real networks; Barrat et al. [14] presented a weighted network model, and studied its dynamic character; Atay et al. [15] studied the synchronization of a complex network with time delay. Hung et al. [11] realized the generalized synchronization of a scale-free network. Qin and Yu [16] achieved the synchronization of the star-network of hyperchaotic Rossler systems. In addition to the above researches, much other work [17, 18] in the field have been done, and complex network synchronization become a focus of attention, such as a random network synchronization, small-world network synchronization, scale-free network synchronization, and so on. However, universal synchronization methods of weighted network still need further exploration and study.

The motivation in this paper lies in the complex network synchronization and chaos control importance. Network synchronization is one of the most practical and valuable issues. A synchronization of network means the situation in which the output of all nodes in the study of the complex network is consistent with any given external input signal under a certain condition. The working mechanism of a single chaotic system to track any given external input signal is relatively interesting

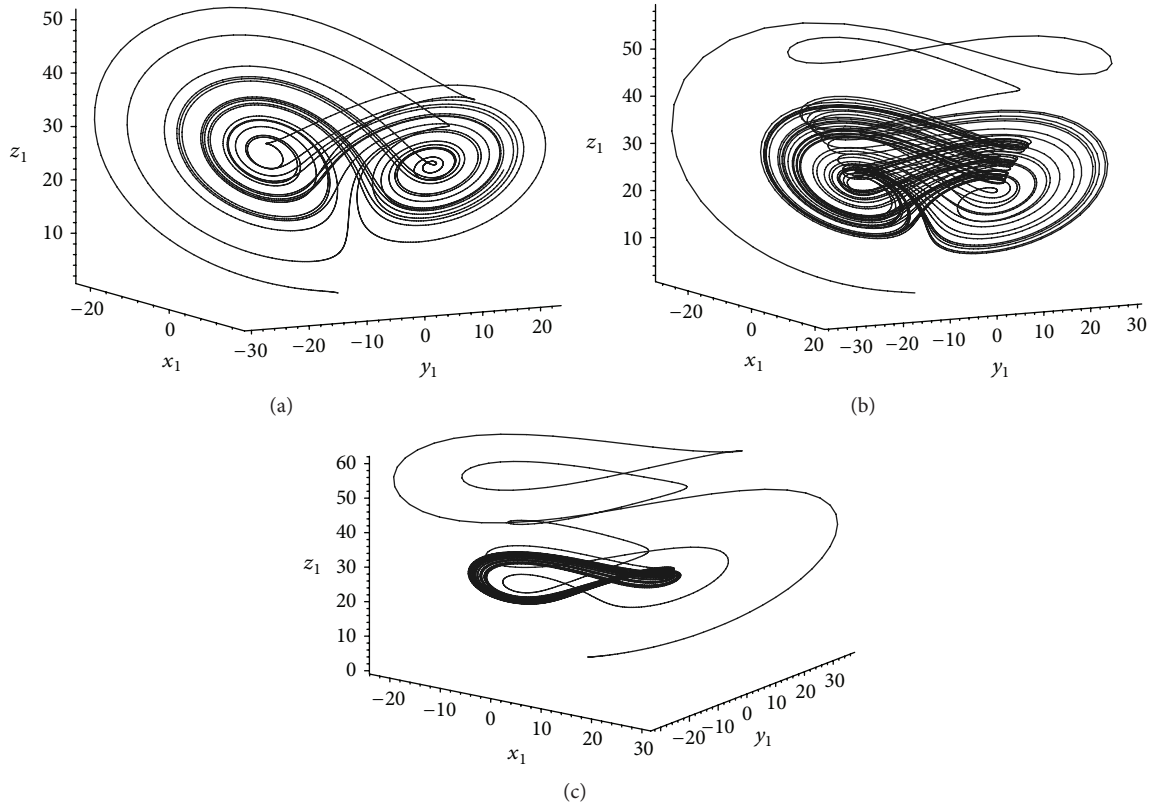

Figure 1: Generlized chaotic attractors: (a) Lorenz, (b) Lü, (c) Chen.

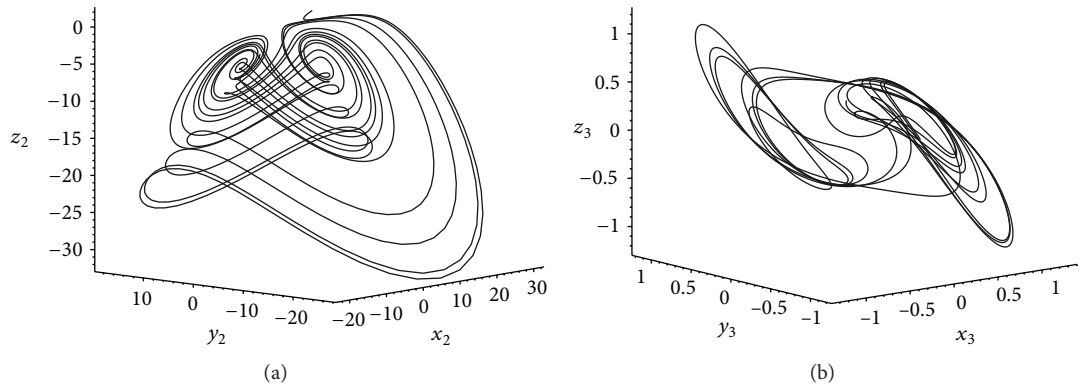

Figure 2: The chaos attractor of new chaotic system (a) and the Coullet system (b).

and significance. Numerical simulations are used to verify the effectiveness of the proposed techniques.

It is organized as follows. Firstly, the theory and the method are presented in Section 2. Then, different order chaotic systems are adopted as the nodes of this complex network; the structure of the coupling functions among the connected nodes is obtained based on Lyapunov stability theory. With the help of symbolic computation, the temporal evolution of variables and node interaction of the dynamic equation are discussed and simulated by computer in Section 3. The theoretical analysis and the numerical simulations show that this is a universal method and the number of the nodes does not affect the stability of the whole network. Finally, the conclusions are given in Section 4.

2. Theory and Method

We summarized the main steps for the complex network synchronization based on Lü et al. [19–23] and Chen et al. [24–27], as follows.

Step 1. Assume the state of node i is x_i, where $x_i = (x_{i1}, x_{i2}, \ldots, x_{in})^T$ and $x_{i1}, x_{i2}, \ldots, x_{in} \epsilon R^n$, then the dynamic

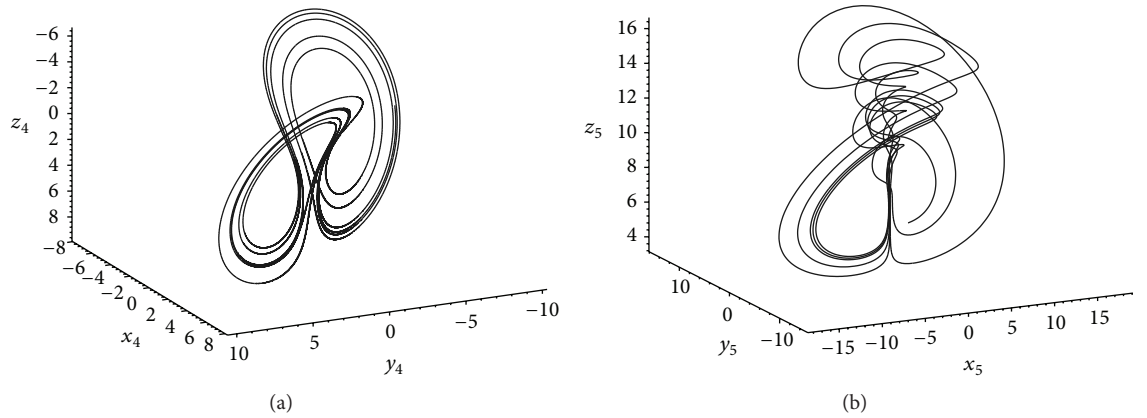

Figure 3: The chaos attractor of (14) system (a) and Chee-Lee system (b).

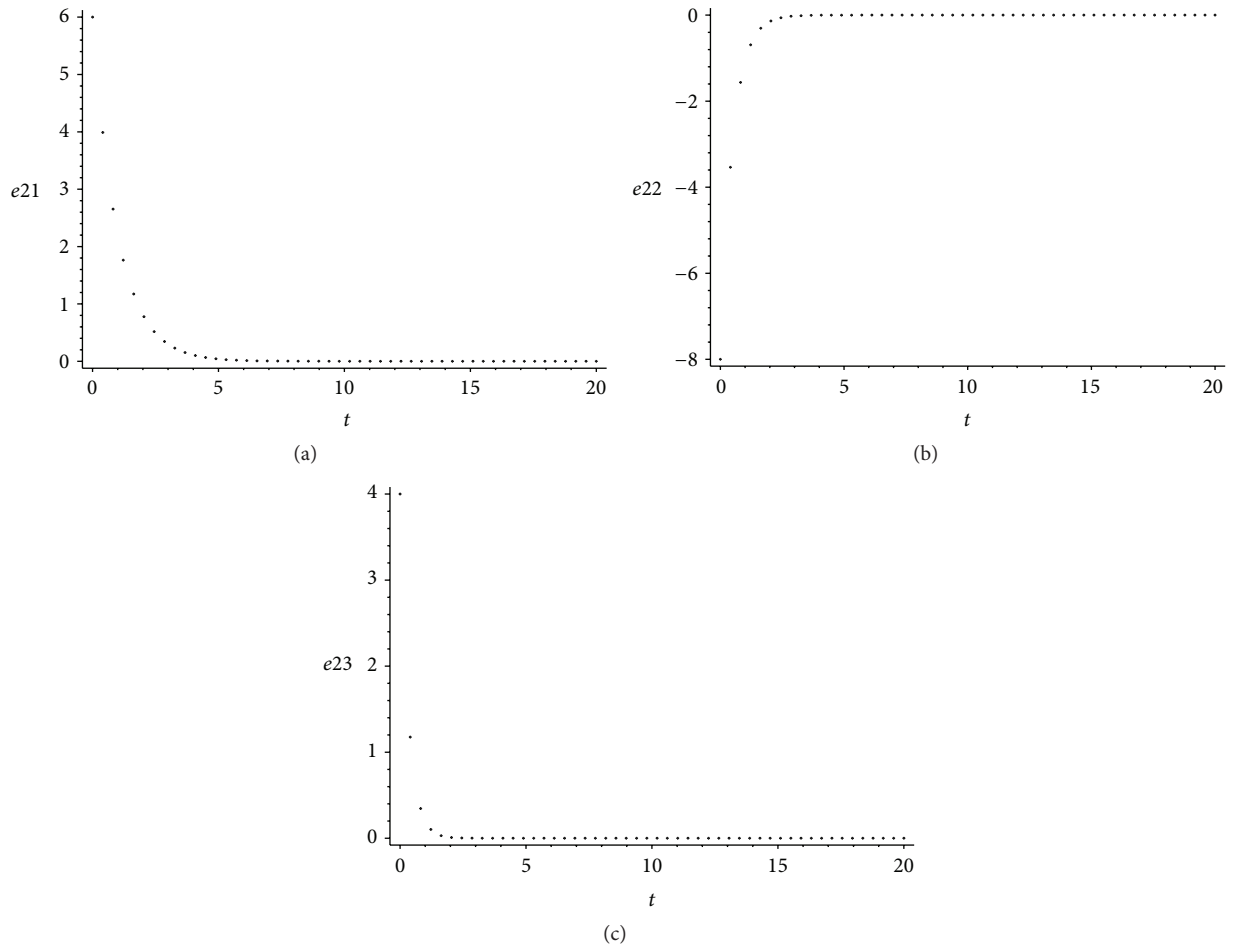

Figure 4: Network synchronization errors between node 1 and node 2.

function for node i without coupling can be described as

$$\dot{x}_i = f_i(x_i) = L_i(x_i) + S_i(x_i), \tag{1}$$

where $L_i(x_i) = (A_i - B_i)x_i$, A_i is the linear coefficient matrix of the system, and B_i is the coefficient matrix of control gain.

Step 2. Considering the coupling of network, the dynamic function for node i can be described as

$$\begin{aligned}\dot{x}_i &= f_i(x_i) + g_i(x_1, x_2, \ldots, x_m) \\ &= (A_i - B_i)x_i + S_i(x_i) + g_i(x_1, x_2, \ldots, x_m),\end{aligned} \tag{2}$$

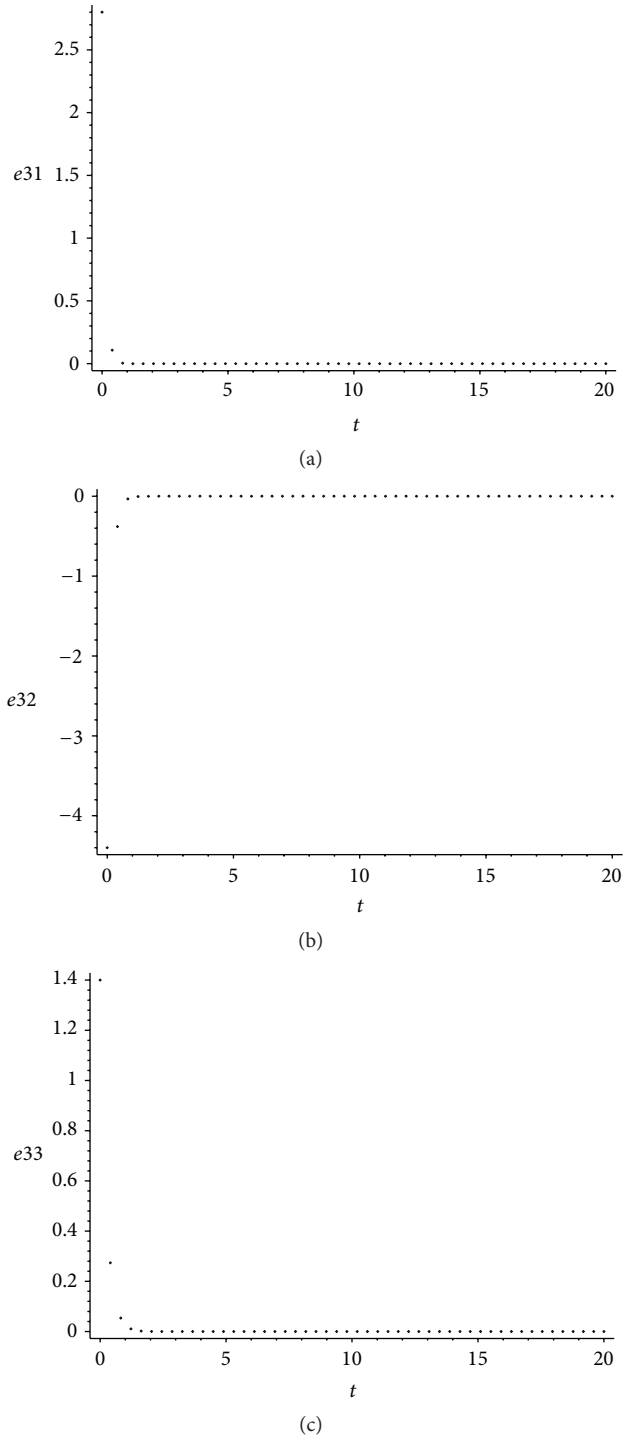

Figure 5: Network synchronization errors between node 2 and node 3.

where $g_i(x_1, x_2, \ldots, x_n)$ denotes the coupling function. The proportional scale for node i is α_i, then we will have $\alpha_i = \mathrm{diag}(\alpha_{i1}, \alpha_{i2}, \ldots, \alpha_{in})$.

Step 3. The errors between the state variables of the network are defined as

$$e_i = \alpha_i x_i + \alpha_{i+1} x_{i+1}. \tag{3}$$

We obtain from (2) and (3)

$$\begin{aligned}
\dot{e}_i &= \alpha_i \dot{x}_i + \alpha_{i+1} \dot{x}_{i+1} \\
&= \alpha_i \left[\left(A_i - B_i \right) x_i + S_i \left(x_i \right) + g_i \right] \\
&\quad + \alpha_{i+1} \left[\left(A_{i+1} - B_{i+1} \right) x_{i+1} + S_{i+1} \left(x_{i+1} \right) + g_{i+1} \right] \\
&= \left(A_i - B_i \right) e_i + S_i \alpha_i + \alpha_i g_i + \alpha_{i+1} \left(A_{i+1} - B_{i+1} \right) x_{i+1} \\
&\quad + \alpha_{i+1} S_{i+1} + \alpha_{i+1} g_{i+1} - \left(A_i - B_i \right) \alpha_{i+1} x_{i+1} \\
&= \left(A_i - B_i \right) e_i + \left[\left(A_{i+1} - B_{i+1} \right) - \left(A_i - B_i \right) \right] \alpha_{i+1} x_{i+1} \\
&\quad + \Delta S_i \left(x_i, x_{i+1} \right) + \Delta g_i \left(x_i, x_{i+1} \right) \\
&= \left(A_i - B_i - K_i \right) e_i + \left[\left(A_{i+1} - B_{i+1} \right) - \left(A_i - B_i \right) \right] \alpha_{i+1} x_{i+1},
\end{aligned} \tag{4}$$

where $\Delta S_i(x_i, x_{i+1}) = \alpha_i S_i + \alpha_{i+1} S_{i+1}$, $\Delta g_i(x_i, x_{i+1}) = \alpha_i g_i + \alpha_{i+1} g_{i+1} + K_i e_i$.

Step 4. Choose $\Delta g_i(x_i, x_{i+1}) = -\Delta S_i(x_i, x_{i+1}) + K_i e_i$, then we will have

$$\alpha_j g_j = -\alpha_1 g_1 - \alpha_1 S_1 \left(x_1 \right) - \alpha_j S_j \left(x_j \right) + k \left(\alpha_1 x_1 + \alpha_j x_j \right), \quad \left(j = 2, 3, \ldots, m \right). \tag{5}$$

If we choose node 1 as target node, then the coupling function of node j $(j = 2, 3, m)$ can be described as

$$g_j = -\frac{\alpha_1}{\alpha_j} g_1 - \frac{\alpha_1}{\alpha_j} S_1 \left(x_1 \right) - S_j \left(x_j \right) + k \left(\frac{\alpha_1}{\alpha_j} x_1 + x_j \right). \tag{6}$$

In order to realize the synchronization of the complex network, if we choose other node as target node, the coupling functions of all nodes can also be obtained.

Step 5. Constructing the Lyapunov function according to the weighted complex network with different nodes,

$$V = \frac{1}{2} \sum_{i=1}^{m-1} e_i^2, \tag{7}$$

and considering (3) and (4), we can obtain the derivative form of V as

$$\begin{aligned}
\dot{V} &= \sum_{i=1}^{m-1} e_i \dot{e}_i \\
&= \sum \left\{ \left(A_i - B_i - K_i \right) e_i \right. \\
&\qquad \left. + \left[\left(A_{i+1} - B_{i+1} \right) - \left(A_i - B_i \right) \right] \alpha_{i+1} x_{i+1} \right\} e_i.
\end{aligned} \tag{8}$$

From (8), we can easily see that if

$$A_i \le B_i + K_i, \qquad A_{i+1} = B_{i+1} + A_i - B_i. \tag{9}$$

Then

$$\dot{V} \le 0. \tag{10}$$

According to Lyapunov stability theory [20] and the weighted complex network [19, 20, 28], the synchronization of the complex network can be realized.

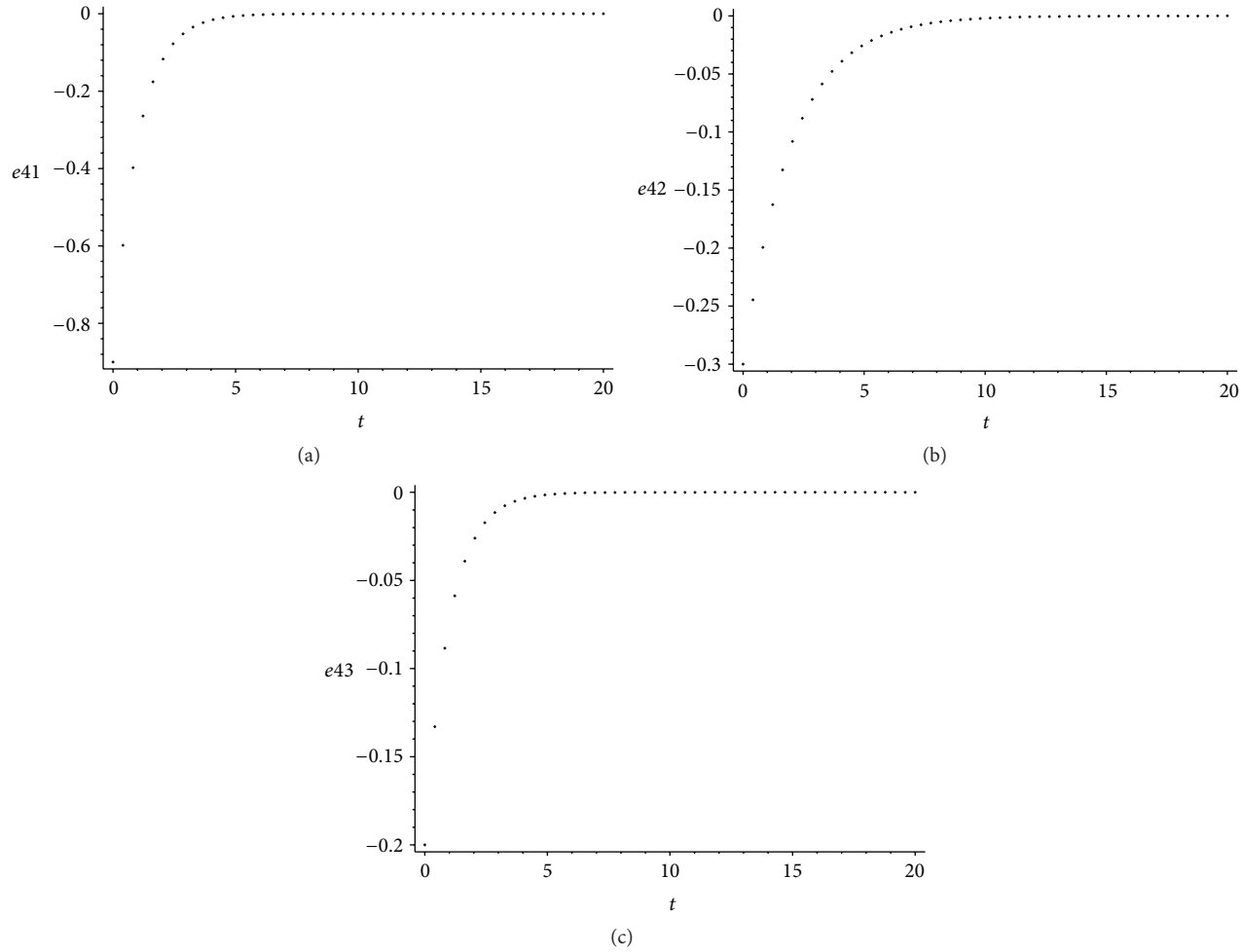

Figure 6: Network synchronization errors between node 3 and node 4.

3. Application of Chaos Control Method to the Network Synchronization

The unified chaotic system, the New system, Coullet system, and Chee-Lee system are taken as nodes of the network to show the synchronization mechanism mentioned above. Simulation is made as the number of the nodes is $m = 5$.

The dynamic equation of the unified chaotic system [21, 29] is presented as follows:

$$\begin{aligned} \dot{x}_1 &= (25\alpha + 10)\left(y_1 - x_1\right), \\ \dot{y}_1 &= (28 - 35\alpha)\, x_1 - x_1 z_1 + (29\alpha - 1)\, y_1, \\ \dot{z}_1 &= x_1 y_1 - \frac{8+\alpha}{3} z_1, \end{aligned} \tag{11}$$

where $\alpha \in [-0.0016, 1.15]$. When $-0.0016 < \alpha < 0.8$, LCL system (11) belongs to the generalized Lorenz system [30]; when $\alpha = 0.8$, LCL system (11) belongs to the generalized Lü system [23]; when $0.8 < \alpha < 1.15$ LCL system (11) belongs to the generalized Chen system [31]. Figures 1(a)–1(c) display these chaotic attractors of the generalized Lorenz system ($\alpha = 0.2$), the generalized Lü system ($\alpha = 0.8$), and the generalized Chen system ($\alpha = 1.12$), respectively.

The new chaotic system of three-dimensional quadratic autonomous ordinary differential equations [22], which can display the chaotic attractors:

$$\begin{aligned} \dot{x}_2 &= -\frac{a_2 b_2}{a_2 + b_2} x_2 - y_2 z_2 + c_2, \\ \dot{y}_2 &= a_2 y_2 + x_2 z_2, \\ \dot{z}_2 &= b_2 z_2 + x_2 y_2, \end{aligned} \tag{12}$$

where a_2, b_2, and c_2 are real constants; and x, y, and z are status variables. This system is found to be chaotic in a wide parameter range and has many interesting complex dynamical characteristics. The system is chaotic for the parameters $a_2 = -10$, $b_2 = -4$, and $\|c\| = 19.2$; it displays the chaotic attractor as shown in Figure 2(a). Detailed dynamic properties of this system can be found in [22].

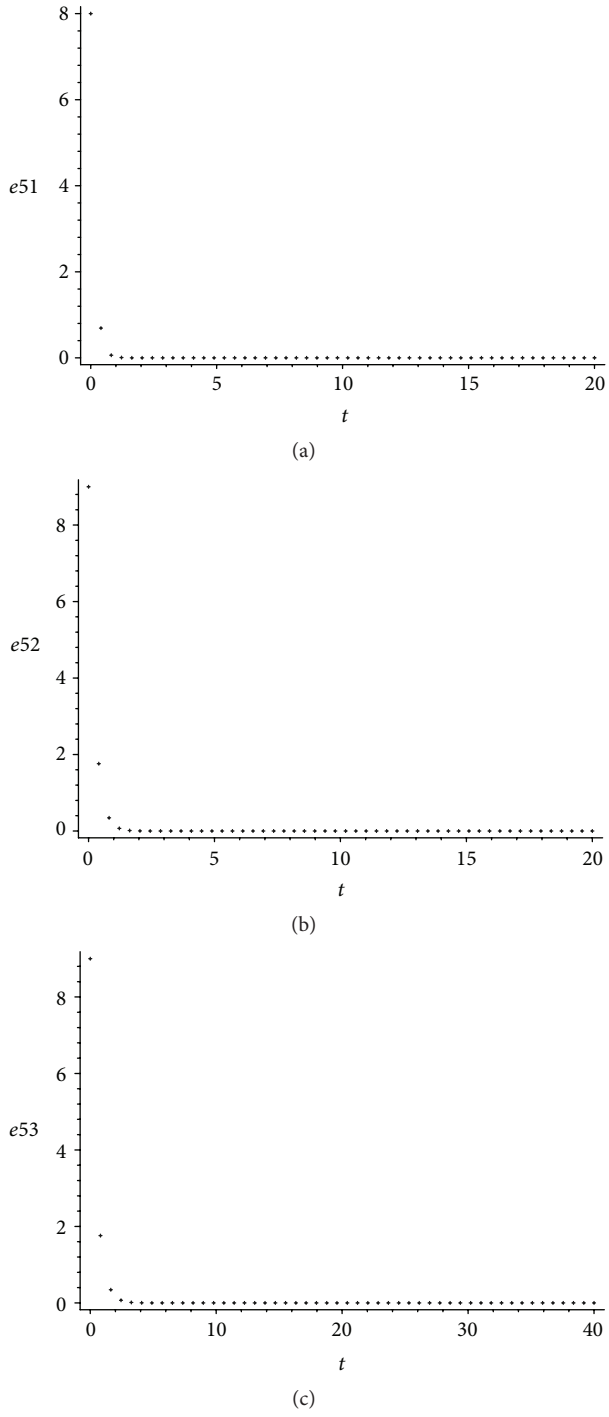

Figure 7: Network synchronization errors between node 4 and node 5.

The dynamic equation of Coullet system [19] is described as follows:

$$\begin{aligned} \dot{x}_3 &= y_3, \\ \dot{y}_3 &= z_3, \\ \dot{z}_3 &= a_3 z_3 + b_3 y_3 + c_3 x_3 + x_3^3, \end{aligned} \tag{13}$$

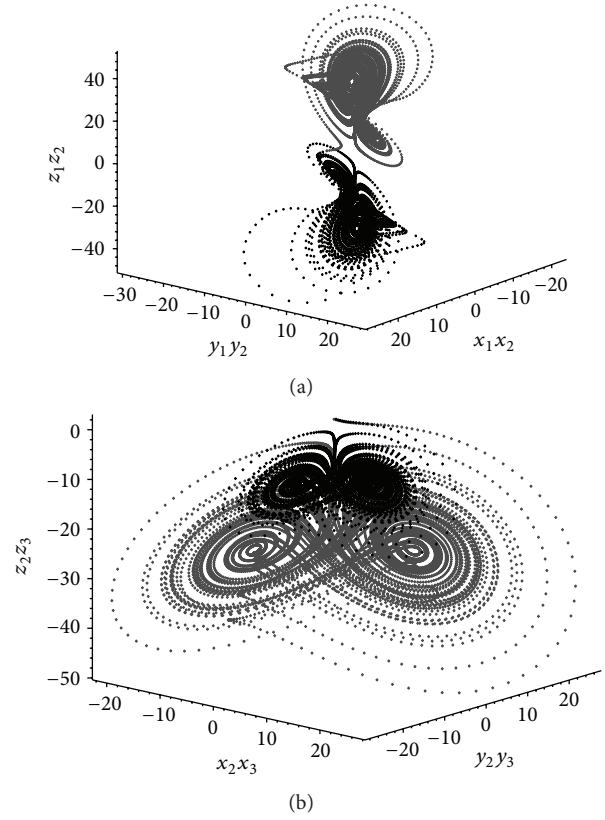

Figure 8: The chaos attractors between node 1 and node 2 (a) and between node 2 and node 3 (b).

where a_3, b_3, and c_3 are parameters of the system. When the parameters are given as $a_3 = 0.45$, $b_3 = 1.1$, and $c_3 = 0.8$, the chaos attractor of (13) is shown in Figure 2(b).

The dynamic equation of new system [23] is described as follows:

$$\begin{aligned} \dot{x}_4 &= d\left(y_4 - x_4\right), \\ \dot{y}_4 &= -y_4 + x_4 z_4, \\ \dot{z}_4 &= e - y_4 x_4 - f z_4, \end{aligned} \tag{14}$$

where d, e, and f are parameters of the system. When the parameters are given as $d = 5$, $e = 16$, and $f = 1$, the chaos attractor of (14) is shown in Figure 3(a).

The dynamic equation of the Chen-Lee system [32] is described as follows:

$$\begin{aligned} \dot{x}_5 &= -y_5 z_5 + a_5 x_5, \\ \dot{y}_5 &= x_5 z_5 + b_5 y_5, \\ \dot{z}_5 &= \frac{1}{3} x_5 y_5 + c_5 z_5, \end{aligned} \tag{15}$$

where $a = 5$, $b = -10$, and $c = -0.38$, (15) is a chaotic system. Figure 3(b) displays the chaotic attractors in (x_1, y_1, z_1)-space. It is easy to see that it admits a symmetry (x_5, y_5, z_5). That is, the system (15) is symmetrical about the three coordinate axes x_5, y_5, and z_5, respectively.

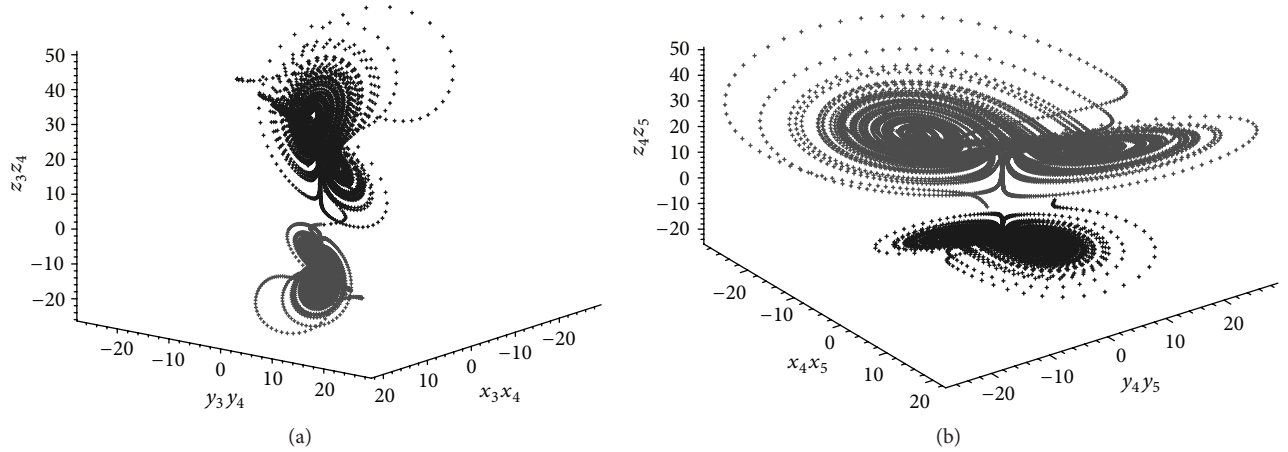

FIGURE 9: The chaos attractors between node 3 and node 4 (a) and between node 4 and node 5 (b).

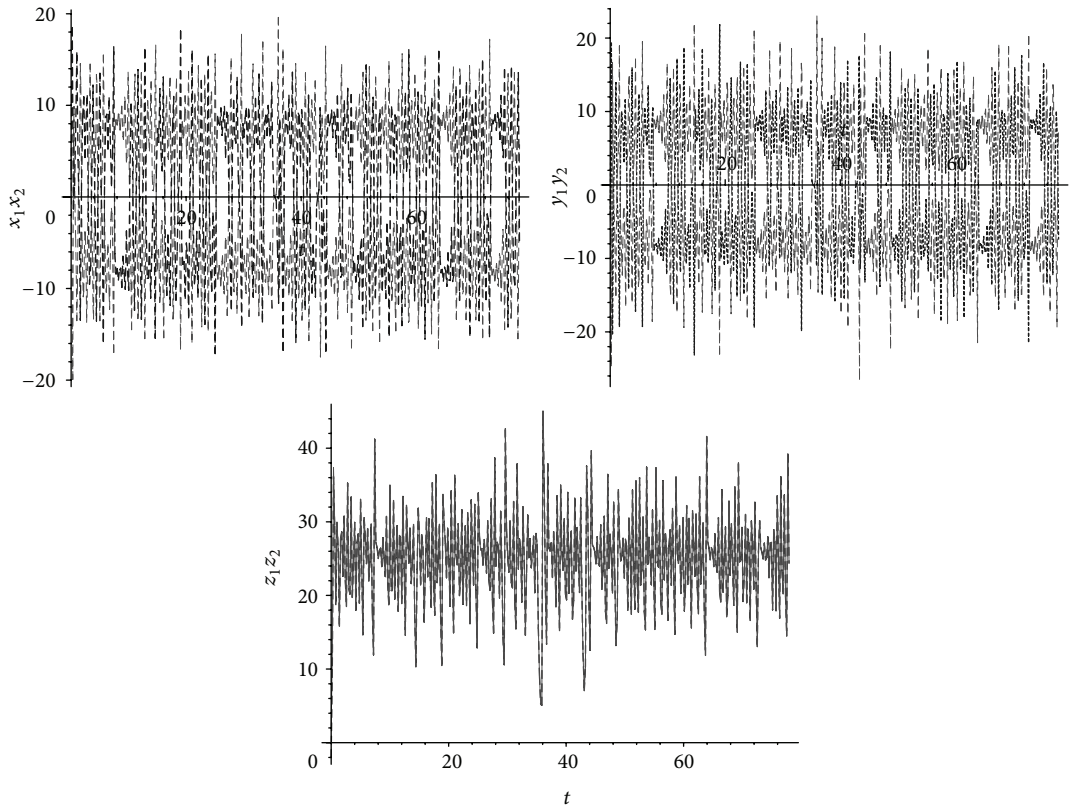

FIGURE 10: The temporal evolution of variables between node 1 ("⋯") and node 2 ("—").

Choose the unified chaotic system (16) (node 1) as a target system, that is, coupling function $g_{1i} = 0$, then the dynamic functions of node 2, node 3, node 4, and node 5 with coupling can be described, respectively, as

$$\begin{aligned} \dot{x}_1 &= (25\alpha + 10)\left(y_1 - x_1\right), \\ \dot{y}_1 &= (28 - 35\alpha)\, x_1 - x_1 z_1 + (29\alpha - 1)\, y_1, \\ \dot{z}_1 &= x_1 y_1 - \frac{8+\alpha}{3} z_1, \end{aligned} \tag{16}$$

$$\begin{aligned} \dot{x}_2 &= -\frac{a_2 b_2}{a_2 + b_2} x_2 - y_2 z_2 + c_2 + g_{21}, \\ \dot{y}_2 &= a_2 y_2 + x_2 z_2 + g_{22}, \\ \dot{z}_2 &= b_2 z_2 + x_2 y_2 + g_{23}, \end{aligned} \tag{17}$$

$$\begin{aligned} \dot{x}_3 &= y_3 + g_{31}, \\ \dot{y}_3 &= z_3 + g_{32}, \\ \dot{z}_3 &= a_3 z_3 + b_3 y_3 + c_3 x_3 + x_3^3 + g_{33}, \end{aligned} \tag{18}$$

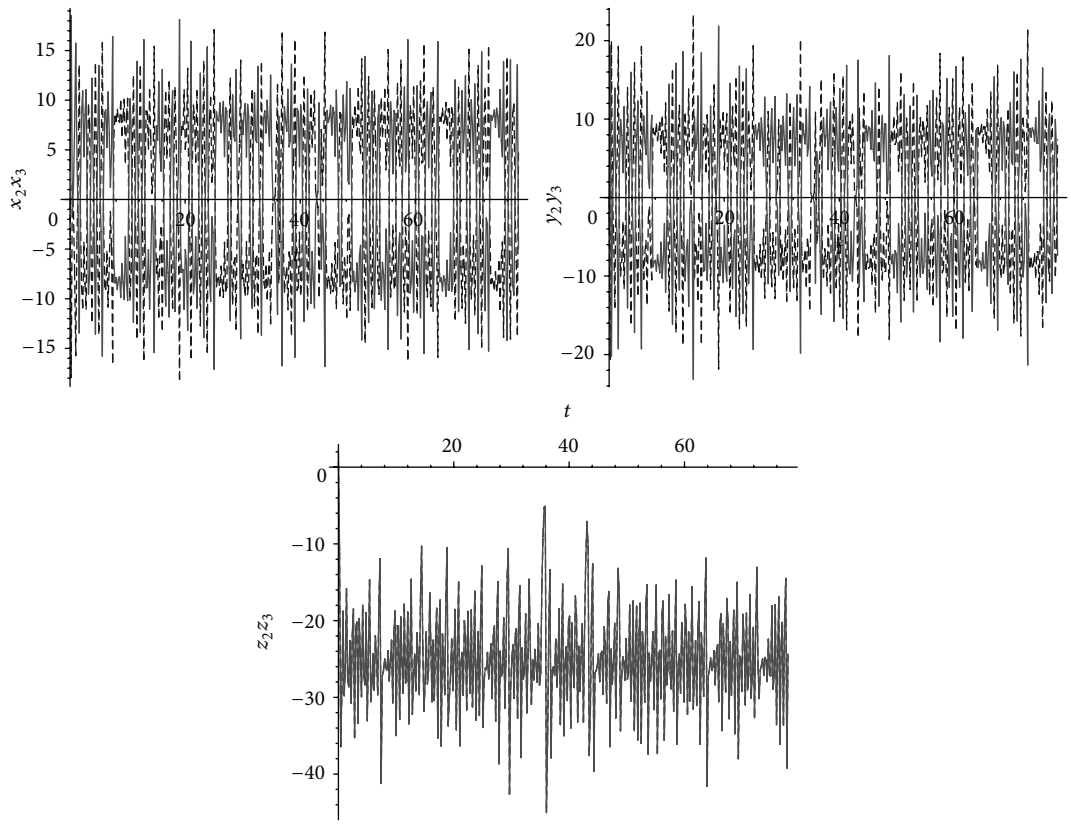

Figure 11: The temporal evolution of variables between node 2 ("···") and node 3 ("—").

$$\begin{aligned}
\dot{x}_4 &= d\left(y_4 - x_4\right) + g_{41},\\
\dot{y}_4 &= -y_4 + x_4 z_4 + g_{42},\\
\dot{z}_4 &= e - y_4 x_4 - f z_4 + g_{43},
\end{aligned} \tag{19}$$

$$\begin{aligned}
\dot{x}_5 &= -y_5 z_5 + a_5 x_5 + g_{51},\\
\dot{y}_5 &= x_5 z_5 + b_5 y_5 + g_{52},\\
\dot{z}_5 &= \frac{1}{3} x_5 y_5 + c_5 z_5 + g_{53},
\end{aligned} \tag{20}$$

where g_j $(j = 2, 3, 4, 5)$ fulfills (6):

$$g_2 = \begin{pmatrix} g_{21} \\ g_{22} \\ g_{23} \end{pmatrix} = \begin{pmatrix} -15y_1 + 14x_1 - \dfrac{27}{7}x_2 - 1 \\ -21x_1 - 6.8y_1 + 8y_2 \\ -0.267z_1 + z_2 \end{pmatrix} + \begin{pmatrix} y_2 z_2 \\ x_1 z_1 - x_2 z_2 \\ -x_1 y_1 - x_2 y_2 \end{pmatrix},$$

$$g_3 = \begin{pmatrix} g_{31} \\ g_{32} \\ g_{33} \end{pmatrix} = \begin{pmatrix} -7.5y_1 + 7x_1 + \dfrac{7}{2}x_2 - y_3 - 8x_1 \\ -10.5x_1 - 3.4y_1 + 2y_2 - z_3 + 6y_3 \\ -0.13z_1 + \dfrac{1}{2}z_2 - 3.55z_3 + 1.1y_3 - 0.8x_3 \end{pmatrix} + \begin{pmatrix} 0 \\ \dfrac{1}{2}x_1 z_1 \\ -\dfrac{1}{2}x_1 y_1 + x_3^3 \end{pmatrix},$$

$$g_4 = \begin{pmatrix} g_{41} \\ g_{42} \\ g_{43} \end{pmatrix} = \begin{pmatrix} 15y_1 - 14x_1 - 7x_2 + 14x_3 - 5y_4 + 4x_4 \\ 21x_1 + 6.8y_1 - 4y_2 + 11y_3 + 0.5y_4 \\ 0.267z_1 - 16 - z_2 + 6z_3 \end{pmatrix} + \begin{pmatrix} 0 \\ -x_1 z_1 - x_4 z_4 \\ x_1 y_1 + x_4 y_4 \end{pmatrix},$$

$$g_5 = \begin{pmatrix} g_{51} \\ g_{52} \\ g_{53} \end{pmatrix}$$

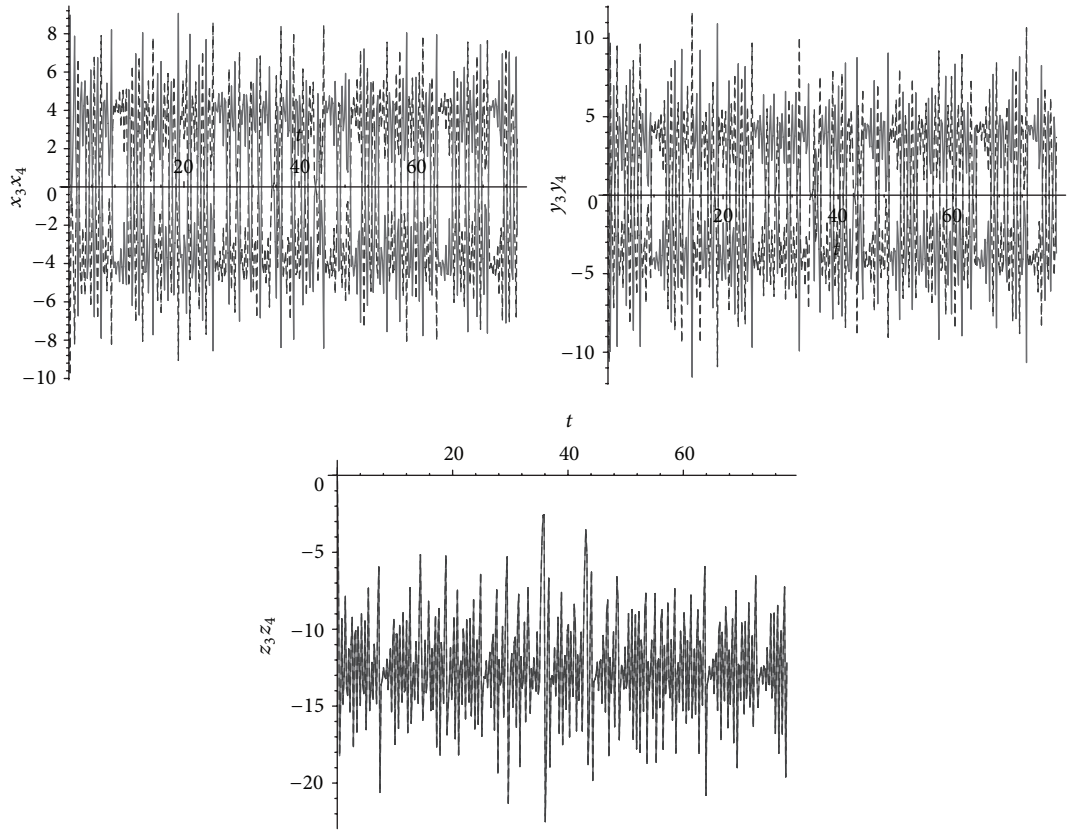

Figure 12: The temporal evolution of variables between node 3 ("···") and node 4 ("—").

$$= \begin{pmatrix} -7.5y_1 + 7x_1 + 3.5x_2 - 7x_3 - 2.5x_4 - 11x_5 \\ -10.5x_1 - 3.4y_1 + 2y_2 - 5.5y_3 - 1.75y_4 + 6y_5 \\ -0.133z_1 + 0.5z_2 - 3z_3 - 0.5z_4 - 1.62z_5 \end{pmatrix} + \begin{pmatrix} z_5y_5 \\ 0.5x_1z_1 - x_5z_5 \\ -0.5x_1y_1 - 0.33x_5y_5 \end{pmatrix}. \quad (21)$$

The relative weight of the coupling strength between the nodes of the network is arbitrarily taken as $K = [-1, -2, -3, 4, 3, 2, -2, -1, -2, -3, -2, -1]$, $\alpha_i = [1, 1, 1, -2, -2, -2, 0.5, 0.5, 0.5, 2, 2, 2]$, then the network synchronization error between system (16) and system (17) will be $e_{21} = x_1 + x_2$, $e_{22} = y_1 + y_2$, and $e_{23} = z_1 + z_2$ and the network synchronization error between system (17) and system (18) will be $e_{31} = x_2 - 2x_3$, $e_{32} = y_2 - 2y_3$, and $e_{33} = z_2 - 2z_3$, and the network synchronization error between system (18) and system (19) will be $e_{41} = x_3 - 0.5x_4$, $e_{42} = y_3 - 0.5y_3$, and $e_{43} = z_3 - 0.5z_4$, and the network synchronization error between system (19) and system (20) will be $e_{51} = x_4 + 2x_5$, $e_{52} = y_4 + 2y_5$, and $e_{53} = z_4 + 2z_5$. The simulations are shown in Figures 4, 5, 6, and 7.

For further details, the dynamic attractors for each node with coupling network synchronization are shown in Figures 8 and 9. The network synchronization temporal evolution of variables is shown in Figures 10, 11, 12, and 13. From Figures 8 and 9, we can see that the network synchronization has been realized on the required proportional scale.

4. Summary and Discussion

In this paper, the complex network synchronization is investigated. With the help of symbolic computation, different order chaotic systems are adopted as the nodes of this complex network; the structure of the coupling functions among the connected nodes is obtained based on Lyapunov stability theory. Being of network and physical interests, the temporal evolution of variables and node interaction of the dynamic equation are discussed and simulated by computer. This method has universal significance for network synchronization, and the weight value of the coupling strength between the nodes and the number of the nodes does not affect synchronization of the whole network.

Acknowledgments

This work is supported by the NSF of China under Grant nos. 11172181, Guangdong Provincial NSF of China under Grant no. 10151200501000008 and 94512001002983,

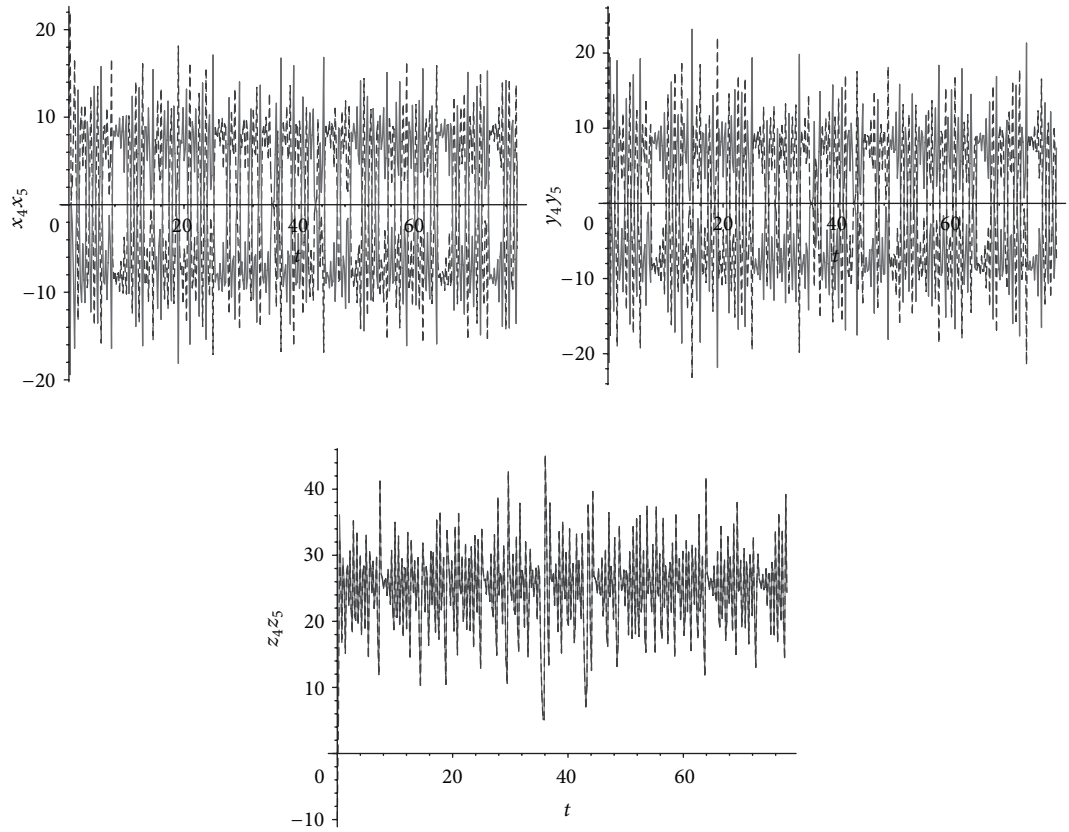

Figure 13: The temporal evolution of variables between node 4 ("···") and node 5 ("—").

Guangdong Provincial UNYIF of China under Grant, and Science Foundation of Shaoguan University.

References

[1] P. Erdös and A. Rényi, "On the evolution of random graphs," *Publication of the Mathematical Institute of the Hungarian Academy of Sciences*, vol. 5, p. 17, 1960.

[2] M. E. J. Newman, S. H. Strogatz, and D. J. Watts, "Random graphs with arbitrary degree distributions and their applications," *Physical Review E*, vol. 64, Article ID 26118, 17 pages, 2001.

[3] F. M. Atay, J. Jost, and A. Wende, "Delays, connection topology, and synchronization of coupled chaotic maps," *Physical Review Letters*, vol. 92, no. 14, pp. 144101–1, 2004.

[4] A. E. Motter, C. Zhou, and J. Kurths, "Network synchronization, diffusion, and the paradox of heterogeneity," *Physical Review E*, vol. 71, Article ID 016116, 9 pages, 2005.

[5] M. Timme, F. Wolf, and T. Geisel, "Topological speed limits to network synchronization," *Physical Review Letters*, vol. 92, Article ID 074101, 4 pages, 2004.

[6] P. Checco, M. Biey, and L. Kocarev, "Synchronization in random networks with given expected degree sequences," *Chaos, Solitons & Fractals*, vol. 35, no. 3, pp. 562–577, 2008.

[7] J. Lü, X. Yu, and G. Chen, "Chaos synchronization of general complex dynamical networks," *Physica A*, vol. 334, no. 1-2, pp. 281–302, 2004.

[8] W. Lu and T. Chen, "Synchronization analysis of linearly coupled networks of discrete time systems," *Physica D*, vol. 198, no. 1-2, pp. 148–168, 2004.

[9] X. Han and J. Lu, "The changes on synchronizing ability of coupled networks from ring networks to chain networks," *Science in China F*, vol. 50, no. 4, pp. 615–624, 2007.

[10] G. He and J. Yang, "Adaptive synchronization in nonlinearly coupled dynamical networks," *Chaos, Solitons and Fractals*, vol. 38, no. 5, pp. 1254–1259, 2008.

[11] Y. C. Hung, Y. T. Huang, M. C. Ho, and C. K. Hu, "Paths to globally generalized synchronization in scale-free networks," *Physical Review E*, vol. 77, Article ID 16202, 8 pages, 2008.

[12] Y. Gao, L. X. Li, H. P. Peng, Y. X. Yang, and X. H. Zhang, "Adaptive synchronization in a united complex dynamical network with multi-links," *Acta Physica Sinica*, vol. 57, no. 4, pp. 2081–2091, 2008.

[13] W. D. Pei, Z. Q. Chen, and Z. Z. Yuan, "A dynamic epidemic control model on uncorrelated complex networks," *Chinese Physics B*, vol. 17, p. 373, 2008.

[14] A. Barrat, M. Barthelemy, and A. Vespignani, "Weighted evolving networks: coupling topology and weight dynamics," *Physical Review Letters*, vol. 92, Article ID 228701, 4 pages, 2004.

[15] Y. Li, Y. Chen, and B. Li, "Anticipated function synchronization with unknown parameters in discrete-time chaotic systems," *International Journal of Modern Physics C*, vol. 20, no. 4, pp. 597–608, 2009.

[16] J. Qin and H. J. Yu, "Synchronization of star-network of hyperchaotic Rossler systems," *Acta Physica Sinica*, vol. 56, pp. 6828–6835, 2007.

[17] Z. Zeng and J. Wang, "Complete stability of cellular neural networks with time-varying delays," *IEEE Transactions on Circuits and Systems*, vol. 53, no. 4, pp. 944–955, 2006.

[18] J. Cao, P. Li, and W. Wang, "Global synchronization in arrays of delayed neural networks with constant and delayed coupling," *Physics Letters A*, vol. 353, no. 4, pp. 318–325, 2006.

[19] L. Ling, L. Gang, G. Li, M. Le, J.-R. Zou, and Y. Ming, "Generalized chaos synchronization of a weighted complex network with different nodes," *Chinese Physics B*, vol. 19, Article ID 080507, 2010.

[20] L. Lü, *Nonlinear Dynamics and Chaos*, Dalian Publishing House, Dalian, China, 2000.

[21] J. Lü, G. Chen, D. Cheng, and S. Celikovsky, "Bridge the gap between the Lorenz system and the Chen system," *International Journal of Bifurcation and Chaos in Applied Sciences and Engineering*, vol. 12, no. 12, pp. 2917–2926, 2002.

[22] J. Lü, G. Chen, and D. Cheng, "A new chaotic system and beyond: the generalized Lorenz-like system," *International Journal of Bifurcation and Chaos in Applied Sciences and Engineering*, vol. 14, no. 5, pp. 1507–1537, 2004.

[23] J. Lü and G. Chen, "A new chaotic attractor coined," *International Journal of Bifurcation and Chaos in Applied Sciences and Engineering*, vol. 12, no. 3, pp. 659–661, 2002.

[24] G. Chen, J. Zhou, and Z. Liu, "Global synchronization of coupled delayed neural networks and applications to chaotic CNN models," *International Journal of Bifurcation and Chaos in Applied Sciences and Engineering*, vol. 14, no. 7, pp. 2229–2240, 2004.

[25] Y. Chen and X. Li, "Function projective synchronization between two chaotic systems," *Zeitschrift für Naturforschung*, vol. 62, p. 176, 2007.

[26] Y. Q. Yang and Y. Chen, "Chaos in the fractional order generalized Lorenz canonical form," *Chinese Physics Letters*, vol. 26, Article ID 100501, 2009.

[27] H. L. An and Y. Chen, "The function cascade synchronization method and applications," *Communications in Nonlinear Science and Numerical Simulation*, vol. 13, no. 10, pp. 2246–2255, 2008.

[28] M. J. Wang, X. Y. Wang, and Y. J. Niu, "Projective synchronization of a complex network with different fractional order chaos nodes," *Chinese Physics B*, vol. 20, Article ID 010508, 2011.

[29] Y. Chen and Z. Yan, "New exact solutions of $(2+1)$-dimensional Gardner equation via the new sine-Gordon equation expansion method," *Chaos, Solitons and Fractals*, vol. 26, no. 2, pp. 399–406, 2005.

[30] E. N. Lorenz, "Deterministic nonperiodic flow," *Journal of the Atmospheric Sciences*, vol. 20, pp. 130–141, 1963.

[31] G. Chen and T. Ueta, "Yet another chaotic attractor," *International Journal of Bifurcation and Chaos in Applied Sciences and Engineering*, vol. 9, no. 7, pp. 1465–1466, 1999.

[32] M. B. Sedra and A. El Boukili, "Some physical aspects of Moyal noncommutativity," *Chinese Journal of Physics*, vol. 47, no. 3, pp. 305–315, 2009.